

# CONSOLIDATION MECHANISMS AND INTERFACIAL PHENOMENA IN THERMOPLASTIC POWDER IMPREGNATED COMPOSITES

THÈSE N° 1413 (1995)

PRÉSENTÉE AU DÉPARTEMENT DES MATÉRIAUX

ÉCOLE POLYTECHNIQUE FÉDÉRALE DE LAUSANNE

POUR L'OBTENTION DU GRADE DE DOCTEUR ÈS SCIENCES TECHNIQUES

PAR

**Marco CONNOR**

Ingénieur en science des matériaux diplômé EPF  
de nationalité irlandaise

acceptée sur proposition du jury:

Prof. J.-A. Manson, directeur de thèse  
Dr M. Barbezat, corapporteur  
Dr R. Gotthardt, corapporteur  
Prof. A. Hult, corapporteur

Lausanne, EPFL  
1995

## ABSTRACT

Thermoplastic powder impregnation of continuous reinforcement filaments is studied in this work, focusing on impregnation mechanisms and interfacial phenomena. Various existing techniques to mingle powdered resins to continuous filaments are reviewed; a powder impregnation line designed at the Laboratoire de Technologie des Composites et Polymères (LTC) is presented. Two important types of powder coated towpregs are addressed: *FIT bundles* (Fibres Imprégnées de Thermoplastique) of powder loaded fibres enclosed in a thin resin sheath, and *molten powder towpregs* in which the particles are fixed to the fibres in an oven by melting the resin.

The impregnation mechanisms of powder coated towpregs are examined. The formation of resin bridges between adjacent fibres is first investigated using a hot stage placed on a microscope. In the absence of externally applied pressure, impregnation is driven by surface energy effects. The driving forces leading to the spreading of the bridge along the fibres are analysed at two levels: at a macroscopic scale, characterising the capillary pressure governing the flow of a liquid into a porous solid, and at a micro-mechanical level analysing the capillary forces in a system defined by a liquid drop in contact with two solid particles.

To achieve impregnation at a satisfactory rate, however, it is essential to apply external pressure to most thermoplastic systems during consolidation. An analytical model for the consolidation stage of unidirectional-powder coated towpregs is presented, placing in context effects due to surface energy, viscous flow, externally applied pressure and fibre bed elasticity. The initial conditions for the computation depend on the impregnation technique used. *FIT bundles*, and *molten powder towpregs* are examined. The model is compared at each stage to experimental data obtained by compression moulding powder impregnated towpregs in an instrumented hydraulic press using a closed matched-die mould. This model optimises the processing conditions of a given fibre-resin system to achieve a void free laminate with improved mechanical properties.

Mechanical properties can further be improved by optimising interfacial adhesion between resin and fibres. Surface energy effects on composite mechanical properties are studied, relating thermodynamic quantities to adhesive strength. A criterion for optimum adhesion is proposed. The influence of the thermodynamic adhesion between fibres and matrix on the mechanical properties of a continuous fibre reinforced composite is studied for two systems: carbon fibre reinforced poly(ether-ether-ketone) and glass fibre reinforced poly(ether-imide). The fibre surface is modified chemically and characterised by optical contact angle measurements of molten resin droplets on the fibres. Unidirectional fibre reinforced laminates are manufactured. Transverse flexural strength is reported as a function of thermodynamic wetting parameters. Adhesion at the fibre-resin interface is found to correlate with both composite strength and void morphology within the laminate after consolidation.

Full potential of powder coated towpregs as a precursor for compression moulded composite parts can be reached by the fabrication of drapeable textile preforms. Corrugated sheets are processed using *FIT* woven fabrics. Mechanical property measurements show that complex high quality parts can be processed at high rates using powder coated towpregs.

# RÉSUMÉ

Le but de ce travail est la caractérisation des mécanismes d'imprégnation et des phénomènes interfaciaux dans la technique d'imprégnation par poudre thermoplastique de fibres continues. Différents procédés permettant de mélanger de fines poudres de résine à des fibres continues sont présentés, ainsi qu'une ligne d'imprégnation conçue et réalisée au Laboratoire de Technologie des Composites et Polymères (LTC). Deux types de mèches imprégnées de poudre sont étudiés dans ce travail: les mèches *FIT* (Fibres Imprégnées de Thermoplastique) où une fine gaine de résine enferme les fibres chargées de poudre, et les *mèches de poudre fondue* où la poudre est fixée aux fibres dans un four en fondant la résine.

Les mécanismes d'imprégnation par poudre des fibres sont analysés. La formation de ponts de résine entre les fibres est étudiée par observation au microscope muni d'une platine chauffante de mèches chargées de poudre. Les effets d'énergie de surface, responsables de l'écoulement des ponts de résine en l'absence de forces mécaniques, sont étudiés à deux niveaux: à l'échelle macroscopique par la caractérisation de la pression capillaire qui provoque l'écoulement d'un liquide dans un solide poreux, et à l'échelle microscopique par l'analyse des forces capillaires dans un système défini par une goutte de liquide en contact avec deux particules solides.

Dans la pratique, une pression mécanique est appliquée afin d'assurer une imprégnation homogène et rapide. Un modèle analytique d'imprégnation par poudre de fibres UD est proposé. Ce modèle décrit l'écoulement visqueux de la résine en fonction de la résistance élastique du lit de fibres et des pressions capillaire et mécanique. Les conditions initiales dépendent de la géométrie du système. Deux cas sont examinés: les mèches FIT et les mèches de poudre fondue. Le modèle est comparé à des données expérimentales obtenues par moulage par compression de fibres chargées de poudre dans un moule fermé monté sur une presse hydraulique. Ce modèle d'imprégnation permet d'optimiser les conditions de mise en oeuvre d'un système fibre-résine donné, et ainsi d'en améliorer les propriétés mécaniques.

Les propriétés mécaniques peuvent être améliorées davantage en optimisant l'adhésion entre les fibres et la résine. Un critère basé sur des grandeurs thermodynamiques permettant l'optimisation de l'adhésion entre deux corps est proposé. L'influence de l'adhésion entre fibres et matrice sur les propriétés mécaniques d'un composite est étudiée pour deux systèmes: poly (ether-ether-cétone) renforcé de fibres de carbone et poly (ether-imide) renforcé de fibres de verre. La surface des fibres est modifiée chimiquement et caractérisée par la mesure de l'angle de contact formé par des gouttelettes de résine déposées à la surface des fibres. Des laminés renforcés de fibres modifiées unidirectionnelles sont mis en oeuvre. La résistance en flexion trois points transverse aux fibres est reportée en fonction de paramètres thermodynamiques de mouillage. On observe que l'adhésion à l'interface résine-fibre corrèle avec la résistance du composite et la morphologie des pores après consolidation.

L'utilisation de mèches imprégnées de poudre thermoplastique comme précurseur pour la fabrication de pièces composites par compression est plus intéressante lorsqu'on utilise des préformes textiles souples. Des plaques ondulées sont mises en oeuvre en utilisant des tissus FIT. La mesure des propriétés mécaniques montre que des pièces à géométrie complexe de haute qualité peuvent être fabriquées à haute vitesse en utilisant des fibres chargées de poudre.

## ACKNOWLEDGEMENTS

During the course of this work I have received the invaluable help of many people; I would like to thank them all for their support and encouragement.

In particular, I wish to acknowledge my thesis supervisor Prof. Jan-Anders E. Månson for his strong support and trust during the course of this work. I am indebted to my advisor Dr. Staffan Toll for his excellent guidance and fruitful discussions, and for his good company. To Prof. Geoffrey Gibson from the University of Newcastle upon Tyne (UK), Prof. John Berg from the University of Washington (USA), and Dr. Jacques-Eric Bidaux from the Ecole Polytechnique Fédérale de Lausanne, I express my gratitude for their educative comments, suggestions, and help.

I acknowledge Dr. Michel Barbezat from Huber+Suhner AG, and Mr. Jean-Pierre Lépine and Mr. Pierre-Eric Chabout from Porcher Textile, for a pleasant and educating collaboration.

My grateful thanks are due to Mr. Philippe Berguerand, who made miracles in designing the experimental tools and equipment, and to the technicians of the Département des Matériaux (DMX) workshop who manufactured them.

Special thanks are due to Mr. Phil Harding from the University of Washington, for his valuable contribution to the study on interfacial strength of composites, and for his sincere friendship. I thank Olivier Rozant, David Mendels, Casper Koster, and Roland Dabbous, students at the Département des Matériaux, for their contribution to this work during their diploma work or semester project.

I wish to thank all the members of the Laboratoire de Technologie des Composites et Polymères who, by their knowledge, advice, good humour, etc., helped me to carry out this study. In particular Mrs. Antoinette Marciano who makes everybody's life easy by taking care of the administrative problems.

Last but not least, I wish to acknowledge the love and encouragement of my family and especially my wife Marta, for her help, support and understanding.

This work was financially supported by the "Commission pour l'Encouragement de la Recherche Scientifique" (CERS) and by Huber+Suhner AG. I would especially like to acknowledge Dr. Hans Widmer from Huber+Suhner AG for providing the extra means needed to make this work possible.

# TABLE OF CONTENTS

Chapter 1: Introduction.....	1
Chapter 2: Background.....	7
2.1 Thermoplastic composite processing.....	7
2.1.1 Constituents of Thermoplastic Composites.....	7
2.1.2 Introduction to processing of advanced composites.....	9
2.1.3 Pre-impregnation processes.....	10
2.1.4 Impregnation after shaping.....	11
2.1.5 Manufacturing of powder impregnated parts.....	14
2.2 Powder coating.....	14
2.2.1 Tow spreading unit.....	16
2.2.2 Particle characterisation.....	18
2.2.2 Powder coating unit.....	21
2.2.3 Towpreg stabilisation unit.....	29
2.2.4 Powder content control.....	32
2.2.5 Review of powder coating lines.....	33
2.3 References.....	38
Chapter 3: Analysis of the impregnation mechanism.....	41
3.1 Resin bridge formation.....	41
3.2 Capillary action.....	44
3.2.1 Background.....	44
3.2.2 Capillary pressure.....	47
3.2.3 Capillary inter-particle forces.....	49
3.3 Summary.....	54
3.4 References.....	56
Chapter 4: Consolidation model.....	57
4.1 Consolidation equation.....	58
4.1.1 Basic assumptions.....	58
4.1.2 Initial and final states.....	59
4.1.3 Viscous pressure.....	60
4.1.4 Capillary pressure.....	61
4.1.5 Spring pressure.....	62
4.1.6 Consolidation rate equation.....	62
4.2 Powder impregnated fibre geometry —examples.....	63
4.2.1 FIT towpreg.....	63
4.2.2 Molten powder towpregs.....	64
4.3 Experimental.....	66
4.3.1 FIT towpreg characterisation.....	66
4.3.2 Molten powder towpreg characterisation.....	67

4.3.3	Consolidation of laminates.....	70
4.4	Results and discussion .....	71
4.4.1	Consolidation of FIT yarns .....	71
4.4.2	Consolidation of molten powder towpregs .....	74
4.5	Summary .....	77
4.6	References .....	78
Chapter 5: A criterion for optimum adhesion.....		79
5.1	Introduction to adhesion.....	80
5.2	Wetting parameters .....	82
5.2.1	Work of adhesion .....	82
5.2.2	Spreading coefficient .....	83
5.2.3	Wetting tension .....	83
5.2.4	Interfacial energy .....	84
5.3	Adhesion optimisation .....	86
5.3.1	Extrema of the wetting parameters .....	86
5.3.2	Maximum wetting tension .....	89
5.4	References .....	93
Chapter 6: Effects of Surface Energy on the Mechanical Properties of Composites ....		95
6.1	Introduction .....	95
6.1.1	Surface energy parameters measurement.....	96
6.1.2	Originality of the present approach.....	98
6.2	Materials and Methods .....	99
6.2.1	Fibres and fibre surface modification .....	99
6.2.2	Contact angle measurement .....	100
6.2.3	Laminate manufacturing and testing.....	103
6.3	Results and Discussion.....	103
6.3.1	Fibre-matrix contact angle .....	103
6.3.2	Transverse flexural strength.....	106
6.3.3	Wetting parameters/interfacial strength relationship .....	111
6.3.4	Discussion .....	111
6.4	Summary .....	113
6.5	References .....	114
Chapter 7: Manufacturing of Complex Geometry Parts.....		117
7.1	Textile preforms .....	117
7.1.1	Woven fabrics .....	118
7.1.2	Braided fabrics .....	119
7.1.3	Powder coated towpreg fabrics .....	120
7.2	Consolidation of woven flat laminates.....	121
7.2.1	Materials characterisation .....	121
7.2.2	Consolidation of flat laminates .....	122
7.2.3	Consolidation model .....	122
7.2.4	Flat laminates consolidation curves .....	123

7.3	Woven corrugated sheets manufacturing .....	125
7.3.1	Corrugated sheets processing .....	126
7.3.2	Characterisation of the corrugated parts .....	128
7.4	Results and discussion .....	130
7.4.1	Void volume content .....	130
7.4.2	Mechanical tests .....	133
7.4.3	Summary .....	137
7.5	References .....	138
Chapter 8: Conclusions .....		139
Appendix: List of Symbols .....		143
Curriculum vitae .....		145

# 1

## INTRODUCTION

When carbon fibres were first introduced, there was a strong interest for processing high performance composite materials based on both thermoplastic and thermoset polymeric matrices. Aerospace industry in particular was exploring the use of these materials for their excellent strength-to-weight performance. Even if the mechanical properties of thermoplastic-based composites show many advantages, in 1990, 97% of the total market for polymer matrix structural composites was covered by thermosetting resins, and in particular epoxy resins [1]. This is mainly due to the high viscosity of thermoplastic resins, which makes impregnation of high volume fraction fibre beds quite difficult. Several solutions were proposed to “pre-impregnate” the fibres, thus obtaining *prepreg* sheets. The resulting prepregs are relatively stiff and boardy, limiting their handling and drapeability during part manufacturing. Consequently, prepregging techniques are particularly suited for the manufacture of relatively small series of large and flat structures. As the interest for the fabrication of larger series of smaller and more complex shape composite parts increases, there is a growing demand for more drapeable and easy-to-handle precursors. Novel processing techniques need to be explored to manufacture complex geometry composite parts made of high viscosity resin at intermediate pressure levels.

In this work, an alternative technique for impregnating high volume content continuous filaments by thermoplastic resins called *powder impregnation* is investigated. The aim of this study is to characterise the relation between *structure*, *processing* and *properties* of powder impregnated composites and to assess the applicability of such a technique to the manufacture of relatively complex shapes at economical rates.

In powder impregnation, dry thermoplastic powder is incorporated into the fibre tow to obtain a flexible towpreg. The powder coated towpreg is then stabilised. This is often achieved by sintering the powder particles onto the fibres by passing the powder laden tow into an oven. Ganga [2] developed a system called FIT (Fibres Imprégnées de Thermoplastique) which allows the fibre/powder tow to be stabilised without melting the resin particles by coating it with a thin sheath of resin using a wire coating die. Towpregs can easily be woven, braided or knitted to obtain drapeable fabrics which can be stacked and shaped into complex geometry parts by applying heat and pressure. In this study, matched-die compression moulding of thermoplastic powder impregnated unidirectional- (UD) and woven-continuous carbon and glass fibres is addressed. Three



thermoplastic resins have been used: one *engineering* resin, polyamide 12 (PA12) and two *high-performance* grades, poly (ether-ether-ketone) (PEEK) and poly (ether-imide) (PEI).

Although the first patent on the production of powder coated towpregs was deposited by Price in 1973 [3] there has been a 15 year gap until the industrial and scientific community showed an interest in the field. Many experimental studies have then been published presenting powder coating lines —these are reviewed in Chapter 2— and the manufacture of powder impregnated composites. To characterise the process-structure-property interrelation of powder impregnated composites, three main topics need to be covered: (i) impregnation mechanisms, (ii) consolidation optimisation, and (iii) surface energy effects on composite strength.

### ***Impregnation mechanisms.***

Only a few authors have proposed an impregnation mechanism for powder coated fibres. Iyer and Drzal [4] examined sintering and droplet formation of fused powder particles in contact with a single fibre. Their work did not consider, however, that the resin particles in a real powder coated towpreg generally are in contact with more than one fibre at the time, yielding a different spreading behaviour. Ye et al. [5] assumed in an analysis on the consolidation of FIT yarns, that the powder particles in the fibre tow took no active part in the consolidation process and were only considered in terms of “reduced voids.” They proposed that consolidation takes place only by “radial impregnation of the resin sheath into the fibre bed,” not considering the actual liquid powder flow. The validity of this description is unclear, however, since longitudinal permeability is known to be considerably larger than transverse permeability in high volume fraction beds [6]. In 1995, Ramani et al. [7] described qualitatively the spreading behaviour of resin droplets in contact with two parallel fibres. Their study, however, did not include the contribution of the capillary effects. Gibson and Månson [8], Connor et al. [9], and later Ye et al. [10] proposed an expression including the additional effects of macroscopic capillary pressure during powder impregnation. Nevertheless, an analysis at a microscopic scale of the capillary forces acting on a number of particles connected by liquid drops is still needed to understand the mechanisms involved in the formation of resin bridges between fibres at the initial stage of impregnation. This defines the initial conditions of the consolidation process during part manufacturing.

### ***Consolidation modelling***

There are two possible approaches to investigate the influence of consolidation parameters on the quality of finished parts. First, a statistical factorial experiment can be designed which allows the relative influence of each parameter investigated to be determined [11]. This approach only provides information on the specific material/process combination studied and does not describe the generic physical properties governing the impregnation and consolidation process. This was done by Thiede-Smet et al. [12], who investigated the influence of time, pressure, and temperature on the quality of CF-PEEK FIT composites manufactured using both autoclave and press forming. Ramani et al. [7] designed a factorial experiment at two

levels (low-high) to determine the effects of time, pressure, tow rate, and temperature on the quality of pultruded parts. The former study showed that improved properties were obtained when time, temperature, and pressure were increased. The latter study showed that temperature and tow rate are the most significant factors affecting the consolidation of pultruded powder coated towpregs. The second possible approach, allowing a quantitative analysis to be made, is to derive a consolidation model describing the role of the factors of interest. Ye et al. [5, 10] have presented a model for the consolidation of FIT laminates based on the radial sheath impregnation mechanism mentioned above. In their work, the liquid powder flow is neglected, while a model would be required to describe the flow of the resin bridges along the channel formed by adjacent parallel fibres, driven by capillary and externally applied pressure as a function of towpreg properties: matrix viscosity, fibre and powder radius and volume content.

### *Surface energy effects on composite strength*

A high degree of impregnation in a composite part is a necessary, but not sufficient, condition to achieve good mechanical properties. It is also necessary to optimise the adhesion at the fibre-resin interface. Indeed, when a composite structure is loaded, the load is transferred from the matrix to the fibres through shear stresses at the fibre-matrix interface. Load transfer is enhanced by strong bonds at the interface. The effects of interfacial strength can be characterised by mechanical tests. If the adhesion between fibres and matrix is poor, the fibres at the fracture surface will be stripped clean, and the composite strength will be lower than if the interfacial strength was high. An example of such effect was observed by Ogden et al. [13], who successfully processed void free CF reinforced LaRC TPI composites, but obtained poor mechanical properties due to a weak interface between matrix and fibres. Today, the mechanisms leading to an optimal interfacial adhesion and the techniques used to characterise the interfaces are still actively debated. Various contradictory criteria for optimising the adhesive strength are proposed in literature, mainly dealing with flat interfaces. Only few theoretical studies are devoted to fibre-matrix adhesion in composites [14, 15]. The characterisation of the fibre-matrix interfacial strength in a composite includes choosing a proper criterion for optimum adhesion which corresponds to the geometry of fibre reinforced composites.

In this work, the three topics mentioned above are systematically investigated and analysed in a unified way to characterise the *process-structure-property* interrelation for powder impregnated composites. Each subject is treated theoretically and illustrated by experimental results on model systems. The theoretical results can be generalised to any system within the assumptions made. The information thus collected is finally scaled up to the production of complex geometry parts of industrial interest.

Chapter 2 presents a concise review of the specific properties of different fibre and resin types, and of the various processing routes for the manufacture of continuous fibre reinforced thermoplastic composites. The techniques used to mingle fine polymer powder and continuous fibres are then examined. The various elements of a powder coating line are reviewed, and a line designed at the Laboratoire de Technologie des Composites et Polymères (LTC) is presented.

The *structure*  $\Leftrightarrow$  *process* relation is studied in Chapter 3, where a mechanism for the impregnation of fibres by molten resin powder is proposed on the basis of

microscopy observation. Surface energy effects on the spreading of polymer droplets on fibre surfaces are discussed. A general equation for the capillary pressure during impregnation is presented and subsequently specialised to particular processes, including powder impregnation [16]. Furthermore, attractive and repulsive forces between particles connected by liquid droplets are analysed, describing when capillary driven impregnation —*spontaneous impregnation*— is present.

The *process*  $\Leftrightarrow$  *properties* relation is examined in Chapter 4 where a quantitative consolidation model is derived, based on the impregnation mechanism proposed in Chapter 3, relating surface energy effects, externally applied pressure, resin flow, and fibre bed elasticity to the consolidation of UD powder impregnated laminates [17]. The composite void content can thus be analysed as a function of time. The predicted consolidation curves are compared to experimental data measured on model systems.

The *structure*  $\Leftrightarrow$  *properties* relation is treated in Chapters 5 and 6, where the influence of the surface energy of the fibres and resin is related to the bond strength of the fibre-matrix interface of the composite. A theoretical study is carried out in Chapter 5 relating the fibre-resin bond strength to a number of thermodynamic quantities. A criterion for optimum adhesion is proposed. An experimental study on composite laminates consisting of chemically altering the fibre surface energy is then presented in Chapter 6, confirming some of the theoretical predictions.

Finally, the consolidation of FIT woven laminates is examined in Chapter 7 defining the processing parameters for the consolidation of corrugated FIT woven laminates. The properties of the FIT corrugated laminates will be compared to laminates of similar geometry made of braided yarns of commingled polymeric and reinforcing fibres.

## REFERENCES

- 1 Cogswell, F. N., "Thermoplastic Aromatic Polymer Composites", Butterworth-Heinemann, 1992, p. 5.
- 2 Ganga, R., 1983, *French Patent* FR 25408084-A1.
- 3 Price, R. V., 1973, *US Patent* 3, 742,106.
- 4 Iyer, S. R. and Drzal, L. T., *J. Thermoplastic Compos. Mater.* 1990, 3, 325.
- 5 Ye, L., Klinkmüller, V and Friedrich, K., *J. Thermoplastic Composite Materials* 1992, 5, 32.
- 6 Lam, R. C. and Kardos, J. L., *3rd Annual Technical Conference American Society for Composites* 1988, p. 3.
- 7 Ramani, K., Borgaonkar, H. and Hoyle, C., *Composites Manufacturing* 1995, 6, 35.
- 8 Gibson, A. G. and Manson, J.-A. E., *Composites Manufacturing* 1992, 3, 223.

- 9 Connor, M., Gibson, A. G., Toll, S. and Manson, J.-A. E., *ICCM-9 1993, III*, p. 575.
- 10 Ye, L., Friedrich, K., Cutolo, D. and Savadori, A., *Composites Manufacturing 1994*, **5**, 41.
- 11 Montgomery, D. C., "Design and Analysis of Experiments," John Wiley and Sons, NY, 1984, pp. 445-474.
- 12 Thiede-Smet, M., Liu, M. and Ho, V. *34th Int. SAMPE Sympos.* 1989, p. 1223.
- 13 Ogden, A. L., Hyer, M. W., Wilkes, G. L. and Loos, A. C., *J. Thermopl. Compos. Mater.* 1992, **5**, 14.
- 14 Nardin, M., Asloun, E. M. and Schultz, J., *Polym. Adv. Technol.* 1991, **2**, 109.
- 15 Schultz, J. and Lavielle, L., *ACS Sympos.* 1989, 391, p. 185.
- 16 Connor, M., Toll, S. and Manson, J.-A. E., *3rd Int. Confer. Flow Processes in Composite Materials '94 1994*, Galway, p. 522. also in *Composites Manufacturing 1995*, in press (issue September).
- 17 Connor, M., Gibson, A. G., Toll, S. and Manson, J.-A. E., *J. Thermoplastic Compos. Mater.* 1995, **8**, 138.



# 2

## BACKGROUND

Fibre reinforced composites can be considered as composed of three elements: the reinforcing fibres, the matrix resin, and the interface between the two constituents. The properties of the final composite part largely depend on the properties of these three elements and the manufacturing conditions. A brief review of the specific properties of the constituents of a composite is presented followed by a summary of the various processing routes available for the manufacture of advanced thermoplastic composites. Finally, the techniques used to mingle fine polymer powder and continuous fibres are examined. The various elements of a powder coating line are reviewed, and a line designed at the Laboratoire de Technologie des Composites et Polymères (LTC) is presented.

### 2.1 THERMOPLASTIC COMPOSITE PROCESSING

#### 2.1.1 Constituents of Thermoplastic Composites

##### *Fibres*

Reinforcements in advanced composite materials are generally in the form of long or continuous fibres. Glass, carbon, and aramid (Kevlar)-fibres are the most common reinforcements used for polymeric matrices. In this study, glass and carbon fibre reinforced composites are used as model systems. There is a variety of grades of glass fibres depending on their composition. The grade used in this work is E-glass from Owens-Corning. The designation E in E glass stands for Electrical, referring to the good insulating properties of E glass.

The carbon fibres used in this study have a diameter of the order of 7  $\mu\text{m}$ , while the diameter of glass fibres ranges between 15 and 20  $\mu\text{m}$ . Small fibre radius,  $R_f$ , is favourable since it increases the specific fibre-matrix interfacial area,  $2/R_f$ . Furthermore, carbon fibres have lower density and superior mechanical properties than glass. Specific mechanical properties of carbon fibres, i.e. mechanical property to density ratio, are particularly good. Typical properties of E glass fibres are compared to carbon fibres in Table 2.1.

Table 2.1: Typical properties of E glass and PAN based carbon fibres

Fibre	Radius [ $\mu\text{m}$ ]	Density [ $\text{g}\cdot\text{cm}^{-3}$ ]	Tensile strength [MPa]	Young's modulus [GPa]
E glass [1]	10–20	2.55	1750	70
carbon (T300)[2]	5–10	1.76	3530	230

### Resins

The polymer matrix of a reinforced composite can be either a thermoplastic or a thermosetting resin. This work is devoted to the analysis of thermoplastic resin composites. It is necessary, however, to present some properties of thermosetting resins to understand the motivations for using thermoplastic resins as a matrix.

Thermosetting polymers consist of a tri-dimensional network connected by covalent bonds. Inter-chain bond energy is very high in this case (20–30  $\text{kJ}\cdot\text{mol}^{-1}$ ). The final thermoset material is obtained as the result of the chemical reaction (curing) of multifunctional low molecular mass compounds (monomers). Part shaping must take place in the liquid state, prior to gelation, i.e. the formation of a continuous network. Processing time of thermoset composites is mainly controlled by their curing kinetics; it can be several hours long. Thermosetting polymers are often amorphous glassy materials.

Table 2.2: High performance thermoplastic resins (after [3])

Polymer	Type	$T_g$ [ $^{\circ}\text{C}$ ]	$T_m$ [ $^{\circ}\text{C}$ ]	Processing T [ $^{\circ}\text{C}$ ]
PEEK (grade 150) (*) ICI	X	143	343	360–400
PEI (Ultem 1000) (*) GE Plastics	A	217	–	300–400
PEI (P-IP) Mitsui Toatsui	X	270	380	380–420
PA12 (*) Elf Atochem, EMS-Chemie	X	49	180	200
Polyimide LaRC-TPI Mitsui Toatsui	A-PTP	250	325 <sup>a</sup>	350
Polyimide Ciba-Geigy	A-PTP	265	–	350

(\*) = material studied in this work;

X = semi-crystalline; A = amorphous; and A-PTP = amorphous pseudo-thermoplastic.

<sup>a</sup> in a semi-crystalline form

Thermoplastic resins are formed of long, linear or branched chains without primary covalent bonds between the chains. They are linked by secondary physical bonds (e.g. van der Waals forces) of low energy (3–5  $\text{kJ}\cdot\text{mol}^{-1}$ ). Thermoplastic resins can be amorphous or partially crystalline. Amorphous polymers can usually be processed at

approximately 50–100°C above the glass transition temperature,  $T_g$ , while semi-crystalline resins can only be processed above their melting temperature,  $T_m$ . The viscosity of molten thermoplastic resins is generally of the order of  $10^2$ – $10^4$  Pa·s, which is two to four orders of magnitude higher than the viscosity of thermosetting resins prior to gelation. Thermoplastic resins usually show higher *toughness* and *elongation to break* than thermosets, but their *stiffness* and *service temperature* are usually lower. Table 2.2 lists  $T_g$ ,  $T_m$ , and processing temperature of a selection of high performance thermoplastic resins. The polymers used in this study are marked with an asterisk (\*). These are: PEEK (grade 150 from ICI), PEI (Ultem 1000 from GE Plastics), and PA12 (from EMS-Chemie AG and Elf-Atochem).

### *Fibre-matrix interface*

Mechanical properties of unidirectional (UD)-fibre reinforced composites are greatly affected by the bond strength of the resin-matrix interface. Load is transferred from the resin to the fibres through shear and tensile stresses at the interface. The strength of the adhesive joint depends on both the flaw density at the interface, and the degree of molecular interactions across a unit area of interface. The surface chemistry of both phases can be modified to optimise their adhesive strength. Examples of fibre treatments enhancing the mechanical properties of CF reinforced composites can be found in Chapter 6.

## 2.1.2 Introduction to processing of advanced composites

Processing of advanced composites consists of impregnating with a resin, shaping, and consolidating high volume fraction fibre beds. One of the critical steps in the preparation of composites is the impregnation of the fibres with matrix resin, as it creates the reinforcing synergy in the final structure. Impregnation generally is the rate determining operation in thermoplastic composites processing. The Darcy law may be used to relate the average flow velocity of a fluid into a porous bed (e.g., fibre bed) to the applied pressure,  $P$ , the solid permeability,  $K$ , the fluid viscosity,  $\eta$ , and the depth of impregnation,  $a$ ,

$$\frac{da}{dt} = \frac{KP}{\eta a} \quad (2.1)$$

By integrating Equation 2.1, and assuming constant permeability during the impregnation process, the time required to fully impregnate the porous solid can be estimated,

$$t = \frac{\eta \cdot a^2}{2K \cdot P} \quad (2.2)$$

As was mentioned above, the viscosity,  $\eta$ , of thermoplastic resins during processing generally ranges between  $10^2$ – $10^4$  Pa·s, which is considerably higher than for thermosets (1–10 Pa·s). It follows from Equation 2.2 that thermoplastic resin composites cannot be



processed at economic rates using the same techniques normally used for thermoset composites, since the impregnation time is proportional to resin viscosity. Higher pressures can be applied to accelerate the impregnation process, but the maximum load,  $P$ , which can be applied is limited by the size of the equipment used, and by the compression resistance of the fibres. Too high pressures may result in fibre damage, significantly lowering the mechanical properties of the composite. Furthermore, the fibre bed permeability,  $K$ , decreases when high pressures are applied, making impregnation more difficult. In techniques traditionally used for thermoset resin composites, such as resin transfer moulding (RTM), filament winding, vacuum bagging, etc., pressures of the order of 0.1 MPa (1 bar) are generally used; higher pressures ranging between 1 and 2 MPa (10–20 bars) can be achieved in autoclave processing. Pressures of the order of 10 MPa (100 bars) are possible in press forming. Specific processing techniques thus need to be applied to manufacture advanced high viscosity resin composites at intermediate pressures.

Processing techniques for advanced thermoplastic composites can be divided in two groups: pre-impregnation processes, and impregnation after shaping [4a]. The former is based on reducing the viscosity term,  $\eta$ , in Equation 2.2, and the latter on reducing the distance to flow,  $a$ . Alternative processing routes for thermoplastic composites are presented in Figure 2.1.

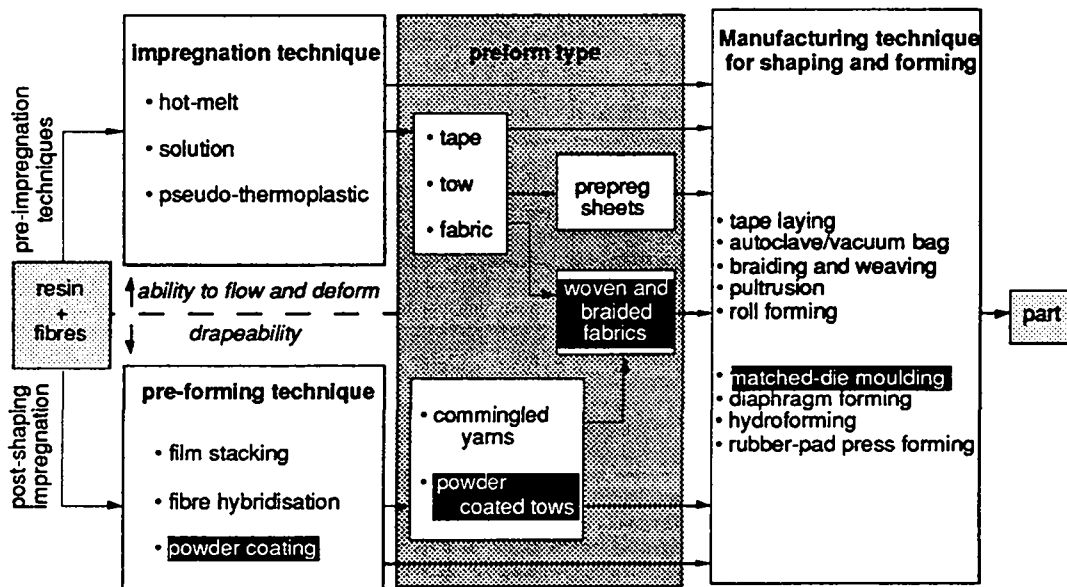


Figure 2.1: Alternative processing routes for thermoplastic based advanced composites (after [5]). The route studied in this work is indicated by black shaded text.

### 2.1.3 Pre-impregnation processes

Three different techniques are used to produce preimpregnated product forms, namely melt impregnation, solution impregnation, and pseudo-thermoplastic impregnation.

*Melt impregnation* of the fibres is an easy operation for low viscosity resins, but severe difficulties arise when high viscosity resins are used. It is, however, possible to

obtain an acceptable wet-out and impregnation if high shear rates and/or pressures are applied [5].

*Solution impregnation* is primarily used for amorphous thermoplastics by dissolving the polymer in a solvent (~10% by weight of polymer). This allows the viscosity of the resin to be considerably reduced. After complete impregnation of the fibres by the solution, the solvent needs to be extracted. This is achieved in two stages: the removal of the bulk of the solvent (about 95% of the solvent is extracted at this stage), followed by the removal of its final traces. The latter operation is particularly difficult. Although attractive in appearance, this technique also has drawbacks. First, it is necessary to find a suitable solvent for the matrix polymer. Second, the presence of residual solvents may compromise processing and reduce service performance [6].

A particular class of thermoplastic resins, the *pseudo-thermoplastics*, undergo some chemical reaction (chain extension) during the processing cycle. Essentially, they may be processed as thermosets due to their low initial viscosity. As they do not form a tri-dimensional network, they yet possess the properties of thermoplastics in terms of toughness. An example of pseudo-thermoplastic material is polyimide (LaRC-TPI) [7]. The main inconvenience here is that only a limited number of pseudo-thermoplastic polymers are available.

The resulting prepreg sheets are then stacked and consolidated by the application of pressure and heat (e.g., autoclave or press forming). The advantage is that the fibres are already fully impregnated before the stacking and shaping operations resulting in a fibre-matrix interface of good and reproducible quality. The major disadvantages are the additional costs and the boardiness of these product forms, which drastically reduces design freedom in the lay-up phase during manufacturing.

#### 2.1.4 Impregnation after shaping

In order to facilitate forming into complex shapes, the impregnation can be postponed until the material has taken its final shape. This requires the solid polymer and reinforcing fibres to be brought into intimate contact. This operation is referred to here as *mingling*. Fibre-matrix mingling aims at reducing the distance the liquid polymer must flow to fully impregnate the fibre bed during the shaping operation (cf. Equation 2.2). Shaping, final impregnation, and consolidation then take place in one step, unlike the prepregging technique where impregnation and consolidation operations are clearly separated.

Three major techniques belonging to the *impregnation after shaping* category should be mentioned: film stacking, cowoven or commingled towpregs, and powder impregnated towpregs. Figure 2.2 illustrates the structure of these three preform types.

##### *Film stacking*

Film stacking was the most used method to manufacture thermoplastic composites for its apparent simplicity. Alternative layers of reinforcing fibres and polymer films are stacked (cf. Figure 2.2a). This stack is then fused under high pressure causing the resin to flow between the fibres and the interface is formed. Flow occurs transverse to the fibre direction, which requires more energy than in the direction parallel to the fibres [8]. Lee and Springer [9] analysed film stacking theoretically confirming that several hours were

required to fully wet out the fibres. Applying high pressures to enhance impregnation also has the effect of increasing the fibre bed density, thus making infiltration by the resin even more difficult. In case of woven reinforcing fibres, high pressures may result in fibre breakage at the cross over points. Complex shapes can hardly be achieved with film stacking since this technique is based on flat films. Film stacks are not readily drapeable, and fibre and matrix are not mingled with great intimacy.

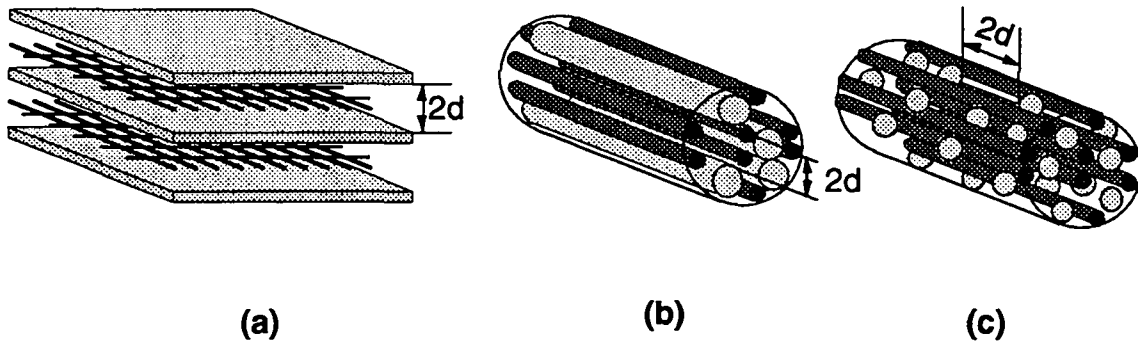


*Figure 2.2: Impregnation after shaping: (a) film stacking (flow transverse to the fibres); (b) commingled (flow transverse to the fibres); and (c) powder coated towpregs (flow parallel to the fibres);  $d$  is the distance to flow to achieve full impregnation.*

### ***Cowoven and commingled towpregs***

A considerably higher degree of intimacy can be achieved by intermingling or coweaving reinforcing fibres and polymer fibres. The resulting towpreg is very flexible and can readily be converted into a drapeable textile form (cf. Figure 2.2b).

Van West et al. [10] presented a theoretical study on impregnation and consolidation of commingled fibres. Again, as for film stacking, flow occurs transverse to the fibre direction, that is in the direction of lower permeability of the fibre bed. Obviously, the theoretical distance of resin flow is much less than for film stacking and should only be, in an ideal case, half a fibre thickness (i.e., 3–4  $\mu\text{m}$  for CF). In reality, reinforcing and polymer fibres tend to segregate and form separate clusters of reinforcements and polymer. Furthermore, carbon fibres usually have a diameter of 7  $\mu\text{m}$  whereas the diameter of polymer fibres is about 20  $\mu\text{m}$  or more. The initial fibre wetting is consequently quite low.

Another problem arising with the use of polymer fibres is that during the spinning process the molecules are strongly oriented in the drawing direction of the fibres. When melted, the orientation induced internal stresses relax causing the fibres to shrink which may cause distortion of the commingled system, and resin starvation at the ends of the yarns.

A variant of commingled products has been commercialised by Schappe Techniques which consists of spinning together stretch-broken long discontinuous fibres of matrix and reinforcement. It appears [11] that a better distribution of polymer/reinforcing fibres is obtained with this system than with traditional commingled continuous fibres. The tow is slightly stretchable due to the discontinuous fibres which provide some extendibility in the fibre direction, and is readily converted into a very drapeable fabric.

### *Powder coated towpregs*

Powder coating (cf. Figure 2.2c), the process under consideration in this study, was first discussed by Price [12] in 1973. The interest for industrial use of powder impregnated composites, however, only started in the late eighties and early nineties. Dry thermoplastic powder is incorporated into the fibre tow (*mingling* stage). The solid particles adhere to the fibres mainly due to electrostatic forces. These forces alone are too weak to adequately stabilise the powder on the fibre surface; the system is usually heated and passed through an oven to sinter the powder particles onto the fibres.

Depending on the surface energetics of the system, molten particles in contact with one single fibre will spread onto its surface driven by capillary pressure and form a film around it. This film will eventually reach an equilibrium geometry consisting of uniform droplets separated at equal distance by a polymer sheath (cf. Figure 2.3a). In reality, polymer droplets are in contact with several fibres at the time. Resin bridges are formed between adjacent fibres and spread along the fibre direction. The resulting towpreg is thus *semi-impregnated*. Impregnation and consolidation can be completed by applying heat and pressure during the final processing stage. The bridges will then spread along the fibres until they meet their next neighbour (cf. Figure 2.3b). The flow length is reduced to half the distance between two adjacent bridges, and flow occurs along the fibre direction rather than transversely as in film stacking and commingled fibres.

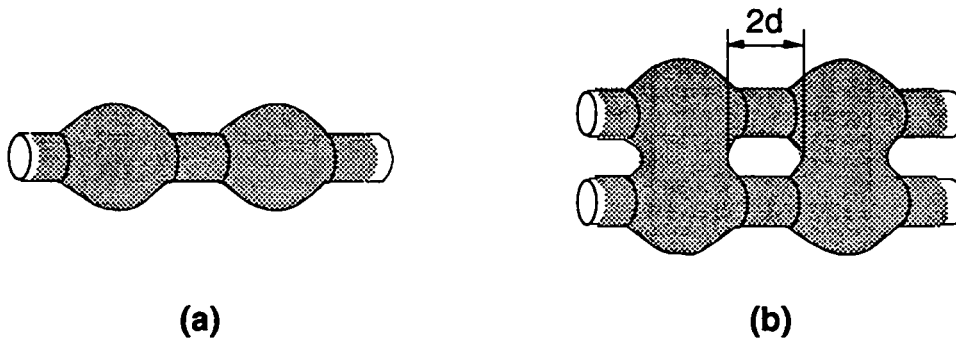


Figure 2.3: Molten particles (a) in contact with one single fibre, and (b) bridging two fibres;  $d$  is the distance to flow to achieve full impregnation.

The particle size is an important parameter as will be demonstrated in Chapter 4. Ideally, particles should be of approximately the same size as the fibres: small particles will improve the dispersion of the matrix into the fibre bed, and facilitate impregnation and consolidation. Based on a geometric analysis of the arrangement of solid particles within parallel fibres, Vodermyer et al. [13] proposed that the distance of flow,  $d$ , to fully impregnate the fibres was proportional to the cube of the particle radius,  $R_m$ . Introducing  $d \propto R_m^3$  for the depth of impregnation into Equation 2.2 we see that the consolidation time is proportional to the sixth power of the particle radius,  $t \propto R_m^6$ . This result will be confirmed in Chapter 4 using a different approach.

An ideal dry powder process presents the following advantages over other processes:

- any matrix can be ground into powder at much lower cost than operations such as fibre spinning; since the distance of flow is considerably reduced, even high viscosity polymers can be processed this way
- no binder, solvent or water need to be evaporated before forming
- powder coating of fibres is a relatively simple operation (cf. §2.2)
- highly flexible towpregs can be obtained, which can readily be transformed into a drapeable textile form

### **2.1.5 Manufacturing of powder impregnated parts**

The flexibility of powder coated towpregs allows a broader range of preforming and parts-manufacturing processes to be used than what is possible with fully impregnated prepregs or film stacking. Towpregs can be woven, knitted, braided, etc., resulting in a drapeable preform. Porcher Textile produces a number of fabrics using FIT yarns which have good draping properties (cf. §7.1.3). Hugh et al. [14] successfully braided powder coated towpregs which were stabilised by fusing the powder in place. Greene and Holty [15] made an evaluation on different part manufacturing techniques using powder coated towpregs. They made preforms by braiding and weaving the yarns. For example, specific properties were obtained in the *fill* and in the *warp* directions (i.e. directions parallel and transverse to the length direction) by cross-weaving glass fibre and carbon fibre reinforced towpregs, yielding parts which were stiffer in the direction of the carbon fibres than in that of the glass fibres. They then shaped these preforms using various processing techniques. Internal bladder moulding yielded good quality parts using braided sleeves as precursor. The authors also evaluated rubber diaphragm forming, rubber stamping and filament winding. Filament winding of GF-PA11 molten powder towpregs was investigated by Wagner and Colton [16]. Among the parameters studied, they found that winding speed had a major effect on the quality of the parts, producing higher quality parts at higher tow speed. Filament winding of FIT yarns was studied by Romagna and Ziegmann [17] using CF reinforced PEI and by Hauptert and Friedrich [18] using GF reinforced PET. Ramani et al. [19] investigated pultrusion and compression moulding of powder coated towpregs. Ye et al.[20] and Connor et al. [21, 22] studied the consolidation behaviour of compression moulded unidirectional (UD) FIT yarns. It can be seen that powder impregnated composites are very versatile in processability and a wide range of techniques are available to shape and produce powder impregnated parts.

## **2.2 POWDER COATING**

The first stage in the manufacturing of continuous fibre reinforced composites using the powder impregnation route is to bring the powder resin into intimate contact with the fibres. This stage is referred to here as the *mingling* of the precursor powder with the

reinforcement fibres. Price [12] emphasises that this stage is designed to create a partial wetting of the fibres that could be completed in subsequent processing operations. This definition, however, cannot be applied to sheath coated powder impregnated tows of the FIT type (Fibres Imprégnées de Thermoplastique) [23], since no wetting is achieved at this stage. We will therefore describe this stage in a more general way as a means of intimately incorporating resin powder into a fibre bundle. It results that the distance the liquid matrix must flow in a subsequent processing operation to fully impregnate the fibre bed is considerably reduced compared to techniques such as film stacking.

Mingling of the powder and fibres can be done in a continuous way by passing a spread fibre tow through a resin powder bed; the powder loaded fibre tow must then be stabilised to prevent the powder from being shaken off during further manipulations. The resulting towpreg should fulfil the following two objectives: (i) achieving a fine enough dispersion of the matrix, and (ii) obtaining a stable and flexible towpreg which can conveniently be converted into a textile preform (woven, braided, knitted, etc.). The former objective, a good dispersion of the matrix, requires that fine powders, with similar diameters as the reinforcement fibres, should be used; although authors report good results obtained with much larger powders [24]. Powder deposition is a key step and care must be taken that powder is delivered at a constant rate and that the fine particles do not agglomerate forming large clusters, thus equivalent to larger particles.

In case the resin powder is melt fused after mingling, the flexibility of the towpreg depends, on the one hand, on the fibre content and, on the other hand, on the amount of tow spreading. Fibre volume fractions of the order of 60–62 % are usually considered as “standard”; higher fractions generally give difficulty in obtaining void free laminates, and lower fibre fractions decrease the mechanical performance [4b]. The flexibility of the tow can only be varied by controlling the spreading of the fibre bundle. Muzzy et al. [24, 25] report an inverse relationship between towpreg rigidity and tow spreading. Figure 2.4 plots the flexural rigidity of a 60 vol. % 3K (3000 filaments per yarn)-carbon fibre (CF) reinforced PEEK 150PF powder as a function of tow spreading as reported by Muzzy et al. [24, 25].

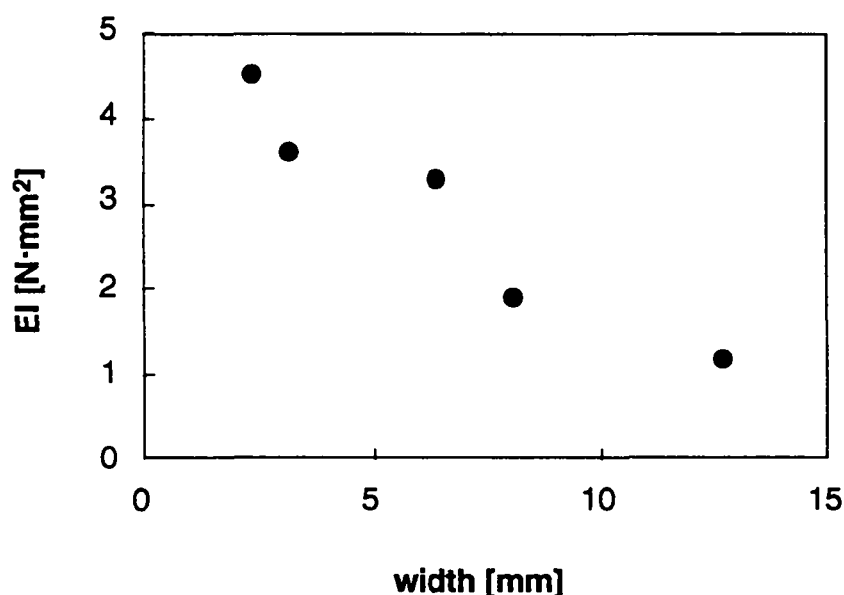


Figure 2.4: Effect of tow spreading on flexural rigidity of a 3K CF bundle (from [24, 25]).

Various solutions to the mingling of powdered matrix with reinforcement fibres, proposed in the literature, will be reviewed in this section. Powder coating of continuous filaments can be schematically divided into three consecutive steps: (i) spreading of the fibre bundle; (ii) mingling of the resin powder and the fibres; and (iii) stabilisation of the powder loaded towpreg (cf. Figure 2.5). Each of the three processing units will be discussed here, exploring the solutions proposed by various authors. Finally, a powder coating line designed at the *Laboratoire de Technologie des Composites et Polymères* (LTC) will be presented.

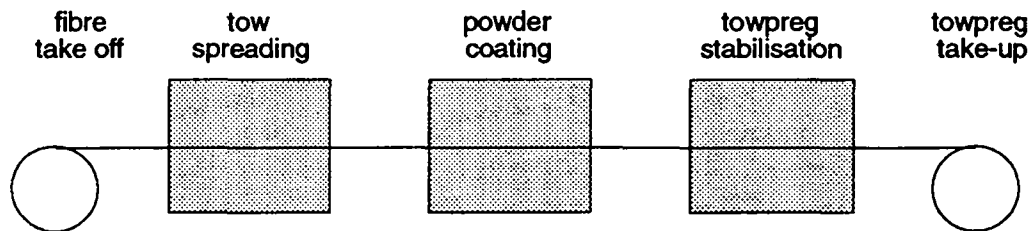


Figure 2.5: General diagram of powder coating lines

### 2.2.1 Tow spreading unit

Spreading of the fibre tow is a critical stage in the powder coating process. Good fibre bundle spreading increases the fibre surface area exposed to the powder, and shortens the path the powder particles need to travel to reach the centre of the tow, yielding a better powder distribution. Furthermore, if the towpreg is stabilised by melt fusing the powder particles in an oven, the flexibility of the final towpreg will depend on the amount of spreading of the fibres during melting. In case the fibres are well spread apart, the molten powder particles will flow and form a sheath around the fibres they are in contact with [26]. Towpreg flexibility then increases with decreasing sheath thickness. In reality, it is quite unlikely that the fibres are sufficiently spread apart for the powder particles to be in contact with only one fibre at the time. In general, resin bridges are formed between two, three or more adjacent fibres (cf. Chapter 3). In this case, the fibres are more restricted in their movements resulting in a stiffer towpreg. This effect can be limited, however, by spreading the towpreg as much as possible during fusion of the powder particles, as illustrated in Figure 2.4. It is possible to stabilise the system without melt fusing the powder particles; for example, by applying a thin resin sheath to the powder coated fibre tow (FIT). In this case, the towpreg is very flexible, and the fibre spreading is only needed during the powder coating stage, to facilitate the mingling of the matrix and the fibres.

#### *Mechanical spreading*

Fibre spreading can be achieved either mechanically or pneumatically. Mechanical spreading consists of passing the fibre tow over and under a series of fixed pins. As depicted in Figure 2.6a, when a tow under a tension,  $T$ , passes over a pin each filament is subject to a force,  $F$ , normal to the pin and equal to:

$$F = T \sin \psi \quad (2.3)$$

where  $\psi$  is the tow wrapping angle. Since the fibre tow has no lateral cohesion, the latter will spread on the pin surface (cf. Figure 2.6b). Edie et al. [27] used convex rollers ( $\text{\O}3$  mm pins with 150 mm curvature) to enhance the spreading of the tow. To further guide the filaments, the pin surface can be finely crenellated. A serious drawback of mechanical spreading, however, is the risk of damaging the fibres. For this reason, pneumatic spreading is often preferred. If the pins are free to rotate, the friction on the fibre tow is reduced, yielding less fibre damage. The resulting spreading, however, is not as good as with fixed pins.

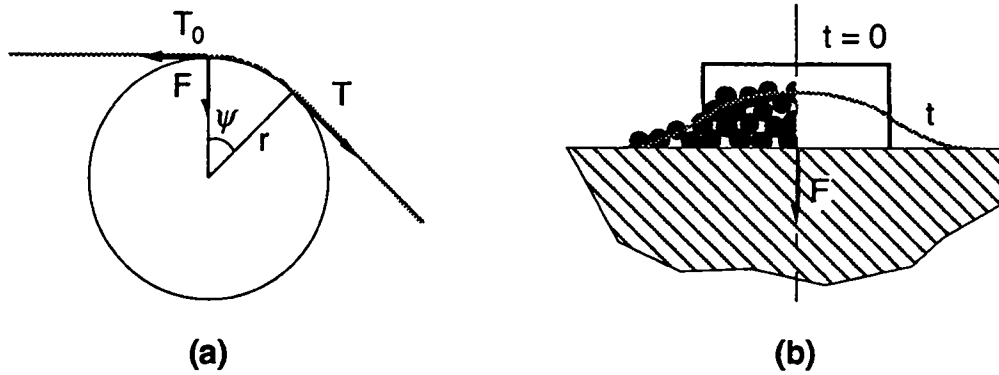


Figure 2.6: Mechanical tow spreading: (a) force balance; and (b) cross-sectional view.

### *Pneumatic spreading*

Pneumatic spreading consists of passing the fibre tow through a Venturi slot tunnel (VST). The bundle enters the spreader at the throat of a flat expansion section; air enters at the tunnel outlet and is drawn through holes in the sidewalls of the tapered section into a vacuum manifold [28] (cf. Figure 2.7a). The fibres are thus subject to the tow tension,  $T$ , (controlled by the break on the feed spool) and the air drag,  $F_w$ , towards the wall. Under these conditions, a fibre would move at an angle,  $\phi(y)$ , given by:

$$\tan \phi(y) = \frac{F_{wy}}{T - F_{wy} \cot \alpha} \quad (2.4)$$

where  $\alpha$  is the angle of  $F_w$  in the  $x$ -direction, and  $F_{wy}$  is the air drag force component in the  $y$ -direction (cf. Figure 2.7).

At the centre of the bundle ( $y = 0$ ,  $F_{wy} = 0$ ), there is no deviation of the fibres. At the sidewall, air drag is normal to the sidewall; the outer fibres can thus be moved parallel to the tunnel sidewall if  $F \geq T \cdot \sin \phi$ . An expression for the air drag,  $F_w$ , is proposed by Baucom et al. [29], where  $F_w$  is proportional to the pressure difference,  $\Delta P$ , drawn in the chamber. The spreading angle can thus be adjusted by changing the tow tension ( $T$ ) or the countercurrent flow ( $\Delta P$ ). Baucom et al. [10] used a 438 mm long tunnel with a  $8^\circ$  taper angle; the outlet is 51 mm wide.



The VST unit used at NASA Langley Research Center presented here is a modified version of a tunnel using both concurrent and countercurrent air flow [30]. The concurrent air flow separated the filaments in the tow, and the countercurrent air flow spread the fibre tow. It appears that the concurrent air flow was not essential to this purpose since it was abandoned.

A typical 3K  $\text{Ø}7 \mu\text{m}$ -carbon fibre tow is 2–4 mm wide. Iyer and Drzal [26] obtained 50–150 mm wide fibre tows after spreading. This seems a very high value when compared to widths reported by other authors, such as Throne and Sohn [31] who measured a spread width of 50–75 mm on a 12K carbon fibre tow using a Venturi tunnel. Authors seem to agree on the final towpreg width, however, which, for 3K-CF tows, ranges between 2.4 mm for poor spreading conditions [25] to a maximum width of 30 mm (cf. Figure 10 of [26]). Rozant [32] obtained 2.5–5.4 mm wide 3K CF-towpregs using polished cylindrical pins and Ogden et al. [30], who used a Venturi slot tunnel report 25 mm wide towpregs using 12K  $\text{Ø}7 \mu\text{m}$ -CF.

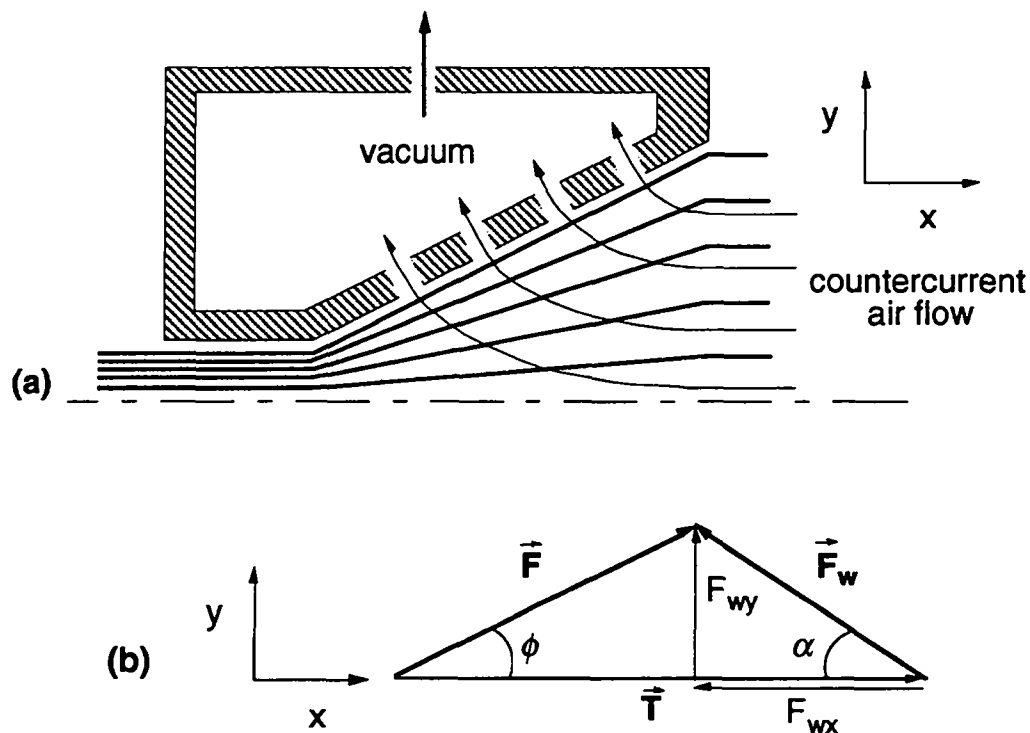


Figure 2.7: Pneumatic spreading unit : (a) schematic ; and (b) force balance.

### 2.2.2 Particle characterisation

Before presenting the powder coating unit, it is necessary to review a number of basic concepts on particle morphological characterisation.

#### Size measurement

It is clear that particle size and size distribution are key parameters, both for the powder coating stage and the composite consolidation stage (cf. Chapter 4). A variety of

conventional diameter definitions has been proposed over the years, which requires statistical averaging to obtain some quantity which can be related to a physical parameter of interest. Among these we will consider three which appear to be the most commonly used ones: the equivalent circle diameter, Martin's diameter, and Feret's diameter, depicted in Figure 2.8a, b, and c respectively.

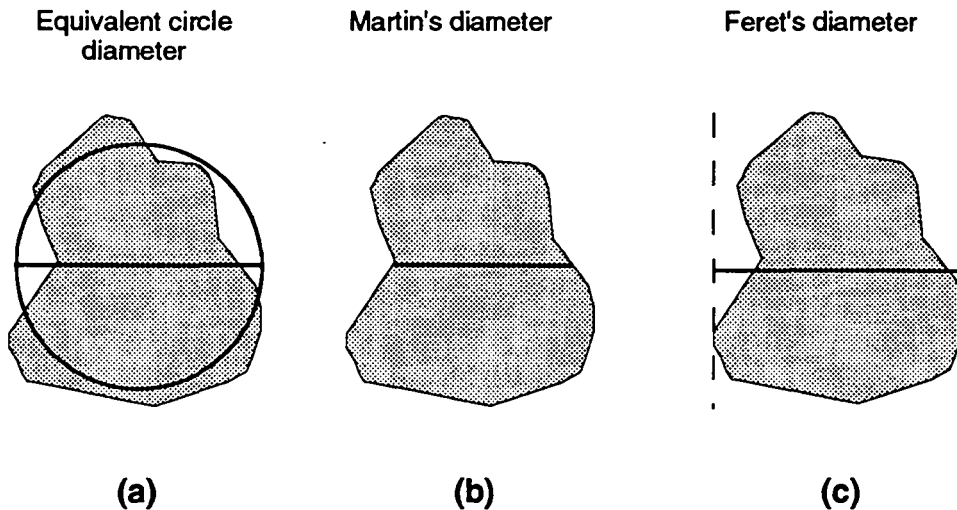


Figure 2.8: Three statistical diameters: (a) equivalent circle diameter; (b) Martin's diameter; and (c) Feret's diameter.

The *equivalent circle diameter* is the diameter of the circle whose area is the same as the area of the particle projected onto a surface. It certainly is the most used statistical diameter.

For the following two measures, one assumes that the 2-D images are randomly situated, and the measures must be taken parallel to an arbitrarily fixed direction. *Martin's diameter* is the distance between opposite sides of the particle measured crosswise of the particle and on a line bisecting the projected area. *Feret's diameter* is the distance between two tangents on opposite sides of the particle [33a].

The three statistical diameters presented above all consider a projection of a particle. They can thus be measured from different types of micrographs of a statistically representative population of particles. Other techniques, consist of dispersing the powder into an aqueous medium and passing a light beam through the suspension. The particle size distribution can be related to the light intensity absorption of the suspension —e.g., Horiba, CAPA-700 used in the powder characterisation of the FIT towpregs in Chapter 4. If the light source is a laser, the diffraction pattern generated by the powder suspension can be related to the size distribution of the particles —e.g., Fritsch Analysette 22 used for particles characterisation of powder coated towpregs manufactured at the university of Newcastle upon Tyne (cf. Chapter 4). A detailed list of particle size and size distribution measurement techniques can be found in Table 3.7 of [33b].

### **Particle shape**

The flow of a powder bed is strongly dependent, not only on the size, but also on the shape of the particles. A qualitative observation of the particle shapes will already yield

valuable information. It is necessary, however, to use a common language for descriptive terms; the British Standard 2955 (1965) includes such terms as: *acicular* (= needle shaped), *fibrous* (= thread like), *angular* (= sharp edged or roughly polyhedral shape), etc.

A quantitative description can be obtained by relating to each other geometrical parameters such as the elongation ratio (= length to breadth ratio). This method seems to be abandoned now, and the *circularity shape factor* is often used instead. It is calculated as

$$\frac{(\textit{perimeter of profile})^2}{4\pi(\textit{area of profile})} \quad (2.5)$$

which is unity for a circular shape. A serious drawback of single number systems as the *circularity shape factor* is that they are ambiguous parameters, since one value corresponds to a multitude of different shapes. Unambiguous shape representations have been developed, but they involve the collection and manipulation of a great deal of data. Further information on such techniques can be found in [33c].

### **Agglomeration**

The behaviour of a given particulate material can be greatly altered if the particles tend to agglomerate. Agglomeration arises from interaction between particles, as a result of which, they adhere to one another to form clusters. The main mechanisms giving rise to agglomeration are as follows [34]:

- *mechanical interlocking*: this can occur particularly if the particles are *acicular*, in which case large masses can be completely interlocked
- *surface attraction*: attractive van der Waals's forces may become important, particularly with small particles ( $\varnothing < 10 \mu\text{m}$ ) which yield a high surface area to volume ratio, giving rise to substantial bonds between particles
- *electrostatic attraction*: particles tend to acquire charge by frictional or sliding contact. Work required to remove an electron from the surface of a particle increases with decreasing particle size; fine particles will thus tend to charge negatively; if there is a broad size distribution, there may be a change in particle charge with decreasing particle size [26]; one can benefit from this effect to enhance adhesion between electrostatically charged particles and electrically grounded fibres [31]
- *effect of moisture*: moisture will tend to collect near the points of contact between particles giving rise to attractive capillary forces; advantage was taken from this effect by Ogden et al. [30] who moistened the fibres prior to powder deposition
- *plastic welding*: when angular particles are in contact, the forces between the particles will be borne in extremely small surfaces and the high contact pressures developed may give rise to plastic welding

### *Powder manufacturing*

Resin powders can be obtained either by mechanical grinding, or by direct synthesis in powdered form. The fracture mechanics of grinding state that it is not possible to comminute materials below their flaw size [4b]. For tough matrices such as PEEK this sets a lower size limit of about 25  $\mu\text{m}$ . Lower sizes can be obtained through cryogenic grinding, but only at significant cost. Ground particles are generally *angular* with jagged edges and irregular shape. Furthermore, grinding yields a broad particle size distribution; further operations such as sieving are required if narrower particle size distributions are wanted. Particle size fractions can be separated by using a nest of sieves, each lower sieve being of smaller aperture size. The sieves should be mounted on a vibrator designed to give a degree of vertical movement in addition to the horizontal vibration. The sizing is based on the linear dimensions of the particle and the lower limit of size which can be used is set by two factors [34b]: the first is that the proportion of free space on the screen surface becomes very small as the size of the aperture is reduced; the second is the tendency of small particles to agglomerate and form larger clusters. The efficiency of screening is defined as the ratio of the weight of material which passes the screen to that which is capable of passing.

Many high performance polymers are polymerised into powders —so called *reaction powders*— the size of which can be finely controlled. Lyon et al. [35] precipitated semicrystalline PEEK particles from amorphous ketimine derivatives. Spherical particles were obtained, the size of which, ranging from 0.5–5  $\mu\text{m}$ , was controlled by selecting the proper conditions for the hydrolysis.

After having characterised some powder particle properties, we will now review a number of techniques allowing their homogeneous mingling with the fibres.

### 2.2.2 Powder coating unit

The key problem in powder impregnation technology, as with commingling, is achieving a fine enough dispersion of the matrix. As precondition, good tow spreading and fine matrix powder will improve the mingling quality. It is thus important to keep the fibre bundle spread when it is brought in contact with the powder. Furthermore, it is important that the powder particles must be deposited onto the fibre surface at a constant rate. Simply running a spread fibre tow through a fixed bed of solid powder particles will yield a towpreg with very irregular powder content. Indeed, the powder bed behaves like a plastic solid and a channel will be formed by the running bundle, which after some time would not collect powder anymore. Depending on the chemical nature, size and morphology of the particles, various solutions to this problem have been proposed in the literature. Powder coating at Georgia Institute of Technology [24, 25, 36], in Porcher Textile [23], at the University of Newcastle upon Tyne [37] and at NASA Langley Research Center [28, 29, 38] is achieved by passing a spread tow through a fluidised powder bed; small variations distinguish the various fluidised bed units used. Ogden et al. [30] simply sprinkled the powder onto the fibre using a 105  $\mu\text{m}$  polyester mesh bag, manually moving it in an oscillatory pattern back and forth across the width of the tow. Powder sprinkling onto the fibre bundle was also tested by Throne and Sohn [31] who used an electrostatic powder coating gun, by Edie et al. [27] with a powder extruder and by Baucom et al. [39] who introduced the term *powder curtain process*. Powder particles

can also be deposited onto the fibre surface by running the fibre tow through an aqueous powder dispersion [13].

In order to enhance adhesion between the powder and fibres, Ogden et al. [30] moistened the fibres prior to their entering into the powder coating unit. Others [24, 25, 31, 36] proposed to deposit electrostatically charged powder particles onto grounded carbon fibres. In both cases, the “fixation” of the powder to the fibre surface is transitory and is only meant to last until the powder coated bundle enters into the *stabilising unit*.

Each of the above techniques show *pros* and *cons* depending on the type of matrix powder used.

### Fluidised powder bed

Running a spread fibre tow through a resin powder fluidised bed appears to be a widely used technique to deposit powders onto the fibre surface [23–25, 28, 29, 36–38]. A fluidised bed is formed by passing a fluid, usually a gas, upwards through a bed of particles supported on a distributor [40]. In streamline gas flows, at low flow rates ( $u_f < 10^{-2} \text{ m}\cdot\text{s}^{-1}$ ) the pressure drop across the bed will be directly proportional to the rate of flow. At higher rates ( $10^{-2} < u_f < 5 \text{ m}\cdot\text{s}^{-1}$ ), when the frictional drag on the particles becomes equal to their apparent weight, the particles rearrange themselves to offer less resistance to the flow of fluid and the bed starts to expand [34c]. At this point, the powder bed is fluidised. At even higher rates ( $u_f > 10 \text{ m}\cdot\text{s}^{-1}$ ) the powder can be recirculated. The fluidised bed behaves in many ways like a fluid of the same density as that of the solids and fluid combined, e.g., solid objects float if their density is lower than that of the bed [34d].

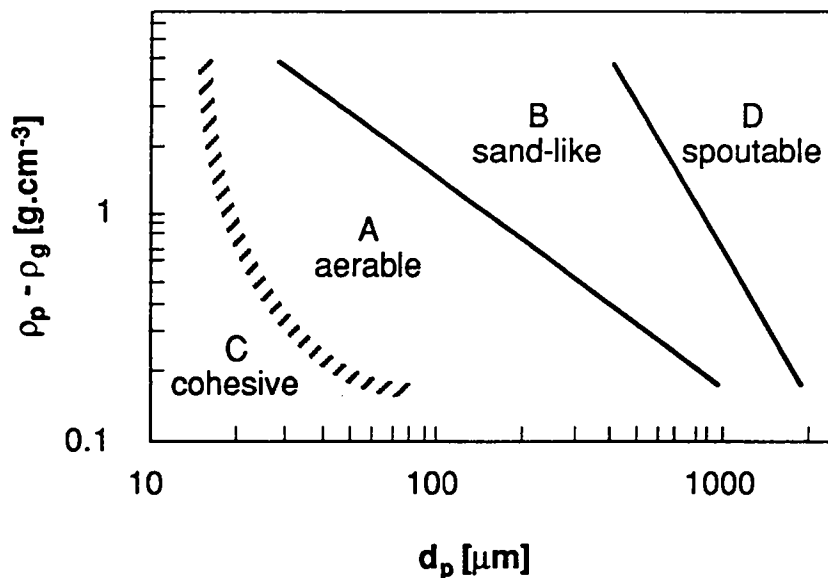


Figure 2.9: Powder groups (after [41]);  $d_p$  and  $\rho_p$  are the particle diameter and density, respectively, and  $\rho_g$  is the fluid density.

Different fluidisation types can be distinguished. Indeed, many particulate solids cannot be well fluidised, particularly those whose shape is non-isometric. The behaviour of reasonably isometric particulate solids in fluidised beds depends largely on a combination of their mean particle size,  $d_p$ , and density,  $\rho_p$ . Geldart [41] constructed a *fluidisation diagram* which can be used to place any powder in one of four groups A, B, C, or D (cf. Figure 2.9). Each group corresponds to a specific fluidisation behaviour.

Powders in group C are cohesive and difficult to fluidise because interparticle forces (van der Waals, electrostatics, and mechanical interlocking) are greater than the hydrodynamic forces exerted on the particle by the fluidising gas. Consequently, the gas forms channels or cracks through which it flows, rather than forming bubbles as in the other three groups (cf. Figure 2.10a). As was pointed out earlier, the presence of moisture enhances powder cohesiveness by forming liquid bridges between particles.

Powders in region A yield the best fluidising properties. Interparticle forces are present in these powders, but they are significantly smaller than the hydrodynamic forces. At low velocities (slightly larger or equal to the minimum fluidising velocity), the flowing gas will form bubbles limited in size forming with the particles a quasi continuous phase often referred to as *emulsion phase* (cf. Figure 2.10b). At higher velocities, the bubbles increase in size, and two phases can clearly be distinguished. The system closely resembles a boiling liquid, and such beds are often referred to as *boiling bed* [34c].

In regions B and D there are no interparticle forces. Bubbles grow indefinitely with gas velocity and when they approach the diameter of the column they are called *slugs* (cf. Figure 2.10c) [40]. These slugs of gas alternate with slugs of fluidised solids which are carried upwards and subsequently collapse, causing the solids to fall back again [34c]. In most solids of group D, the gas bubbles rise slower than the gas surrounding the individual particles; consequently, gas enters the bottom of the bubble and leaves through the top, giving rise to a phenomenon called *jetting* (cf. Figure 2.10d). Figure 2.10 illustrates the various types of fluidisation listed above.

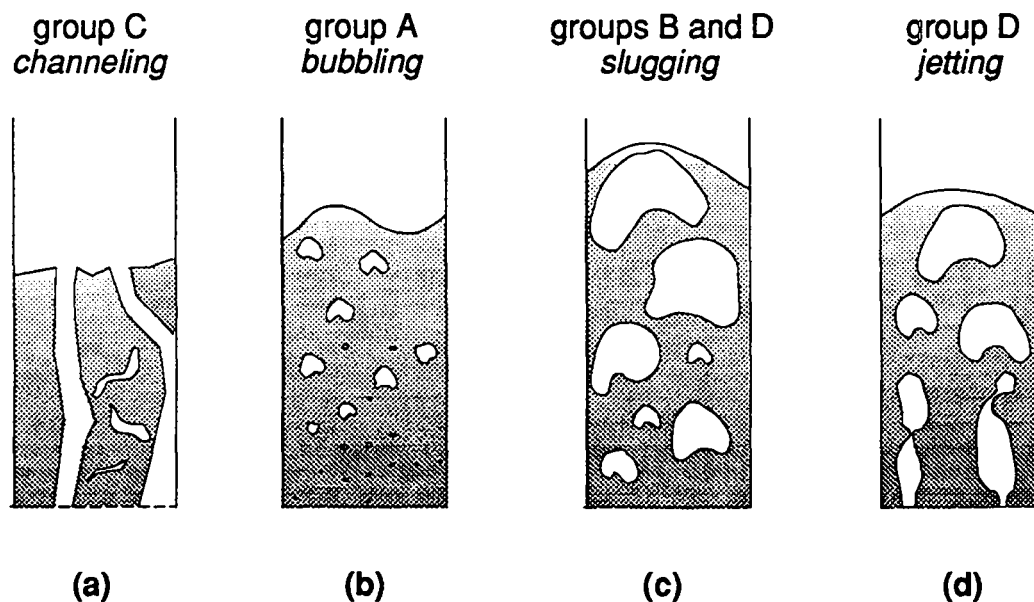


Figure 2.10: Types of fluidisation of various groups represented in Figure 2.9 (after [33]).

If the pressure drop,  $\Delta P$ , across the whole fluidised bed is plotted against the fluid velocity,  $u_f$ , using logarithmic coordinates (cf. Figure 2.11), the relationship is linear up to the point where expansion of the bed takes place (A in Figure 2.11). As the velocity is increased, the pressure drop becomes independent of fluid velocity (AB). Point A corresponds to the maximum stable porosity for a fixed bed of the given particles; the corresponding velocity,  $u_{fm}$ , is the minimum fluidisation velocity. In reality, a slight over pressure (M) is needed to overcome frictional forces between particles before rearrangement can take place [34e].

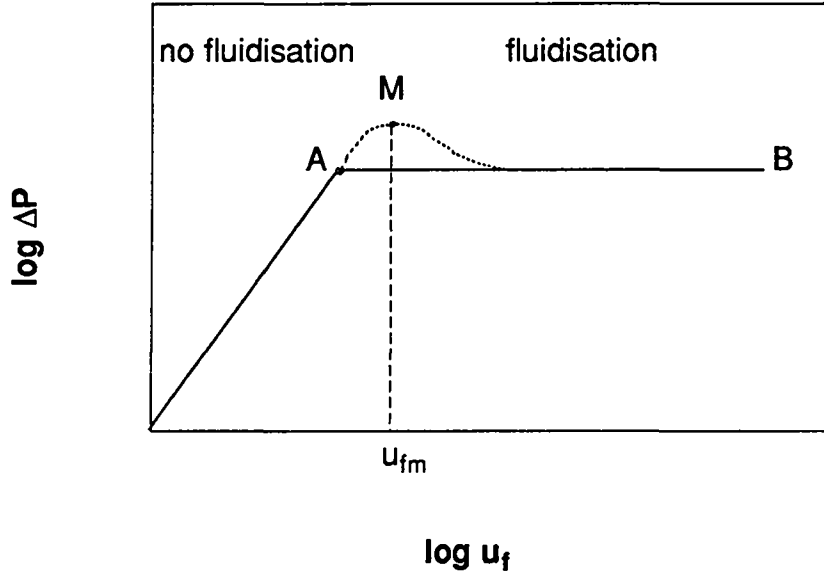


Figure 2.11: Pressure drop over fixed and fluidised beds.

When the bed is fluidised ( $u_f \geq u_{fm}$ ) the pressure drop across the powder bed is constant and equal to the submerged weight of the bed divided by the cross-sectional area,  $A$ , of the column [40],

$$\Delta P = (\rho_p - \rho_g)(1 - \varepsilon_{fm})h_{fm}g \cong \rho_{BS}h_{BS}g = \frac{m_B g}{A} \quad (2.6)$$

where  $\rho$  is the density,  $\varepsilon$  the bed porosity,  $h$  its height,  $g$  the gravitational acceleration, and  $m$  the mass; the subscripts  $p$  and  $g$  refer to particle and gas, respectively, and  $B$  and  $BS$  to bed and gently settled bed, respectively.

The minimum fluidisation velocity,  $u_{fm}$ , can be predicted using the expression proposed by Wen and Yu [42]:

$$u_{fm} = \frac{\eta}{\rho_g d_s} (1135.7 + 0.0408 \sqrt{Ar}) - 33.7 \quad (2.7)$$

where  $\eta$  is the fluid viscosity,  $d_s$  the diameter of a sphere having the same diameter as the particle, and the Archimede's number,  $Ar$  is given by

$$Ar = \frac{\rho_s d_s^3}{\eta^2} (\rho_p - \rho_s) \quad (2.8)$$

### *Fluidised beds in powder coating lines*

As was pointed out earlier, several authors have deposited powder into a fibre tow by passing it through a fluidised bed [23–25, 28, 29, 36–38]. This approach is appealing since by fluidising the particulate solids, the system resembles liquid impregnation, a well characterised processing technique for thermosetting resin composites. Some of the solutions chosen by various institutes are presented here.

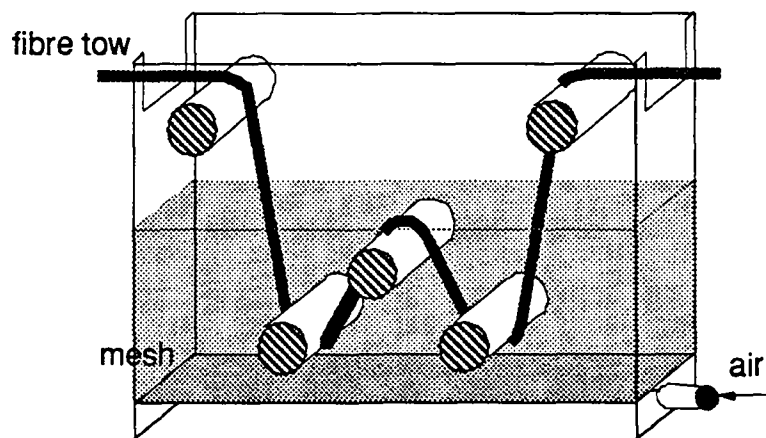


*Figure 2.12: Fluidised bed unit used at the University of Newcastle upon Tyne*

### *Fluidised bed developed at the University of Newcastle upon Tyne (UK)*

The fluidised bed developed at the University of Newcastle upon Tyne [32, 37], which we have used to manufacture a series of towpregs used in this study (cf. Chapter 4), consisted of a rectangular vessel with five fixed Ø20 mm pins around which the fibre bundle was passed (cf. Figure 2.12). The pins have a triple function. First, for a given vessel volume, they increase the path length where the fibres are in contact with resin particles. Secondly, they force the powder particles into the fibre bundle, and lastly, they keep the tow spread while it is in contact with the particles (cf. Figure 2.9) —this is the reason why the pins were not allowed to rotate. The latter can be a drawback if fibre damage occurs. If this is the case, and pneumatic rather than mechanical spreading is used (cf. Figure 2.7), the pins can be mounted on bearings, so that they can rotate freely and the frictional forces on the fibres are substantially reduced. No problems of the kind occurred, however, perhaps owing to the smoothness of the pins polished surface. To evenly distribute the air flow at the bottom of the bed, compressed air was injected through a thin cavity between the bottom of the container and a woven wire mesh plate ( $\text{Ø}_{\text{mesh}} = 50 \mu\text{m}$ ) on top of which was sitting the powder bed. A Pitot tube could be used to monitor the pressure drop across the bed and thus control the fluidisation mode.



Powder was supplied manually to the bed, and its level could be checked through the transparent sidewalls (PMMA).

*Fluidised bed developed at the NASA Langley Research Center (USA)*

The fluidised bed version used by Baucom and Marchello at NASA Langley Research Center [28, 29] is presented in Figure 2.13. This version is a combination of fluidised bed and powder seeding techniques. The pneumatically spread fibre tow enters the fluidised bed through a narrow slot on one side, passes through three horizontally slotted baffles, enters the main chamber—containing the fluidised bed—then the powder laden tow passes through three slotted baffles and a wall slot to leave the unit.

In this version, a bubbling bed feeder was used to supply resin powder to the system at a rate of about  $1 \text{ g}\cdot\text{min}^{-1}$  depending on the tow speed, powder losses, and desired powder content in the towpreg.

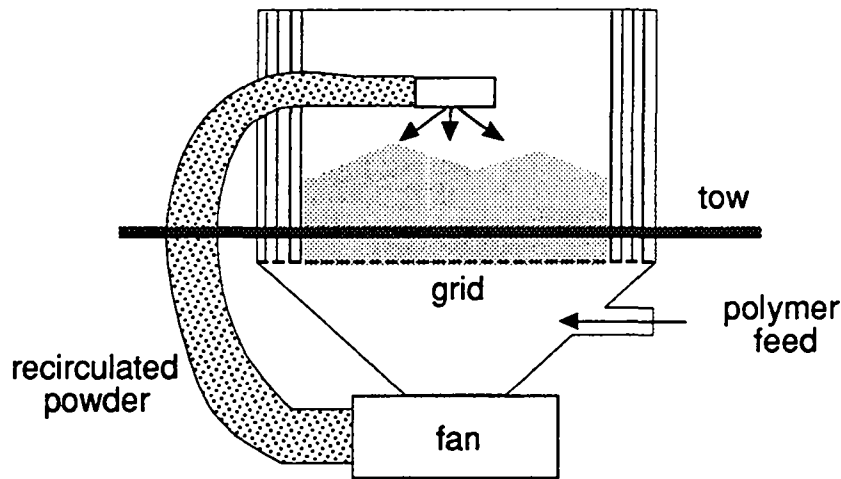


Figure 2.13: Fluidised bed unit used at NASA Langley Research Center (after [28])

No pins are used here; the spreading of the fibre tow is done pneumatically. The powder is collected in the 150 mm long chamber by the expanded tow—which behaves like a fibrous filter—by momentum impaction, inception owing to van der Waals and sometimes electrostatic forces. Baucom and Marchello [29] propose a theoretical relation between towpreg resin weight fraction,  $w_m$ , resin cloud density,  $n$ , and tow speed,  $u_t$ , of the type,

$$w_m = 1 - \frac{u_t}{\alpha n} \quad (2.11)$$

where  $\alpha$  is a term depending on the type of powder and fibre tow, the chamber dimensions, and recirculation level. For their powder coating unit (150 mm long), using a 12K carbon fibre tow, they found  $\alpha = 195 \text{ cm}^4\cdot\text{g}^{-1}\cdot\text{s}^{-1}$ , which was in good agreement with experimental data (cf. Table 2 in [29]).

*Fluidised bed developed at the Georgia Institute of Technology (USA)*

Deposition of electrostatically charged particles onto electrically grounded (and spread) carbon fibres was investigated at Georgia Institute of Technology [24, 24, 36]. The powder coating unit has here the double function of electrostatically charging and depositing the particulate solids onto the electrically grounded fibre tow. This will enhance adhesion between fibres and particles until the powder laden tow reaches the stabilising unit. It appears that electrostatic forces are not sufficient to keep the powder in place during further manipulations, such as weaving. The electrostatic fluidised bed is represented in Figure 2.14.

It should be possible to apply Equation 2.11 derived by Baucom and Marchello [29] to predict the powder take up rate. For similar conditions, though, the parameter,  $\alpha$ , should be larger in the case of electrostatically charged particles which are attracted by the grounded fibres, due to attractive electrostatic forces.

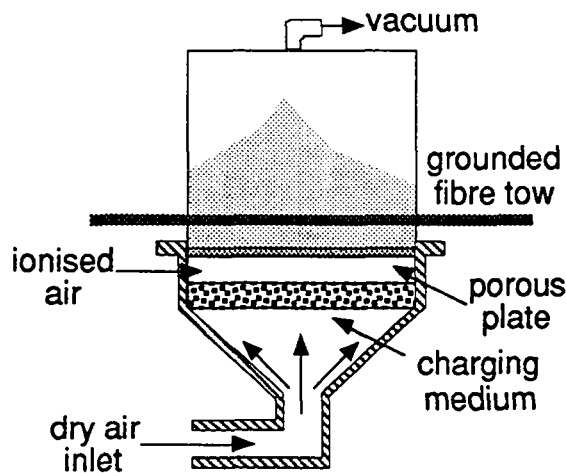


Figure 2.14: Electrostatic fluidised bed of Georgia Institute of Technology (after [24]).

*Aqueous polymer powder dispersion*

If we consider the *fluidisation diagram* in Figure 2.9, it can be seen that polymer particles of density ranging between 1.0 and 1.5, become cohesive when smaller than 10–20  $\mu\text{m}$ . Such powders yield poor fluidising behaviour. A solution to overcome this problem is to use an aqueous powder dispersion. Fine and homogeneous dispersions can be obtained with finer powders than with gas fluidisation. The key problem, as for solution impregnation, is that the aqueous medium needs to be eliminated completely to assure good quality towpregs.

Vodermayer et al. [13] designed a powder impregnation line by aqueous dispersion at the Technical University of Berlin (D). The unspread roving is guided under controlled tension into the impregnation bath which is agitated by magnetic stirrers. In the bath the fibre tow is passed over and under a series of five  $\text{Ø}10\text{ mm}$  polished steel pins with a clasp angle of  $128^\circ$ . The tow is spread by the powder particles which act as spacers. The reacting force of the pins enhances diffusion of the powder towards the centre of the roving. Leaving the bath, the impregnated fibre tow is run through a drying chamber to completely evaporate the water; this is done by blowing hot air on the roving.

The dry powder laden bundle then passes into the stabilising unit. The drying process is the rate-determining step in the production of towpregs by powder aqueous dispersion.

### ***Powder seeding***

Powder seeding or, as Baucom et al. [39] call it, “the powder curtain towpreg process” is attractive for its simplicity of realisation. Ogden et al. [30] form a *powder curtain* by simply sprinkling the powder through a mesh bag moving it manually in an oscillatory pattern.

Edie et al. [27] constructed a small powder extruder to deposit the powder directly onto the fibre tow. The deposition rate could be controlled by varying the extruder motor speed, and a powder feed hopper was used to provide sufficient powder agitation to prevent clogging of the extruder assembly. Apparently, neither the hopper nor the screw design were optimised for feeding fine polymer particles, thus causing quite large matrix content variations during continuous coating [27]. The authors also suspect that such a deviation could be due to variations in tow spreading, further stressing the importance of the spreading stage.

Throne and Sohn [31] at the University of Akron (USA) used a powder gun well suited for fine particles ( $\text{\O} 0.1\text{--}40\ \mu\text{m}$ ). Powder was aspirated from a vibrated hopper by a partial vacuum caused by air drawn over a Venturi opening in a tube. The vacuum is used to lift powder into the air stream (cf. Figure 2.15). In this process, the particles are electrostatically charged by passing the powder through an electrostatic field to enhance adhesion between charged particles and electrically grounded fibres.

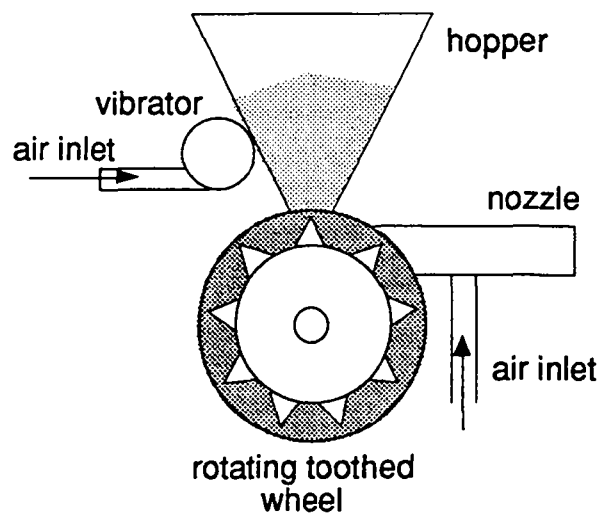


Figure 2.15: Powder seeder used at the University of Akron (after [31]).

Baucom et al. [39] use a helix drive powder feeder to propel the powder down a tube or sleeve. The powder is exhausted through a series of holes in the tube wall, creating a “powder curtain” which rains down on the spread tow. They pointed out a major drawback of seeding techniques: since seeding is a gravity controlled process, only the top of the fibre bundle is in contact with the fibres. It must be noted that electrostatic charging of the particles reduces this effect. To overcome this problem, the spread fibre tow is run a first time through a “powder curtain” coating unit, passed through the

stabilising unit (here an oven) and fed over a roller which inverts it so that the predominantly coated surface is now facing downwards. The poorly coated side of the towpreg is run through another “powder curtain” coating unit and stabilised a second time.

### 2.2.3 Towpreg stabilisation unit

At the exit of the powder coating unit, resin powder particles are finely dispersed into the fibre tow. The powder laden bundle, however, is highly unstable and the powder can easily be shaken off, yielding large variations in the resin content of the towpreg. Such an unstable system cannot be conveniently converted into a textile preform. The powder loaded fibre yarn thus needs to be stabilised. Two solutions are commonly used: the first solution is to melt fuse the particles in place, and the second is to enclose the powder coated fibre tow into a polymer sheath, usually of the same resin as the powder.

#### *Powder fusing*

By far the most popular solution is to melt fuse the powder particles in place. The fused particles will spread onto the surface of the fibres they are in contact with, driven by capillary forces (cf. Chapter 3). Intimate contact at the interface between the molten resin and the fibres causes adhesive forces between the two phases (cf. Chapter 5). When the system is cooled, the solidified droplets adhere to the fibres and the towpreg is stabilised. This can be achieved either by running the towpreg through an oven [24, 25, 26, 28–32, 36–40] or, for conductive fibres (e.g., carbon fibres), by applying direct current to the fibres [27].

The most common technique used to melt the resin is to drive the powder laden tow through an oven (cf. Figure 2.16). The residence time,  $t_{oven}$ , of a particle in the oven is given by,

$$t_{oven} = \frac{L_{oven}}{u_t} \quad (2.12)$$

where  $L_{oven}$  is the oven length and  $u_t$  is the tow velocity.

Iyer and Drzal [26] applied a lumped model to predict the time for the towpreg to reach a given temperature. They justify the use of a lumped model arguing that the external heat transfer resistance (heat convection at the surface of the solid) is much larger than internal one (heat conduction within the solid). For a lumped system of mass,  $m$ , specific heat,  $c_p$ , surface area,  $A$ , and heat transfer coefficient,  $h$ , the time,  $t$ , required to raise its temperature from the ambient temperature,  $T_a$ , to  $T$  when the temperature of the heater is  $T_h$ , is given by [26],

$$t = \frac{mc_p}{hA} \ln \frac{T_h - T_a}{T_h - T} \quad (2.13)$$

Based on microscopy observations, they concluded that during the melting phase, arrays of fibre-matrix clusters were formed, with diameters strongly dependent on the amount of

of tow spreading. Figure 2.17 shows a plot of the theoretical time, calculated with Equation 2.13, required by a 50 vol.% carbon fibre-polyamide cluster of diameter,  $D$ , to reach the set temperature of  $180^{\circ}\text{C}$ . The heater temperature is  $200^{\circ}\text{C}$ , and ambient temperature is  $20^{\circ}\text{C}$ . It is clear that the residence time,  $t_{oven}$  (Equation 2.12) must be larger than or equal to  $t$ . The maximum tow velocity per meter length of oven is thus  $u_t^{max} = 1 / t$ , which is also plotted in Figure 2.17. This shows the importance of the tow spreading, which will determine the maximum rate of production when powder fusing is used to stabilise the system.

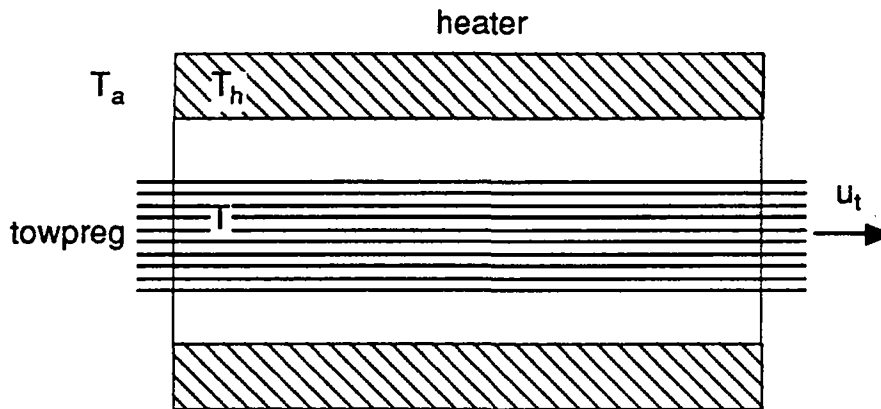


Figure 2.16 Impregnated tow passing through the heater.

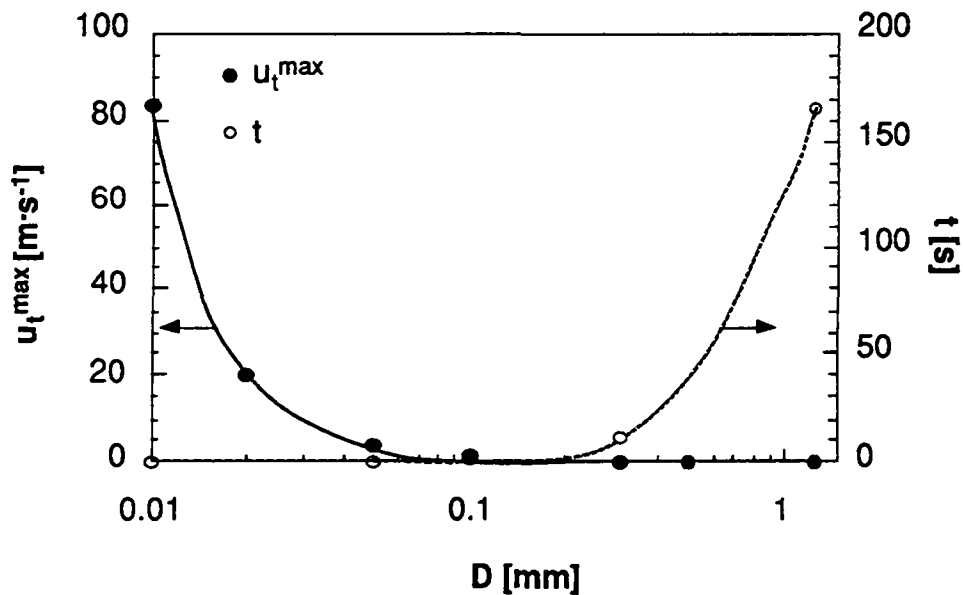


Figure 2.17: Estimated heating times,  $t$ , and maximum specific tow speeds,  $u_t^{max}$  as a function of cluster diameter,  $D$ , for polyamide-CF (AS4) towpregs to reach a temperature of  $180^{\circ}\text{C}$  (after Table 4 in [26]).

Powder fusing by passing direct current through the resin coated fibres was investigated by Edie et al. [27]. As a precondition, the fibres need to be electrically conductive (e.g., carbon fibres). After the powder coating unit, the powder laden fibres are run through a section delimited by two rollers. A DC-power supply is turned on to

apply a voltage between the two rollers. The temperature of the tow was recorded using an infrared pyrometer; temperatures up to 280°C were measured for a polyimide resin. Good results were obtained only for fibre volume contents higher than about 55–60 %. At lower values, resin rich areas were formed which acted as insulators, hindering the electrical contact between the fibres and the rollers. The result is uneven heating and thus uneven coating of the fibres. There might be risks of resin degradation due to local overheating. In this case too, good spreading is of paramount importance. A good spreading favours good electrical contact yielding, a homogeneous temperature within the tow.

### Sheath coating

Ganga [23] introduced a new technique to stabilise the powder coated fibres without melting the resin. At the exit of the powder coating unit, the towpreg is passed through an extruder wire coating die. A thin resin sheath —usually the same polymer as the powder— thus encloses the unmolten powder coated fibre bundle, resulting in an extremely flexible towpreg. This product, known as *FIT* (Fibres Imprégnées de Thermoplastique) will be used during our investigation. Figure 2.18 illustrates the principle of the technique. The FIT materials used in this work were supplied by Porcher Textile.

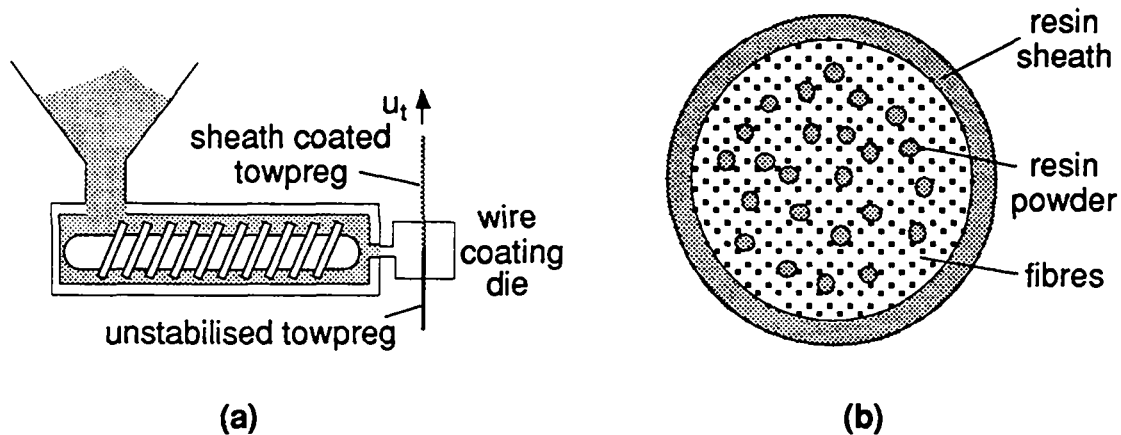


Figure 2.18: Sheath coating of the powder laden fibre tow : (a) wire coating die; and (b) cross-sectional view of a FIT towpreg (after [23]).

FIT yarns are very well suited for weaving, braiding or knitting operations, due to their high flexibility. Furthermore, the resin sheath protects the fibres from abrasion, which is a well known problem in these operations.

The proportion of resin as powder or sheath in the towpreg can be varied by varying the sheath thickness, and by using fibre tows of different size (e.g., 3K-, 6K-, and 12K-carbon fibres). Table 2.3 lists standard FIT towpregs presently manufactured by Porcher Textile.

Table 2.3: FIT towpregs by Porcher Textile

system	PEEK	PEI	PA12
CF (3K)	60	/	/
CF (6K)	67 and 60	58	70
CF (12K)	-	-	70
E-glass 600 tex	-	67	-

*fibre weight fraction in %*

## 2.2.4 Powder content control

The amount of powder laden by the fibre tow can be controlled by:

- controlling the fibre spreading: good fibre spreading increases the fibre surface area exposed to the powder
- controlling the depth of the fluidised bed, or the powder concentration of the powder curtain [39] or the aqueous dispersion [13]
- controlling the tow velocity

The *off-line* technique generally applied to measure the powder content of towpregs is to weigh a given length of towpreg and to report its mass to the specific weight of the fibre tow. Obviously, an *on-line* powder content measurement technique is preferable, allowing the various parameters listed above to be tuned to assure a constant powder take up during continuous coating operations.

Based on the observation that the towpreg width is proportionally related to powder content (cf. Figure 3 in [13]), Vodermyer et al. [13] optically measured the wet towpreg width at the exit of the powder coating unit. The tow width measurement is used for the calibration of the final powder content: in the case of a negative deviation from the nominal value of the towpreg width, a definite amount of dispersion is supplied to the bath to change the powder concentration.

Based on the same principle, a special device was recently developed at the university of Newcastle upon Tyne to measure the thickness of the towpreg at the exit of the powder coating unit. The towpreg passes between two nylon low friction rollers (cf. Figure 2.19). The distance between rollers is measured by an LVDT strain gauge which is directly connected to a shaker, consisting of a pin mounted on a loudspeaker, to shake off the excess powder in the tow.

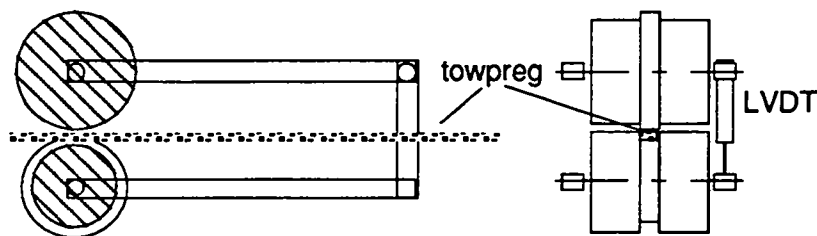


Figure 2.19: Powder content measuring device (powder coating line at the University of Newcastle upon Tyne).

Marchello and Baucom [28] developed a technique to measure powder content in conductive fibres. The towpreg is composed of conducting carbon fibres and dielectric polymer resin; the resin level monitor measures the electric capacitance of the towpreg, at the exit of the towpreg stabilising unit (oven). This quantity can be related to the towpreg resin content.

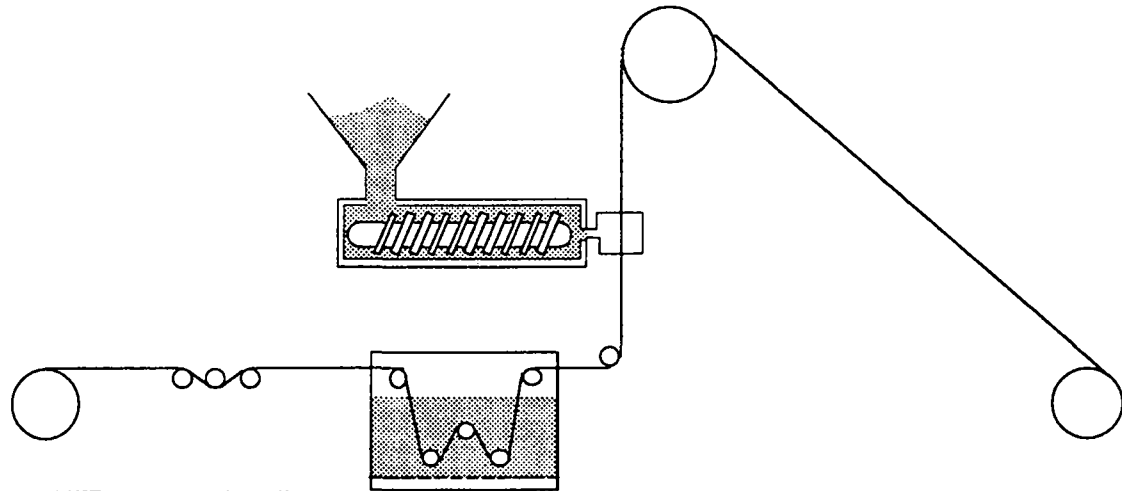
### 2.2.5 Review of powder coating lines

Table 2.4 lists the various solutions adopted by the investigation centres for the processing units —tow spreading, powder coating, and towpreg stabilisation unit. Diagrams of the powder coating lines studied above are presented in Figure 2.20.

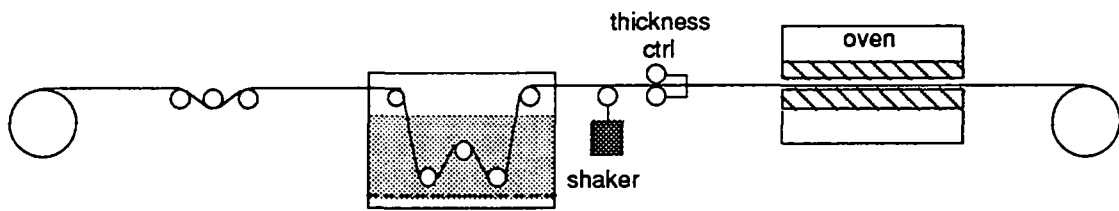
**Table 2.4: Powder coating lines**

location & refs.	spreader	powder deposition	stabilising unit
FIT (Groupe Porcher & Enichem) [23]	pins	fluidised bed	polymer sheath enclosing the powder coated fibre bundle
Univ. Newcastle upon Tyne [32, 37]	pins	fluidised bed	radiation and convection oven
Georgia Institute of Technology [24, 26, 36]	air banding jet spreading the tow about 5 cm wide	fluidised bed with electrostatically charged powder on grounded fibres	oven
NASA Langley Research Center [28, 29, 38]	pneumatic tow spreader	bubbling bed feeder delivers powder to the fluidised bed	oven, followed by $v_m$ on line ctrl by measuring the tow electric capacity
Akron University [31]	aerodynamic Venturi laminar flow slot tunnel (VST) spreads tow from 6-7 mm to 50-75 mm	electrostatic powder coating gun distributes powder onto grounded CF	- electrostatic charges - radiation/convection oven
Clemson University [27]	spreading bars	powder extruder sprinkles powder onto fibre tow	DC heating
NASA Langley Research Center (1994) [39]	pneumatic spreader	powder curtain (needs two runs, flipping the tow)	oven
T.U. Berlin [13]	not reported	aqueous powder dispersion followed by optical tow depth measurement ( $v_m = f(d)$ )	drying oven, followed by powder fusing oven
Virginia Polytechnic Institute and State University [30]	Venturi slot tunnel . ( $w = 2.5$ cm)	deposition of powder on moistened CF	oven to eliminate fibre moisture + melt fuse the powder particles in place
Michigan State University [26]	(?) $w = 5 - 15$ cm; final width: 1-3 cm	impregnation chamber (?)	oven

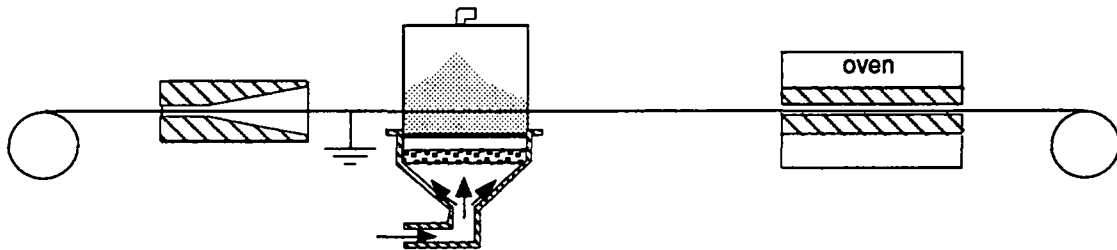




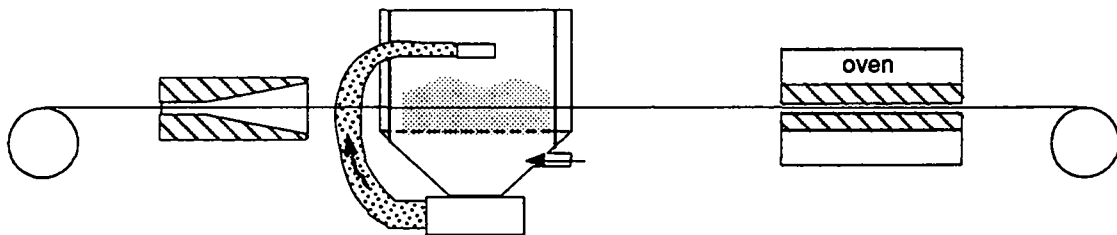
(a) FIT processing line



(b) the University of Newcastle upon Tyne, UK

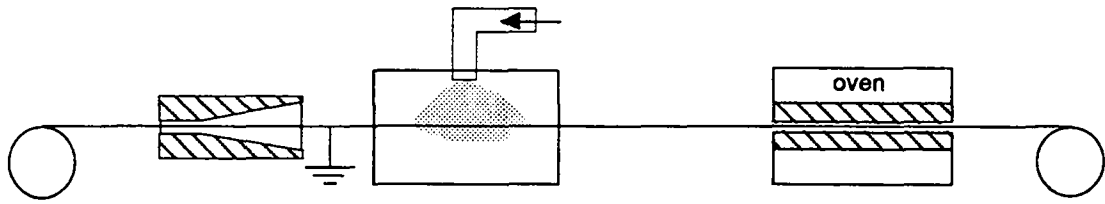


(c) Georgia Institute of Technology, USA

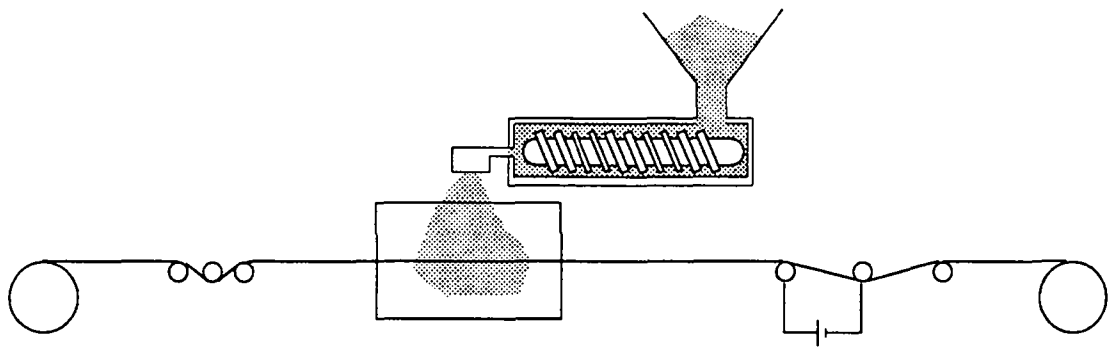


(d) NASA Langley Research Center (1994), USA

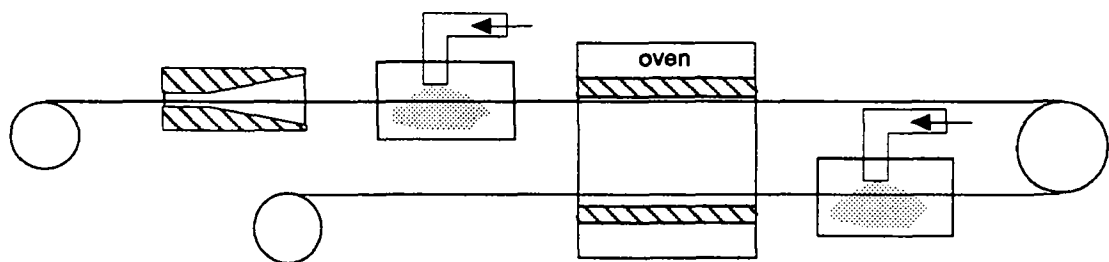
Figure 2.20: Powder coating lines in the world: (a) FIT processing line, at Enichem, I, and Porcher Textile, F (after [23]); (b) the University of Newcastle upon Tyne, UK (after [37]); (c) Georgia Institute of Technology, USA (after [24]); (d) NASA Langley Research Center (1991), USA (after [28]); continues next page



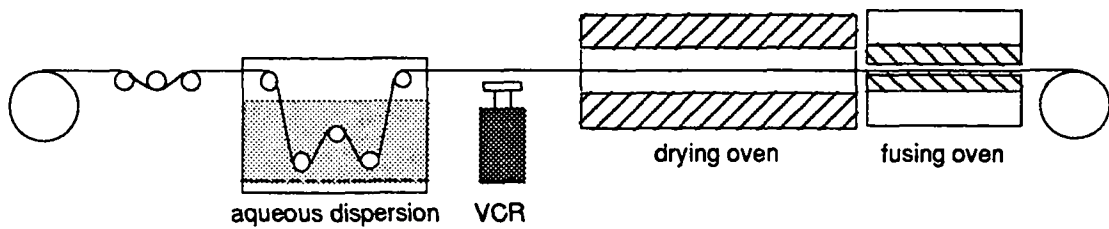
(e) Akron University, USA



(f) Clemson University & BASF, USA



(g) NASA Langley Research Center (1994), USA



(h) T. U. Berlin, D

Figure 2.20 (continued): (e) Akron university, USA (after [31]); (f) Clemson university, USA (after [27]); (g) NASA Langley Research Center (1994), USA (after [39]); and (h) T.U. Berlin, D (after [13]).

### *Powder coating line developed at LTC*

A powder coating line has been designed at the Laboratoire de Technologie des Composites (LTC). The spreading unit consists of a Venturi slot tunnel depicted in Figure 2.21. The tunnel is 220 mm long with a  $8^\circ$  taper angle. The tapered section is 170 mm long. Nine holes on each sidewall are connected to a vacuum manifold. The top of the channel is covered with a transparent lid in PMMA which permits the spreading of the tow to be controlled.

Polymer particles are deposited onto the fibre surface by running the fibre bundle through a fluidised powder bed. The fluidised bed unit (cf. Figure 2.22) consists of an aluminium box with five  $\text{Ø}20$  mm pins; the pins can either be fixed or allowed to rotate. The fibre yarn can be positioned by removing the second and fourth pins, laying the bundle on the remaining three pins, and place the two removable pins back to their original position. Air is injected through a cavity at the bottom of the box connected to the powder bed by a porous, loosely sintered aluminium plate. A constant air flow is thus passed upwards through the powder bed, assuring a controllable fluidisation of the bed.

The powder laden towpreg is stabilised by melt fusing the powder in place into an oven (cf. Figure 2.23). The 914 mm long oven is made of three identical sections with cylindrical heating elements (Superthal HAS 100-250-55 which can heat up to  $1100^\circ\text{C}$ ). It can be opened and a set of five  $\text{Ø}18$  mm fixed pins can be placed in the middle section of the oven to fully impregnate the towpregs *on line*, if desired [43].

This powder coating line is composed of modules which can be modified easily. For example, tow spreading can be achieved pneumatically, or mechanically by either using the Venturi tunnel or a series of spreading pins. This would allow different processing solutions to be investigated. The amount of impregnation of the fibre tows can be controlled by the number of pins placed in the oven. If flexible towpregs are desired, no pins should be used in the oven. On the other hand, if fully impregnated tapes are desired, then all the five pins should be used.

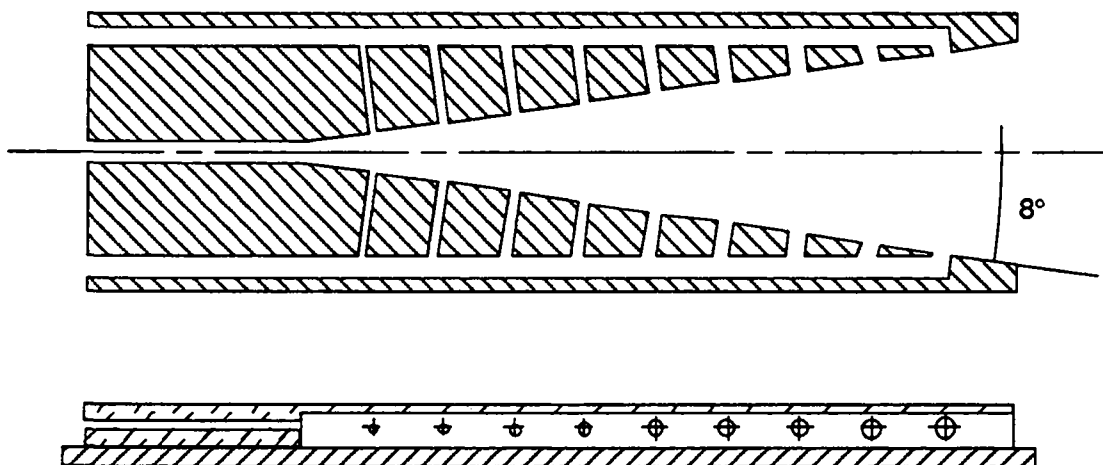


Figure 2.21: Fibre spreading unit: Venturi slot tunnel (a) side view; (b) top view.

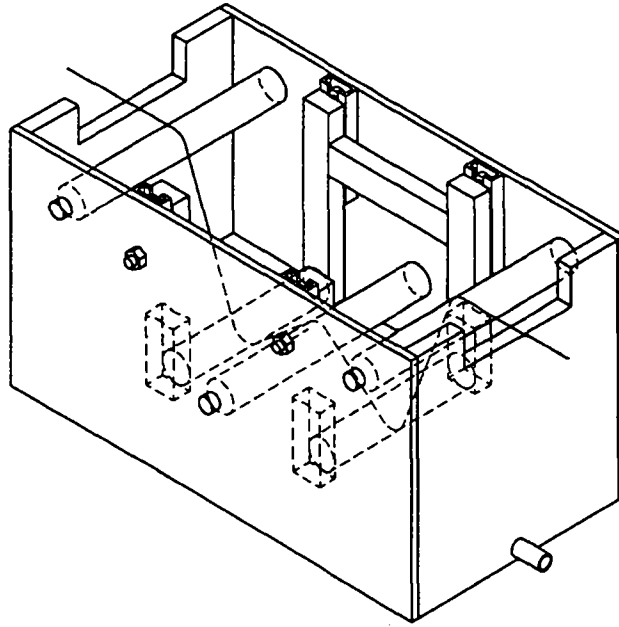


Figure 2.22: Powder coating unit: fluidised powder bed box.

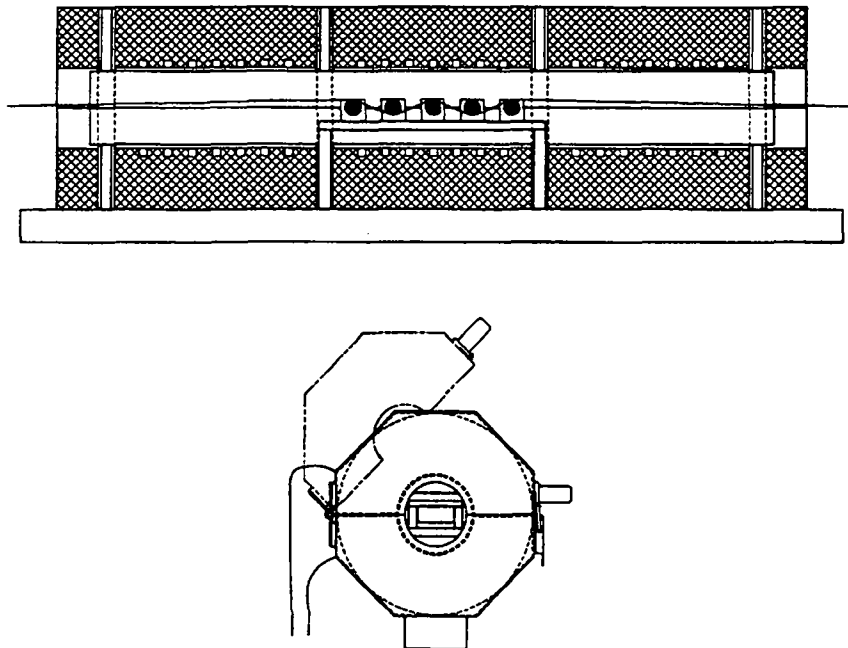


Figure 2.23: Stabilising unit: cylindrical oven with the possibility of placing a set of five pins in the middle section to fully impregnate the running towpreg.

## 2.3 REFERENCES

- 1 Chawla, K. K., "Composite Materials", Springer-Verlag, 1987, p. 7.
- 2 Torayca Technical data sheet, ST2B/1992, Soficar, 1992.
- 3 Hartness, T., *J. Thermoplastic Compos. Mater.* 1988, 1, 210.
- 4a Cogswell, F. N., "Thermoplastic Aromatic Polymer Composites", Butterworth-Heinemann, 1992, p. 51.
- 4b *Ibid.*, p. 80.
- 5 Månson, J.-A. E., in "Advanced Thermoplastic Composites", (Kausch, H. H. Ed.), Hanser Publishers (Munich, etc.), 1993, p. 273.
- 6 Nelson, K. M., Månson, J.-A. E. and Seferis, J. C., *J. Thermoplastic Compos. Mater.* 1990, 3, 216.
- 7 Hartness, T., *32nd Int. SAMPE Sympos.* 1987, 32, p. 154.
- 8 Lam, R. C. and Kardos, J. L., *3rd Annual Technical Conference , American Society for Composites* 1988, p. 3
- 9 Lee, W.I. and Springer, G. S., *J. Compos. Mater.* 1987, 21, 1017.
- 10 Van West, B. P., Pipes, R. B. and Advani, S. G., *Polymer Composites* 1991, 12, 417.
- 11 Bontemps, G., *Schappe Techniques ITF* 1992, 7bis.
- 12 Price, R. V., 1973, *US Patent* 3, 742,106.
- 13 Vodermyer, A. M., Kaerger, J. C. and Hinrichsen, G., *J. Thermoplastic Compos. Mater.* 1993, 4, 123.
- 14 Hugh, M. K., Marchello, J. M., Hartness, J. T., Goodwin, S., Schukla, J. G. and Johnston, N. J., *39th Int. SAMPE Sympos.* 1994, p. 551.
- 15 Greene, T. L. and Holty, D. W., *39th Int. SAMPE Sympos.* 1994, p. 214.
- 16 Wagner, P. and Colton, J., *39th Int. SAMPE Sympos.* 1994, p. 1536.
- 17 Romagna, J. and Ziegmann, G. *3rd Int. Confer. Flow Processes in Composite Materials '94* 1994, Galway, p. 291.
- 18 Hauptert, F. and Friedrich, K., *3rd Int. Confer. Flow Processes in Composite Materials '94* 1994, Galway, p. 279.
- 19 Ramani, K., Borgaonkar, H. and Hoyle, C., *Composites Manufacturing* 1995, 6, 35.
- 20 Ye, L., Klinkmüller, V and Friedrich, K., *J. Thermoplastic Composite Materials* 1992, 5, 32.
- 21 Connor, M., Gibson, A. G., Toll, S. and Månson, J.-A. E., *J. Thermoplastic Compos. Mater.* 1995, 8, 138.
- 22 Connor, M., Gibson, A. G., Toll, S. and Månson, J.-A. E., *Proceed. ICCM9* 1993, III p. 575.

- 23 Ganga, R., 1983, French Patent FR 2548084-A1
- 24 Muzzy, J., Varughese, B. and Yang, P. H., *ANTEC'90* 1990, p. 1385.
- 25 Varughese, B., Muzzy, J. and Baucom, R. M., *21st Int. SAMPE Technical Confer.* 1989, p. 536.
- 26 Iyer, S. R. and Drzal, L. T., *J. Thermoplastic Compos. Mater.* 1990, **3**, 325.
- 27 Edie, D. D., Gantt, B. W., Lickfield, G. C., Drews, M. J. and Ellison, M.S., in "Advances in Thermoplastic Composite Materials, ASTM STP 1044," (G. M. Newaz, Ed.), ASTM, Philadelphia, 1989, pp. 50–61.
- 28 Marchello, J. M. and Baucom, R. M., *36th Int. SAMPE Sympos.* 1991, p. 68.
- 29 Baucom, R. M. and Marchello, J. M., *35th Int. SAMPE Sympos.* 1990, p. 175.
- 30 Ogden, A. L., Hyer, M. W., Wilkes, G. L. and Loos, A. C., *J. Thermoplastic Compos. Mater.* 1992, **5**, 14.
- 31 Throne, J. L. and Sohn M.-S., *35th Int. SAMPE Sympos.* 1990, 2086.
- 32 Rozant, O., Diploma Project, LTC-EPFL, Feb. 1994.
- 33a Hawkins, A. E., in "Principles of Powder Technology", M. Rhodes Ed., John Wiley & sons, 1990, p. 19.
- 33b Ibid., p. 54
- 33c Ibid., p. 22
- 34a Coulson, J. M., Richardson, J. F., Backhurst, J. R. and Harker, J. H., "Chemical Engineering", 3rd Ed., Pergamon Press, 1985, vol. 2, p. 13.
- 34b Ibid., p. 3.
- 34c Ibid., p. 230.
- 34d Ibid., p. 231.
- 34e Ibid., p. 232.
- 35 Lyon, K. R., Texier, A., Gungor, A., Davis, R. M. and Mc Grath, J. E., *37th Int. SAMPE Sympos.* 1992, p. 1301.
- 36 Muzzy, J. D., in "The Manufacturing Science of Composites: presented at MI '88 Atlanta," (T. G. Gutowski, ed.) 1988, p. 27
- 37 Miller, A., Gibson, A. G., Wei, C., Connor, M., Rozant, O. and Manson, J.-A. E., *6th Int. Confer. on Fibre Reinforced Composites* 1994, Newcastle (UK)
- 38 Hugh, M. K., Marchello, J. M., Baucom, R. M. and Johnston, N. J., *37th Int. SAMPE Sympos.* 1992, p. 1040.
- 39 Baucom, R. M., Marchello, J. M. and Hugh, M. K., *Proceedings of 39th Int. SAMPE Sympos.* 1994, p. 793.
- 40 Geldart, D., in "Principles of Powder Technology", (M. Rhodes Ed.) John Wiley & sons, 1990, p.119.
- 41 Geldart, T., *Powder Technol.* 1973, **7**, 285.
- 42 Wen, C. Y. and Yu, Y. H., *A.I.Ch.E.J.* 1966, **12**, 610.

43 Gibson, A. G. and Manson, J.-A. E., *Composites Manufacturing* 1992, 3, 223.

# 3

## ANALYSIS OF THE IMPREGNATION MECHANISM

The principal techniques for the incorporation of a resin powder into reinforcement fibres were reviewed in Chapter 2. This step was defined in the introduction section of this work as the *mingling* stage. Two major types of powder impregnated fibre yarns were presented: *FIT bundles* which consist of powder loaded fibres enclosed in a thin resin sheath, and *molten powder towpregs* in which the particles are fixed to the fibres in an oven by melting the resin. In this chapter, the mechanisms involved during the *impregnation* and *consolidation* stages of the powder loaded fibre bundles, when the temperature is raised above the polymer melting (or softening) point are examined. This study will focus on the case of no externally applied pressure, so that only surface energy effects are responsible for the impregnation. The formation of resin bridges between adjacent fibres is first investigated using a hot stage placed under a microscope. The driving forces leading to the spreading of the bridge along the fibres are then analysed at two levels: at a macroscopic scale first, with the characterisation of the capillary pressure responsible for the flow of a liquid into a porous solid, and second, at a micro-mechanical level with the analysis of the capillary forces in a system defined by a liquid drop in contact with two solid particles.

### 3.1 RESIN BRIDGE FORMATION

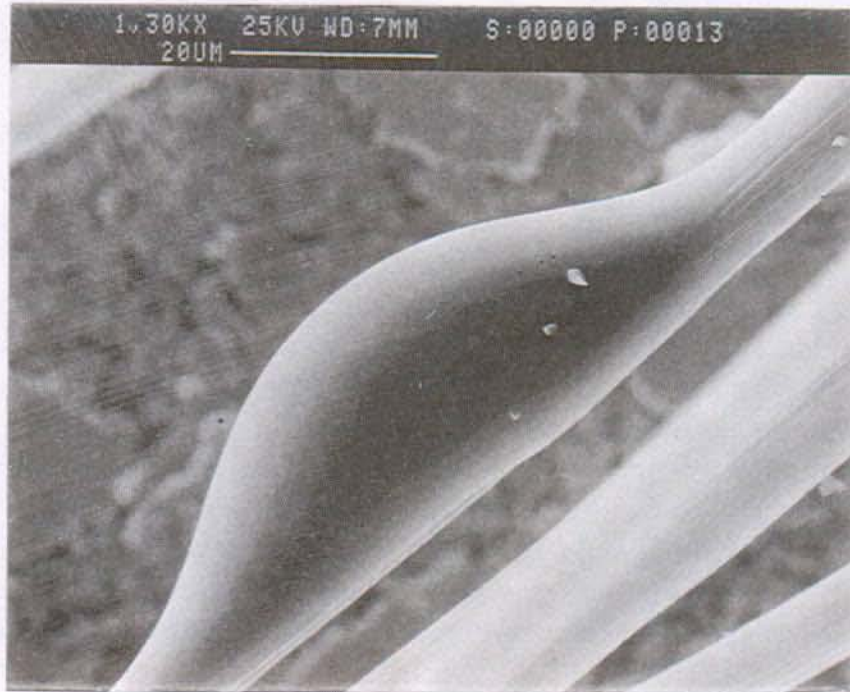
When the temperature is raised to an appropriate level above the glass transition temperature (or crystalline melting point in the case of a semi-crystalline polymer) the polymer viscosity falls to a value where the powder particles are first able to adopt a thermodynamically favourable spherical shape. As the powder particles are in contact with the fibres, the initially spherical droplets spread along the surface of the fibres, driven by surface energy. To make the manufacturing process rapid enough to be viable, however, it is necessary to assist the spreading process by the application of external pressure, whose effects will be considered in Chapter 4.

In the absence of externally applied pressure, the droplet and the fibres will eventually reach an equilibrium geometry dictated by the surface energies of the interfaces present. One significant parameter influencing the final geometry is the contact angle,  $\theta$ ,

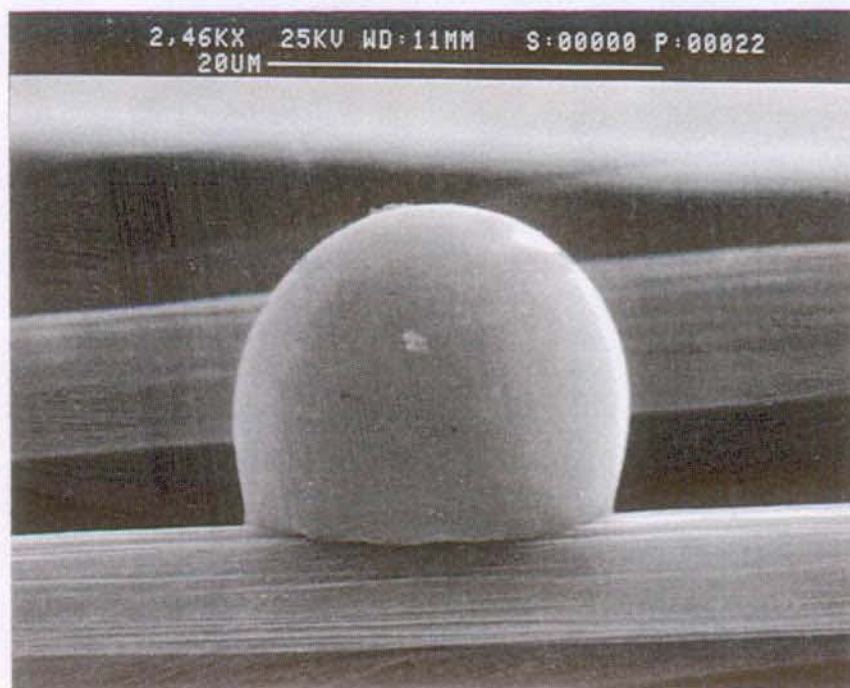


at the contact line between the resin drop and the fibre surface. Young [1] proposed that, at equilibrium, the contact angle is related to the surface energies per unit area of the solid-liquid, liquid-air and air-solid interfaces,  $\gamma_{sl}$ ,  $\gamma_l$  and  $\gamma_s$ , respectively, by

$$\cos \theta = \frac{\gamma_s - \gamma_{sl}}{\gamma_l} \quad (3.1)$$



(a)



(b)

Figure 3.1: Molten resin drops on the surface of a carbon fibre (SEM): (a) PEEK, the contact angle  $\theta = 0^\circ$  at the tip of the protruding foot; and (b) PEI,  $\theta = 66^\circ$ .

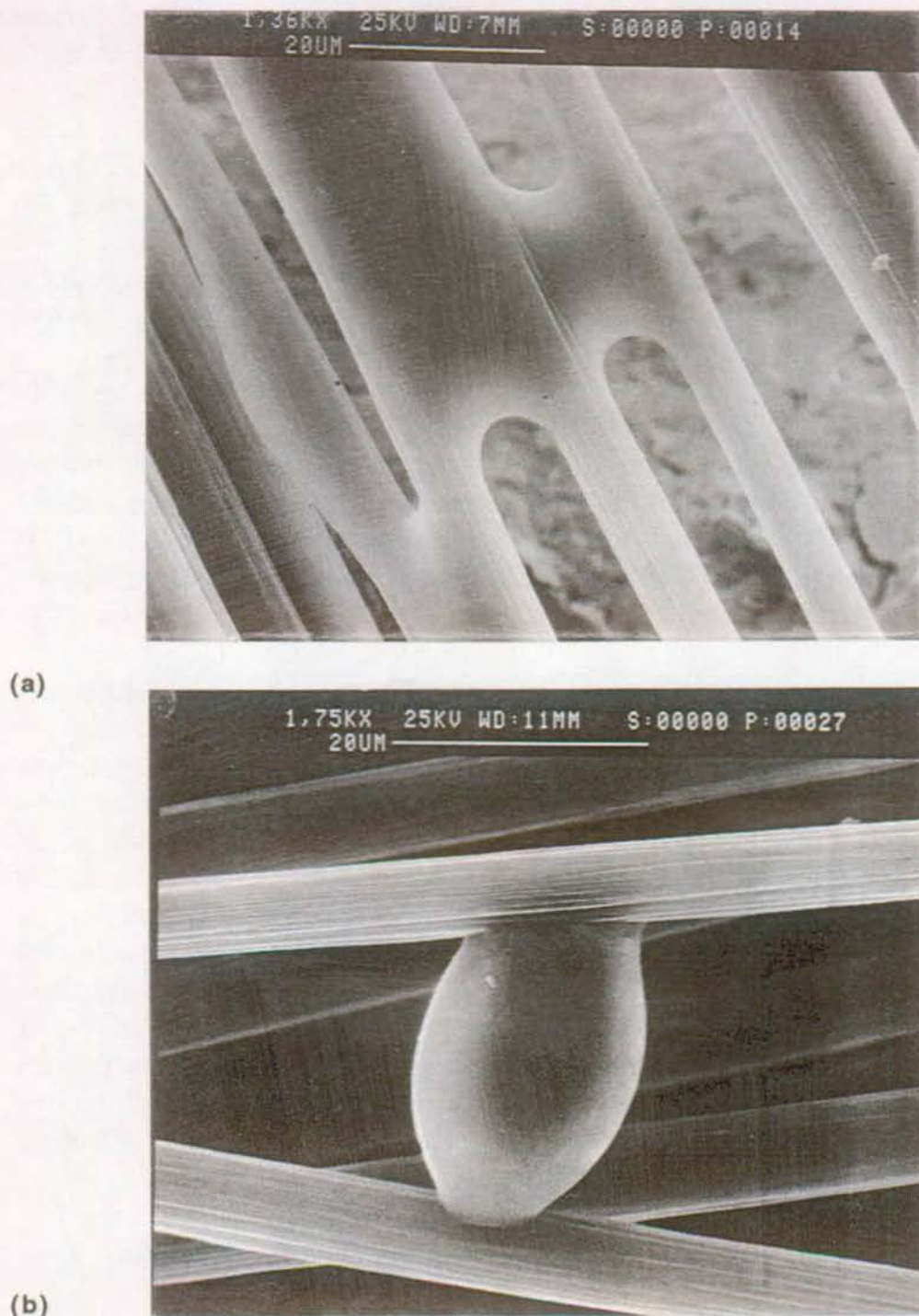


Figure 3.2 : Resin bridges formed between two carbon fibres (SEM): (a) PEEK forms an angle close to zero with the fibres; (b) an angle of about  $66^\circ$  can be measured for PEI resin.

As will be shown more in details in Chapter 5, the contact angle will be strongly influenced by factors such as the surface energy and polarity of the two phases in contact and can vary substantially from one system to another (e.g., fibre sizing, polymer polarity, etc.). This is demonstrated in Figure 3.1, which compares the contact angles of droplets of poly(ether-ether-ketone) (PEEK) and poly(ether-imide) (PEI) on carbon fibres. Both micrographs show samples of polymer powder in contact with the fibre, cooled after approximately five minutes at  $380^\circ\text{C}$  for PEEK and  $280^\circ\text{C}$  for PEI. Although

it is not clear whether the full equilibrium geometry has been reached in these micrographs, it is assumed that the observed contact angle is close to that which would pertain at rest. The PEEK droplet does not form a spherical cap on the carbon fibre but shows a *protruding foot* typical of high-viscosity polymers with good wetting properties [2]; the contact angle at the end of the protruding foot is close to zero. The PEI/carbon system, by contrast, forms a “clam-shell drop,” showing an angle of about  $66^\circ$  characterising poor wetting properties. The technique used to measure the contact angle of a resin drop sitting on a cylindrical fibre is presented in details in Chapter 6 (cf. §6.2.2).

In a real powder-impregnated composite, each resin particle will be in contact with more than one fibre at a time. Looking at the case of a polymer in contact with two parallel fibres, it is observed that when the resin melts, a bridge is formed between the fibres, and the final geometry of this bridge depends on the surface energies of the components. Figure 3.2 shows examples of such bridges that were obtained by heating the polymer particles and fibres under an optical microscope using a hot-stage; once the samples were cooled, pictures were taken in a scanning electron microscope (SEM). In the CF-PEEK system in Figure 3.2a, characterised by a very small contact angle, the droplets have spread along the fibres, drawing them together. In contrast to this, the CF-PEI system in Figure 3.2b shows a bridge that has not spread and is indeed holding the fibres apart. The dynamics of the fibre/resin interaction was clearly visible under real time observation.

Based on the observations presented above, the following mechanism for the impregnation and consolidation of fibre impregnated towpregs is proposed: when the resin particles melt, they will bridge two, three or more adjacent fibres, and will spread along the channels formed between the fibres, driven by capillary pressure and applied pressure. In the absence of externally applied pressure, the resin bridges spread on the fibre surface in order to reduce the difference of hydrostatic capillary pressure across the various interfaces. In composite materials, this effect can be quite important due to their generally large specific interfacial area. The system tends to minimise its Helmholtz free energy by decreasing the surface area of the most energetic interfaces, expanding the least energetic ones. The resin will stop flowing, and the system reach an equilibrium configuration, when the pressure difference drops to zero. Surface energy effects in composite impregnation and consolidation are studied in the following section.

## **3.2 CAPILLARY ACTION**

Macroscopic capillary pressure and microscopic inter-particle forces due to surface tension are examined. A general equation for the capillary pressure during consolidation is derived and subsequently specialised to particular processes.

### **3.2.1 Background**

Composite impregnation and consolidation processes usually involve the flow of a liquid matrix into an assembly of closely spaced particles of the order of  $10\ \mu\text{m}$  size (e.g., fibres). The liquid must flow through long and narrow channels and wet a large surface area of particles. Under such conditions the surface energies of the various phases are

likely to play an important role. Surface energy effects can be described on at least two levels: the macroscopic level, where they appear as a capillary pressure, and the micromechanical level, where they appear as forces acting between individual particles. This chapter addresses both levels.

Capillary pressure,  $p_c$ , is the difference of hydrostatic pressure across a liquid-fluid interface due to surface tension, which causes the liquid front to move so as to reduce this pressure gradient. The classical treatment to quantify capillary pressure is to use the Laplace equation, which was first proposed in 1806:

$$p_c = \gamma_l \left( \frac{1}{R_1} + \frac{1}{R_2} \right) \quad (3.2)$$

where  $\gamma_l$  is the surface tension per unit length of the liquid, and  $R_1$  and  $R_2$  are the principal radii of curvature of the liquid front. This classical treatment of capillarity is readily applied to systems in which the solid surfaces form closed cylindrical channels and in which a single liquid front is moving [3, 4]. In more complex geometries, however, (e.g., fibre beds in composites, woven fabrics, etc.) this approach based on curvature calculations is impractical. For these applications, it will be more appropriate to directly consider the macroscopic pressure contribution,  $P_c$ , due to capillarity, which is the average of  $p_c$  over the total volume,  $V$ . Macroscopic capillary pressure can thus be defined as,

$$P_c = - \left( \frac{\partial F}{\partial V} \right)_T \quad (3.3)$$

where  $F$  is the Helmholtz free energy of the system of total volume,  $V$ , at constant temperature, adsorption equilibrium, chemical potential, etc. Definition (3.3) allows a mean value of the capillary pressure over the volume of the system,  $V$ , to be calculated independently of the geometry and of number of flow fronts. The capillary pressure determines whether spontaneous impregnation can occur: if the total amount of surface energy decreases upon impregnation the capillary pressure will be negative and impregnation (decrease of volume) will tend to be spontaneous; if the energy increases, the system resists impregnation causing impregnation to take place only under externally applied pressure.

The capillary force between particles connected by a resin droplet will be defined similarly

$$f_c = \left( \frac{\partial F}{\partial a} \right)_T \quad (3.4)$$

where  $a$  is the distance between the particles. The capillary forces between particles are then the microscale origin of the macroscopic capillary pressure.

Figure 3.3 illustrates the most common impregnation or consolidation situations. Figure 3.3a shows the case of resin transfer moulding (RTM), melt impregnation or infiltration; Figure 3.3b shows radial impregnation of a fibre bundle [5]; Figure 3.3c shows impregnation by commingled resin fibres [6]; and Figure 3.3d shows the case of

a liquid dispersed among the solid particles, e.g., consolidation of powder impregnated tows [7]. One can further distinguish low-pressure techniques, using applied pressures of the order of  $10^5$  Pa, (e.g., vacuum bagging, filament winding) from higher-pressure techniques using the order of  $10^6$ – $10^7$  Pa, usually for high viscosity thermoplastic matrices (e.g., autoclave forming, compression moulding). Capillary effects are more likely to be significant when applied pressures are low.

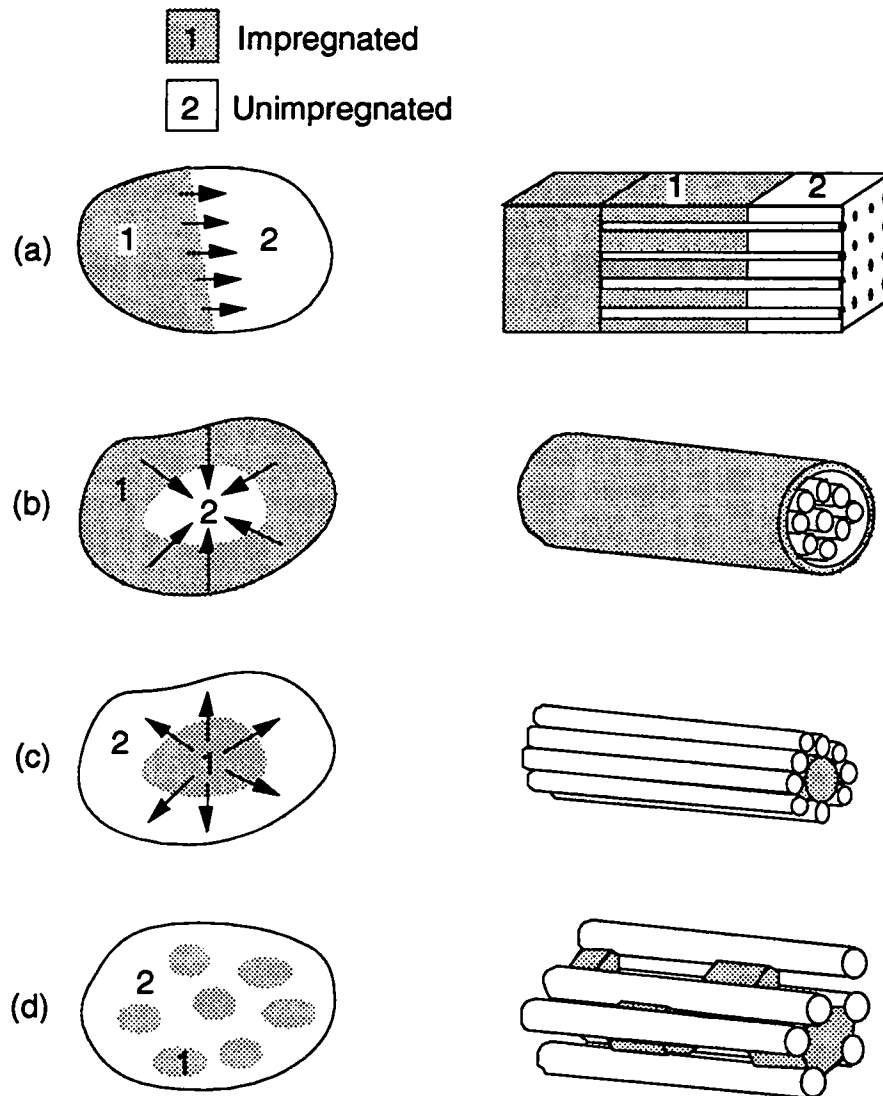


Figure 3.3: Different impregnation situations: (a) advancing front (e.g., RTM); (b) radial impregnation of a fibre bundle; (c) commingled fibres; and (d) liquid dispersed among the solid particles (e.g., powder impregnation).

In this chapter, a general expression for the capillary pressure is derived based on Equation 3.3, allowing for a completely general pore geometry and a solids volume fraction that may vary during impregnation. Specialisation is then made to the various cases in Figure 3.3. Next, the capillary forces between particles connected by liquid

droplets are examined by considering two different geometries: parallel square-section fibres and parallel plates.

### 3.2.2 Capillary pressure

#### *General theory*

Consider a volume  $V$  divided into two types of subdomains: the impregnated volume,  $V_I$ , consisting of solid and liquid, and the unimpregnated volume  $V_2$ , consisting of solid and void, see Figure 3.3. Both solid and liquid are considered incompressible. Now mass conservation of solid and fluid requires:

$$V_l = V_1(1 - \phi_1) \quad (3.5)$$

$$V_s = V_1\phi_1 + V_2\phi_2 \quad (3.6)$$

where  $V_s$  and  $V_l$  are the (constant) volumes of solid and liquid in  $V$ , respectively, and  $\phi_1$  and  $\phi_2$  are the solid volume fractions in  $V_1$  and  $V_2$ , respectively. This can be rearranged to express  $V_1$  and  $\phi_1$  in terms of the total volume  $V$  and volume fraction  $\phi_2$  only:

$$V_1(V, \phi_2) = \frac{V_s + V_l - V\phi_2}{1 - \phi_2} \quad (3.7)$$

$$\phi_1(V, \phi_2) = 1 - \frac{V_l}{V_1} \quad (3.8)$$

If  $S_s$  and  $S_l$  are the surface area per unit volume of solid and liquid, respectively, then the Helmholtz free energy can be expressed as

$$F = S_s[\phi_1 V_1 \gamma_{sl} + \phi_2 V_2 \gamma_s] + S_l V_1 \gamma_l \quad (3.9)$$

where  $\gamma_l$ ,  $\gamma_s$ , and  $\gamma_{sl}$  are the surface energy per unit area of liquid, solid, and solid-liquid interface, respectively. By substituting Equations 3.7 and 3.8 into (3.9),  $F$  can be written as a function of  $V$  and  $\phi_2$ :

$$F = \frac{1}{1 - \phi_2} (V_s + V_l)(S_s \gamma_{sl} + S_l \gamma_l) - \frac{\phi_2}{1 - \phi_2} (V_s + V_l) S_s \gamma_s + \frac{V\phi_2}{1 - \phi_2} (S_s \gamma_s + S_l \gamma_l - S_s \gamma_{sl}) - V_l S_s \gamma_s \quad (3.10)$$

Allowing for  $\phi_2$  (the solids volume fraction in the regions under impregnation) to vary during impregnation, the capillary pressure according to Equation 3.3 can be expressed as

$$-P_c = \left( \frac{\partial F}{\partial V} \right)_{T, \phi_2} + \left( \frac{\partial F}{\partial \phi_2} \right)_{T, V} \frac{d\phi_2}{dV} \quad (3.11)$$

which, together with Equation 3.10, gives the final result:

$$P_c = -\gamma_l (S_s \cos \theta + S_l) \left( \frac{\phi_2}{1 - \phi_2} - \frac{\phi \phi_v}{(1 - \phi_2)^2} \frac{d\phi_2}{d\phi} \right) \quad (3.12)$$

where  $\phi_v$  is the void volume fraction and  $\theta$  is the contact angle, related to the surface energies through the Young Equation 3.1. Equation 3.12 is the general result valid for all the processes under consideration in this chapter.

### ***Fibre composites – examples***

The specific impregnation processes illustrated in Figure 3.3 can be divided into two classes: (i) processes where the impregnated and unimpregnated domains are separated on a scale significantly larger than the inter-particle spacing (Figure 3.3a–c), and (ii) processes where the liquid pools are dispersed among the particles in domains comparable in size to the inter-particle spacing (Figure 3.3d). In the case of cylindrical reinforcement (fibres) the specific surface area,  $S_s$ , is equal to  $2 / R_f$ , where  $R_f$  is the fibre radius. In both examples  $S_l$  will be considered negligible compared to  $S_s$ .

(i) *Full separation (e.g., RTM or melt impregnation)*. This comprises cases (a) through (c) in Figure 3.3, where the impregnated and non-impregnated regions are fully separated. In these cases the fibre volume fraction in the region under impregnation (region 2) will be assumed to be constant. Thus  $d\phi_2 / d\phi = 0$ , and Equation 3.12 can be written as

$$P_c = -\frac{2\gamma_l}{R_f} \left( \frac{\phi_2}{1 - \phi_2} \right) \cos \theta \quad (3.13)$$

This equation is identical to the result proposed by Ahn et al. [8] for resin transfer moulding.

(ii) *Full dispersion (e.g., powder impregnation)*. Since the liquid phase is fully dispersed among the solid particles, the fibre volume fraction is homogeneous, so  $\phi_2 = \phi$ , and  $d\phi_2 / d\phi = 1$ . Equation 11 can thus be written as

$$P_c = -\frac{2\gamma_l}{R_f} \left( \frac{\phi}{1 - \phi} \right)^2 \left( \frac{1 - \phi}{\phi} \right)_{Final} \cos \theta \quad (3.14)$$

This is the same expression as proposed in [9] for powder impregnated composites. It should be noted that our neglect of the free liquid surface restricts Equation 3.14 to the final stages of an impregnation process. In order to capture the early stages it would be necessary to model the free liquid surface area per unit volume of liquid  $S_l$ , which unlike

$S_s$  is a function of  $V$ . This requires a more detailed description on the particle level, and is thus left for the next section.

Equations 3.13 and 3.14 are plotted as a function of  $\phi_2$  in Figure 3.4 using parameters typical of a fibre-resin system, i.e.,  $\gamma_l = 4.0 \times 10^{-2} \text{ Pa}\cdot\text{m}$ ,  $\theta = \pi/6$ ,  $R_f = 3.5 \mu\text{m}$ , and the final fibre content,  $\phi_{final} = 0.65$ . In the *fully separated* case (Equation 3.13), the fibre volume fraction does not vary during impregnation. The solid line therefore gives the capillary pressure for all volume fractions. By contrast, in the *fully dispersed* case (Equation 3.14),  $P_c$  evolves during the impregnation of one system; this evolution (dashed line) is determined by the fibre volume fraction at the fully consolidated state,  $\phi_{final}$ , where Equations 3.13 and 3.14 become equivalent.

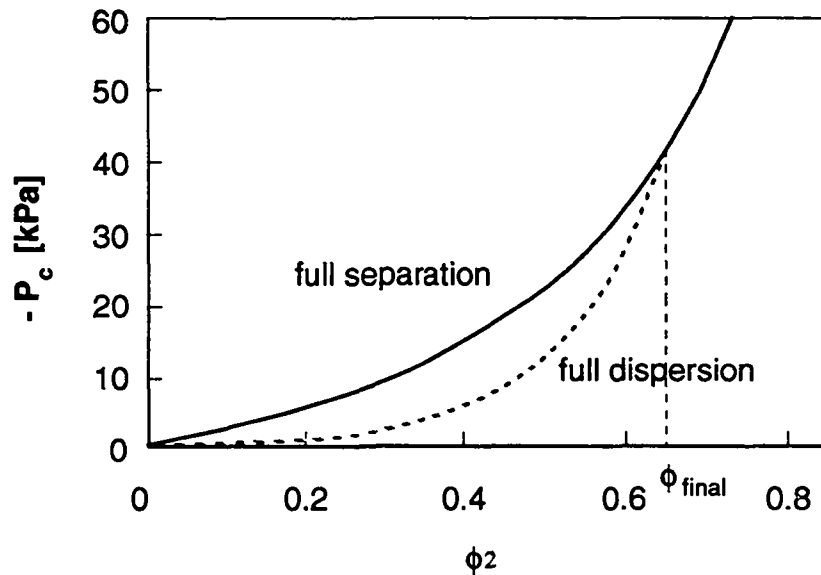


Figure 3.4: Capillary pressure as a function of the fibre volume fraction: the full separation case correspond to Eq. 3.13 and the full dispersion one to Eq. 3.14.

### 3.2.3 Capillary inter-particle forces

It has been shown that the macroscopic effects of surface energy can be evaluated based on average geometrical quantities such as volume fractions and surface area per unit volume of the various phases. An understanding of the capillary forces acting on the micromechanical level requires, however, a detailed description of particle shape and arrangement. Here the analysis will be focused on the situation in Figure 3.3d, where the liquid is dispersed as small droplets between the solid particles. This situation may arise in thermoplastic powder impregnation, where the liquid droplets are formed by the melting of powder grains, or in resin transfer moulding or melt impregnation, where droplets may form by splitting of a flow front [10]. The liquid droplets will tend to adopt a shape which minimises the surface energy. If a droplet makes contact with two or more particles, it may either repel or attract the particles depending on the various surface energies. A value of the particle spacing may also exist for which the capillary force vanishes. This then corresponds to an equilibrium state to which the system tends in the



absence of applied pressure. Capturing this effect requires geometric modelling of  $S_l$  and is thus missed by our previous result (Equations 3.13 and 3.14), which neglects  $S_l$ . Here we shall merely illustrate the nature of the capillary microforces and show when an equilibrium state exists. Many different geometries can be envisaged. Two have been chosen here based on analytical and experimental feasibility: a droplet in contact with, in the first case, two parallel square-section fibres, and, in the second case, two parallel plates; the former has a simple analytical solution, whereas the latter requires a numerical solution but can be experimentally realised.

### *Droplet in contact with two parallel square-section fibres*

A good description, at the qualitative level, is afforded by the idealised geometry depicted in Figure 3.5, where two cases are represented:  $\theta < \pi/2$  and  $\theta > \pi/2$ . The contact angle is of course bounded by  $0 \leq \theta \leq \pi$ . To calculate the capillary inter-particle force, the following assumptions are made: both liquid and solid are incompressible; the drop volume,  $V$ , is constant,  $dV/da = 0$ ; the contact angle,  $\theta$ , is constant,  $d\theta/da = 0$ ; and the curved liquid surface is cylindrical. The capillary force,  $f_c$ , is taken positive when the fibres are pulled together.

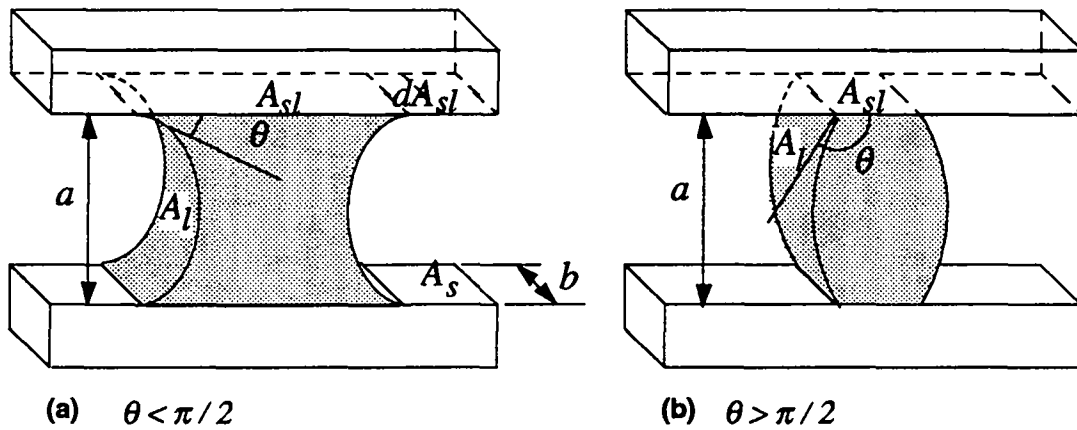


Figure 3.5: A liquid droplet bridging two parallel square section fibres: (a)  $\theta < \pi/2$ , and (b)  $\theta > \pi/2$ .

Statically, the work,  $f_c da$ , required to move the fibres a distance,  $da$ , apart is equal to the variation of the Helmholtz free energy,  $dF$  of the system,

$$f_c da = dF = \gamma_l dA_l + \gamma_s dA_s + \gamma_{sl} dA_{sl} \quad (3.15)$$

Based on the geometry represented in Figure 3.5 the various surface area variations,  $dA$ , can be related to the variation of distance,  $da$ , between the fibres as,

$$dA_l = 2b \frac{(\frac{\pi}{2} - \theta)}{\cos \theta} \cdot da \quad (3.16)$$

and

$$dA_{sl} = -dA_s = \left[ -2 \frac{V}{a^2} + b \left( \frac{\frac{\pi}{2} - \theta}{\cos^2 \theta} - \tan \theta \right) \right] \cdot da \quad (3.17)$$

Introducing Equations 3.16 and 3.17 into Equation 3.15 and using the Young equation (Equation 3.1) allows the capillary force,  $f_c$ , to be expressed as a function of the distance between the two fibres,  $a$ , as,

$$f_c(a, \theta) = \gamma_l \left( b \frac{\left( \frac{\pi}{2} - \theta \right)}{\cos \theta} + b \sin \theta + 2 \frac{V}{a^2} \cos \theta \right) \quad (3.18)$$

which is plotted in Figure 3.6 for an angle,  $\theta$ , smaller and greater than  $\pi/2$ , respectively. For angles smaller than  $\pi/2$ , the force is always attractive ( $f_c > 0$ ) and increases as the fibres are pulled together. For angles greater than  $\pi/2$ , however, the fibres are first driven closer together, until they reach an equilibrium distance,  $a_0$ , at which point the capillary force,  $f_c$ , is zero. Any attempt to drive them closer would require the application of an external force.

The equilibrium distance,  $a_0$ , can be found by setting the force,  $f_c$ , in Equation 18 to zero. This can be written as a dimensionless distance,  $a_0^* = a_0 \sqrt{b/V}$  as

$$a_0^* = \frac{2 \cos \theta}{\sqrt{2\theta - \pi - \sin 2\theta}} \quad (3.19)$$

which is defined for angles greater than  $\pi/2$  only, and is plotted in Figure 3.7.

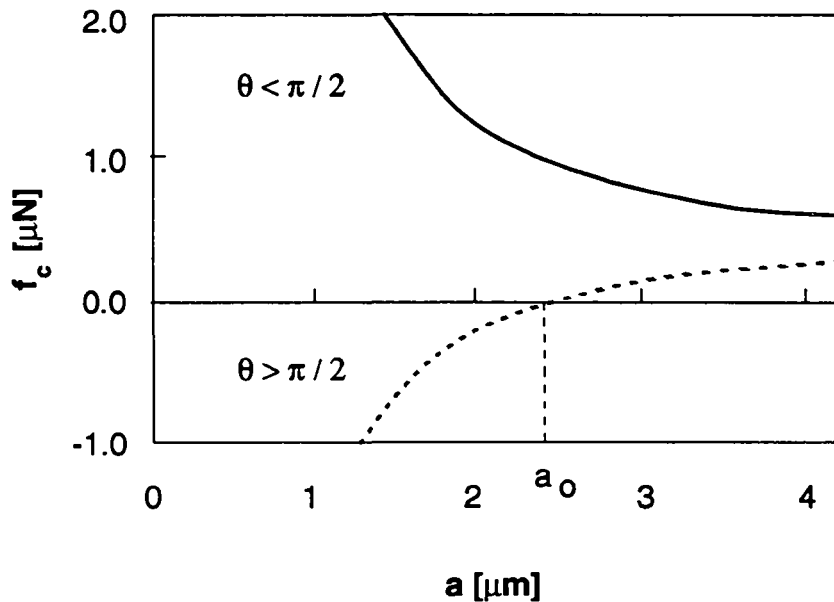


Figure 3.6: Capillary force as a function of the distance between fibres (Eq. 3.18) with  $\gamma_l = 4.0 \times 10^{-2} \text{ Pa}\cdot\text{m}$ ,  $b = 5 \mu\text{m}$ ,  $V = 10^3 \mu\text{m}^3$ ,  $\theta = 87.7^\circ$  (solid line), and  $\theta = 91.7^\circ$  (dashed line).

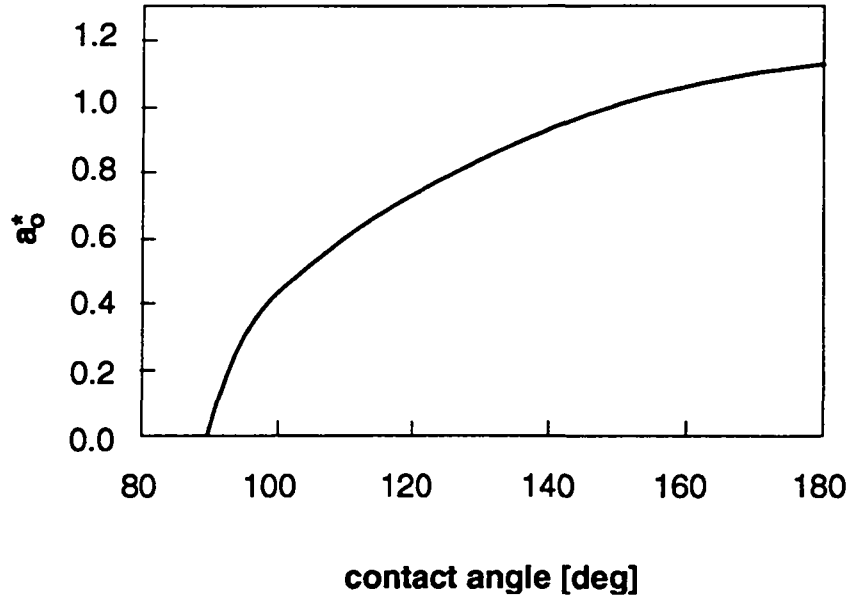


Figure 3.7: Equilibrium distance,  $a_0^*$ , as a function of the contact angle (Eq. 3.19).

#### *Droplet in contact with two parallel plates*

The geometry depicted in Figure 3.8, an axi-symmetric droplet of fluid generated by the rotation of a circular arc, in contact with two parallel plates is relatively close to the geometry shown in Figure 3.2, yet allowing a fairly simple derivation. Furthermore, it can readily be reproduced experimentally. Following the same procedure as in the previous section, an expression for the force as a function of the distance between the two plates and the contact angle can be derived from Equation 3.15:

$$f_c(a, \theta) = 2\pi\gamma_l \left[ R + a \frac{dR}{da} + \frac{a}{2} \tan \theta + \frac{a}{2 \cos^2 \theta} \left( \theta - \frac{\pi}{2} \right) - 2R \frac{dR}{da} \cos \theta \right] \quad (3.20)$$

where

$$\frac{dR}{da} = \frac{1}{2} \frac{\frac{a}{8} \Phi^2 - \frac{a}{2} \Theta + \frac{v}{a^2 \pi}}{\sqrt{\frac{a^2}{16} \Phi^2 - \frac{a^2}{4} \Theta + \frac{v}{a\pi}}} - \frac{\Phi}{4}$$

with

$$\Phi = \tan \theta + \frac{\left( \theta - \frac{\pi}{2} \right)}{\cos^2 \theta}$$

and

$$\Theta = \frac{1}{\cos^2 \theta} + \frac{\tan \theta}{\cos^2 \theta} \left( \theta - \frac{\pi}{2} \right) - \frac{1}{3}$$

where  $R$  is the radius of the solid-liquid interfacial area (cf. Figure 3.8). Equation 3.20 is plotted in Figure 3.9 for an angle  $\theta = 145^\circ$  and compared to experimental data presented in the following section of this chapter.

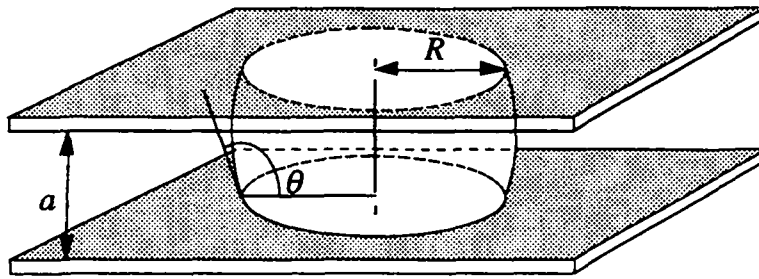


Figure 3.8: Axi-symmetric droplet bridging two parallel plates.

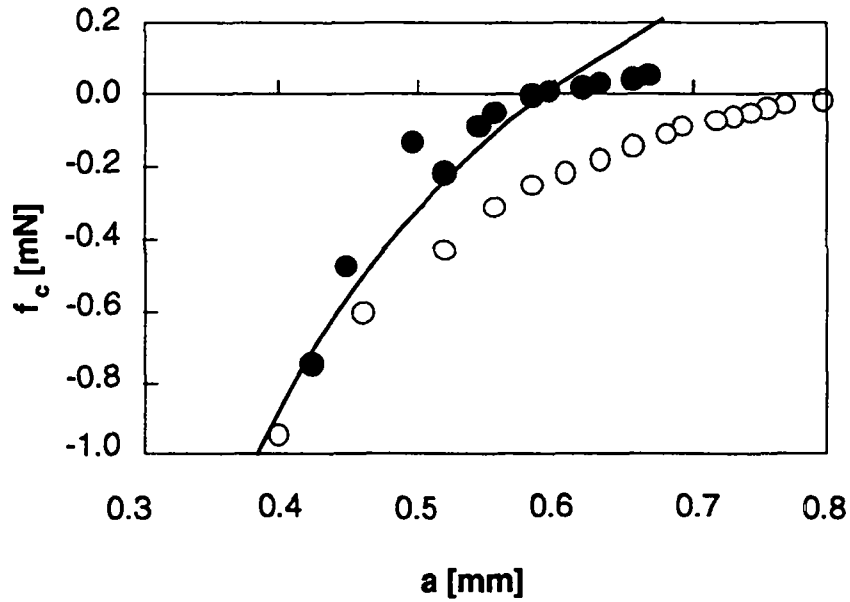


Figure 3.9: Capillary force as a function of the distance between plates. The solid line is obtained with Eq. 3.20 the circles are experimental data obtained by lowering (white) then raising (black) the upper plate.

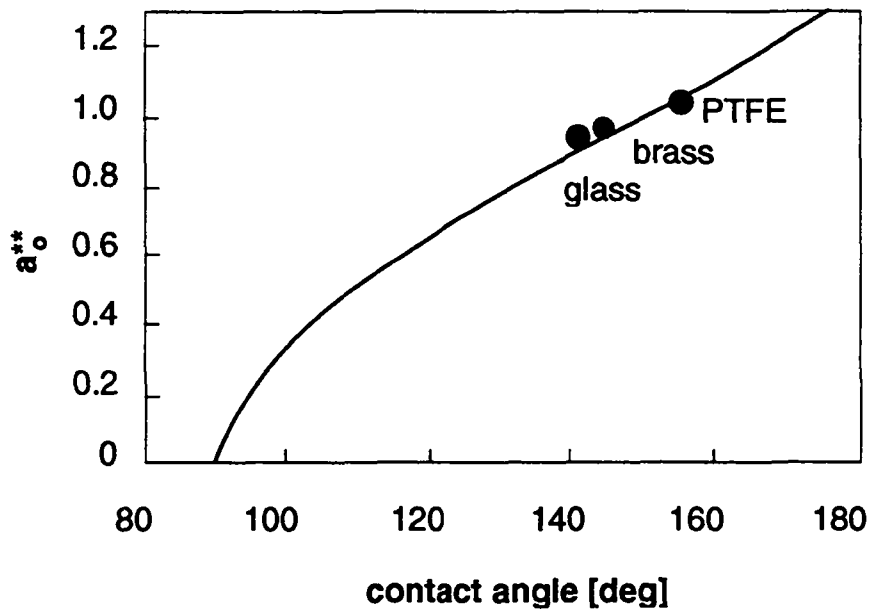


Figure 3.10: Equilibrium distance,  $a_0^{**}$ , as a function of the contact angle. The solid line is obtained by numerically solving  $f_c = 0$  in Eq. 3.20. The circles are experimental data.

It can be seen that the force is positive (attractive) when the plates are some distance apart. As they are brought together the force falls, reaching zero at  $a_0 = 680 \mu\text{m}$ , the equilibrium condition, then becoming negative (repulsive). In order to obtain the dimensionless equilibrium separation,  $a_0^{**} = a_0 V^{-1/3}$ , as a function of the contact angle, the force value in Equation 3.20 is put to zero and the resulting relationship is evaluated numerically. The result is shown in Figure 3.10 and compared to experimental data. It can be seen that, as found in the previous section for the square-section fibre geometry, for all contact angle values lower than  $\pi/2$  the equilibrium plate separation distance is zero, while for higher contact angles the equilibrium separation is finite and increases with contact angle.

### ***Experimental***

To test our capillary force analysis, the case of a drop in contact with two parallel plates, examined above, was realised experimentally. A mercury droplet was brought into contact with two plates forming an angle,  $\theta$ , with the liquid. Three different plate materials were used: glass, brass, and PTFE plates producing contact angles of  $141^\circ$ ,  $145^\circ$  and  $156^\circ$ , respectively. The mercury drop and the lower plate were placed on an electronic balance. The upper plate was put into contact with the droplet, then lowered and successively raised with a micrometric screw. The magnitude of the capillary force was directly read on the balance for different plate separations,  $a$ . Figure 3.9 reports the values of the measured force as a function of distance,  $a$ , for a contact angle of  $145^\circ$  (brass plate) and compares them to Equation 3.20. The equilibrium distance  $a_0^{**}$  reported in Figure 3.10 for the different plate materials was obtained when the force value read on the balance was zero.

## **3.3 SUMMARY**

### ***Impregnation mechanism***

The observations made under microscope when polymer particles in contact with two or more parallel fibres are molten are well illustrated by Figure 3.2. The liquid resin forms bridges between adjacent fibres and will flow along the channel formed by the fibres. In the absence of applied pressure, flow is driven by surface energy effects and stops when the system reaches a thermodynamic equilibrium, which depends on its geometry (inter-fibre distance) and on the surface energetics of the components in contact.

### ***Mean capillary pressure***

The calculation of the mean capillary pressure,  $P_c$ , (Eq. 3.12–3.14) allows the magnitude of the surface energy effects to be directly compared to other processing parameters, such as the mechanical pressure applied during manufacturing of fibre reinforced laminates. Capillary pressure takes a value, for parameters typical of carbon fibre reinforced composites, that can be of the order of  $\pm 10^4 \text{ Pa}$  ( $= 0.1 \text{ bar}$ ), enhancing impregnation for small contact angles, and impeding it for large ones. Depending on the mechanism of impregnation, Equation 3.12 can often be simplified. If the fibre bed is not being compressed during impregnation, such as in RTM or low pressure melt impregnation, the capillary pressure is constant during impregnation and proportional to  $\phi_2 / (1 - \phi_2)$ , where

$\phi_2$  is the fibre volume fraction in the “dry” fibre bed (Equation 3.13.) If, on the other hand, impregnation is accompanied by a compression of the fibre bed, the capillary pressure increases during impregnation (Equation 3.14).

As was pointed out in §3.2.1, the value of the capillary pressure calculated from Equation 3.3 is an average value over the whole volume of the system. For an ideal porous medium, in which all pores are of equal size and regular shape, e.g., a network of perfectly aligned and equidistant straight cylinders, definition 3.3 describes the capillary pressure in any point of the system. In real systems, however, pores are often tortuous channels with a broad size distribution. The local capillary pressure thus varies from point to point and *imbibition* of the flow front (i.e., liquid front stops flowing) can occur if the local capillary pressure,  $p_c$ , (Equation 3.2) drops to zero due to, for example, a locally larger pore size, although the average thermodynamic driving force predicts that it should advance. Equations 3.3, and 3.12–3.14 do not take this effect into account. Some authors [8] proposed the introduction of an empirical numerical factor which depends on the fibre bed geometry in order to correct for deviations from an “ideal” case.

### *Capillary forces*

A study at the microscopic level of the capillary forces acting between individual particles elucidates the mechanisms responsible for the magnitude of the capillary pressure. Figure 3.2 shows, for the case of powder impregnated fibres, how the surface energy of the various phases of a composite dictates the geometry of the resin bridge formed between adjacent fibres. The geometry can be characterised by the contact angle,  $\theta$ , at the interface. The analysis of the model geometries presented in section 3.2.3 shows that systems with contact angles smaller than  $\pi/2$  undergo capillary forces that enhance the melt impregnation—one can talk of spontaneous impregnation—whereas they impede it in systems with greater angles. Figure 3.2a illustrates the spontaneous impregnation undergone by a CF-PEEK system; the resin bridge spread under the action of the capillary pressure pulling the fibres closer together, until the system was frozen by quenching it out of the hot stage. For angles greater than  $\pi/2$ , there is an equilibrium distance,  $a_0$ , between the fibres which corresponds to a minimum of the energy of the system (cf. Figure 3.6b).

It must be noted that the analysis in §3.2.3 describes a simplified situation with constant interfacial energies and contact angle, and simplified geometries. In reality, interfacial phenomena are quite complex. The dynamic contact angle differs from the equilibrium contact angle measured at rest, and will be different whether the solid-liquid-air intersecting line advances or recedes. This explains the existence of a hysteresis, in Figure 3.9, between the advancing and receding forces [11, 12]. Such considerations, however, lie beyond the scope of this chapter. The agreement between the experimental values and the model, in Figures 3.9 and 3.10, is good and already affords a fair understanding of the effects of the surface energies in connection with composite manufacturing.

### *Discussion*

The capillary pressure can have a significant influence on the impregnation quality and rate in low pressure processes, such as bagging technique or filament winding. Bascom et al. [13] observed that the void content in filament wound rings was markedly reduced

when resins showing small contact angles with the fibres were used. In thermoplastic composites processing, however, mechanical pressures of the order of  $10^5$ – $10^7$  Pa are usually applied, such as in autoclave forming or compression moulding, for instance. In this situation the driving force from surface energy effects will be small compared to that arising from the externally applied pressure, as will be shown in Chapter 4. This is not to imply that surface energy effects are unimportant, however: in many systems a quantity of air may be entrapped during wet-out, and this will remain in the part after processing. This may affect the composite properties as studied by Kohn et al. [14] who measured a linear inverse relation between the interlaminar shear strength and the microvoid content. The surface energy effects on the mechanical properties of a composite will be studied more in details in Chapters 5 and 6.

Now that the impregnation and consolidation mechanisms are better understood, a quantitative model of the time evolution of the consolidation of a powder impregnated composite is proposed in Chapter 4. This model describes the role of surface energy effects, externally applied pressure, resin flow and fibre bed elasticity on the consolidation of thermoplastic matrix composites manufactured by the powder impregnation route.

### 3.4 REFERENCES

- 1 Young, T., *Phil. Trans.* 1805, **95**, 82.
- 2 de Gennes, P. G., *Reviews of Modern Physics* 1985, **57**, 827.
- 3 Schwartz, A. M. and Minor, F. W., *J. colloid sci.* 1959, **14**, 572.
- 4 Schwartz, A. M. *Ind. Eng. Chem.* 1969, **61**, 10.
- 5 Roychowdhury, S. and Advani, S. G., *Composites Manufacturing* 1991, **2**, 97.
- 6 Van West, B. P., Byron Pipes, R. and Advani S. G., *Polymer Composites* 1991, **12**, 417.
- 7 Iyer, S. R. and Drzal, L. T., *J. Thermoplastic Composite Materials* 1990, **3**, 325.
- 8 Ahn, K. J., Seferis, J. C. and Berg, J. C., *Polymer Composites* 1991, **12**, 146.
- 9 Connor, M., Toll, S., Manson, J.-A. E. and Gibson, A. G., *J. Thermoplastic Composite Materials* 1995, **8**, 163.
- 10 Lee, W. I. and Springer, G. S., *J. Composite Materials* 1987, **21**, 1017.
- 11 Giannotta, G., Morra, M., Occhiello, E., Garbassi, F., Nicolais, L. and D'Amore, A. J., *Colloid and Interface Science* 1992, **148**, 571.
- 12 Giannotta, G., Morra, M., Occhiello, E., Garbassi, F., Nicolais, L. and D'Amore, A., *Composites Manufacturing* 1992, **3**, 59.
- 13 Bascom, W. D. and Romans, J. B., *Ind. Eng. Chem., Prod. Res. Develop.* 1968, **7**, 172.
- 14 Kohn E. J., Sands, A. G. and Clark, R. C., *Ind. Eng. Chem., Prod. Res. Develop.* 1968, **7**, 179.

# 4

## CONSOLIDATION MODEL

The optimisation of the processing stage of a composite is necessary to obtain good properties at minimum cost. This requires a model of the process, describing the role and influence of the various parameters involved (e.g., applied pressure, time, temperature, and fibre content).

A consolidation model for commingled fibre yarns has been developed by van West et al. [1] who used the Darcy law to describe the radial flow of resin across a fibre bundle whose permeability varies with the fibre volume fraction. Iyer and Drzal [2] have examined the consolidation of powder impregnated tows which have been heated to melt the resin particles and form a film around each fibre. They describe the consolidation of this system, qualitatively, as a two-step process where the matrix films are first brought into intimate contact followed by the interdiffusion of polymer chains across the interface. However, none of these models offer a quantitative description of the consolidation of powder impregnated towpregs.

Ye et al. [3, 4] have presented a quantitative consolidation model for FIT laminates. In their model, consolidation takes place by radial impregnation of the resin sheath into the fibre bed and the powder is only considered in terms of reduced void content between the fibres and takes no active part in the consolidation process. However, the validity of this description is unclear since longitudinal permeability is known to be considerably larger than transverse permeability in high volume fraction fibre beds.

In this chapter, an analytical model for the consolidation stage of powder impregnated towpregs is presented, based on the consolidation mechanism described in Chapter 3, placing in context the effects due to surface energy, viscous flow, externally applied pressure and fibre bed elasticity. The initial conditions for the computation depend on the impregnation technique used. Two cases are examined: (i) FIT bundles, which are stabilised by the application of a resin sheath surrounding the powder loaded fibres (without melting the particles), and (ii) *molten powder towpregs*, in which the particles are molten *on line* during impregnation (cf. Chapter 2). The case of unidirectional (UD) flat laminates is examined here. The model is compared at each stage to experimental data obtained by compression moulding powder impregnated towpregs in an instrumented hydraulic press using a closed match-die mould. The consolidation behaviour of FIT satin 8 weave will be investigated and compared to Schappe Techniques commingled yarns in Chapter 7.



## 4.1 CONSOLIDATION EQUATION

### 4.1.1 Basic assumptions

As the resin particles melt, each drop will form a bridge between adjacent fibres. In a real powder towpreg there will be a range of different types of resin bridges, whose topology will be determined by geometrical factors such as powder particle size, fibre diameter, and local fibre packing, as well as by surface energy effects. In the present model, it will be assumed that all the bridges are of similar geometry and that each bridge is in contact with three adjacent fibres, as shown in Figure 4.1. During the impregnation process each resin bridge will spread along the fibres driven by the applied pressure and capillary forces. The bridge spreading will displace air from the composite and will be accompanied by a reduction in the inter-fibre spacing. If there were no other forces acting in the system the bridge spreading process would continue until all adjacent bridges came into contact, at which point the void volume fraction would be zero.

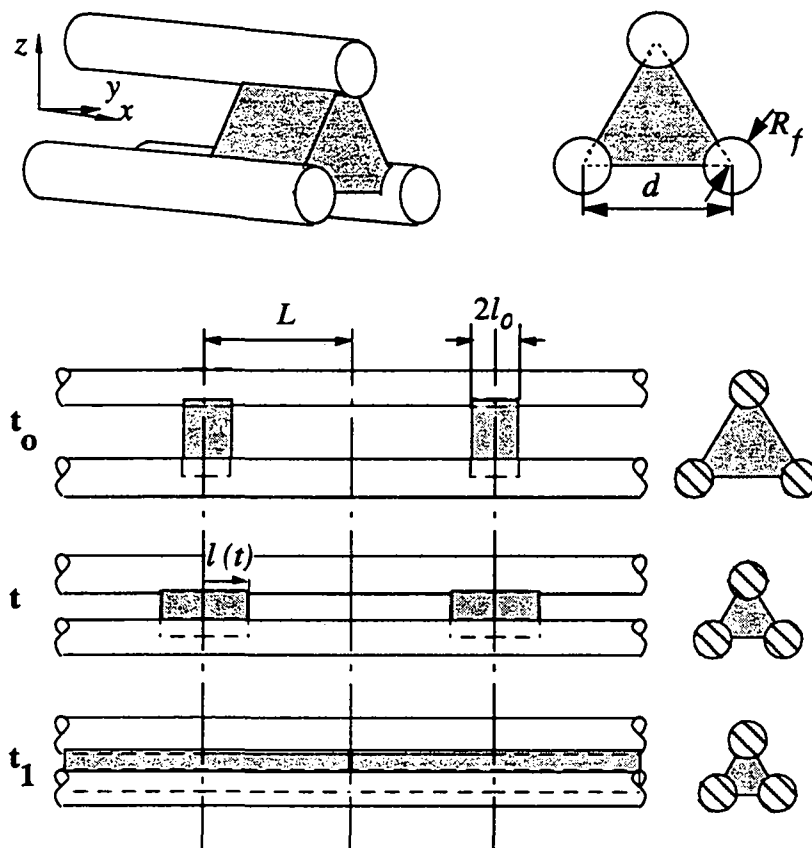


Figure 4.1: Modelled bridge geometry used for the derivation of the impregnation model:  $l_0$  is the initial half-length of the resin bridge,  $l$  is the actual bridge half-length at any time, and  $L$  is the distance to flow to achieve full impregnation.

The pressure,  $P_a$ , applied to the laminate is resisted by three components: the viscous pressure contribution from the flowing resin,  $P_v$ ; the capillary pressure,  $P_c$ ; and the spring-like pressure,  $P_s$ , which arises due to the transverse compression of the woven or imperfectly aligned fibres, which respond like a non-linear spring. The four pressures are therefore linked by the equilibrium relationship,

$$P_a = P_v + P_c + P_s \quad (4.1)$$

In the sign convention used here the capillary pressure is positive when it resists flow. Its sign, which depends on the surface properties of the different components, will therefore be negative for small contact angles when it enhances flow.

In the model to be proposed, the following assumptions have been made:

1. the resin flow transverse to the fibres can be considered negligible compared to that in the axial direction;
2. the centre of each resin droplet remains stationary and its volume constant;
3. all resin bridges have the same geometry.

Calculation of transverse and axial permeability of fibre tows lends support to assumption 1, and microscopic observations of partially impregnated systems also supports this assumption. Assumption 3 is more restrictive and supposes a monodisperse powder size distribution as well as a hexagonal fibre packing. Real systems involve powder with a distribution of particle sizes and fibre tows in which the transverse packing is irregular and the fibre alignment imperfect. In the simple cell model proposed here, the cell characteristics are effectively assumed to be representative of the population of geometries present in real systems.

It is now necessary to define the initial and end conditions and then to derive expressions for the pressure terms in Equation 4.1 as a function of previously defined parameters.

#### 4.1.2 Initial and final states

When a powder particle melts, it is assumed to form a bridge as shown in Figure 4.1, whose initial length,  $2l_0$ , is equal to the initial fibre spacing,  $d_0$ . The subscript 0 refers to the state at the beginning of the consolidation process. The progression of the consolidation of the laminate is followed by calculating the time evolution of the bridge half-length,  $l$ , which varies from the initial value,  $l_0$ , to a final length,  $L$ . It is therefore necessary to define these two values.

The initial bridge half length,  $l_0$ , is found by expressing the initial volume of each resin bridge,  $V_0$ , as a function of the bridge dimensions at the initial state:

$$V_0 = 2l_0 \left( \frac{\sqrt{3}}{4} l_0^2 - \frac{\pi}{2} R_f^2 \right) \quad (4.2)$$

where  $R_f$  is the fibre radius.

The final bridge half length,  $L$ , which is half the distance separating two adjacent bridges, can be obtained by expressing the volume of resin in each bridge in terms of its dimensions at the final state:

$$V_0 = \pi L R_f^2 \left( \frac{v_{m1}}{v_{f1}} \right) \quad (4.3)$$

giving for  $L$

$$L = \frac{V_0}{\pi R_f^2} \frac{v_{f1}}{v_{m1}} \quad (4.4)$$

where  $v_{f1}$  and  $v_{m1}$  are the final fibre and matrix volume fraction, respectively.

The value of the volume of each bridge,  $V_0$ , depends on the mean used to stabilise the powder within the reinforcement fibres (cf. Chapter 2). In the present section we will keep using  $V_0$  for the bridge volume so as to obtain a general flow rate equation independent of the geometry of the towpreg. This equation will be specialised in § 4.2 considering two cases: FIT, and *powder molten towpregs*.

### 4.1.3 Viscous pressure

The viscous pressure,  $P_v$ , which is equal to the applied pressure less the spring pressure and capillary pressure (Equation 4.1), is intensified in the ratio,  $L/l$ , when acting on the resin bridge (cf. Figure 4.1). The viscous pressure,  $P_v$ , is thus given by

$$P_v = \bar{P} \frac{l}{L} \quad (4.5)$$

where  $\bar{P}$  is the average *hydrodynamic pressure in the resin bridge*. The Hagen-Poiseuille equation for flow of a Newtonian fluid in a cylindrical channel can be modified empirically for the case of a channel of arbitrary cross-section by using the *hydraulic radius* argument [5, 6], which states that the channel radius can be replaced by an equivalent term,  $2r_h$ , where  $r_h$  is the hydraulic radius, defined as the area available for flow divided by the wetted perimeter. This gives

$$\frac{dP}{dx} = -\frac{2\eta}{r_h^2} V(x) \quad (4.6)$$

where  $V(x)$  is the mean flow velocity along the fibre axis,  $\eta$  is the viscosity and  $dP/dx$  is the pressure gradient along the fibre axis. The velocity field in the axial direction can be deduced by assuming that the fibres are parallel and that no transverse flow occurs. In this case, continuity dictates that  $d^2V/dx^2 = 0$ , and it therefore follows that  $V(x)$  must vary linearly with  $x$ . Since  $V = 0$  at  $x = 0$ ,

$$V(x) = \frac{x}{l} \frac{dl}{dt} \quad (4.7)$$

where  $dl/dt$  is the rate of expansion of the spreading droplet. Putting this into Equation 4.6 and integrating enables the axial pressure distribution along the droplet to be evaluated, and this can be seen to be parabolic. Integrating this again to find the average pressure,  $\bar{P}$ , acting over all the resin bridge and using Equation 4.5 to express  $P_v$  gives

$$P_v = \frac{2\eta L^2}{3r_h^2} \left(\frac{l}{L}\right)^2 \frac{d}{dt} \left(\frac{l}{L}\right) \quad (4.8)$$

Using the definition of hydraulic radius given previously, this quantity can be expressed as

$$r_h = \frac{1}{2} R_f \frac{L v_{m1}}{l v_{f1}} \quad (4.9)$$

Combining Equations 4.4, 4.8 and 4.9 allows the viscous component of the pressure to be expressed as

$$P_v = \frac{8\eta}{3\pi^2} \left(\frac{V_0}{R_f^3}\right)^2 \left(\frac{v_{f1}}{v_{m1}}\right)^4 \left(\frac{l}{L}\right)^4 \frac{d}{dt} \left(\frac{l}{L}\right) \quad (4.10)$$

#### 4.1.4 Capillary pressure

Capillary pressure,  $P_c$ , was analysed in Chapter 3. The expression corresponding to the powder impregnated case is given by Equation 3.13, which can be expressed in terms of the parameters represented in Figure 4.1 as,

$$P_c = -\frac{2\gamma_l}{R_f} \left(\frac{v_f}{1-v_f}\right) \cos \theta \quad (4.11)$$

where  $\gamma_l$  is the resin surface energy per unit area.

It can be seen that as expected the capillary pressure is negative and therefore enhances the flow for angles smaller than  $90^\circ$  and is positive for larger angles. Its magnitude, however, for a typical resin surface energy of  $40 \text{ mJ/m}^2$  and a fibre radius of  $3.5 \text{ }\mu\text{m}$ , is at most of the order of  $10^4 \text{ Pa}$  ( $= 10^{-1} \text{ bar}$ ), which is considerably smaller than the external pressures currently applied, which are of the order of  $10^5$ – $10^6 \text{ Pa}$ . Capillary pressure, however, plays an important role in the initial impregnation state during resin bridge formation, since no external pressure is applied at this stage.

#### 4.1.5 Spring pressure

Several workers have investigated the non-linear elastic compression of fibre beds and have fitted theoretical or empirical expressions to the rapidly stiffening stress-strain relationships observed. Any of these approaches would be suitable for use in the present model, provided the fibre bed behaviour is described adequately. The expression for spring pressure chosen in this investigation is the one proposed by Gutowski [7, 8], which in terms of the variables used here can be written as follows:

$$P_s = A_s \frac{\sqrt{\frac{v_{f1}l}{\phi_0 v_{f1}l + \phi_0 v_{m1}L} - 1}}{\left( \sqrt{\frac{\phi_a(v_{f1}l + v_{m1}L)}{v_{f1}l} - 1} \right)^4} \quad (4.12)$$

where  $A_s$  is a spring constant,  $\phi_0$  is the fibre volume fraction at which the fibres start to interfere with each other, and  $\phi_a$  is the maximum available fibre content. The values proposed by Gutowski [4] for a poorly aligned bed of carbon fibres,  $A_s = 862$  Pa,  $\phi_a = 0.829$ , and  $\phi_0 = 0.5$ , give for a final fibre volume fraction of 0.67 a maximum value of the spring pressure of 0.85 MPa.

#### 4.1.6 Consolidation rate equation

Substituting Equation 4.10 into Equation 4.1 enables a solution for the flow front velocity to be found:

$$\frac{d}{dt} \left( \frac{l}{L} \right) = \frac{3\pi^2}{8\eta} \left( \frac{R_f^3}{V_0} \right)^2 \left( \frac{v_{m1}}{v_{f1}} \right)^4 \left( \frac{L}{l} \right)^4 (P_a - P_s - P_c) \quad (4.13)$$

This expression must now be integrated, starting from the condition  $l = l_0$  at  $t = 0$  to find the variation of bridge length with time for a given set of processing conditions. The time for complete impregnation is given when  $l = L$ . The void content at any point in time is easily derived as a function of  $l/L$  from the geometry shown in Figure 4.1:

$$v_v = \frac{1 - \frac{l}{L}}{1 + \frac{l}{L} \frac{v_{f1}}{v_{m1}}} \quad (4.14)$$

In most situations it is necessary to integrate Equation 4.13 numerically. When the spring pressure and capillary pressure terms are small enough to be neglected, however, Equation 4.13 simplifies sufficiently to permit analytical integration. The spring pressure can be neglected when the fibre volume fraction is close to or smaller than

$\phi_0$  as defined in Equation 4.12 or for external applied pressures well above the maximum value of the spring pressure, which is, for a 60% volume content of unidirectional carbon fibres, approximately 1 MPa. The capillary pressure can be neglected when external applied pressures greater than approximately 0.1 MPa are used. Thus the analytical solution neglecting  $P_s$  and  $P_c$  is

$$\left(\frac{t \cdot P_a}{\eta}\right) = \frac{8}{15\pi^2} \left(\frac{V_0}{R_f^3}\right)^2 \left(\frac{v_{f1}}{v_{m1}}\right)^4 \left[\left(\frac{l}{L}\right)^5 - \left(\frac{l_0}{L}\right)^5\right] \quad (4.15)$$

In all but the very beginning of the consolidation process,  $(l/L)^5$  is usually much larger than  $(l_0/L)^5$ , so the latter can be neglected in Equation 4.15:

$$\left(\frac{t \cdot P_a}{\eta}\right) = \frac{8}{15\pi^2} \left(\frac{V_0}{R_f^3}\right)^2 \left(\frac{v_{f1}}{v_{m1}}\right)^4 \left(\frac{l}{L}\right)^5 \quad (4.16)$$

The time to full consolidation,  $t_1$ , is now obtained by putting  $l/L = 1$ , which indicates that two adjacent bridges have met, thus achieving full impregnation:

$$\left(\frac{t_1 \cdot P_a}{\eta}\right) = \frac{8}{15\pi^2} \left(\frac{V_0}{R_f^3}\right)^2 \left(\frac{v_{f1}}{v_{m1}}\right)^4 \quad (4.17)$$

## 4.2 POWDER IMPREGNATED FIBRE GEOMETRY —EXAMPLES

Equations 4.13 and 4.15–4.17 describe the impregnation time of a powder impregnated composite in terms of the volume of a bridge,  $V_0$ , which is not a parameter directly measurable on a powder coated towpreg. It is more convenient to express the volume,  $V_0$ , as a function of the particle radius,  $R_m$ . The relation between bridge volume and particle radius, however, depends on the geometry of the powder coated towpreg, and in particular on the method used to stabilise the powder. Two powder coated towpreg geometries are examined: FIT and *molten powder towpreg*, respectively.

### 4.2.1 FIT towpreg

In a FIT bundle the powder impregnated fibres are enclosed into a resin sheath which stabilises the system without melting the powder particles (cf. §2.2.3). Prior to processing, i.e., before the melting (or softening) temperature is reached, the fibres are thus separated by a distance corresponding to the particle size. It is therefore allowed to assume that once the processing temperature is reached, each resin particle will form one

bridge, the volume of which is equal to the volume of the particle. Assuming that the powder particles are roughly spherical of radius,  $R_m$ , the bridge volume,  $V_0$ , is thus given by,

$$V_0 = \frac{4}{3}\pi R_m^3 \quad (4.18)$$

Replacing  $V_0$  by its value in Equation 4.15 yields a consolidation equation for *FIT towpregs*:

$$\left(\frac{t \cdot P_a}{\eta}\right) = \frac{128}{135} \left(\frac{R_m}{R_f}\right)^6 \left(\frac{v_{f1}}{v_{m1}}\right)^4 \left[ \left(\frac{l}{L}\right)^5 - \left(\frac{l_0}{L}\right)^5 \right] \quad (4.19)$$

It is clear that if the spring pressure or the capillary pressure cannot be neglected,  $V_0$  should be replaced in Equation 4.13 instead and then integrated numerically. The consolidation time predicted by Equation 4.19 is compared to experimental consolidation curves in §4.3.1.

#### 4.2.2 Molten powder towpregs

In the case of *molten powder towpregs*, the system is stabilised by melting the powder particles on line by pulling the fibre tow through an oven (cf. §2.2.3). The bridges are thus formed at this stage of processing, that is at the *mingling* stage, unlike *FIT towpregs* in which the bridges are only formed at the consolidation stage. This will influence the bridge geometry. Indeed, unlike *FIT*, in *molten powder towpregs*, the fibres are under tension during bridge formation. While they are wavy and corrugated prior to their passage through the oven, due to the presence in the bundle of solid powder particles, the fibres will straighten up by penetrating into the molten particles as soon as the melting temperature is reached. This process is illustrated in Figure 4.2.

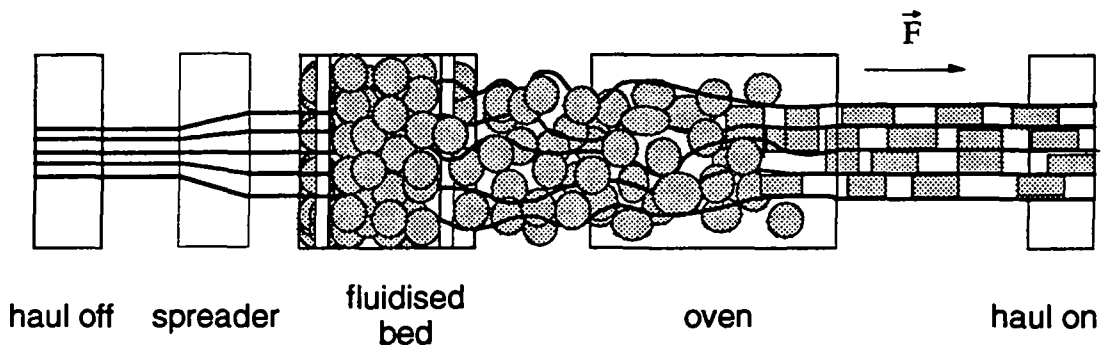


Figure 4.2: Resin bridge formation and inter-fibre distance for molten powder towpregs.

The inter-fibre spacing,  $d_o$ , was measured on a series of unconsolidated *molten powder towpregs* of various resin particle size and content manufactured in collaboration with the University of Newcastle upon Tyne [9, 10]. The samples were prepared for

microscopy observation by embedding them, both longitudinally and transversally, into an acrylate resin and subsequently polishing them. They were then observed and photographed with an optical microscope. For each sample the distance between fibres were measured on various micrographs and then averaged. The results are shown graphically in Figure 4.3, where  $d_0$  is plotted as a function of  $R_m$ . The black and white symbols represent carbon and glass fibre reinforced composites, respectively. The inter-fibre distance was found to be independent of the matrix used. It can be seen that the distance,  $d_0$ , between fibres first increases linearly for particle radii smaller than  $\sim 40 \mu\text{m}$  and then stabilises and become independent of  $R_m$ . As was described above, the fibre rearrangement takes place into the oven during a time  $t = A/u_t$ , where  $A$  is the oven length and  $u_t$  is the tow velocity. In our case  $t \approx 2 \text{ m} / 0.05 \text{ m/s} = 40 \text{ s}$ . During these 40 s, the fibres do penetrate into the melting resin particles until the bridge solidifies again at the exit of the oven. At this stage the system is frozen and the resin bridges present the initial geometry that we attempt to capture. Based on Figure 4.3, the initial inter-fibre distance can be expressed as a function of  $R_m$ , as:

- for carbon fibres:

$$d_0 = 15 + \frac{R_m}{2} \mu\text{m} \quad 0 \leq R_m \leq 40 \mu\text{m} \quad (4.20a)$$

$$d_0 = 35 \mu\text{m} \quad R_m \geq 40 \mu\text{m} \quad (4.20b)$$

- for glass fibres:

$$d_0 = 35 + \frac{7}{8} R_m \mu\text{m} \quad 0 \leq R_m \leq 40 \mu\text{m} \quad (4.21a)$$

$$d_0 = 70 \mu\text{m} \quad R_m \geq 40 \mu\text{m} \quad (4.21b)$$

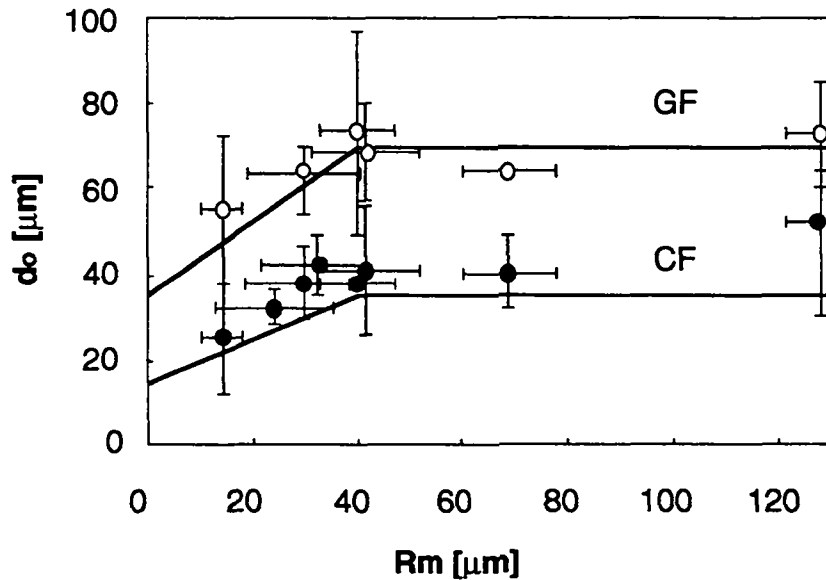


Figure 4.3: Plot of the initial inter-fibre distance,  $d_0$ , as a function of the powder particle radius,  $R_m$ . Black symbols refer to carbon fibres, and white symbols to glass fibres reinforced composites.



Assuming that the initial half-length,  $l_0$ , of the bridge is equal to  $R_m$ , the initial geometry of the bridge is fully characterised and the volume of each bridge can be calculated:

$$V_0 = R_m \left( \frac{\sqrt{3}}{2} d_0^2 - \pi R_f^2 \right) \quad (4.22)$$

which can be introduced into Equation 4.15 to obtain an expression for the consolidation of *molten powder towpregs*:

$$\frac{t \cdot P_a}{\eta} = \frac{8}{15\pi^2} \left( \frac{R_m}{R_f^3} \right)^2 \left( \frac{\sqrt{3}}{2} d_0^2 - \pi R_f^2 \right)^2 \left( \frac{v_{f1}}{v_{m1}} \right)^4 \left[ \left( \frac{l}{L} \right)^5 - \left( \frac{l_0}{L} \right)^5 \right] \quad (4.23)$$

where  $d_0$  is defined by Equation 4.20 and 4.21 for carbon fibres and glass fibres, respectively. It can be seen from Equations 4.19 and 4.23, that the consolidation time of FIT yarns is more sensitive to particle size than molten powder towpregs; the consolidation time of the former shows a power six dependence on particle radius, while the latter exhibits a square dependence. The consolidation time predictions of Equation 4.23 are compared to experimental consolidation curves in §4.3.2.

### 4.3 EXPERIMENTAL

A series of unidirectional laminates were manufactured using *FIT* and *molten resin towpregs*, respectively. The former were supplied by Porcher Textile, and the latter were manufactured in collaboration with Prof. A. G. Gibson using an impregnation line developed in his laboratory at the University of Newcastle upon Tyne. Since *FIT* is a commercial product, it was not possible to vary the powder size and content, and it was only possible to compare Equation 4.19 to experimental consolidation curves for a limited number of systems; some data from the literature are also examined. On the other hand, *molten powder towpregs* with a large variety of both particle size and content were manufactured allowing the influence of the various parameters to be studied.

#### 4.3.1 FIT towpreg characterisation

Two types of carbon-fibre-reinforced FIT materials, with different matrix resins, were investigated in the consolidation study. One contained a semi-crystalline resin, poly(ether-ether-ketone) (CF-PEEK), and the other contained an amorphous polymer, poly(ether imide) (CF-PEI). Both were supplied in the unconsolidated state by Porcher Textile. In each case the 3000 fibre carbon tows (3K-T300 from Soficar) were mingled with finely powdered resin, having a radius,  $R_m$ , in the range of 15-25  $\mu\text{m}$  and enclosed in a sheath of the same resin. The global fibre volume fraction was found to be 52%, and the local values of  $v_{f1}$  and  $v_{m1}$  within the fibre bundle, which is where the powder impregnation actually takes place, were found to lie between 65 and 68% after consolidation. The

values of the parameters used in the computation are given in Table 4.1. The fibre radius and cross-sectional area required for the determination of  $v_{f1}$  were measured on SEM micrographs. The weight average radius of the powder particles was obtained using the photo centrifuge technique (Horiba, CAPA-700). The final local fibre content,  $v_{f1}$ , was evaluated by counting the number of fibres present in a given area within a bundle on cross-sectional micrographs of fully consolidated laminates. The dynamic melt viscosity was determined using a dynamic melt rheometer (Rheometrics, RDA-II) with parallel plates of 8 mm radius at a frequency of 1 Hz in the temperature range 350-400°C for PEEK resin and 230-300°C for PEI.

**Table 4.1: Parameters used in the consolidation modelling of FIT**

Parameter	PEEK value	PEI value	Unit
Fibre radius, $R_f$	3.5	3.5	$\mu\text{m}$
Matrix powder radius, $R_m$	23	16	$\mu\text{m}$
Final fibre vol. fraction, $v_{f1}$	0.67	0.67	-
Applied pressure, $P_a$	5 and 10	2 and 10	MPa
Processing Temp., $T_p$	380	280	°C
Melt viscosity, $\eta$	1	70	kPa·s

#### 4.3.2 Molten powder towpreg characterisation

Two types of fibres and four polymers with different particle size were used. This selection of samples allowed the various terms in Equation 4.23 to be varied over a wide range. Glass fibres (2400 filament E-glass from Owens-Corning) and carbon fibres (3K filament T300 from Soficar) were impregnated with particles of poly(ether-ether-ketone) (PEEK, grade 150G from ICI), poly(ether-imide) (PEI, Ultem 1000 from GE) and two different grades of polyamide 12 (PA12) (from EMS-Chemie AG and Elf-Atochem). Resins viscosity were determined using a dynamic melt rheometer Rheometrics, RDA-II (cf. §4.3.1), and the fibre radius was measured on SEM micrographs. The following processing parameters are listed in Table 4.2: fibre radius, viscosity at processing temperature and applied pressure during consolidation.

**Table 4.2: Parameters used in the consolidation modelling**

Parameter	Value	Unit
Applied pressure, $P_a$	5	MPa
Fibre radius, $R_f$ :		
- Glass fibres	10	$\mu\text{m}$
- Carbon fibres	3.5	$\mu\text{m}$
Melt viscosity, $\eta$ at temperature, $T$ :		
- PEEK at 380°C	1	kPa·s
- PEI at 310°C	40	kPa·s
- PA12 (ATO) at 200°C	3.6	kPa·s
- PA12(EMS) at 200°C	0.68	kPa·s

The ball-milled resin powders that we received were separated into narrower particle size fractions by passing the powder through a nest of stacked sieves with different mesh aperture in the sequence:  $\phi = 150; 106; 75; 63; \text{ and } 45 \mu\text{m}$ . The particle size distribution of the resulting fractions were analysed using a laser particle sizer Analysette 22 from Fritsch. The size distribution is obtained through a diffraction pattern characteristic of the interaction between the laser beam and the particle shape and size. Table 4.3 lists the mean radius and standard deviation of the various powder size fractions, and an example of particle size distribution is given in Figure 4.4 for PEEK coarsest size fraction #4. It can be seen that the size distributions are quite broad, which is detrimental to the correlation between experimental and theoretical consolidation curves, since the model only considers monodisperse powder size distributions.

**Table 4.3: Particle size fractions**

Polymer	Size Fraction #	$\bar{R}_m$ [ $\mu\text{m}$ ]	std. dev. [ $\mu\text{m}$ ]
PA12-EMS	#1	92	8
PA12-Atochem	#1	64	9
	#2	70	9
PEI	#1	14	4
	#2	40	7
	#3	42	10
	#4	128	6
PEEK	#1	24	11
	#2	30	11
	#3	33	11
	#4	69	9

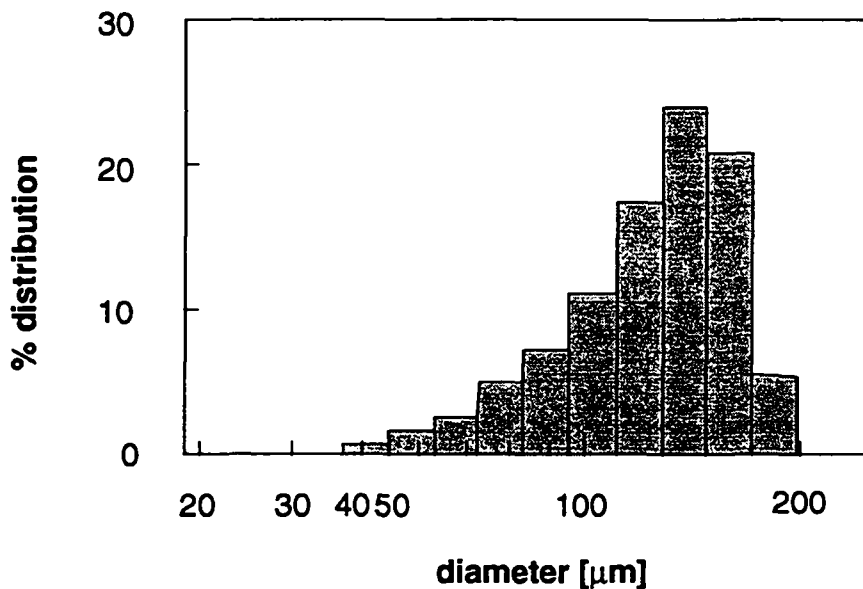


Figure 4.4: Particle size distribution curve of PEEK powder ( $\bar{R}_m = 69 \mu\text{m}$  and standard deviation  $9 \mu\text{m}$ ).

The two types of fibres (glass and carbon) were impregnated with different amounts of the powders listed in Table 4.3 using the impregnation line of the University of Newcastle upon Tyne described in Chapter 2. Powder volume fraction was determined by comparing the weight of 1 m of powder impregnated tow to the specific linear weight of the fibres. Table 4.4 lists the powder impregnated samples with their final matrix content,  $v_{m1}$ , and the average particle radius,  $R_m$ .

Table 4.4: List of molten powder towpregs

PA12			PEI			PEI			PEEK		
Fibre	$v_{m1}$	$R_m$	Fibre	$v_{m1}$	$R_m$	Fibre	$v_{m1}$	$R_m$	Fibre	$v_{m1}$	$R_m$
<i>EMS-Chemie</i>			G	37	14	C	38	14	G	77	30
G	19	92	G	37	14	C	54	14	G	80	30
G	24	92	G	51	14	C	57	14	G	83	30
G	30	92	G	51	14	C	57	14	G	21	69
G	36	92	G	54	14	C	59	14	G	73	69
C	42	92	G	54	14	C	50	40	G	80	69
C	43	92	G	69	14	C	54	40	G	82	69
C	51	92	G	69	14	C	64	40	C	56	24
C	55	92	G	53	40	C	69	40	C	64	24
<i>Atochem</i>			G	53	40	C	29	42	C	66	24
G	49	64	G	69	40	C	29	42	C	75	24
G	50	64	G	69	40	C	45	42	C	35	30
G	65	64	G	71	40	C	55	42	C	48	30
G	70	64	G	71	40	C	55	42	C	67	30
G	70	64	G	79	40	C	61	42	C	75	30
G	85	64	G	79	40	C	61	42	C	55	33
G	85	64	G	42	42	C	62	42	C	59	33
G	34	70	G	42	42	C	62	42	C	68	33
G	40	70	G	63	42	C	14	128	C	73	33
G	60	70	G	65	42	C	14	128	C	12	69
G	68	70	G	65	42	C	20	128	C	44	69
C	11	64	G	70	42	C	20	128	C	51	69
C	72	64	G	78	42	C	22	128	C	66	69
C	79	64	G	78	42	C	22	128			
C	88	64	G	36	128	C	41	128			
C	89	64	G	38	128	C	41	128			
C	42	70	G	43	128						
C	45	70	G	46	128						
C	60	70	G	46	128						
C	74	70									
C	86	70									

G = Glass fibres; and C = Carbon fibres,  $R_m$  [ $\mu\text{m}$ ], and  $v_m$  [%].

### 4.3.3 Consolidation of laminates

Unconsolidated unidirectional plies were prepared (cf. Figure 4.5):

- FIT flexible yarns were wrapped around an 80-mm-diameter cylinder and the thus aligned bundles were welded together every 50 mm; and
- molten powder towpregs, which are stiffer, were cut into 50 mm long tows and aligned into a 50 x 50 mm<sup>2</sup> cavity.

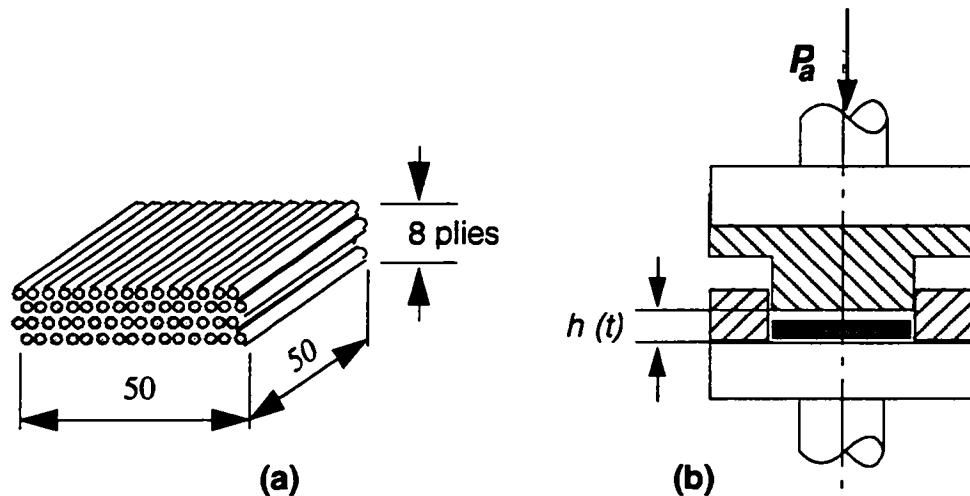


Figure 4.5: (a) Powder impregnated preform; and (b) closed matched-die mould.

Each consolidation sample consisted of 8 plies of this material, and were consolidated in a temperature-controlled match die mould, with a 50 mm-square cavity, under constant pressure. Prior to consolidation, the samples were held in the mould for 15 minutes at the processing temperature (cf. Tables 4.1 and 4.2) in order to equilibrate thermally. The upper and lower parts of the experimental mould were attached to the load cell and crosshead of a servo-hydraulic testing machine (Interlaken, Series 3300), thus facilitating very accurate control of externally applied consolidation pressure. The relative displacement of the mould parts was measured via an LVDT gauge and recorded as a function of time during each consolidation experiment.

As the area of the laminate is constant (50 x 50 mm<sup>2</sup>) throughout the consolidation experiment, the void volume fraction,  $v_v(t)$ , can be found from the instantaneous laminate thickness,  $h(t)$ , using the relationship

$$v_v(t) = \frac{(h(t) - h_1)}{(h_0 - h_1)} (v_{v0} - v_{v1}) + v_{v1} \quad (4.24)$$

The initial void volume fraction,  $v_{v0}$ , was calculated by the ratio between the sample weight and the volume of the cavity when the upper part of the mould was just touching the heated precursor prior to consolidation. The final void volume fraction,  $v_{v1}$ , was measured on the consolidated laminates after cooling to room temperature using an immersion technique (ASTM D792).

## 4.4 RESULTS AND DISCUSSION

### 4.4.1 Consolidation of FIT yarns

Experimental and predicted relationships between void volume fraction and time are shown in Figure 4.6. Figure 4.6a shows the results for CF-PEEK laminates at applied pressures of 5 and 10 MPa, while Figure 4.6b shows the corresponding plots for the CF-PEI laminates at pressures of 2 and 10 MPa. The predicted curves, obtained using the analytical solution given in Equation 4.19, which neglects the spring pressure and capillary pressure are represented by solid lines. The full solution including  $P_s$  and  $P_c$  (Equation 4.13) is represented by dashed lines; it is almost identical to the analytical solution, and differs only slightly towards the end of the consolidation for CF-PEI processed at 2 MPa.

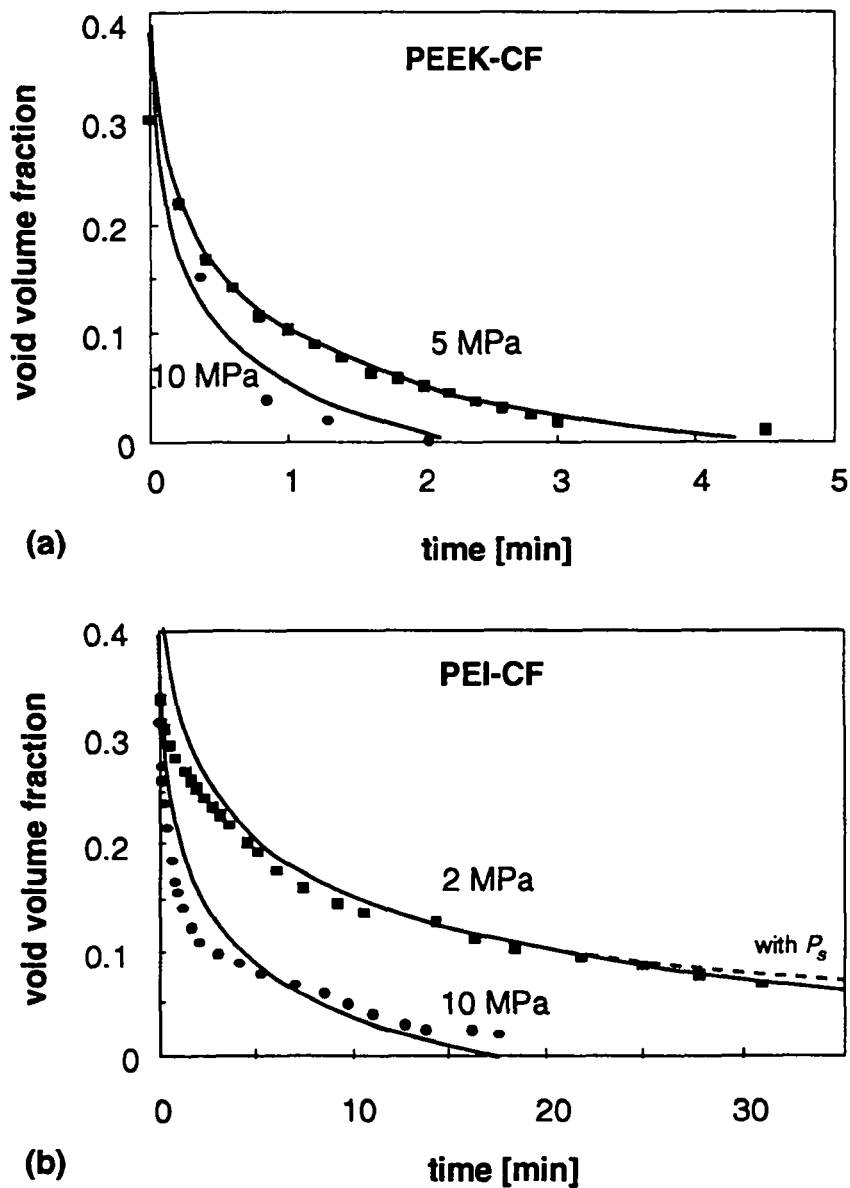


Figure 4.6: Consolidation curves of (a) a CF-PEEK 8-ply UD-FIT laminate at 380°C and an applied pressure of 5 MPa and 10 MPa, and (b) CF-PEI 8-ply UD-FIT laminate at 280°C and an applied pressure of 2 MPa and 10 MPa. Solid curves represent Equation 4.19.

Figure 4.7 compares experimental consolidation points of CF-PEEK FIT unidirectional laminates taken from [4] to Equation 4.19, using the following parameters:  $R_m / R_f = 6.1$ ,  $v_{f1} / v_{m1} = 2.6$ , and  $\eta = 526, 1634, \text{ and } 2337 \text{ Pa}\cdot\text{s}$  at temperature of 390, 370, and 360°C, respectively. The resulting microstructure of the consolidated 8-ply laminates is shown in Figure 4.8 which shows micrographs of polished transverse sections of a CF-PEEK and a CF-PEI laminate, both consolidated at 10 MPa.

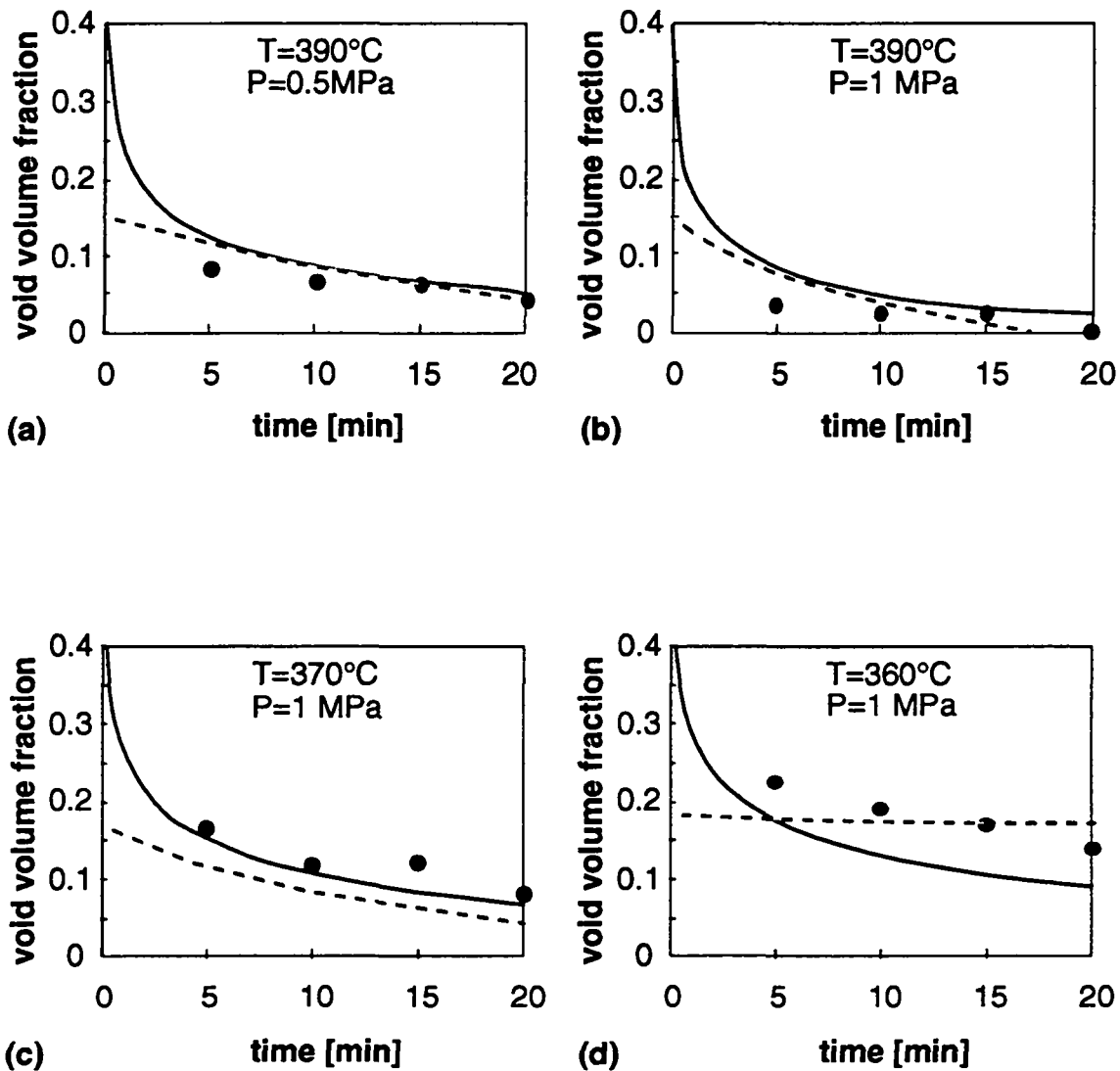
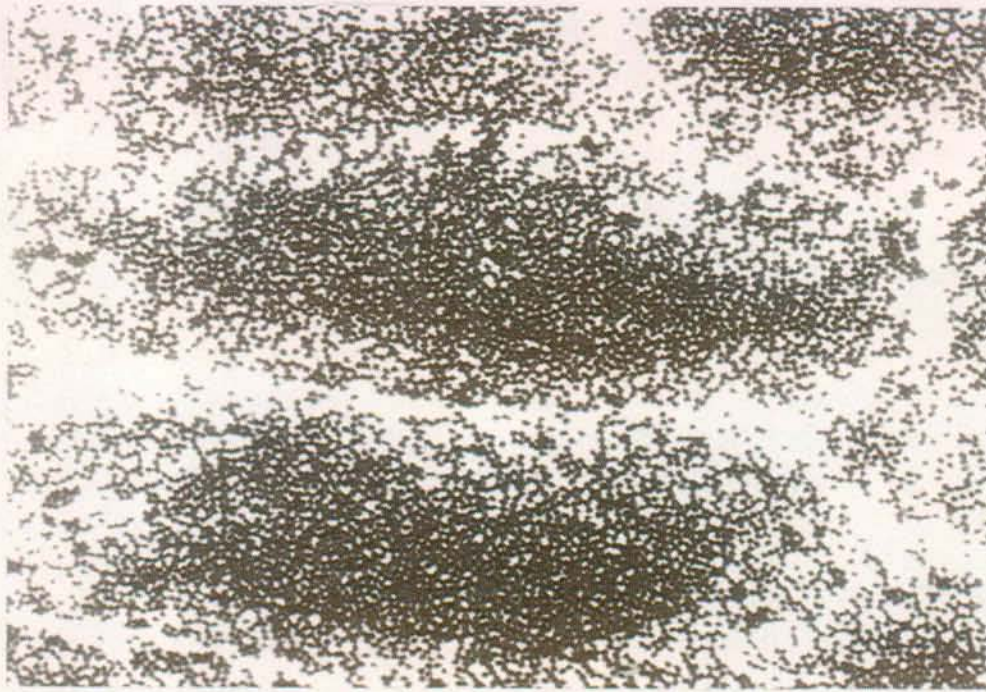
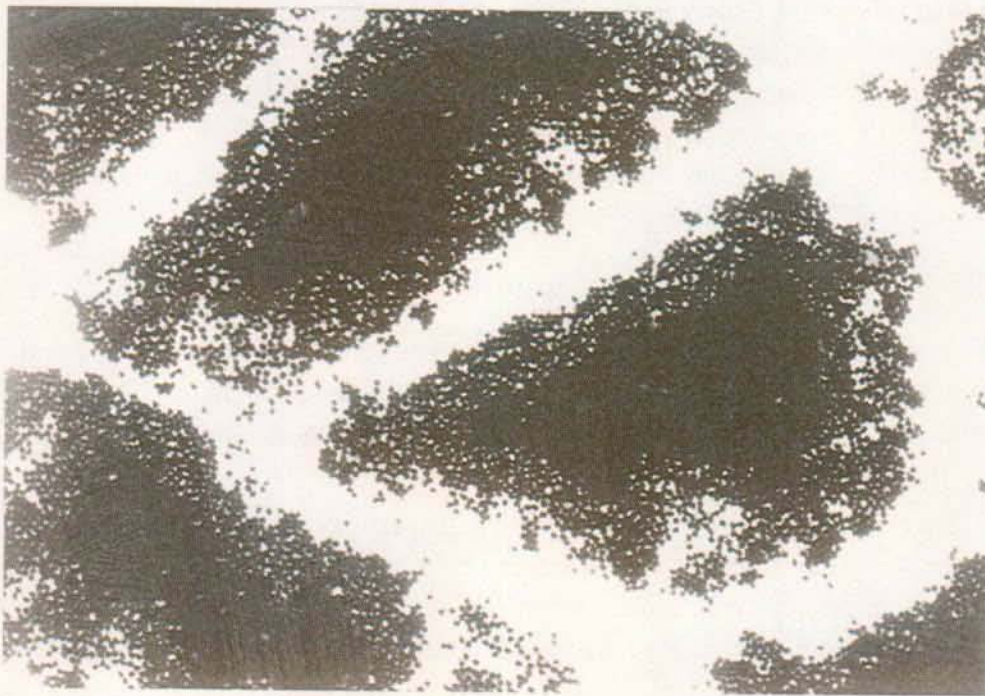


Figure 4.7: Consolidation curves predicted by Equation 4.19 (solid line) compared to experimental data (black circles) and model (dashed line) presented by Ye et al. [4]: (a)  $T = 390^\circ\text{C}$ ,  $P = 0.5 \text{ MPa}$ ; (b)  $T = 390^\circ\text{C}$ ,  $P = 1 \text{ MPa}$ ; (c)  $T = 370^\circ\text{C}$ ,  $P = 1 \text{ MPa}$ ; and (d)  $T = 360^\circ\text{C}$ ,  $P = 1 \text{ MPa}$ .



(a)



(b)

2 mm

Figure 4.8 : Transverse sections of FIT laminates: (a) CF-PEEK, (b) CF-PEI, both consolidated at 10 MPa.

The presence of the resin sheath in FIT yarns enclosing each bundle, which is not allowed for in the model, does not significantly affect the correlation. Observation of the cross-sections of the different laminates (Figure 4.8) confirms that there is no significant penetration of the resin sheath into the individual fibre bundles, which are still visible. This result confirms our initial assumption that, in this material, resin flow transverse to the fibre axis is negligible compared to axial flow. This was to be expected, since the ratio of axial to transverse permeability of aligned fibre beds is known to increase with the



fibre volume fraction and is of the order of 10 for high fibre contents [11]. These results suggest that, for a FIT yarn of given fibre content, it is favourable to maximise the resin fraction in the form of particulate, and minimise the thickness of the sheath, since the latter does not have a significant influence on the impregnation and mainly act as a “spacer” between fibre bundles (cf. Figure 4.8).

The influence of viscosity is quite visible by comparing the impregnation times of CF-PEEK to CF-PEI both processed at 10 MPa in Figure 4.6a and b, and of CF-PEEK processed at 1 MPa and 390°C, 370°C, and 360°C, respectively, in Figure 4.7b–d. The very high viscosity of 70 kPa·s of PEI measured at 280°C explains the long consolidation time of 17.2 min compared to the 2.2 min calculated for PEEK-CF with Equation 4.17. The effect of pressure on the consolidation time can be seen in Figures 4.6 and 4.7a and b. No fibre damage was observed in the laminates processed at 10 MPa.

The effect of the *spring pressure*, the resistance offered by the compressed fibre bed to the applied pressure, is only visible towards the end of consolidation when low external pressures are applied. The maximum value of the spring pressure, which is found when the laminate is fully consolidated (i.e., for  $v_v = 0$ ), is estimated to 0.85 MPa, indicating that a void free laminate cannot be produced at an applied pressure lower than this value. This value is obtained solving Equation 4.12 using data from the literature, so it is not known whether it realistically describes the system under investigation. For technical reasons, however, the experimental set-up did not allow the laminates to be processed at a lower pressure than 1.5 MPa, so the spring pressure can quite safely be neglected and the consolidation described by Equation 4.15.

#### 4.4.2 Consolidation of molten powder towpregs

Experimental and modelled (Equation 4.23) consolidation curves are compared in Figure 4.9 for two systems: CF-PA12 from Elf-Atochem ( $R_m = 70 \mu\text{m}$ ,  $v_{f1} = 0.4$ , and  $\eta = 3670 \text{ Pa}\cdot\text{s}$ ) and a CF-PA12 from Ems-Chemie A.G. ( $R_m = 92 \mu\text{m}$ ,  $v_{f1} = 0.7$ , and  $\eta = 700 \text{ Pa}\cdot\text{s}$ ).

To characterise the influence of each quantity on the consolidation rate, a parameter study can be made by expressing each parameter in terms of Equation 4.23; this new function can then be compared to experimental data. This was done for the particle to fibre radius ratio,  $R_m / R_f$  and the final fibre to matrix volume fraction ratio,  $v_{f1} / v_{m1}$ , by defining the functions  $f(t) = (R_m / R_f)^2$  and  $g(t) = (v_{f1} / v_{m1})^4$ , as:

$$f(t) = \left( \frac{R_m}{R_f} \right)^2 = \frac{15\pi^2 t \cdot P_a}{8 \eta} \left( \frac{v_{m1}}{v_{f1}} \right)^4 \frac{R_f^4}{\left( \frac{\sqrt{3}}{2} d_0^2 - \pi R_f^2 \right)^2 \left[ \left( \frac{l}{L} \right)^5 - \left( \frac{l_0}{L} \right)^5 \right]} \quad (4.25)$$

and

$$g(t) = \left( \frac{v_{f1}}{v_{m1}} \right)^4 = \frac{15\pi^2 t \cdot P_a}{8 \eta} \frac{R_f^6}{R_m^2} \frac{1}{\left( \frac{\sqrt{3}}{2} d_0^2 - \pi R_f^2 \right)^2 \left[ \left( \frac{l}{L} \right)^5 - \left( \frac{l_0}{L} \right)^5 \right]} \quad (4.26)$$

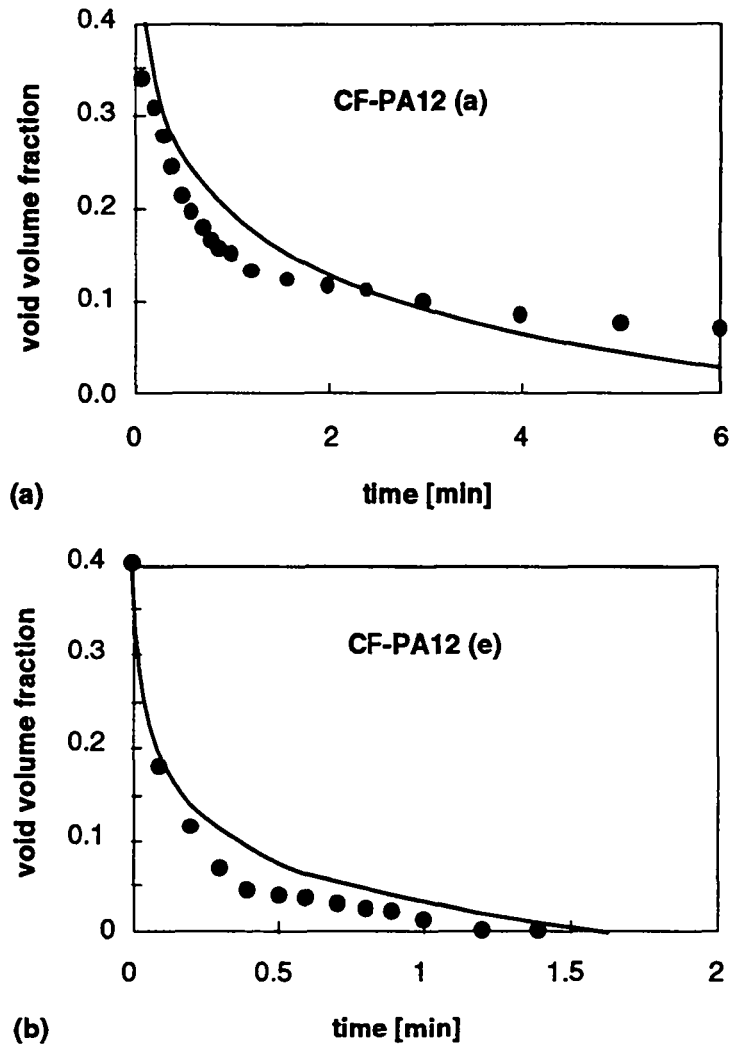


Figure 4.9: Consolidation of (a) a CF-PA12 (Atochem), and (b) CF-PA12 (Ems-Chemie) 8-ply unidirectional molten powder laminates at 200°C and an applied pressure of 5 MPa. Solid lines represent Equation 4.23.

The function  $f(t)$  (Equation 4.25) describes the influence of the particle and fibre radius,  $R_m$  and  $R_f$ , on the consolidation rate, and can be called the *radius function*. Similarly, the function  $g(t)$  (Equation 4.26), which describes the influence of the final fibre and matrix volume fraction,  $v_{f1}$  and  $v_{m1}$ , can be named the *volume fraction function*.

Figure 4.10 compares the experimental results to the radius and volume fraction functions,  $f(t)$  and  $g(t)$ , plotted as a function of  $R_m/R_f$  and  $v_{f1}/v_{m1}$ , respectively. The white symbols stand for glass fibre reinforced composites, and the black symbols for carbon fibre. The error bars on  $f(t)$  and  $g(t)$ , are calculated considering for each parameter the uncertainties reported in Table 4.5.

Table 4.5: Error on the terms of Eqs. 4.25 and 4.26

Parameter	$\Delta R_f/R_f$	$\Delta v_f/v_f$	$\Delta P_a/P_a$	$\Delta \eta/\eta$	$\Delta t$
Error	2%	2%	5%	5%	1.5 s
Cause	non uniform fibre radius	non uniform powder pick up	friction at the mould walls	non uniform temperature	1/2 measurement time step

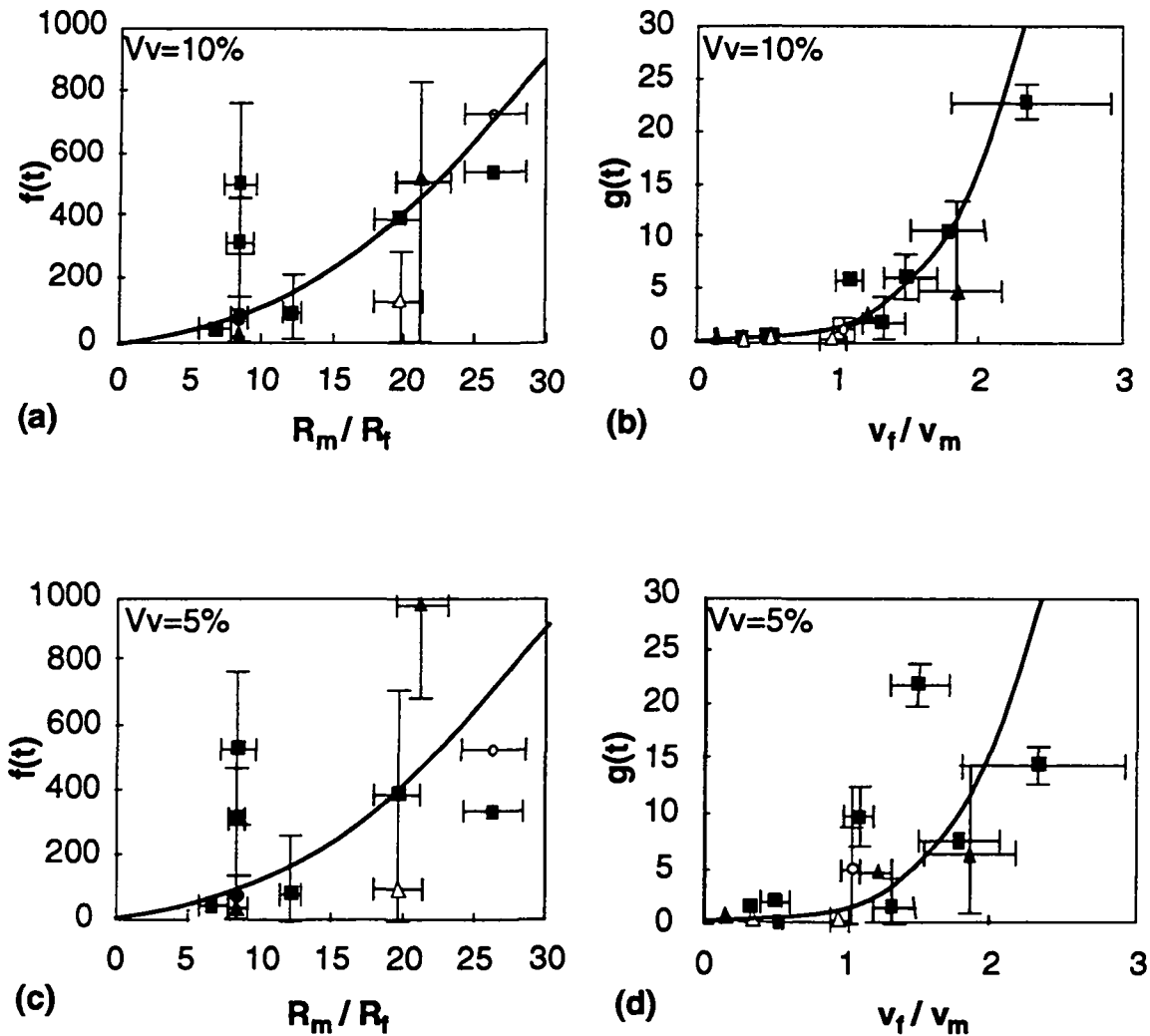


Figure 4.10: Plot of  $f(t)$  and  $g(t)$  (Equations 4.25 and 4.26) compared to experimental consolidation data : (a)  $f(t)$  at  $v_v = 0.1$ ; (b)  $g(t)$  at  $v_v = 0.1$ ; (c)  $f(t)$  at  $v_v = 0.05$ ; and (d)  $g(t)$  at  $v_v = 0.05$ .

The influence of the fibre and resin particle size, and fibre volume fraction on the consolidation time of laminates made of molten powder towpregs are described by the *radius function*,  $f(t)$  (Equation 4.25), and the *volume fraction function*,  $g(t)$  (Equation 4.26), respectively. The two functions are compared to experimental data measured at 10 and 5% void content on the consolidation curves recorded during compression moulding of the laminates. The resulting curves (cf. Figure 4.10), show acceptable agreement with the experimental data. For small particle sizes, the model seems to underestimate the time required to fully impregnate the fibre bed. This may be attributed to the relatively broad particle size distribution (cf. Table 4.3 and Figure 4.4) in the towpregs which is not accounted for by the model. The particle size used for the computation is the mean radius; the presence of particles larger than the mean radius will slow down the impregnation process. The large error bars, calculated on the basis of the relative error on each parameter listed in Table 4.5, are mainly due to the high exponents in the *radius function*,  $f(t)$  and the *volume fraction function*,  $g(t)$ .

## 4.5 SUMMARY

The proposed model is intended to incorporate the primary factors involved in the consolidation process. Some secondary factors have been disregarded and some restrictive assumptions made: the effect of the particle size distribution of the polymer powder has so far been ignored and regular packing of the particles into the fibre tows has been assumed. The geometry has been regarded as being identical for each resin bridge when, in the real composite, one may expect irregularly spaced bridges spanning two, three, four or more fibres. It can be said, however, that the model does take account of the key factors involved in the process. The main effect of the simplifying assumptions would probably be to introduce an error into the constant terms which precede the brackets on the right hand side of Equations 4.13 and 4.15–17. It could be argued that in a general powder composite the dimensionless term,  $V_0/R_f^3$ , in Equations 4.13 and 4.15–17 could be replaced by an empirical constant representing the system in question. The experimental procedure described here involving the use of an instrumented consolidation test would be an excellent means of determining this constant for other systems. It has been chosen, however, to propose an expression representing  $V_0$  which depends on the geometry of the towpreg.

Having given the necessary caveats in relation to the proposed model it does appear that, for the particular composite systems examined in this study, it works very well at the quantitative level both for FIT yarns and molten powder towpregs. The resin bridge cell model depicted in Figure 4.1 seems to describe correctly the impregnation mechanism during the manufacturing of powder impregnated composites. This can be seen from the correlation between model predictions and experimental results in Figures 4.6, 4.7 and 4.9. Furthermore, Figure 4.8 shows that there is no significant flow transverse to the fibres, confirming our initial assumption that flow occurs mainly parallel to the fibre direction. The impregnation rate seems to be mainly controlled by the applied pressure, the resin viscosity, the ratio between individual bridge volume and fibre size and the ratio between the matrix and fibre volume fraction. The different means used to stabilise the powder coated towpregs, i.e. FIT yarns and molten powder towpregs, have an influence on the geometry—and volume,  $V_0$ —of each bridge. It was therefore necessary to consider the consolidation behaviour of the two systems separately.

FIT yarns appear to be more sensitive to particle size than molten powder towpregs. The consolidation time Equation 4.19 for FIT shows a sixth power dependence on the matrix particle radius,  $R_m$ , compared to a square dependence for molten powder towpregs (cf. Equation 4.23). The use of small powder particles is therefore advisable for both types of system. It allows both towpregs with a finer matrix distribution to be manufactured, and faster processing cycles to be achieved. The latter is a particularly sensitive issue for FIT filaments.

The maximum value of the spring pressure, calculated from Equation 4.12 for UD laminates, is estimated to 0.85 MPa. For applied pressures higher than 4–5 MPa, the effects of the spring pressure on the consolidation rate will therefore be minimal.

It should be noted that the maximum value of the capillary pressure calculated from Equation 4.11 is between two and three orders of magnitude lower than either the applied pressure or the spring pressure. Its influence on the rate of consolidation can therefore be neglected in most situations. Surface energy effects on the mechanical

properties of the composite, however, cannot be overlooked. Adhesion between the resin and the reinforcement depends on molecular and chemical forces which are strongly influenced by the surface properties of the components in contact. Capillary pressure phenomena will also affect both the physical elimination of voids from the composite during consolidation and the topology of any voids remaining. The influence of surface energy phenomena on the fibre-matrix adhesion and on the topology of the voids remaining in the final composite will be studied in Chapters 5 and 6.

#### **4.6 REFERENCES**

- 1 Van West, B. P., Pipes, R. B. and Advani, S. G., *Polymer Composites* 1991, **12**, 417.
- 2 Iyer, S. R. and Drzal, L. T., *J. Thermoplastic Composite Materials* 1990, **3**, 325.
- 3 Ye, L., Klinkmüller, V. and Friedrich, K., *J. Thermoplastic Composite Materials* 1992, **5**, 32.
- 4 Ye, L., Friedrich, K., Cutolo, D. and Savadori, A., *Compos. Manufact.* 1994, **5**, 41.
- 5 Denn, M. M. "Process Fluid Mechanics", Prentice-Hall, Inc, 1980.
- 6 Åström, B. T., Pipes, R. B. and Advani, S. G., *J. Composite Materials* 1992, **26**, 1351.
- 7 Gutowski, T. G., Kingery, J. and Boucher, D., *SPE ANTEC'86* 1986, p. 1316.
- 8 Gutowski, T. G., Cai, Z., Kingery, J. and Wineman, S. J., *SAMPE Quarterly* 1986, **17**, 54.
- 9 Rozant, O. Diploma project, LTC-EPFL, Feb. 1994.
- 10 Connor, M. Activity Report, LTC94081.MTC, Aug. 1994.
- 11 Lam, R. C. and Kardos, J. L., *3rd Annual Technical Conference. American Society for Composites* 1988, p. 3.

# 5

## A CRITERION FOR OPTIMUM ADHESION

Mechanical properties of composites are strongly dependent on both processing conditions and materials structure. In Chapter 3, the mechanism of consolidation of powder impregnated fibres was investigated, which allowed a consolidation model to be derived in Chapter 4. This model allows the processing conditions of a given fibre-resin system to be optimised, permitting a void free laminate to be manufactured, and thus improving mechanical properties. Mechanical properties can further be improved by optimising the interfacial adhesion between resin and fibres, thus increasing stress transfer from the matrix to the reinforcing fibres. The interfacial strength of a composite part depends on the surface energy of its different components. Surface energy effects on mechanical properties of a composite are studied in this chapter. Extensive work on the study of the influence of the shear strength at the fibre-resin interface on mechanical properties of composites is reported in literature [1–7]. Shear strength, which depends on the quality of adhesion at the interface has often been measured on single fibre model systems embedded in resin [8–10]. Gent and co-workers [11, 12] proposed that the measured adhesive strength is a product of two terms: an equilibrium term of detachment given by thermodynamic considerations, and a numerical factor representing the inelastic contribution to fracture. The latter term can be very large, and in the case of viscoelastic materials, it is strain rate dependent. This suggests that, with a given inelastic contribution, there is a strong correlation between interfacial strength and thermodynamic adhesion. Various attempts to correlate the bond strength to different thermodynamic *wetting parameters* can be found in the literature. Today, the choice of a criterion for optimum adhesion is still actively debated. Bond strength was alternately compared to the work of adhesion,  $W_a$  [13], spreading coefficient,  $\lambda$  [14], wetting tension,  $\Delta F_i$ , and interfacial energy per unit area,  $\gamma_{sl}$ , respectively [15–17].

In this chapter, a short introduction to the principal mechanisms responsible for adhesion is presented. Then, four criteria for optimum adhesion found in literature are reviewed and discussed. The wetting parameters related to adhesion,  $W_a$ ,  $\lambda$ ,  $\Delta F_i$ , and  $\gamma_{sl}$  are first presented, followed by an analytical analysis which leads to their optimisation. This is done by considering two cases separately: (i) for a given adhesive what surface properties of the substrate yields optimum adhesion, and (ii) for a given substrate, which is the optimal adhesive. In Chapter 6, experimental results on fibre reinforced composites will be compared to the theory presented herein.

## 5.1 INTRODUCTION TO ADHESION

Interfaces in a fibre reinforced composite structure usually represent a thin layer (1 to 10 Å) located at the surface of contact between the fibres and the matrix. This can thus represent a large area; as an example, if we consider a 60 vol.% carbon fibre reinforced laminate of volume  $V = 50 \times 50 \times 3 \text{ mm}^3$ , such as those presented in Chapter 4, the interfacial area represents about  $V \cdot \phi / R_f \cong 3 \text{ m}^2$ , where  $R_f$  is the fibre radius and  $\phi$  the fibre volume content.

When a composite structure is loaded, the load is transferred from the matrix to the fibres mainly through shear stresses at the fibre-matrix interface (cf. Figure 5.1a). Load transfer increases with strong bonds, thus improving the composite strength. The influence of bond strength on the composite toughness, however, is less clear than for its strength. In a composite made of relatively brittle materials (e.g., glass fibre reinforced epoxy) with a strong interface, a crack will propagate linearly, crossing straight through the interface. Limited energy will be dissipated resulting in a brittle behaviour. On the other hand, more energy can be dissipated by the composite if the crack is deviated along a weaker interface, thus increasing the crack length (cf. Figure 1b). The mechanical strength of the system with a weak interface is lower than the one of the composite with a strong interface, but the former has higher toughness. In the case of a tough matrix (e.g., thermoplastic resins), more energy can be dissipated through the resin deformation than through the crack deviation along the interface; in this case, a strong interface is preferred, yielding both high strength and high toughness.

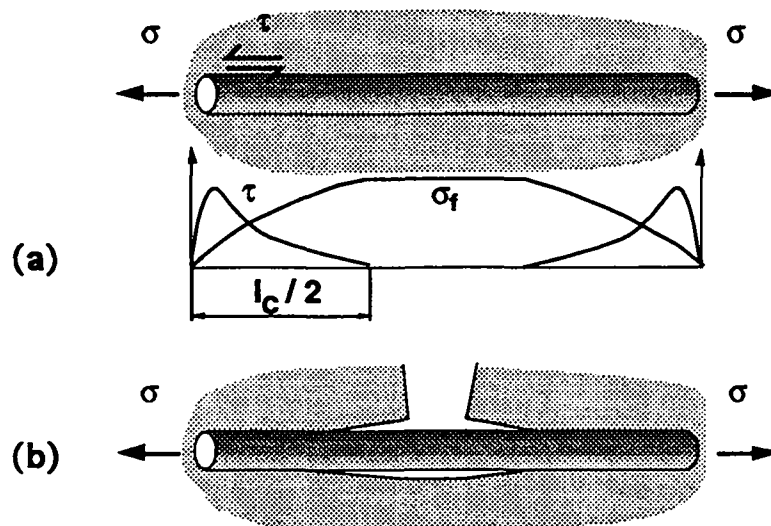


Figure 5.1: Influence of the interface on the mechanical properties of a composite: (a) a strong bond improves the load transfer from the matrix to the fibres; and (b) a weak bond can increase the toughness of brittle composites by deviating the crack along the interface.

Adhesion mechanisms can be divided into four groups, according to the type of interaction forces in presence: physical, chemical, mechanical and molecular inter-diffusion forces, respectively, as illustrated in Figure 5.2. Physical interactions, the subject of this chapter, include secondary forces —van der Waals type— which are active over a very short distance ( $< 10 \text{ \AA}$ ). These are weak forces ( $1\text{--}3 \text{ kJ}\cdot\text{mol}^{-1}$ ) and result from the dispersive component of the surface energy of the two phases in contact. All materials, if brought into a sufficiently intimate contact, will thus adhere due to dispersive interactions across the interface. A much stronger physical bond can be obtained if electrons are exchanged across the interface. This is the case when an electron donor (i.e., Lewis acid, e.g.,  $\text{H}^+$ ) faces an electron acceptor (Lewis base, e.g.,  $\text{OH}^-$ ); acid-base interactions can be of the order of  $20 \text{ kJ}\cdot\text{mol}^{-1}$ .

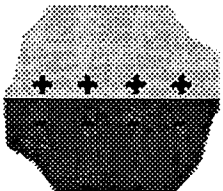
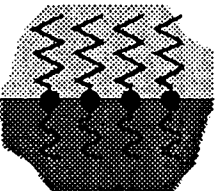
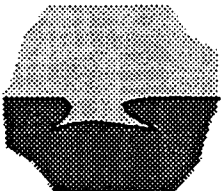
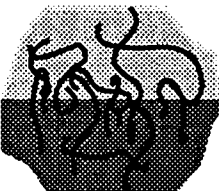
Foces	physical	chemical	mechanical	inter-diffusion
Type				
Energy [kJ/mol]	$\gamma^d = 1 - 3$ $\gamma^{AB} = 1 - 20$	covalent: 5 - 40 ionic: 35 - 60 metal: 5 - 20		

Figure 5.2: Four types of adhesion mechanisms: physical, chemical, mechanical and interdiffusion.

When two materials are incompatible, the bond strength can be improved by grafting a reactive group at the interface, which will form a covalent bond between molecules on both sides of the interface. Chemical bonds are much stronger than physical bonds and can be of the order of  $40\text{--}50 \text{ kJ}\cdot\text{mol}^{-1}$ . One example of chemical bonding is given by the grafting of maleic acid (MAH) to polypropylene (PP) which is used to improve the bond strength of PP with polyamide 6 (PA6) [18].

A strong bond can be obtained when the liquid can penetrate into the topological roughness of the solid surface, thus forming mechanical interlocking. Interdiffusion of long chains across the interface can be interpreted as mechanical interlocking at a molecular scale. Such processes are very slow and can be described by the reptation theory [19].

In fibre reinforced composites, most of the fibre-matrix interactions are of the physical type. Chemical bonding is used, for instance, with glass fibres sized with silane groups to improve their adhesion with very non-polar resins such as polypropylene; but these are specific cases which will not be considered here. Physical adhesion can be conveniently characterised by thermodynamic *wetting parameters* which are reviewed in the next section.



## 5.2 WETTING PARAMETERS

Four wetting parameters are presented here, which are considered in the literature as characteristic of the quality of the physical adhesion between two phases. These are, the work of adhesion,  $W_a$ , the spreading coefficient,  $\lambda$ , the wetting tension,  $\Delta F_i$ , and the interfacial energy per unit area,  $\gamma_{sl}$ .

### 5.2.1 Work of adhesion

The work of adhesion,  $W_a$ , is the work required to disjoin a unit area of the solid-liquid interface, thereby creating a unit area of liquid-vacuum and solid-vacuum interface [20]; this situation is illustrated in Figure 5.3a. It is expressed by the Dupré equation [21],

$$W_a = \gamma_l + \gamma_s - \gamma_{sl} \quad (5.1)$$

where  $\gamma_l$  is the liquid surface tension, and  $\gamma_s$  is the solid surface energy per unit area. Using the Young equation [22],

$$\cos \theta = \frac{\gamma_s - \gamma_{sl}}{\gamma_l} \quad (5.2)$$

which relates the finite equilibrium contact angle,  $\theta$ , to the surface and interfacial energies, allows the thermodynamic work of adhesion (Equation 5.1) to be expressed as,

$$W_a = \gamma_l(1 + \cos \theta) \quad (5.3)$$

which permits *direct* determination of the work of adhesion from surface tension and contact angle measurements. Equations 5.2 and 5.3 are written in a form which neglects the adsorption of vapours from the resin liquid onto the solid surface, a good practical assumption when the liquid is non volatile.

Several workers have shown that the thermodynamic work of adhesion correlates well with adhesive bond strength of a flat interface [23–25] and with composite strength [26]. Although it is intuitively easy to accept that there is a correlation between work of adhesion and adhesive strength, it must be kept in mind that the former is a thermodynamic quantity referring to the reversible work needed to create two new surfaces from a defect free interface, while the latter is a mechanical quantity also affected by irreversible processes like inelastic deformations, and the presence of voids at the interface. The work of adhesion is thus not sufficient to characterise the interfacial strength. Wu [27] calculated the theoretical bond strength of a flaw free interface typical of a polymer-polymer bond, and obtained a value of about two orders of magnitude greater than what is experimentally observed with real interfaces. De Bruyne [28] proposed that voids located at the interface, the size of which he related to the contact angle between adhesive and adherend, could act as

nuclei for crack propagation. Later, Wu [27] related the void size to the spreading coefficient,  $\lambda$ .

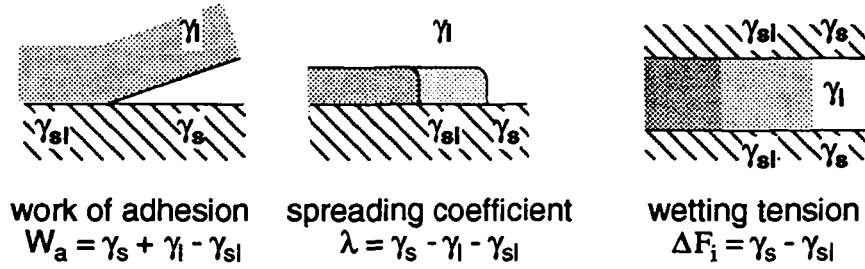


Figure 5.3: Physical representation of the wetting parameters.

### 5.2.2 Spreading coefficient

The *spreading coefficient* can be defined as the work required to expose a unit area of solid-vacuum interface while destroying a corresponding amount of the solid-liquid and liquid-vacuum interfaces [20],

$$\lambda = \gamma_s - \gamma_l - \gamma_{sl} \quad (5.4)$$

which together with the Young Equation 5.2 can be expressed as

$$\lambda = \gamma_l(\cos\theta - 1) \quad (5.5)$$

A negative value results in a finite equilibrium contact angle and a positive value predicts instantaneous spreading. This situation is illustrated in Figure 5.3b. Wu [27] suggests that the interfacial strength,  $\sigma_f$ , can be related to the spreading coefficient as

$$\sigma_f = \frac{K_m \lambda}{1 - \frac{\lambda}{\gamma_s}} \quad (5.6)$$

where  $K_m$  is a mechanical parameter characteristic of the system. According to Equation 5.6, it is clear that the interfacial strength is maximum at maximum spreading coefficient.

### 5.2.3 Wetting tension

Various authors [15, 16, 29–31] proposed that maximum adhesive strength is obtained at maximum *wetting tension* (or *adhesive tension*),  $\Delta F_i$ . The wetting tension can be defined as the work expended in eliminating a unit area of the solid-liquid interface while exposing a unit area of the solid-vacuum interface [20],

$$\Delta F_i = \gamma_s - \gamma_{sl} \quad (5.7)$$

which is actually the arithmetic mean of the work of adhesion and the spreading coefficient. This approach thus gives an equal weight to the influence of the work of adhesion and the presence of flaws at the interface. This situation is illustrated in Figure 5.3c. It can be seen that this situation is the most representative of a resin impregnating a fibre bed, since in a fibre-reinforced composite the liquid-vacuum interface area can be neglected compared to the fibre-vacuum and fibre-resin interface areas.

### 5.2.4 Interfacial energy

Finally, it was proposed [15, 16, 30, 32] that minimising the interfacial energy,  $\gamma_{sl}$ , would yield a more stable system and hence increase the adhesive strength. Various expressions were proposed for the interfacial energy. Four definitions are presented: the Sell-Neumann expression, the Good-Girifalco equation for dipolar interactions with two different definitions of the interaction parameter,  $\phi$ , and finally an expression based on acid-base interactions.

The Sell-Neumann relationship [33, 34] expresses the interfacial energy in terms of the surface energies of the adhesive and adherend only:

$$\gamma_{sl} = \frac{(\sqrt{\gamma_s} - \sqrt{\gamma_l})^2}{1 - 0.015\sqrt{\gamma_s\gamma_l}} \quad (5.8)$$

The validity of this equation is contested, however, and will not be used in this study. Good and Girifalco [35–38] introduced an interaction parameter,  $\phi$ , into their definition of interfacial energy:

$$\gamma_{sl} = \gamma_s + \gamma_l - 2\phi\sqrt{\gamma_s\gamma_l} \quad (5.9)$$

It was first assumed that the surface energy of a phase  $i$  could be expressed in terms of a dispersive and a polar component, such that

$$\gamma_i = \gamma_i^d + \gamma_i^p \quad (5.10)$$

where  $d$  and  $p$  refer to dispersive and polar, respectively. Following the dispersive-polar theory, Wu [27] proposed that the interaction parameter,  $\phi$ , between a low and a high energy material, is well described by the geometric mean equation,

$$\phi = \sqrt{x_s^d x_l^d} + \sqrt{x_s^p x_l^p} \quad (5.11)$$

and the *harmonic-mean equation* is preferred for interaction between a polymer and a low energy material,

$$\phi = 2 \left( \frac{x_s^d x_l^d}{\sqrt{\frac{\gamma_l}{\gamma_s} x_l^d} + \sqrt{\frac{\gamma_s}{\gamma_l} x_s^d}} + \frac{x_s^p x_l^p}{\sqrt{\frac{\gamma_l}{\gamma_s} x_l^p} + \sqrt{\frac{\gamma_s}{\gamma_l} x_s^p}} \right) \quad (5.12)$$

where  $x_i^k = \gamma_i^k / \gamma_i$ , ( $i = s, l$  and  $k = d, p$ ). The sum of the polar and dispersive components of the surface energy is unity,

$$x_i^d + x_i^p = 1 \quad (5.13)$$

Some authors [39] argued that while the geometric mean and the harmonic mean equally well describe the dispersive component of the interaction parameter, neither combining rule can be applied satisfactorily to the polar component. A more recent approach considers the acid-base interaction between molecules and expresses the surface energy of a compound in terms of the Lifshitz-van der Waals component,  $\gamma^{LW}$ , and the acid-base component,  $\gamma^{AB}$ , as

$$\gamma_i = \gamma_i^{LW} + \gamma_i^{AB} = \gamma_i^{LW} + 2\sqrt{\gamma_i^A \gamma_i^B} \quad (5.14)$$

where  $\gamma^A$  and  $\gamma^B$  are the (Lewis) acid and base parameter of surface free energy, respectively. The interfacial energy is defined as,

$$\gamma_{sl} = \gamma_s^{LW} + \gamma_l^{LW} + 2\left(\sqrt{\gamma_s^A \gamma_l^B} + \sqrt{\gamma_l^A \gamma_s^B} - \sqrt{\gamma_s^{LW} \gamma_l^{LW}} - \sqrt{\gamma_s^A \gamma_l^B} - \sqrt{\gamma_s^B \gamma_l^A}\right) \quad (5.15)$$

Note that a molecule can be both a Lewis acid (electron acceptor) and a Lewis base (electron donor); such substance is called *bipolar*, as for example water. A substance is *apolar* if neither the acid nor the basic property is appreciable. If only one of the properties is appreciable, it is termed a *monopolar* substance. More details on the acid-base approach can be found in the review made by Good on wetting and adhesion science [39].

It can be shown that the acid-base interaction Equation 5.15 can be expressed in terms of the Good-Girifalco Equation 5.9 by defining the acid-base interaction parameter,  $\phi^{AB}$ , as,

$$\phi^{AB} = \sqrt{x_i^{LW} x_j^{LW}} + \sqrt{x_i^A x_j^B} + \sqrt{x_i^B x_j^A} \quad (5.16)$$

where, as for the dispersive-polar theory,  $x_i^k = \gamma_i^k / \gamma_i$ , with

$$x_i^{LW} + x_i^A + x_i^B = 1 \quad (5.17)$$

so that  $\phi^{AB}$  can be characterised by two parameters:  $x_i^{LW}$  and  $x_i^A$ .

Four wetting parameters, work of adhesion, spreading coefficient, wetting tension, and interfacial energy, have been presented above. It is now necessary to study how to optimise them to maximise the interfacial strength.

### 5.3 ADHESION OPTIMISATION

Four wetting parameters have been considered alternately by various authors as criteria for optimum adhesion: maximum work of adhesion,  $W_a$ , spreading coefficient,  $\lambda$ , and wetting tension,  $\Delta F_i$ , respectively, and minimum interfacial energy,  $\gamma_{sl}$ . In this section, we will analyse what are the conditions required to optimise these parameters individually, and then we will discuss what criterion is more representative of adhesion. The validity of the selected criterion will be tested experimentally on composite parts in Chapter 6.

#### 5.3.1 Extrema of the wetting parameters

In the case phase  $j$  is kept constant, the four wetting parameters,  $W_a$ ,  $\lambda$ ,  $\Delta F_i$ , and  $\gamma_{sl}$ , referred to by the symbol,  $\chi$ , depend on the surface energy of phase  $i$ ,  $\gamma_i$ , and on its polar component,  $x_i^p$ , for the polar-dispersive theory (Equations 5.11 and 5.12) and the LW- and acid-components,  $x_i^{LW}$  and  $x_i^A$ , respectively for the acid-base theory (Equations 5.15 and 5.17). The maximum possible work of adhesion,  $W_a$ , spreading coefficient,  $\lambda$ , and wetting tension,  $\Delta F_i$ , respectively (assuring maxima exist), and minimum of interface energy,  $\gamma_{sl}$ , as a function of phase  $i$  can thus be found by setting equal to zero the variations of Equations 5.1, 5.4, 5.7 and 5.9 upon an arbitrary variation in the  $i$ -surface energy,  $\gamma_i$ , and its  $k$ -component,  $x_i^k$ , ( $k = p$  or  $LW$  and  $A$ , depending on the theory under consideration) at constant  $\gamma_j$ :

$$d\chi = \frac{\partial\chi}{\partial\gamma_i} d\gamma_i + \sum_k \frac{\partial\chi}{\partial x_i^k} dx_i^k = 0 \quad (5.18a)$$

Supposing that we can vary all  $\gamma_i$ 's and  $x_i^k$ 's independently, Equation 5.18 is satisfied when each term on the right hand side vanishes, i.e.,

$$\frac{\partial\chi}{\partial\gamma_i} = 0 \quad (5.18b)$$

and

$$\frac{\partial\chi}{\partial x_i^k} = 0 \quad (5.18c)$$

Two cases need to be considered separately: (i) for a given adhesive what surface property of the substrate will optimise adhesion, and (ii) what adhesive will adhere optimally to a given substrate.

**Optimum surface properties of the substrate for a given adhesive**

Work of adhesion, spreading coefficient, wetting tension and interface energy are plotted in Figure 5.4 as a function of the substrate surface energy. It can be seen that, for a given adhesive, the first three wetting parameters follow parallel curves when plotted as a function of  $\gamma_s$ . Thus maximising  $W_a$ , is equivalent to maximising the next two parameters.

For a given adhesive, the subscript  $i$ , refers to the substrate, and  $j$  to the adhesive. Differentiating Equations 5.4, 5.7, and 5.9 with respect to  $\gamma_s$  and  $x_s^k$  gives,

$$\frac{\partial W_a}{\partial \gamma_s} = \frac{\partial \lambda}{\partial \gamma_s} = \frac{\partial \Delta F_i}{\partial \gamma_s} = 1 - \frac{\partial \gamma_{sl}}{\partial \gamma_s} \tag{5.19a}$$

and

$$\frac{\partial W_a}{\partial x_s^k} = \frac{\partial \lambda}{\partial x_s^k} = \frac{\partial \Delta F_i}{\partial x_s^k} = -\frac{\partial \gamma_{sl}}{\partial x_s^k} = 2\sqrt{\gamma_s \gamma_l} \frac{\partial \phi}{\partial x_s^k} \tag{5.19b}$$

Hence Equations 5.18b and 5.18c yield two alternative criteria for  $\partial \gamma_{sl} / \partial \gamma_s$  and a single criterion for  $\partial \gamma_{sl} / \partial x_s^k$ :

$$\frac{\partial \gamma_{sl}}{\partial \gamma_s} = 1 \tag{5.20a}$$

or

$$\frac{\partial \gamma_{sl}}{\partial \gamma_s} = 0 \tag{5.20b}$$

and

$$\frac{\partial \gamma_{sl}}{\partial x_s^k} = 0 \tag{5.20c}$$

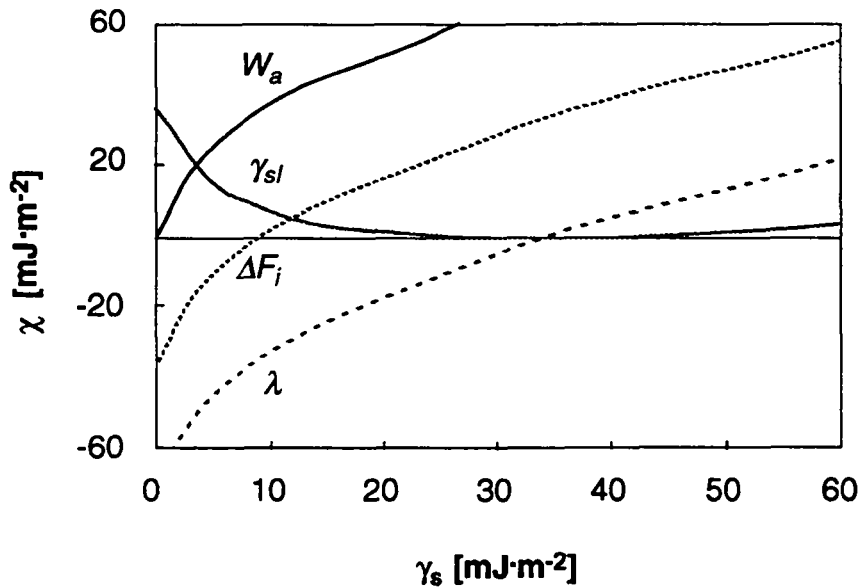


Figure 5.4: Wetting parameters as a function of the substrate surface energy using Equations 5.1, 5.4, 5.7, and 5.9, respectively, with  $\phi = 1$  and  $\gamma_l = 35 \text{ mJ.m}^{-2}$ .

The criterion based on maximum  $W_a$ ,  $\lambda$ , and  $\Delta F_i$  (Equation 5.20a), however, is in contradiction with the criterion of minimum interfacial energy (Equation 5.20b). The validity of minimum interfacial energy as a criterion for optimum adhesion is, however, arguable since interfacial energy is only one component of the total surface energy of the system. A valid criterion should consider the total surface energy and not one of its components only. For this reason, we suggest that:

*for a given adhesive, optimum adhesion is obtained when  $W_a$ ,  $\lambda$ , and  $\Delta F_i$  are maximum, i.e., when Equations 5.20a and 5.20c are satisfied.*

**Optimum adhesive for a given substrate:**

Figure 5.5 shows a plot of the wetting parameters as a function of the adhesive surface energy, with a constant adherend surface energy. This situation corresponds to testing various adhesives on a given substrate.

For a given substrate, the subscript  $i$ , refers to the adhesive, and  $j$  to the substrate. Again, differentiating the various parameters represented by  $\chi$  gives,

$$\frac{\partial W_a}{\partial \gamma_i} = 1 - \frac{\partial \gamma_{sl}}{\partial \gamma_i} \quad (5.21a)$$

$$\frac{\partial \lambda}{\partial \gamma_i} = -1 - \frac{\partial \gamma_{sl}}{\partial \gamma_i} \quad (5.21b)$$

$$\frac{\partial \Delta F_i}{\partial \gamma_i} = -\frac{\partial \gamma_{sl}}{\partial \gamma_i} \quad (5.21c)$$

and

$$\frac{\partial W_a}{\partial x_i^k} = \frac{\partial \lambda}{\partial x_i^k} = \frac{\partial \Delta F_i}{\partial x_i^k} = -\frac{\partial \gamma_{sl}}{\partial x_i^k} = 2\sqrt{\gamma_s \gamma_i} \frac{\partial \phi}{\partial x_i^k} \quad (5.21d)$$

With Equation 5.18b and c we obtain three alternative criteria for  $\partial \gamma_{sl} / \partial \gamma_i$  and a single one for  $\partial \gamma_{sl} / \partial x_i^k$ :

$$\frac{\partial \gamma_{sl}}{\partial \gamma_i} = 1, -1, \text{ or } 0 \quad (5.22a-c)$$

and

$$\frac{\partial \gamma_{sl}}{\partial x_i^k} = 0 \quad (5.22d)$$

It can be seen from Equations 5.22a-c that all three parameters cannot be maximised simultaneously, and Equation 5.21c shows that the maximum of the wetting tension corresponds to the minimum of the interfacial energy. Maximising the work of

adhesion ( $\gamma \rightarrow \infty$ ) yields a negative value of the spreading coefficient, hence a high flaw density at the interface might be expected; whereas the maximum spreading coefficient corresponds to a low value of the work of adhesion. As pointed out by Wu [27], the optimum conditions must be a compromise between these two antagonistic mechanisms. The optimum condition should correspond to the situation where the work of adhesion is maximum within the region where spontaneous wetting occurs, i.e.,  $\lambda \geq 0$ :

*these two conditions are fulfilled when the wetting tension is maximum.*

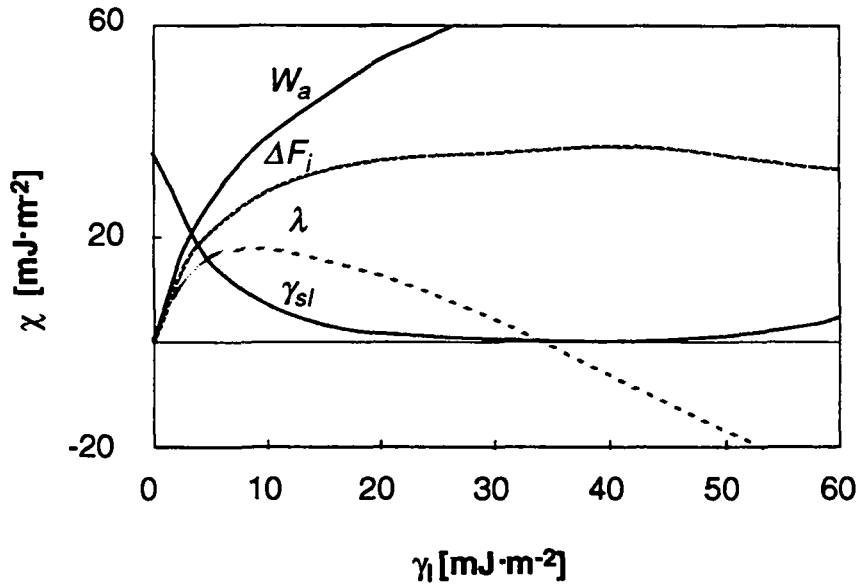


Figure 5.5: Wetting parameters,  $W_a$ ,  $\lambda$ ,  $\Delta F_i$ , and  $\gamma_{sl}$  as a function of adhesive surface tension, using Equations 5.1, 5.4, 5.7 and 5.9, respectively, with  $\phi = 1$  and  $\gamma_s = 35 \text{ mJ}\cdot\text{m}^{-2}$ .

Maximum wetting tension can thus be used as a criterion for optimising adhesion in both situations of a given adhesive, i.e.,  $\partial\gamma_{sl} / \partial\gamma_s = 1$  and  $\partial\gamma_{sl} / \partial x_s^k = 0$  (Equations 5.19a and c), and a given substrate, i.e.,  $\partial\gamma_{sl} / \partial\gamma_l = \partial\gamma_{sl} / \partial x_l^k = 0$  (Equations 5.22c and d), respectively. Conditions required to maximise the wetting tension are studied in the following section.

### 5.3.2 Maximum wetting tension

Conditions leading to maximum wetting tension can be found by solving Equations 5.19a and c if the substrate is being optimised for a given adhesive, and Equations 5.22c and d if it is the adhesive which is to be optimised. The solution to both sets of equations depends on the definition of the interfacial energy selected. The Good-Girifalco Equation 5.9 will be examined here using three different mixing rule theories for  $\phi$ : the geometric mean definition 5.11, the harmonic mean equation 5.12 and the acid-base equation 5.16, respectively. All equations 5.9–5.12 and 5.16 are



symmetric with respect to  $\gamma_i$  and  $\gamma_s$ , so henceforth the subscripts  $i$  and  $j$  will be used instead of  $s$  and  $l$ .

According to the Good-Girifalco Equation 5.9, the derivative of the interface energy with respect to the  $i$ -surface energy is defined as

$$\frac{\partial \gamma_{sl}}{\partial \gamma_i} = 1 - \phi \frac{\sqrt{\gamma_j}}{\sqrt{\gamma_i}} - 2\sqrt{\gamma_i \gamma_j} \frac{\partial \phi}{\partial \gamma_i} \quad (5.23)$$

As all three Equations 5.19, 5.22 and 5.23 depend on the interaction parameter,  $\phi$ , it is now necessary to examine its different definitions separately.

### Geometric mean Equation

In the case the *geometric mean* equation 5.11 is used, it can be shown that the solution to Equations 5.19c and 5.22d, i.e.,  $\partial \phi / \partial x_i^k = 0$  is given by:

$$x_s^p = x_i^p \quad (5.24)$$

As the geometric mean definition 5.11 is independent of  $\gamma_i$ , the last term on the right-hand side of Equation 5.23 is zero. The optimum substrate surface energy for a given adhesive is thus found by solving Equation 5.19a, i.e., by setting

$$\frac{\partial \gamma_{sl}}{\partial \gamma_s} = 1 - \phi \frac{\sqrt{\gamma_i}}{\sqrt{\gamma_s}} = 1 \quad (5.25)$$

which yields the solution

$$\gamma_s \rightarrow \infty \quad (5.26)$$

The optimum adhesive surface energy for a given substrate is found by solving Equation 5.22c, i.e., by setting

$$\frac{\partial \gamma_{sl}}{\partial \gamma_i} = 1 - \phi \frac{\sqrt{\gamma_s}}{\sqrt{\gamma_i}} = 0 \quad (5.27)$$

which yields the solution:

$$\gamma_i = \gamma_s \phi^2 \quad (5.28)$$

It must be noted that when condition 5.24 is fulfilled,  $\phi = 1$ , and condition 5.28 simplifies to  $\gamma_i = \gamma_s$ .

It can thus be concluded that, according to the Good-Girifalco Equation 5.9, using the geometric mean mixing rule for  $\phi$ ,

the maximum wetting tension between an adhesive and a substrate is obtained when the substrate surface energy is very high (cf. Equation 5.26), and when the two phases have the same polarity (cf. Equation 5.24) and surface energy (cf. Equation 5.28).

### Harmonic mean Equation

In case the *harmonic mean* equation 5.12 is used it can be shown that Equations 5.19c and 5.22d yield the same solution 5.24 as with the geometric mean mixing rule, i.e.,

$$x_s^p = x_l^p \quad (5.24)$$

The optimum substrate surface energy for a given adhesive can be found by solving Equation 5.19a which also yields the same solution 5.26 as with the geometric mean mixing rule, i.e.,

$$\gamma_s \rightarrow \infty \quad (5.26)$$

Equation 5.22d, however, which defines the optimum adhesive surface energy for a given adherend, cannot be solved analytically and a numerical solution is required, because the last term in Equation 5.23,  $\partial\phi_H/\partial\gamma \neq 0$ . Figure 5.6 describes the  $\gamma_l/\gamma_s$  and  $\gamma_{sl}/\gamma_s$  ratios yielding maximum wetting tension as a function of the polarity of the adhesive for an adherend polarity of,  $x_s^d = 0.2$ . The solutions using the two mixing rules—geometric and harmonic—are compared. It can be seen that the geometric solution (Equation 5.28) is very similar to the harmonic solution found numerically; particularly when the polarity of the two phases are similar.

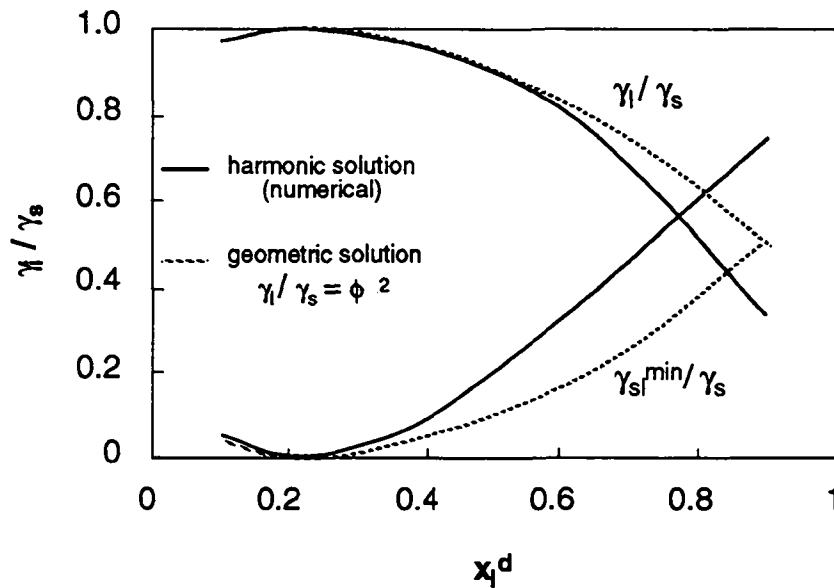


Figure 5.6:  $\gamma_{sl}/\gamma_s$  and  $\gamma_l/\gamma_s$  ratios yielding maximum wetting tension as a function of  $x_l^d$ , with  $x_s^d = 0.2$ . The harmonic solution to Equation 22c (solid line) found numerically is compared to the geometric solution  $\gamma_l = \gamma_s \phi^2$  (dotted line).

It can be concluded that, according to the Good-Girifalco Equation, using the harmonic mean mixing rule,  $\phi_H$ ,

*the same criterion for optimum adhesion of a given adhesive on various substrates as with the geometric mean mixing rule (solutions 5.24 and 5.26) can be used. When various adhesives are tested on a given substrate, the geometric and harmonic solution are very similar; Equation 5.28 can thus be used to approximate the harmonic solution.*

#### **Acid-Base Interaction Equation**

In case the acid-base interaction theory is used, it can easily be shown that  $\sum_k \partial \phi / \partial x_i^k = 0$  ( $k = LW, A, \text{ and } B$ ) when

$$x_i^{LW} = x_j^{LW} \quad (5.29a)$$

$$x_i^A = x_j^B \quad (5.29b)$$

$$x_i^B = x_j^A \quad (5.29c)$$

As the acid-base interaction parameter,  $\phi^{AB}$ , is independent of  $\gamma_i$ , the last term on the right-hand side of Equation 5.23 is zero. The optimum substrate surface energy for a given adhesive is thus easily found by solving Equation 5.19a, which, as for the geometric mean mixing rule, yields the solution

$$\gamma_s \rightarrow \infty \quad (5.26)$$

The optimum adhesive surface energy is found by solving Equation 5.22c, which yields the solution:

$$\gamma_t = \gamma_s \phi^2 \quad (5.28)$$

Again when condition 5.29 is fulfilled,  $\phi = 1$ , and condition 5.28 simplifies to  $\gamma_t = \gamma_s$ .

It can now be concluded that:

*according to the acid-base interaction theory, maximum adhesive tension is obtained when the substrate surface energy is very high (cf. Equation 5.26), and when the two phases have the same surface energy (cf. Equation 5.29) such as their Lifshitz-Van der Waals component are equal (cf. Equation 5.29a), and the acid component of one phase is equal to the basic component of the other (cf. Equations 5.29b and 5.29c).*

Table 5.1 summarises the solutions to the criterion of maximum wetting tension found using the Good-Girifalco Equation 5.9 together with the geometric mean, harmonic mean and an "acid-base" mixing rule defined by Equations 5.11, 5.12, and 5.16, respectively.

An experimental study on the influence of the fibre surface energy on the mechanical properties of fibre reinforced composites is presented in Chapter 6 in order to illustrate the theory presented here. The solid (fibre) surface energy is varied, keeping the adhesive (resin) surface tension constant (cf. Equations 5.19a and 5.19).

**Table 5.1: solution to maximum wetting tension for various mixing rules**

mixing rule $\phi$	fixed adhesive ( $\gamma_f = \text{const.}$ )	fixed substrate ( $\gamma_s = \text{const.}$ )
geometric mean (Eq. 5.11):	$\gamma_s \rightarrow \infty$ $x_s^p = x_l^p$	$\gamma_l = \gamma_s \phi^2$ (a) $x_s^p = x_l^p$
harmonic mean (Eq. 5.12):	$\gamma_s \rightarrow \infty$ $x_s^p = x_l^p$	$\gamma_l \cong \gamma_s \phi^2$ (a) $x_s^p = x_l^p$
acid-base (Eq. 5.16):	$\gamma_s \rightarrow \infty$ $x_s^{LW} = x_l^{LW}$ $x_s^A = x_l^B$ $x_s^B = x_l^A$	$\gamma_l = \gamma_s \phi^2$ (a) $x_s^{LW} = x_l^{LW}$ $x_s^A = x_l^B$ $x_s^B = x_l^A$

(a) Note that if the respective  $x_i^k$  terms are equal, then  $\phi = 1$ , and  $\gamma_f = \gamma_s$

## 5.4 REFERENCES

- 1 Riley, V. R., *J. Composite Materials* 1968, **2**, 436.
- 2 Fraser, W. A, Ancker, F. H., Dibenedetto, A. T. and Elbirli, B., *Polymer Composites* 1983, **4**, 238.
- 3 Madhukar, M. S. and Drzal, L. T., *J. Composite Materials* 1991, **25**, 932 .
- 4 Piggott, M. R., *Comp. Sci. and Tech.* 1987, **30**, 295.
- 5 Drzal, L. T., Rich, M. J. and Lloyd, P. F., *J. Adhesion* 1982, **16**, 1.
- 6 Hancox, N. L., *J. Materials Science* 1975, **10**, 234.
- 7 Verpoest, I. and Springer, G. S., *J. Reinforced Plastics and Composites* 1988, **7**, 23.
- 8 Drzal, L. T. and Herrera Franco, P. J. in "Engineered Materials Handbook. Vol. 3 Adhesive and Sealants," (Dostal, C. A., Ed.) ASM Int., 1990, p. 391.
- 9 Favre, J. P., *Interfacial Phenomena in Composite Materials '89 Conf.* 1989, Sheffield (UK), p. 7.
- 10 Piggott, M. R., and M. M. Reboredo., *34th Int. SAMPE Symp* 1989, p. 1923.
- 11 Gent, A. N. and Kinloch, A. J., *J. Polymer Sci.* 1971, **9**, 659.
- 12 Gent, A. N. and Schultz, J., *J. Adhesion* 1972, **3**, 281.

- 13 Zisman, W. A., in "Contact Angle, Wettability and Adhesion." Adv. Chem. Ser. 43, American Chemical Society, Washington, D. C., 1964.
- 14 Wu, S., *J. Adhesion* 1973, 5, 39.
- 15 Kitazaki, Y. and Hata, T., *J. Adhesion* 1972, 4, 123.
- 16 Gray, V. R., *Chem. and Ind.* 1965, 969.
- 17 Gray, V. R., *Forest Product J.* 1962, 12, 452.
- 18 Bidaux, J.-E., Smith, G. D., Bernet, N., Hilborn, J. and Manson, J.-A. E., submitted to *Polymer* 1995.
- 19 Jud, K., Kausch, H. H. and Williams, J. G., *J. Materials Science* 1981, 16, 204.
- 20 Berg, J. C., in "Wettability". (Berg, J. C. Ed.) M. Dekker, 1993, p. 76.
- 21 Dupré, A., "Théorie Mécanique de la Chaleur" Gaitjoer-Villars, Paris (1869).
- 22 Young, T., *Phil. Trans.* 1805, 95, 82.
- 23 Raraty, L. E. and Tabor, D., *Proc. Roy. Soc.* 1958, 245A, 184.
- 24 Levine, M. Ilka, G. and Weiss, P., *J. Polymer Sci.* 1964, B-2, 915.
- 25 Barbaris, M. J., *Nature* 1967, 215, 383.
- 26 Nardin, M., Asloun, E. M. and Schultz, J., *J. Polym. Adv. Technol.* 1991, 2, 171.
- 27 S. Wu., "Polymer Interfaces and Adhesion," M. Dekker, 1982, Chapter 11.
- 28 de Bruyne N. A. *Nature* 1957, 10, 262.
- 29 Levine, M., Ilkka, G. and Weiss, P., *J. Polym. Sci. Polym. Lett. Ed.* 1964, 2, 915.
- 30 Mittal, K. L., *Polym. Eng. Sci.* 1977, 17, 467.
- 31 Neumann, A. W., *Staub-Reinhalt. Luft* 1968, 28, 24.
- 32 Dyckerhoff, G. A. and Sell, P.-J., *Angew. Makromol. Chem.* 1972, 21, 169.
- 33 Driegger, D., Neumann, A. W. and Sell, P. J., *Kolloid Z. u. Z. Polymere* 1965, 201, 52.
- 34 Sell, P. J. and Neumann, A. W., *Angew. Chem.* 1966, 78, 321.
- 35 Girifalco, L. A. and Good, R. J., *J. Phys. Chem.* 1957, 61, 904.
- 36 Good, R. J. and Elbing, E., *Ind. Eng. Chem.* 1970, 62, 55.
- 37 Good, R. J., *Adv. Chem. Ser.* 1964, 43, 74.
- 38 Good, R. J., in "Treatise on Adhesion and Adhesives, Vol. 1" (Patrick, R. L. Ed.) M. Dekker, 1967, p. 9.
- 39 Good, R. J., in "Contact Angle, Wetting, and Adhesion" (Mittal, K. L. Ed.) VSP, Utrecht, 1993, p. 3.

# 6

## EFFECTS OF SURFACE ENERGY ON THE MECHANICAL PROPERTIES OF COMPOSITES

A criterion for optimum adhesion was proposed in Chapter 5. It consists of maximising the wetting tension,  $\Delta F_i$ , which is the solution yielding maximum work of adhesion,  $W_a$ , under the condition of positive or null spreading coefficient,  $\lambda \geq 0$ . Two cases were examined separately:

- (i) for a given adhesive, what surface properties of the adherend allow an optimisation of adhesion, and
- (ii) what adhesive adheres optimally to a given substrate

In the case of composite materials, the surface energy of the fibres can easily be modified by, for instance, sizing, oxidising or chemically etching their surface. This corresponds to case (i), defined by conditions 5.19a and 5.19c, the solution of which is given by Equations 5.25 and 5.28 when the acid-base approach is considered.

The aim of this chapter is to experimentally verify the validity of Equation 5.19a on unidirectional fibre reinforced composite materials with modified fibre surface energy. Two systems are investigated: carbon fibre reinforced poly(ether-ether-ketone) and glass fibre reinforced poly(ether-imide). The fibres are modified chemically and characterised by measuring the contact angle formed by molten resin on the fibres. Various fibre treatments yield a wide range of contact angles, which are determined optically. Unidirectional fibre reinforced laminates are manufactured and transverse flexural strength is measured to characterise the interfacial strength of the laminates. The strength properties are plotted against the wetting parameters —work of adhesion,  $W_a$ , spreading coefficient,  $\lambda$ , and wetting tension,  $\Delta F_i$ . The results obtained in Chapter 5 state that, by modifying the solid surface energy, all three wetting parameters should be maximised to increase the adhesive strength (cf. §5.3.1). This will be clearly verified. It will also be shown that adhesion at the fibre-resin interface correlates with both the composite strength and the void morphology within the laminate after consolidation.

### 6.1 INTRODUCTION

Among the factors generally recognised to influence mechanical properties of composites is the adhesion of the matrix material to the fibre surface. The criterion proposed in

Chapter 5 suggests that adhesion is optimised when the wetting tension is maximum. In case the adhesive is kept unmodified, and only the substrate surface energy is varied, Equations 5.19a and 5.19c suggest that the work of adhesion,  $W_a$ , the spreading coefficient,  $\lambda$ , and the wetting tension,  $\Delta F_i$  (Equations 5.1, 5.4, and 5.7) which follow parallel curves (cf. Figure 5.2) are all correlated to the adhesive strength.

Various test methods have been developed to measure adhesive strength of adhesive joints or composite systems, including single fibre pull-out, fragmentation, peel, and micro-tension tests, as reviewed elsewhere [5–8]. These tests allow mechanical characterisation of the interfacial strength.

### 6.1.1 Surface energy parameters measurement

Thermodynamic characterisation of fibre-resin composite interfaces in terms of capillary measurements is difficult for several reasons. First, experiments must be performed at high processing temperatures (up to 400°C) for thermoplastic resins. Optical determination of the contact angle is difficult because the solid is in the form of a fine fibre, and any profile view of the meniscus reflects the influence of the fibre curvature [9]. Also, hydrodynamic effects may convolute the measurement of the fibre-resin contact angle because of the high viscosity of molten thermoplastic resins [10]. For the surface tension measurement by the Wilhelmy method, high microbalance sensitivity is required. Even when working with standard probe fluids at room temperature, this is a delicate operation because the diameter of the fibres typically used in composites is small ( $\text{Ø}7\text{--}20\ \mu\text{m}$ ) [11]. For these reasons, the fibre and resin surface energies are often determined *separately* using auxiliary probe fluids and in a temperature range in which the resin is solid. The work of adhesion between fibre and resin is then determined indirectly, a process which inevitably requires theory to relate the interfacial energy to the resin and fibre surface energies.

#### *Polar-dispersive approach*

One example of how capillary measurements have been used by many investigators to assess the solid surface characteristics of fibres and resins and then *indirectly* predict the work of adhesion between them proceeds as follows. For reasons of clarity, only the work of adhesion is considered in this discussion; it is clear that the same arguments can be applied to both the spreading coefficient and wetting tension. First, as presented in Chapter 5, one *assumes* that surface energies and the work of adhesion can be described as the sum of dispersive and polar components; a proposal first made by Fowkes [12, 13]:

$$\gamma_i = \gamma_i^d + \gamma_i^p \quad (5.9)$$

$$W_a = W_a^d + W_a^p \quad (6.1)$$

where  $d$  and  $p$  denote the dispersive and polar components. Fowkes proposed that only dispersion forces can operate across an interface, and that this interaction obeys a geometric mean relationship:

$$W_a = 2\sqrt{\gamma_s^d \gamma_i^d} \quad (6.2)$$

Since,

$$W_a = \gamma_l + \gamma_s - \gamma_{sl} \quad (5.1)$$

this leads to the following expression for the interfacial energy,

$$\gamma_{sl} = \gamma_s + \gamma_l - 2\sqrt{\gamma_s^d \gamma_l^d} \quad (6.3)$$

The dispersive component of the solid surface energy,  $\gamma_s^d$ , can be calculated by performing contact angle and interfacial tension measurements with a probe liquid of null polar component (i.e.  $x_l^p = 0$  and  $x_l^d = 1$ ) and of known surface tension and using Equations 6.2 or 5.1 together with 6.3. However, Equation 6.1 suggests that polar interactions across the interface may also be of significance. The polar component of the solid surface energy,  $\gamma_s^p$ , becomes accessible if a mixing rule is applied also to the *non*-dispersive interactions across an interface. Owens and Wendt [14] and Kaelble [15] suggested that the geometric mean mixing rule could be applied to both components (Equation 5.10). Wu [16a] proposed that the harmonic mean (Equation 5.11) or a combination of the two mixing rules could equally be used, yielding the following possible expressions for the work of adhesion:

$$W_a = 2\sqrt{\gamma_s^d \gamma_l^d} + 2\sqrt{\gamma_s^p \gamma_l^p} \quad (6.4a)$$

$$W_a = 4 \frac{\gamma_s^d \gamma_l^d}{\gamma_s^d + \gamma_l^d} + 4 \frac{\gamma_s^p \gamma_l^p}{\gamma_s^p + \gamma_l^p} \quad (6.4b)$$

$$W_a = 2\sqrt{\gamma_s^d \gamma_l^d} + 4 \frac{\gamma_s^p \gamma_l^p}{\gamma_s^p + \gamma_l^p} \quad (6.4c)$$

A value for  $\gamma_s^p$  is obtained by performing contact angle measurements with a probe liquid for which both the surface tension and polarity are known and using Equations 5.3 and 6.1. The objective, a predicted work of adhesion between a given fibre and resin, is attained using knowledge of the solid surface energy components and Equation 6.4 where the subscripts *s* and *l* denote the fibre and resin surfaces, respectively. The validity of this indirect approach to estimating the work of adhesion, however, is questioned by some authors, arguing that the "polar" component of surface tension and surface energy are better described by Lewis acid-base interactions than by dipole interactions [17]. Also, Kwok et al. [18] have questioned the validity of Equations 6.3 and 6.4 based on highly accurate contact angle measurements.

#### ***Lewis acid-base approach***

Good [19] proposed that the Wilhelmy method with probe liquids described above could also be applied to the acid-base definition. It was pointed out in Chapter 5 that the interface energy,  $\gamma_{sl}$ , may be better described by the introduction of an acid-base interaction parameter,  $\phi^{AB}$  (Equation 5.15), which, introduced into Equation 6.3, yielded the Good-Girifalco expression (Equation 5.8). The components of the work of adhesion can then be determined by measuring the contact angle between the solid surface



and a minimum of three liquid probes of known surface tension and  $LW$ -,  $A$ -, and  $B$ -components, and solving the system of three equations with three unknowns thus defined.

Another experimental technique that has been used to assess separately the surface energies for fibres and resins is inverse gas chromatography (IGC) [11, 20–24]. In this technique, the material of interest is packed into a gas chromatograph column, and a dry inert carrier gas, e.g.,  $N_2$ , is passed over the sample. Vapour probes are injected, and the adsorptive behaviour is monitored. The propensity of the surface to engage in dispersive interactions is determined with alkane probes, and a value for  $\gamma_s^d$  is obtained by relating the retention times of those probes to the dispersive component of the work of adhesion,  $W_a^d$  [11, 25]. A predicted value for  $W_a^d$  between a fibre and resin is calculated using the  $\gamma_s^d$  values and Equation 6.2. The Lewis acid-base component of the work of adhesion,  $W_a^{AB}$  is obtained by comparing the adsorptive behaviour of alkanes with probes of known functionality and using relationships previously proposed [16, 26]. The IGC technique allows expeditious surface characterisation of solids in geometries difficult to handle with capillary measurements, e.g., powders and fibres. The implementation of its results to yield complete values of  $W_a$ , however, requires theory which is still under development.

### **6.1.2 Originality of the present approach**

The present work focuses on the fibre-resin systems of carbon fibre reinforced poly(ether-ether-ketone) (PEEK) and glass fibre reinforced poly(ether-imide) (PEI). The former system has been studied by both Hodge et al. [27] and Nardin et al. [20–23] using indirect methods. Hodge et al. performed capillary measurements on PEEK and three different carbon fibre surfaces using standard probe fluids. The dispersive and polar components of the fibre and resin surface energies were estimated, and work of adhesion values at fibre-resin interfaces were predicted as above using the multiple probe liquid method proposed by Kaelble et al. [28, 29]. They reported a correlation between mechanical strength and the predicted work of adhesion. The measured work of adhesion, however, did not vary over a wide range, making it difficult to draw conclusions. Nardin et al. [20–23] separately characterised PEEK and differently treated carbon fibre surfaces with IGC, then predicted the level of interaction between the different fibre-resin combinations. Values for the dispersive and acid-base components of the work of adhesion were obtained as described above. Their values for the total work of adhesion were surprisingly high, ranging from 115 to 208  $mJ\cdot m^{-2}$ . While, they observed monotonic relationships between the predicted work of adhesion and both yield strength and elongation at yield, interlaminar shear strength did not correlate with the predicted work of adhesion.

Bucher and Hinkley [30] and Mayer et al. [31] have reported *direct* measurements of fibre-resin interfacial properties and attempted to relate these to the mechanical properties of continuous fibre composites. Bucher and Hinkley studied the carbon fibre reinforced poly(ether-ketone-ketone) (PEKK) system, measuring contact angles of liquid resin on three commercial carbon fibres and comparing these results with mechanical properties of unidirectional composites. The work of adhesion, however, varied by only 3%, as calculated using Equation 5.3 and the contact angle range of 3 to 20 degrees. Also, they allowed a variation in interfacial area by using different fibre diameters, ranging from 6.2 to 7.9  $\mu m$ . This corresponds to a variation of 50 % in interfacial area at

constant fibre volume fraction, a change expected to have profound effects on mechanical properties [32]. Finally, in their optical profile method for determining contact angles [9], insufficient time was allowed for their liquid resin drops to reach equilibrium; the measured values were reported as "apparent contact angles". They observed scattered results for interlaminar fracture toughness and a monotonically decreasing relationship between apparent contact angle and transverse flexural yield strength.

Finally, Mayer et al. [31] sintered poly(ethylmethacrylate) powder onto carbon fibres oxidised at different temperatures and measured the contact angle as a function of time and treatment temperature. The sintering time allowed, however, did not provide an equilibrium contact angle, and they reported contact angle differences between surfaces of less than 8 degrees in all cases, corresponding to only a maximum of 9 percent change in the work of adhesion. Direct comparison of these contact angle data with the mechanical properties of weft knitted composites was not made, but it was reported that the oxidative treatment increased strength by up to 25 %.

Investigations to date into the relationship between the mechanical properties of fibre-matrix composites and the work of adhesion for the fibre-matrix interface have suffered a number of shortcomings as noted above and have not always produced convincing correlations. It is therefore the objective of the present work to seek results overcoming these difficulties. The wetting parameters, work of adhesion,  $W_a$ , spreading coefficient,  $\lambda$ , and wetting tension,  $\Delta F_i$ , are to be determined *directly* through the equations

$$W_a = \gamma_l(1 + \cos \theta) \quad (5.3)$$

$$\lambda = \gamma_l(\cos \theta - 1) \quad (5.5)$$

$$\Delta F_i = \gamma_l \cos \theta \quad (6.5)$$

using measurements of the equilibrium contact angle between molten resin drops and the surfaces of chemically treated carbon and glass fibres, ample equilibration time being given. It is clear that this technique can only be applied in the range of validity of the Young Equation 5.2, i.e. for  $0 \leq \theta \leq \pi$ . Chemical treatments of the fibre surfaces are used to provide a large range of contact angles and thus significantly alter the work of adhesion at the fibre-resin interface. Finally, the composite systems to be compared will differ *only* in their interfacial properties. The experimental methods used also permit characterisation of the void topology in the composites, providing an opportunity for interesting subsidiary observations on the effect of contact angle on inclusion formation. The complexities involved in measuring contact angles on cylindrical fibres are discussed.

## 6.2 MATERIALS AND METHODS

### 6.2.1 Fibres and fibre surface modification

The fibre-resin systems selected for this work were FIT powder coated yarns, i.e. bundled fibres surrounded by a resin sheath with fine resin powder dispersed throughout the bundle (cf. §2.2.3). Two fibre-resin systems were studied: carbon fibres (CF) (T300,

Soficar) with PEEK (grade 150, ICI) and glass fibres (GF) (E-type, Owens-Corning) with Poly(ether-imide) (PEI) (Ultem 1000, G. E. Plastics). The use of commercially available FIT yarns, where the matrix powder and the reinforcement fibres are already in intimate contact, did not allow fibre surface modifications such as plasma treatment [33, 34] or fibre surface oxidation [35]. The surface of the fibres was altered by chemically removing the sizing deposited on the fibre surface during manufacture. This sizing is applied by the manufacturers for two reasons [36]: (i) the thin film formed around the fibre protects it from abrasion when the yarns pass through looms, and (ii) it improves the adhesion between the fibre and the resin. The second reason is disputed by Vu-Khanh and Denault [37] who suggested that the processing temperature for PEEK is well above the degradation temperature of the sizing agents. The treatments summarised in Table 6.1 were applied to the fibres to modify their surface energy.

**Table 6.1: Chemical treatments of FIT systems**

Carbon fibre-PEEK	
System	Treatment conditions
C1	unmodified
C2	6 h in methyl ethyl ketone (MEK) at 25°C
C3	6 h in MEK at 50°C, then 2 h in CH <sub>3</sub> OH at 25°C
C4	6 h in MEK then 12 h in CH <sub>2</sub> Cl <sub>2</sub> at 50°C, 2 h in CH <sub>3</sub> OH at 25°C

Glass fibre-PEI	
System	Treatment conditions
G1	unmodified
G2	6 h in 0.25M HCl at 25°C, 2 h in distilled water
G3	6 h in 0.25M HCl at 50°C, 2 h in distilled water

Chemical treatments were performed by first dipping the FIT fibre bundles into the chemical solution vertically with the tips protruding from the solution and allowing 15 min for the treatment solution to wick up the fibres. They were then totally immersed and agitated for the remainder of the time indicated in Table 6.1. After treatment, the fibre bundles were placed in a vacuum oven at 80°C for 24 h to evaporate remaining solvent and moisture. Obviously, no improvement of the adhesion is expected from these chemical treatments; on the contrary, the aim here is not to improve but only to alter the surface energetics, and show its influence upon mechanical properties. The chemical treatment did not alter the resins properties.

### 6.2.2 Contact angle measurement

The direct determination of the wetting parameters for a fibre-resin system requires measurement of the contact angle of molten resin against the fibre and use of Equations 5.3, 5.5, and 6.5. However, the measurement of contact angles of liquid drops on cylindrical surfaces is complicated by competing curvatures, a phenomenon studied by various authors [9, 38, 39]. A liquid drop resting on a fibre can adopt either

the stable geometry of an axi-symmetric unduloid or the metastable geometry of the “clam-shell” [40], as shown in Figures. 6.1a and 6.1b. The unduloid form prevails when the drop is large relative to the fibre and the contact angle is relatively low. Carroll [41] defined the transformation of an unduloid drop into a clam-shell drop as the “roll-up” process. For both geometries, the tangent optical method is inappropriate, and it is more accurate to find an analytical expression dependent on the equilibrium geometry of the drop.

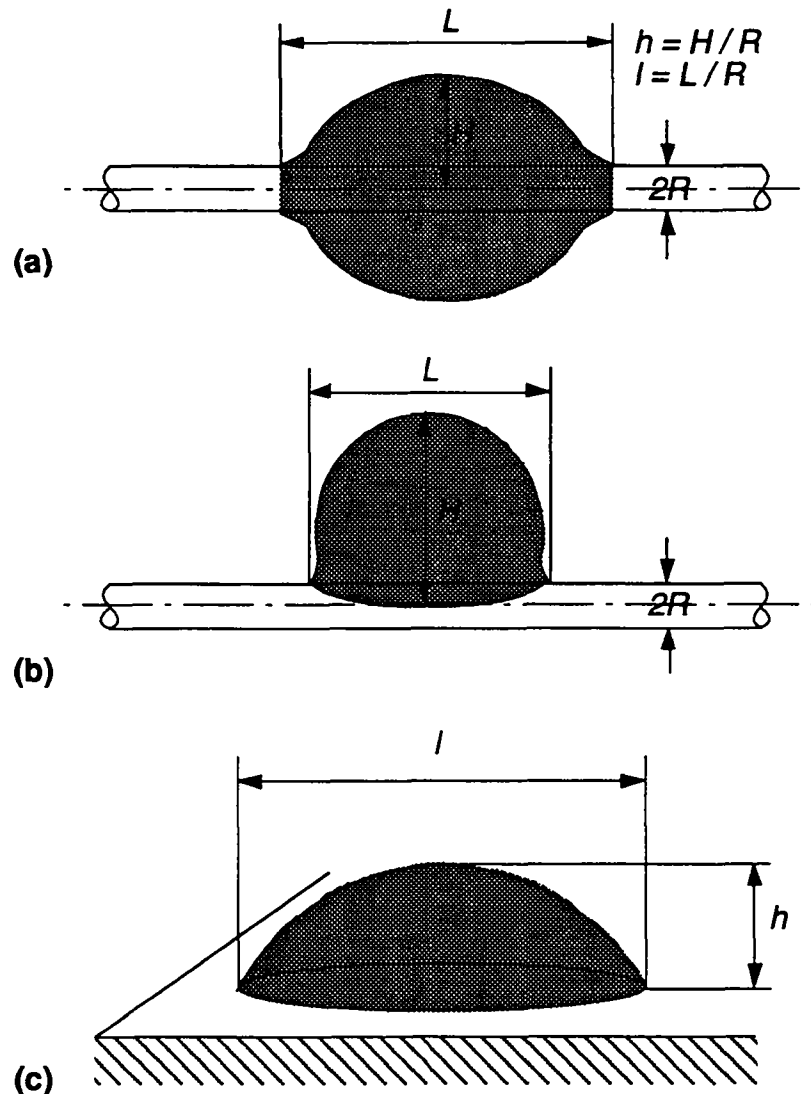


Figure 6.1 Various geometries for a liquid drop on a solid surface: (a) cylindrical surface (unduloid), low contact angle; (b) cylindrical surface, high contact angle (clam-shell); and (c) flat surface.

A numerical solution for the unduloid geometry was proposed simultaneously by Carroll [38] and Yamaki and Katayama [39], and later by Wagner [9]. In this study, the solution proposed by Wagner [9] was used. For a given dimensionless height,  $h = H/R$ ,

and dimensionless diameter,  $l = L/R$ , it gives a value of the contact angle,  $\theta$  (see Figure 6.1a for variable definition).

For clam-shell drops, the apparent contact angle of which is a function of drop volume, Walliser [40] proposed a semi-empirical method to measure contact angles. The case of a given liquid forming an angle  $\theta$  with a flat surface is first considered. When gravity effects are negligible, i.e., low Bond number values, the contact angle is independent of the drop volume and is given by

$$\theta = 2 \arctan\left(2 \frac{h}{l}\right). \quad (6.6)$$

Thus the dimensionless height of the drop,  $h$ , is proportional to its dimensionless diameter,  $l$ . For a clam-shell drop sitting on a cylindrical fibre, Walliser suggested that the curve  $h-l$  can be well-fit by the relation

$$h = a \cdot l^2 + b \cdot l, \quad (6.7)$$

where  $a$  and  $b$  are statistical regression results. He observed that this curve, for a given set of materials, was tangent at the origin to the linear  $h-l$  curve obtained for the liquid sitting on a flat surface (see Figure 6.1c). This is the condition necessary to admit Equation 6.7 as a satisfactory form because the origin is defined as the flat surface limit, i.e.,  $h, l \rightarrow 0$ . It is easily shown that the value of the curve-fit slope at the flat surface limit is  $b$  and that this value can be substituted for the height-width ratio in Equation 6.6 to yield

$$\theta = 2 \arctan(2b). \quad (6.8)$$

Geometric data for drops of various sizes can thus be collected and used to estimate the contact angle for the liquid against a cylindrical surface. This approach is only a suggestion and should be validated. It seems, however, the most appropriate available measuring technique for the clam-shell drop geometry.

A few yarns of each of the systems listed in Table 6.1 were cut open and placed into an oven at the processing temperature (390°C for CF-PEEK and 340°C for GF-PEI) for sintering. The drops were allowed four hours to attain an equilibrium contact angle between the molten resin and the fibre surface, but the drop shape was found not to vary with time after two hours. The fibres were then rapidly removed from the oven and quenched at room temperature to "freeze" the molten resin in place. The captured drop geometry is considered representative of the thermodynamic state *at the processing temperature*. Images of the resin on the treated surfaces were obtained using scanning electron microscopy (SEM).

Values of  $h$  and  $l$  were measured on a minimum of fifteen drops for each system. In the case of unduloid drops, contact angle values were determined using Figure 3 in [9]. In the case of clam-shell drops, an  $h-l$  plot was constructed. Care was taken to select a wide range of drop volumes, and a best fit of Equation 6.7 was determined using the Marquart-Levenberg algorithm, as suggested by Walliser [40]. The contact angle was then calculated with Equation 6.8. The results were in agreement with angles measured using the tangent optical method for small drop volumes.

### 6.2.3 Laminate manufacturing and testing

FIT yarn was wound around an 80 mm-radius cylinder and melted together in spots. Squares of 50x50 mm<sup>2</sup> were cut and stacked to form a “towpreg” as described in §4.3.3. Various towpreg thicknesses were manufactured and tested: CF-PEEK laminates with 10, 12 and 15 plies, and GF-PEI laminates with 12 and 16 plies. The mould, a square match die mould of 50x50 mm<sup>2</sup>, was heated to the processing temperature (390°C for CF-PEEK, and 340°C for GF-PEI) and the towpreg was placed into the mould and left for 15 min to reach iso-thermal conditions. A pressure of 5 MPa was then applied and the mould displacement recorded with an LVDT. After 7 min, the mould was cooled at approximately 60°C·min<sup>-1</sup> under constant pressure. After 5 min of cooling, the mould was opened and the laminate extracted. The weight, thickness, void content (ASTM D792) and fibre content (matrix burn out, only for GF-PEI) were measured. All the laminates showed less than 3 % porosity. The measured fibre volume fraction of GF-PEI and CF-PEEK was 65 % and 67 %, respectively.

Transverse flexural strength (ASTM-790M) was chosen as a mechanical test representative of the adhesion properties of the composite. It is defined in [30] as a “means of characterising the tensile strength of the fibre-matrix interfacial bond” of a composite. Force-deflection traces are obtained and values of the transverse modulus,  $E_b$ , yield stress,  $\sigma_y$ , and elongation at yield,  $\varepsilon_y$ , at the bottom surface are calculated using

$$E_b = \frac{l^3 m}{4wd^3} \quad (6.9)$$

$$\sigma_y = \frac{3P_y l}{2wd^2} \quad (6.10)$$

$$\varepsilon_y = \frac{6D_y d}{l^2}, \quad (6.11)$$

where  $l$  is the beam span,  $w$  and  $d$  are the width and depth of the sample, respectively,  $P_y$  and  $D_y$  are the load and displacement at yield, respectively, and  $m$  is the slope of the  $P$ - $D$  curve. The 50x50 mm<sup>2</sup> laminates described were cut into three 10x50 mm<sup>2</sup> bands, with the fibres transverse to the length. These were randomly tested with a Zwick mechanical tester using a beam span of 37 mm and a cross-head speed of 0.8 mm·min<sup>-1</sup>. The stress-strain curves were recorded and Equations 6.9 through 6.11 were used to calculate mechanical strength parameters. The fracture surface of the mechanically tested CF-PEEK samples were studied with SEM. Polished cross-sections were prepared and used to analyse the void topology with SEM.

## 6.3 RESULTS AND DISCUSSION

### 6.3.1 Fibre-matrix contact angle

The only systems forming axi-symmetric unduloid drops were the CF-PEEK samples, C1 and C2. The CF-PEEK systems C3, C4, and all of the GF-PEI systems formed clam-shell drops. Figure 6.2 shows micrographs of PEEK resin drops in contact with carbon fibres for the four treatments used on those fibres.

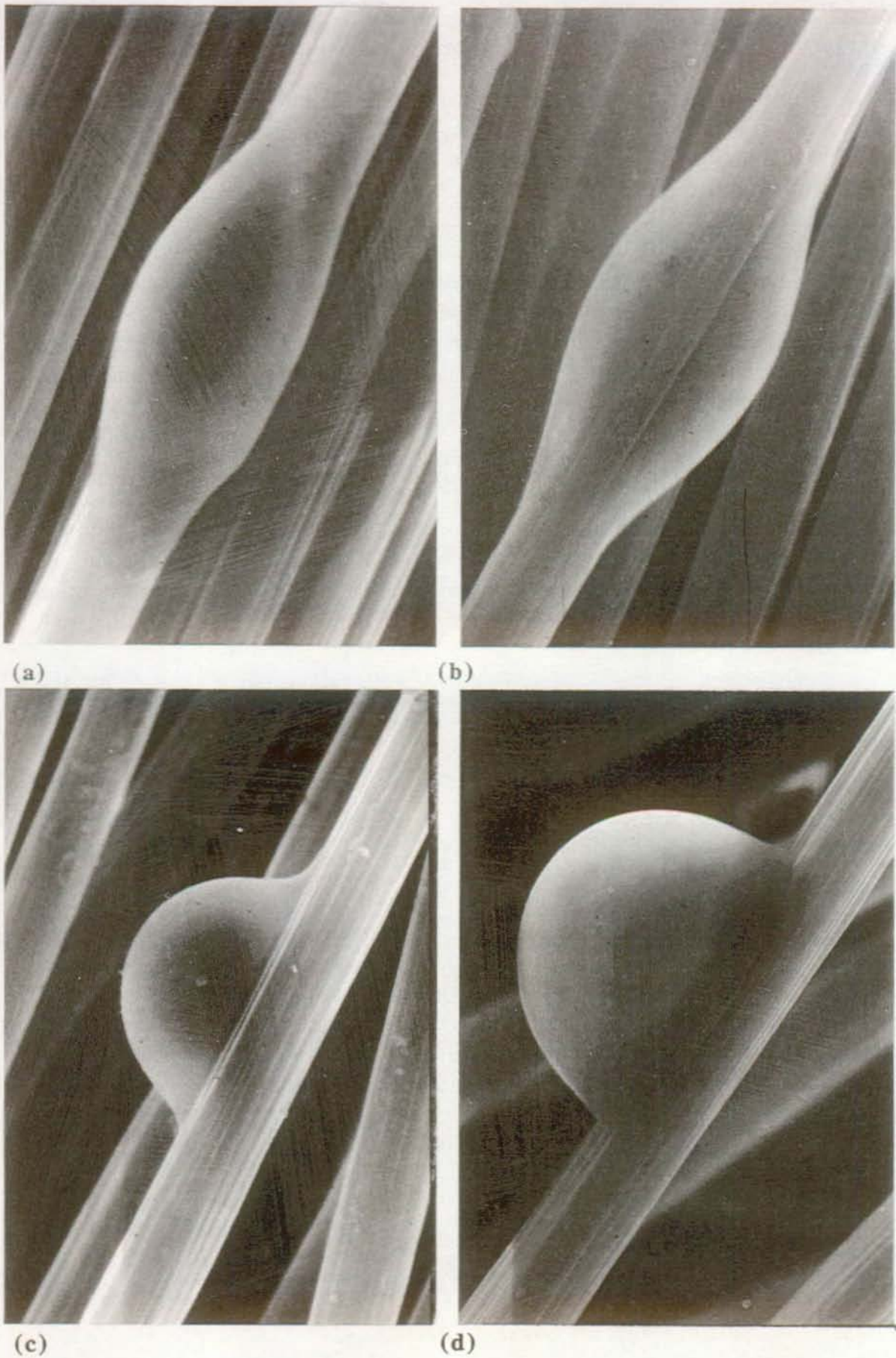


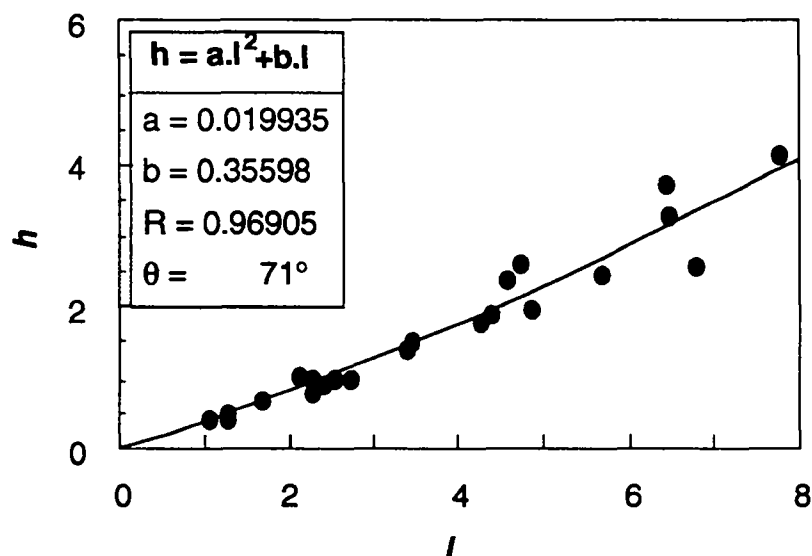
Figure 6.2: Micrographs of PEEK in contact with treated carbon fibres: (a) C1,  $\theta = 1^\circ$ ; (b) C2,  $\theta = 10^\circ$ ; (c) C3,  $\theta = 54^\circ$ ; and (d) C4,  $\theta = 80^\circ$ .

Determination of a standard deviation was only possible with the unduloid drops, because one drop picture corresponds to one contact angle measurement. The specific work of adhesion,  $W_a/\gamma$ , spreading coefficient,  $\lambda/\gamma$ , and wetting tension,  $\Delta F_i/\gamma$ , were calculated from contact angle data using Equations 5.3, 5.5, and 6.5. These quantities are, of course, directly proportional to the wetting parameters when the wetting fluid is not changed, as is the case here. Table 6.2 summarises the results of contact angle measurements and calculated values of the specific wetting parameters. For clam-shell drops, all of the drop measurements are collected on one graph to obtain a single value of the contact angle. An example of an  $l$ - $h$  plot used to measure the contact angle is given in Figure 6.3, with the values of  $a$  and  $b$  of Equation 6.7 determined using the Marquart-Levenberg algorithm.

Table 6.2: Contact angle measurement results

System	$\theta$ [deg]	$W_a/\gamma$	$\lambda/\gamma$	$\Delta F_i/\gamma$	Drop shape
C1	$1 \pm 2$	2.00	0.00	1.00	unduloid
C2	$10 \pm 5$	1.99	-0.01	0.99	unduloid
C3	54	1.59	-0.41	0.59	clam-shell
C4	80	1.17	-0.83	0.17	clam-shell
G1	66	1.41	-0.59	0.41	clam-shell
G2	71	1.33	-0.67	0.33	clam-shell
G3	127	0.40	-1.60	-0.60	clam-shell

The results listed in Table 6.2 show that the chemical treatments altered the surface energy of the fibres by removing the sizing from the surface. This increased the value of the contact angle formed by the molten resin and hence decreased the value of the specific work of adhesion.

Figure 6.3:  $l$ - $h$  plot for G2 used to determine contact angle for clam-shell drops [40].



### 6.3.2 Transverse flexural strength

The macroscopic values of  $\sigma_y$  and  $\epsilon_y$  showed a strong dependence on sample thickness. This dependence was attributed to a difference in internal stresses built up during the rapid cooling of the laminate. The centre of the laminate cools faster in a thinner section, giving potential for larger build up of internal stresses and, therefore, yielding lower values of yield stress and strain. The bending modulus was independent of number of plies. Table 6.3 shows the values of  $\sigma_y$  and  $\epsilon_y$  as a function of the number of plies,  $n$ , for the untreated CF-PEEK and GF-PEI samples (C1 and G1).

The ply dependence was well-fit by straight lines, i.e.,  $\sigma_y = a_1 \cdot n + b_1$  and  $\epsilon_y = a_2 \cdot n + b_2$ , and therefore a basis was chosen for the number of plies. The stress and strain values were then normalised using

$$\sigma_y(n_{base}) = a_1 \cdot (n_{base} - n) + \sigma_y(n) \quad (6.12)$$

$$\epsilon_y(n_{base}) = a_2 \cdot (n_{base} - n) + \epsilon_y(n). \quad (6.13)$$

The values of  $a_1$ ,  $a_2$ ,  $n_{base}$  and the coefficients of correlation,  $r_1$  and  $r_2$ , are also reported in Table 6.3. The basis of 12 plies corresponded to thicknesses of approximately 2.3 mm and 2.6 mm for the CF-PEEK and GF-PEI systems, respectively. Henceforth, all the values of  $\sigma_y$  and  $\epsilon_y$  presented are values normalised with Equations 6.11 and 6.13 using the parameters listed in Table 6.3.

**Table 6.3: Thickness dependence of  $\sigma_y$  and  $\epsilon_y$**

System	n	$\sigma_y$ [MPa]	$\epsilon_y$ [%]
C1	8	32	0.90
	10	38	0.94
	15	47	1.18
$a_1$ (MPa/n) = 1.99		$r_1 = 0.988$	
$a_2$ (%/n) = 0.554		$r_2 = 0.990$	
G1	8	19	0.40
	12	28	0.47
	16	33	0.60
$a_1$ (MPa/n) = 1.78		$r_1 = 0.987$	
$a_2$ (%/n) = 0.024		$r_2 = 0.978$	

Figure 6.4 compares examples of the normalised stress-strain curves of the four CF-PEEK systems, reflecting the obvious differences in yield stress and yield strain observed experimentally. Yield stress of CF-PEEK samples C1, characterised by a null contact angle,  $\theta$ , is about 30% higher than that of the C4 treatment, characterised by a contact angle of  $80^\circ$ , reflecting the surface energy effects on composite strength. The values of the yield stress and yield strain and the bending modulus for the different systems and treatments studied are summarised in Table 6.4.

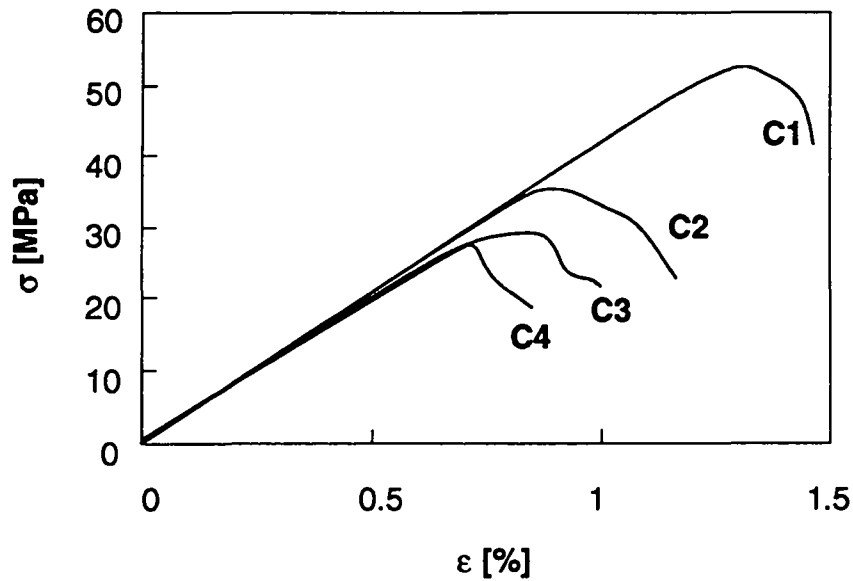


Figure 6.4: Typical stress-strain curves for the carbon fibre-PEEK laminates.

Table 6.4: Normalised transverse flexural strength values ( $n_{base} = 12$ )

Carbon fibre-PEEK			
System	$\sigma_y$ [MPa]	$\epsilon_y$ [%]	$E_b$ [GPa]
C1	$41.3 \pm 6.8$	$1.04 \pm 0.16$	$4.4 \pm 0.4$
C2	$36.1 \pm 3.9$	$0.98 \pm 0.13$	$4.3 \pm 0.5$
C3	$29.9 \pm 3.9$	$0.76 \pm 0.15$	$4.2 \pm 0.5$
C4	$27.8 \pm 1.5$	$0.74 \pm 0.08$	$4.4 \pm 0.4$
Glass fibre-PEI			
System	$\sigma_y$ [MPa]	$\epsilon_y$ [%]	$E_b$ [GPa]
G1	$26.6 \pm 3.4$	$0.49 \pm 0.04$	$6.3 \pm 0.8$
G2	$23.4 \pm 2.5$	$0.54 \pm 0.07$	$6.2 \pm 0.4$
G3 #1	$16.8 \pm 1.8$	$0.39 \pm 0.06$	$4.8 \pm 0.7$
G3 #2	$32.6 \pm 0.8$	$0.66 \pm 0.03$	$6.3 \pm 0.1$

CF-PEEK fracture surfaces for the four different treatments are presented in Figure 6.6. In the untreated laminates, C1, the fracture propagated mainly through the resin, exposing little bare fibre surface. This suggests that the failure was cohesive. The resin is severely torn and strained, likely resulting in higher fracture energies. The area density of bare fibres increases with the severity of the chemical treatments, following the sequence C2, C3, and C4. By contrast to the untreated laminates, the C4 laminates exhibit surfaces in which the print of the fibre crenellation is still clearly visible, indicating a weak interface. The GF-PEI laminates all showed a high density of bare fibres and are quite similar to each other.

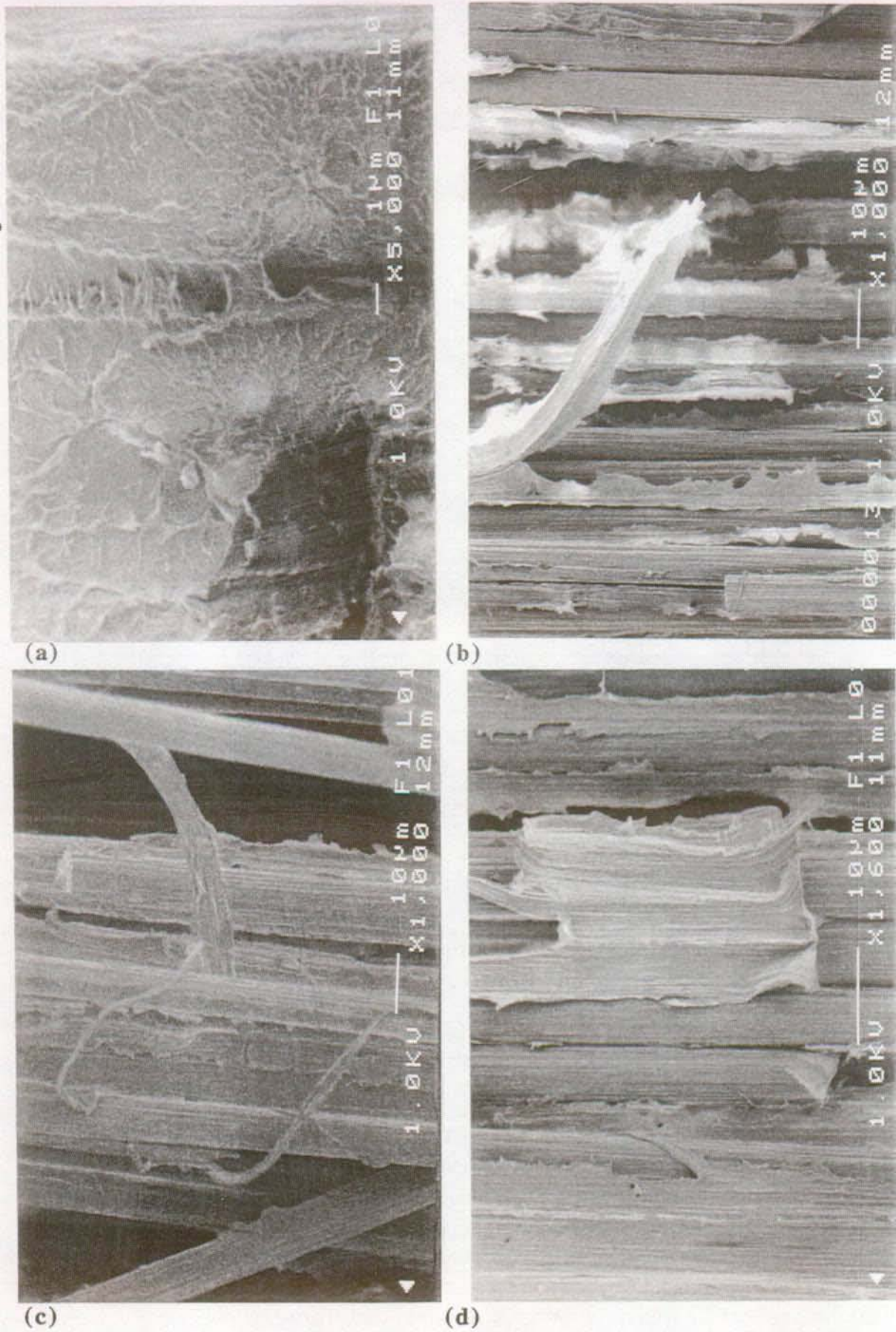
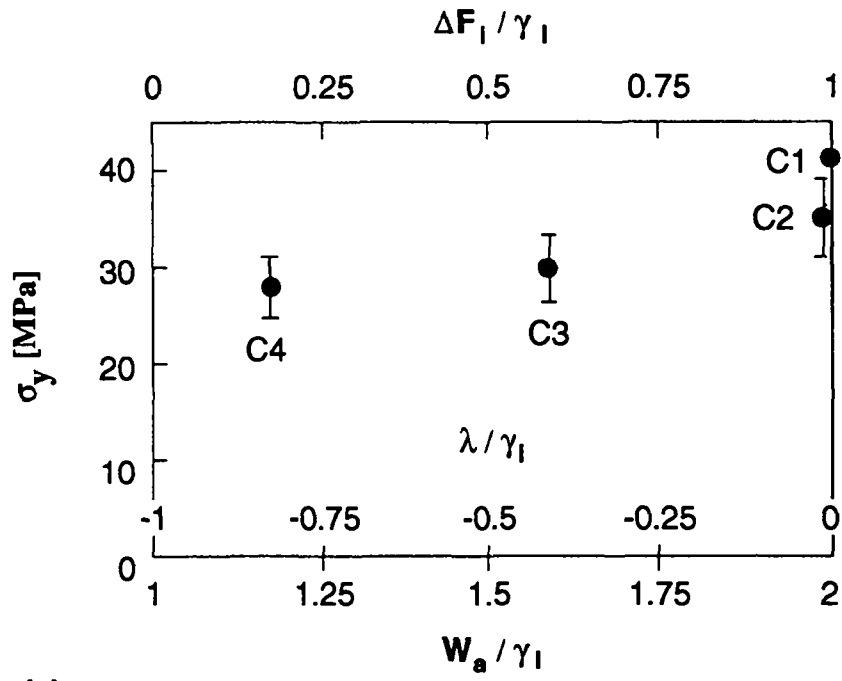
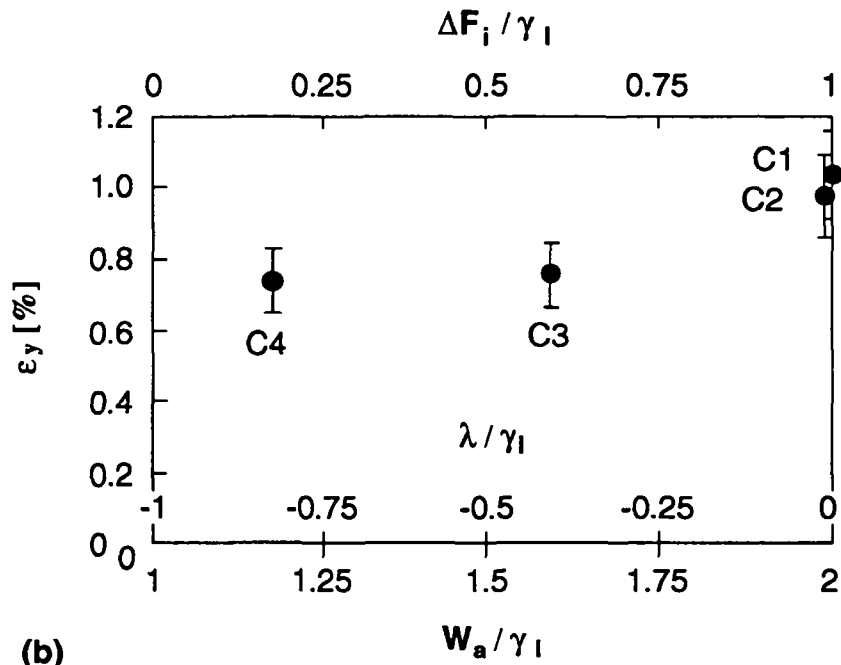


Figure 6.5: Fracture surfaces for carbon fibre-PEEK laminates: (a) C1,  $\theta = 1^\circ$ ; (b) C2,  $\theta = 10^\circ$ ; (c) C3,  $\theta = 54^\circ$ ; and (d) C4,  $\theta = 80^\circ$ .

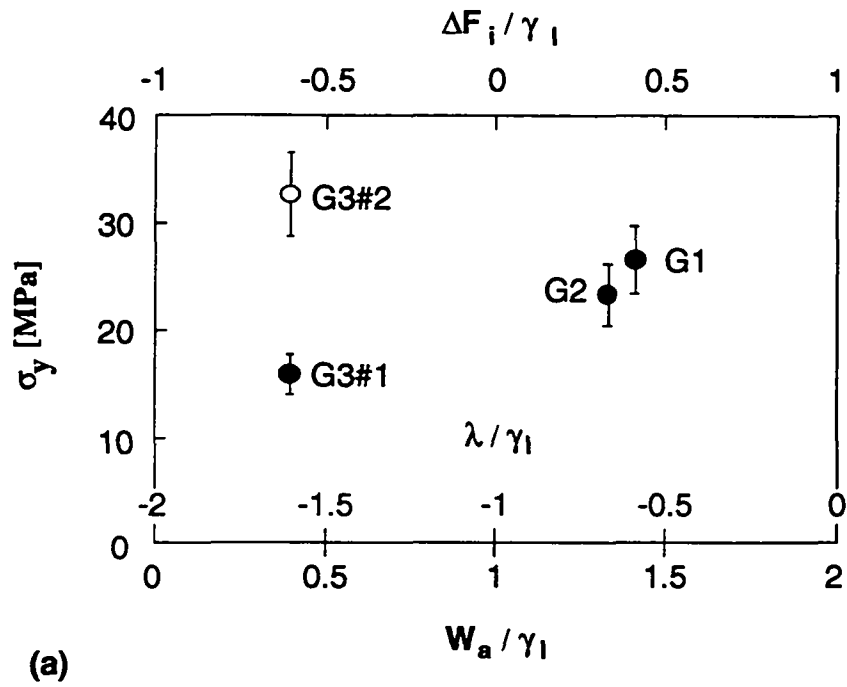


(a)

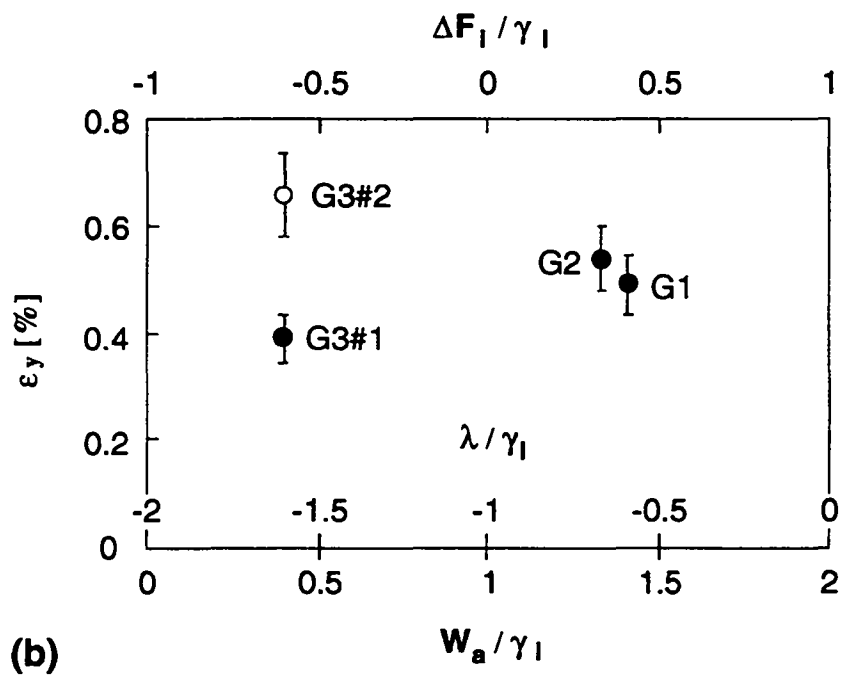


(b)

Figure 6.6: Carbon fibre-PEEK system: (a) yield stress versus specific work of adhesion; and (b) elongation at yield versus specific work of adhesion.



(a)



(b)

Figure 6.7: Glass-fibre-PEI system: (a) yield stress versus specific work of adhesion; and (b) elongation at yield versus specific work of adhesion.

### 6.3.3 Wetting parameters/interfacial strength relationship

Figures 6.6 and 6.7 demonstrate the apparent relationship between composite mechanical properties and the specific wetting parameters: work of adhesion,  $W_a/\gamma$ , spreading coefficient,  $\lambda/\gamma$ , and wetting tension,  $\Delta F_i/\gamma$ . It can be seen that as proposed in Chapter 5, there is a monotonically increasing relationship between the fibre-matrix adhesive strength and the wetting parameters. The relationship between mechanical interfacial strength and the thermodynamic work of adhesion is intuitive, because both characterise the energy required to destroy an interface and create new surfaces. The work of adhesion, however, corresponds to reversible thermodynamic conditions while measured mechanical properties include phenomena such as void volume in the composite, viscoelasticity, etc. The mechanical strength will obviously be decreased by void volume, particularly if the voids are at the interface and one would expect the void topology to be a function of the interfacial energy. Wu [16b] has related the presence and size of inclusions to the contact angle via the specific spreading coefficient,  $\lambda$ : a more negative  $\lambda$  will lead to a higher flaw density at the interface. During composite manufacturing, a finite quantity of air will always be trapped and will remain in the part after processing. Under favourable wetting conditions, i.e. positive  $\lambda$ , the area of the solid/air interface will be minimised and any entrapped air will tend to coalesce in regions away from the fibres. This is clear in Figure 6.8a. Under poor wetting conditions, i.e. more negative  $\lambda$ , the large contact angle provides no mechanism to expel the air from the surface and the void space will be concentrated at the fibre-resin interface, as shown in Figure 6.8b. The porosity of the composites did not vary significantly, and the low value, about 3%, likely did not greatly affect mechanical strength properties.

The additive effect of these two mechanisms —molecular interaction across the interface ( $=f(W_a)$ ), and presence of flaw at the interface ( $=f(\lambda)$ )— supports the choice made in Chapter 5 of maximising the wetting tension as a criterion for the characterisation of interfacial adhesion. Since the wetting tension is the arithmetic mean of the work of adhesion and the spreading coefficient, it takes both effects into account.

### 6.3.4 Discussion

Our results can be compared with those of Nardin et al. [20–23], who studied the adhesion of carbon fibre-PEEK systems; using the same fibre type (T300 from Soficar) as the present study but with different surface treatments. As described, the values they reported for the predicted work of adhesion varied from 115 to 208  $\text{mJ}\cdot\text{m}^{-2}$  for their different fibre surfaces. Their IGC measurements, made between 40 and 100°C, were used to obtain these values. Introducing these values into Equation 5.3, and using  $\gamma = 44.7 \text{ mJ}\cdot\text{m}^{-2}$  [42], yields *zero* contact angles for all their systems, i.e. the resin would spread spontaneously on all the fibres investigated. These results are in disagreement with ours; we found finite contact angles for all of our treatments. The difference between our respective results can be explained by the different techniques used. In this study, the wetting parameters were measured directly from fibre-matrix contact angle and Equations 5.3, 5.5, and 6.5. Nardin et al. [20–23] used IGC measurements to predict the level of interaction between the different fibre-resin combinations.

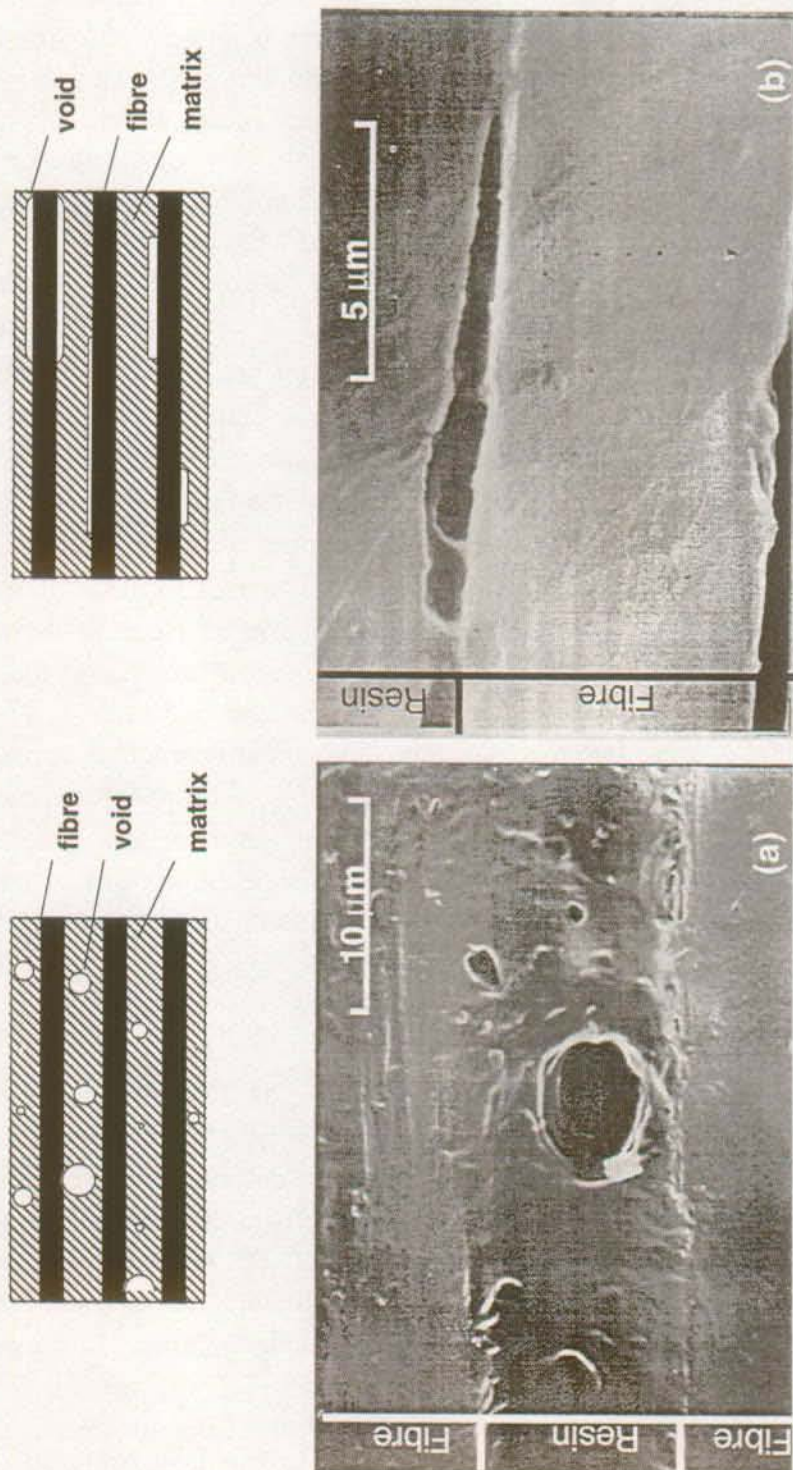


Figure 6.8: Laminate void topology: (a) C1,  $\theta = 1^\circ$ ,  $\Delta F_i / \eta = 1$ ; and (b) C4,  $\theta = 80^\circ$ ,  $\Delta F_i / \eta = 0.17$ .

In predicting their values for the work of adhesion, Nardin et al. used a relationship proposed by Fowkes [17] that calculates the Lewis acid-base component of the work of adhesion as the product of the acid-base enthalpy of adsorption,  $\Delta H^{ab}$ , the number of acid-base adduct sites per unit area,  $n^{ab}$ , and an entropic correction factor,  $f$ . The theory supporting this characterisation technique, however, is still under development, and subject to several uncertainties.  $\Delta H^{ab}$  is not determined directly, but from a predictive model based on the adsorption of functionally specific IGC probes on the surfaces of interest. The value for  $n^{ab}$  is not determined independently, but is presumably obtained from a liquid packing density. The entropic correction factor is assumed to be unity, although it has been demonstrated that the value of  $f$  may range as low as 0.1 for some systems [43]. These considerations may partially explain the very high values, compared to our results, of the apparent work of adhesion obtained in their work. It should also be noted that the measurements of Nardin et al. for the carbon fibre-PEEK system were made at 40 to 100°C while the present ones were made at 390°C.

The glass fibre-PEI systems gave results less clear than those of the carbon fibre-PEEK systems. Although the chemical treatments listed in Table 6.2 can be considered as successful for the large range of contact angles obtained, the mechanical results of GF-PEI laminates were more scattered than for CF-PEEK laminates. Particularly the samples cut from two different GF-PEI laminates treated in warm acid, G3#1 and G3#2, yielded different mechanical properties (cf. Table 6.4 and Figure 6.7). No reason was found to explain this difference.

Finally, there are factors regarding composite manufacture that this study has not considered. Most importantly, previous investigators have discussed the formation of an "interphase" zone that forms at the fibre-resin interface, the properties of which are dependent on the cooling rate used in composite manufacture and, possibly, interfacial energy [22, 37].

## 6.4 SUMMARY

The experiment presented here shows that the mechanical properties of a given composite system (e.g., CF-PEEK, GF-PEI) processed in the same conditions, can be greatly altered by modifying the surface energetics of the fibres. Interfacial properties of fibre reinforced composites can be characterised directly from fibre-matrix contact angle measurement—a simple and reliable technique, provided the contact angle is larger than zero. Transverse flexural strength was measured to characterise the interfacial strength. Yield stress of CF-PEEK was almost doubled from system C4 ( $\theta = 80^\circ$ ) to system C1 ( $\theta = 1^\circ$ ) (cf. Table 6.4). These results demonstrate the important influence of surface energy effects on fibre-matrix bond strength and on mechanical properties of a composite. Furthermore, they are in agreement with Equation 5.19a presented in Chapter 5 which proposes that physical adhesion in a composite material can be improved by modifying the fibre surface energy such as to increase the wetting parameters, work of adhesion,  $W_a$ , spreading coefficient,  $\lambda$ , and wetting tension,  $\Delta F_i$ .



## 6.5 REFERENCES

- 1 Dupré, A., "Théorie mécanique de la chaleur", Gaitjoer-Villars, Paris, 1869.
- 2 Young, T., *Phil. Trans.* 1805, **95**, 82.
- 3 Jacob, P. N. and Berg, J. C., *J. Adhesion* 1995, (in press).
- 4 Mittal, K. L., in "Adhesion Science and Technology" (Lee, L.-H., Ed.) Plenum Press, New-York, 1975, p. 129.
- 5 Drzal, L. T. and Herrera Franco, P.J., in "Engineered Materials Handbook" (Dostal, C. A., Ed.) ASM Int., 1990, p. 391.
- 6 Favre, J. P., *Interfacial Phenomena in Composite Mater.* '89 1989, p. 7.
- 7 Piggott, M. R. and Reboledo, M. M., *34th Int. SAMPE Symp.* 1989.
- 8 Piggott, M. R., *Comp. Sci. Tech.* 1991, **42**.
- 9 Wagner, H. D., *J. Appl. Phys.* 1990, **67**, 1352.
- 10 Seeberg, J. E. and Berg, J. C., *Chem. Eng. Sci.* 1992, **47**, 4456.
- 11 Schultz, J., Lavielle, L. and Martin, C., *J. Adhesion* 1987, **23**, 46.
- 12 Fowkes, F. M., *J. Phys. Chem.* 1962, **66**, 382.
- 13 Fowkes, F. M., *Ind. Eng. Chem.* 1964, **56**, 40.
- 14 Owens, D. K. and Wendt, R. C., *J. Appl. Polymer Sci.* 1969, **13**, 1741.
- 15 Kaelble, D. H., *J. Adhesion* 1970, **66**, 2.
- 16a Wu, S., "Polymer Interface and Adhesion", Marcel Dekker, Inc., New-York, 1982, p.101.
- 16b *Ibid.*, p. 361.
- 17 Fowkes, F. M., *J. Adhesion Sci. Tech.* 1987, **1**, 7.
- 18 Kwok, D. Y., Li, D. and Neumann, A. W., *Langmuir* 1994, **10**, 1323.
- 19 Good, R. J., in "Contact Angle, Wetting and Adhesion" (Mittal, K. L., Ed.) VSP, Utrecht, 1993, p. 3.
- 20 Nardin, M., Asloun, E. M. and Schultz, J., *Polym. Adv. Technol.* 1991, **2**, 109.
- 21 Nardin, M., Asloun, E. M. and Schultz, J., *Polym. Adv. Technol.* 1991, **2**, 116.
- 22 Nardin, M., Asloun, E. M., Muller, F. and Schultz, J., *Polym. Adv. Technol.* 1991, **2**, 161.
- 23 Nardin, M., Asloun, E. M., Schultz, J., Brandt, J. and Richter, H., *Polym. Adv. Technol.* 1991, **2**, 171.
- 24 Schultz, J. and Lavielle, L., *ACS Sympos.* 1989, 391, p. 185.
- 25 Dorris, G. M. and Gray, D. G., *J. Colloid & Interface Sci.* 1980, **77**, 353.
- 26 Saint-Flour, C. and Papirer, E., *J. Colloid & Interface Sci.* 1982, **91**, 69.
- 27 Hodge, D. J., Middlemiss, B. A. and Peacock, J. A., *Mat. Res. Soc. Symp. Proc.*, 1990, 170, p. 327.
- 28 Kaelble, D. H., Dynes, D. J. and Cirlin, E. H., *J. Adhesion* 1974, **6**, 23.
- 29 Dynes, P. J. and Kaelble, D. H., *J. Adhesion* 1974, **6**, 196.
- 30 Bucher, R. A. and Hinkley, J. A., *J. Thermopl. Compos. Mater.* 1992, **5**, 3.

- 31 Mayer, J., Giorgetta, S., Koch, B., Wintermantel, E., Patsheider, J. and Spescha, G., *Composites* 1994, **25**, 763.
- 32 Pukánzky, B., Fekete, E. and Tüdös, F., *Makromol. Chem., Macromol. Symp.*, 1989, **28**, p. 165.
- 33 Occhiello, E., Morra, M., Guerrini, G. L. and Garbassi, F., *Composite* 1991, **23**, 193.
- 34 Yuan, L. Y., Shyu, S. S. and Lai, J. Y., *Comp. Sci. Tech.* 1992, **45**, 9.
- 35 King, T. R., Adams, D. F. and Buttry, D. A., *Comp. Sci. Tech.* 1992, **44**, 351.
- 36 Piggott, M. R., *Polymer Composites* 1982, **3**, 179.
- 37 Vu-Khanh, T. and Denault, J., *J. Reinf. Plast. Compos.* 1993, **12**, 916.
- 38 Carroll, B. J., *J. Colloid Interface Sci.* 1976, **57**, 488.
- 39 Yamaki, J.-I. and Katayama, Y., *J. Applied Polymer Sci.* 1975, **19**, 2897.
- 40 Walliser, A., "Caractérisation des Interactions Liquide-Fibre Elémentaire par Mouillage" PhD Thesis, Université de Haute Alsace (F), 92-MULH-0248 (1992).
- 41 Carroll, B. J., *Langmuir* 1988, **2**, 248.
- 42 Pangelinan, A. B. and Mc Cullough, R. L., *J. Thermopl. Compos. Mater.* 1994, **7**, 192.
- 43 Vrbanac, M. D. and Berg, J. C. *J. Adhesion Sci. Technol.* 1990, **4**, 256.



# 7

## MANUFACTURING OF COMPLEX GEOMETRY PARTS

It was shown in Chapter 2 how polymer powder and continuous fibres could be mingled together. The impregnation mechanism of powder coated towpregs was studied in Chapter 3, and a consolidation model was proposed in Chapter 4 to optimise the processing parameters of powder impregnated UD composites. Good correlation was found between experimental consolidation curves and model prediction. It is our goal here to demonstrate the applicability of the powder impregnation route to the manufacture of complex geometry parts of industrial interest, processed by matched-die compression moulding. FIT yarns and stretch broken commingled fibres (cf. Chapter 2) have been used in this study.

The full potential of powder coated towpregs as a precursor for compression moulded composite parts can be reached by the fabrication of drapeable textile preforms. These can be woven or knitted fabrics, braided sleeveings, etc. The highly flexible FIT yarns are particularly suited for the fabrication of textile preforms. A sheath enclosing the powder coated bundle protects the fibres from abrasion and loss of resin powder during the weaving or braiding operation.

In this chapter, a number of commercially available textile preforms are presented. Satin 8 woven FIT yarns from Porcher Textile have been used to process flat laminates. Experimental consolidation curves are compared to the model for powder impregnated UD composites presented in Chapter 4. Two model systems have been used: carbon fibre reinforced poly (ether-ether-ketone) (CF-PEEK) and polyamide 12 (CF-PA12). Finally, parts with a more complex geometry—corrugated sheets—have been produced by matched-die compression moulding, to investigate the influence of pressure gradients. Their microstructure and mechanical properties are compared to parts of similar geometry and processed under the same conditions using braided stretch broken commingled fibres from Schappe Techniques.

### 7.1 TEXTILE PREFORMS

Fabrication of net-shape parts using powder impregnated tows is most efficiently done by using a textile preform. The objective is to create a drapeable fabric made of powder

coated yarns, which is preshaped to approximate the geometry of the desired moulded part. A fabric can be defined as a manufactured assembly of fibres or yarns which has a substantial surface area in relation to its thickness, and having sufficient mechanical strength to give it cohesion [1]. Fabrics may be woven, knitted, braided or non woven (bonded). A fabric less than 15 cm wide is often described as a *tape*. The two types of fabric used, woven and braided fabrics, are shortly reviewed:

### 7.1.1 Woven fabrics

In woven fabrics, the *warp* fibres, called “*ends*”, generally run in the length direction (except in bias fabrics which can have for example a  $\pm 45^\circ$  arrangement). The *weft* – or *fill* – fibres run at right angles to the *warp* and are called “*picks*” [2a]. Many weave types are available, ranging from simple unidirectional arrangement to twill or satin weaves. Three weave types of interest in composite manufacturing, schematised in Figure 7.1, are presented: plain, twill, and satin.

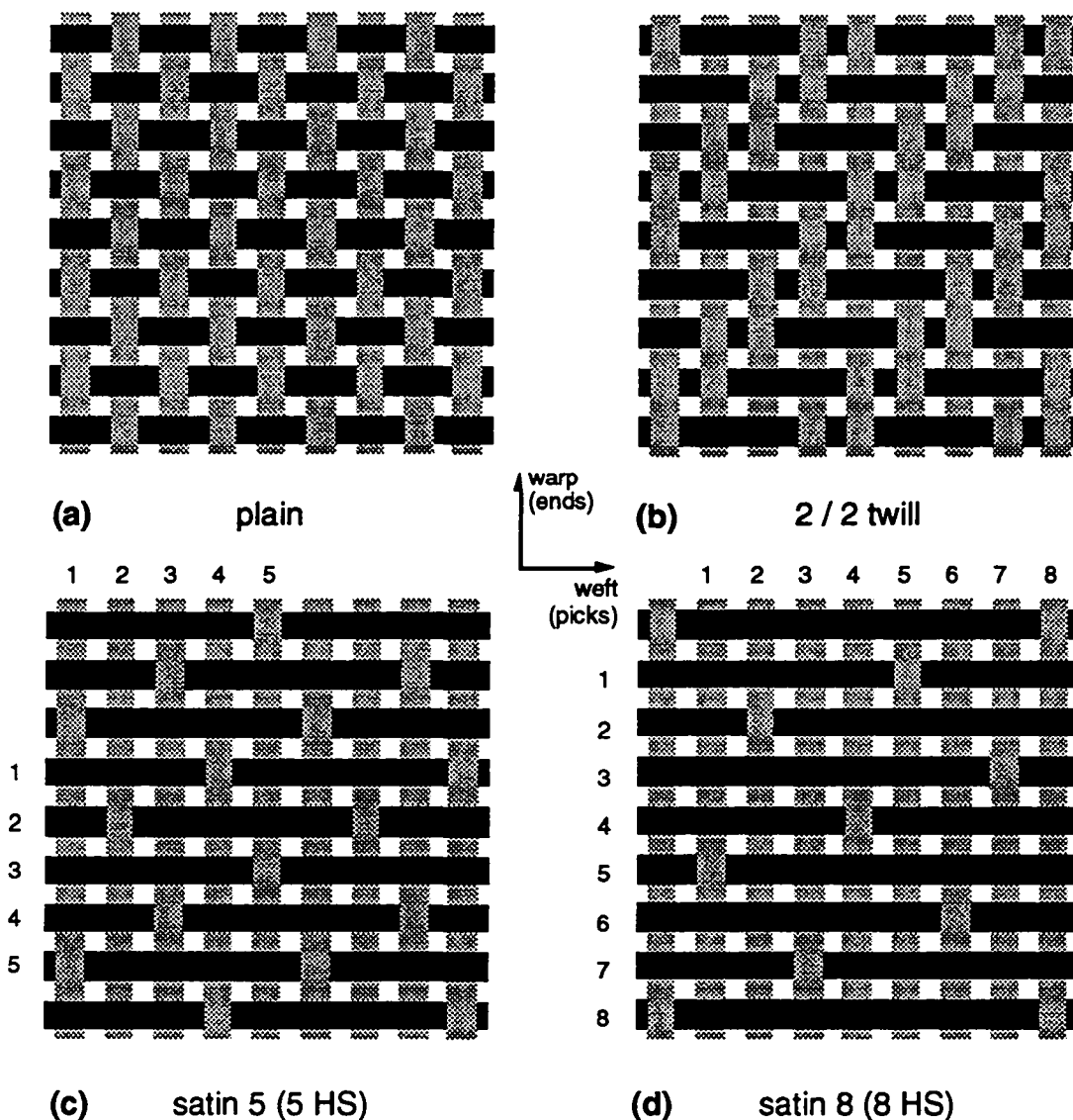


Figure 7.1: Weave styles: (a) plain; (b) 2 / 2 twill; (c) 5 HS; and (d) 8 HS.

They can be defined as follows.

- **Plain** (or *square*) weave: each warp and weft pick passes over one crossing thread and under the next (cf. Figure 7.1a)
- **Twill** weave: each end and pick floats over more than one and under a number of crossing threads, moving one thread for each end or pick; it is described as “ $N_1 / N_2$  twill” where  $N_1$  and  $N_2$  refer to the number over, respectively under which each end and pick passes, e.g., 2 / 2 or 2 / 1 twill (cf. Figure 7.1b); this produces a pattern of diagonal lines on the face of the fabric, which has more drape than that of plain weave
- **Satin** weave: each end and pick passes over  $N$  threads and under one crossing thread; the weave is therefore described by  $(N+1)$ ; for example a satin 5 weave, also referred to as 5 HS (cf. Figure 7.1c), has the ends and picks passing over four and under one end, while in a satin 8, or 8 HS (cf. Figure 7.1d), they pass over seven and under one end. Satin fabrics have a “warp face” and a “weft face”, both relatively smooth. Satin weaves have even better drape than twill fabrics, but the structure may be less stable.

### 7.1.2 Braided fabrics

Braids are obtained by interlacing three or more threads in such a way that they cross one another and are laid together in a diagonal formation [2b]. Conventional braided structures are classified into the following three groups: flat braid, tubular braid (sleeving) (cf. Figure 7.2a and b), and through-the-thickness 3D-braid. The bias interlacing nature of the braided fabrics makes them highly conformable and shear resistant. Resistance in the  $0^\circ$  direction can be enhanced by braiding in three directions,  $0 \pm \theta$ , as shown in Figure 7.2c [3].

The most common commercially available braided products are under the form of tubular sleeveings. In a *diamond* braid (1 / 1), each thread passes over one crossing thread and under the next. Similarly, in a *regular* braid (2 / 2) each thread follows a pattern of two up and two down, and in a *hercules* braid (3 / 3), they follow a three up and three down pattern [6]. In this Chapter, corrugated sheets using *regular* braid (2 / 2) precursors with a braiding angle,  $\theta$ , of  $34^\circ$  are processed.

The inside diameter,  $d$ , of a sleeving depends on the number of carriers,  $N$ , in the machine, the fibre tow bandwidth,  $w$ , and the braiding angle,  $\theta$ . These quantities are related to each other through [4],

$$d = \frac{w \cdot N}{2\pi \cos \theta} \quad (7.1)$$

The major requirements for a braidable yarn using conventional braiding equipment are good yarn integrity which promotes consistent feed through the guide mechanisms for braid formation, and good flexibility to follow the tortuous path through typical braiding

machines. Similar requirements can be applied to weaving, although the weaving process is not as abusive to the tow.

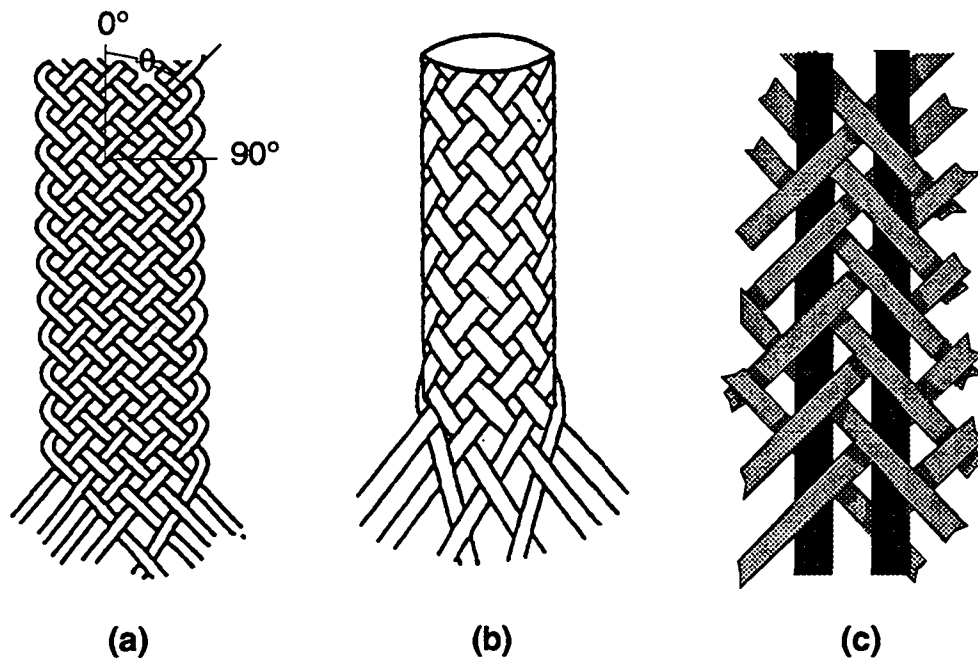


Figure 7.2: Braided structures: (a) 2D flat braid; (b) 2D tubular braid; and (c) 3D braid (after [3]).

### 7.1.3 Powder coated towpreg fabrics

Hugh et al. [5] investigated the weaving of satin 8 powder coated towpregs stabilised by melt fusing the powder particles in place. They pointed out that the maximum allowed rigidity for a yarn to be woven in a conventional rapier loom was 10 g-cm. Initial weaving experiments revealed problems with loose filaments in the tow bundle accumulating in the *heddles* and *comb*. Twisting of the tow (15 twists per meter) gave a marginal improvement in weavability. They finally concluded that to conveniently weave molten powder towpregs, tension on the tow, and the number of eyelets, bends and other contact points of the tows should be minimised. It was also pointed out that for a total amount of fibres, the use of small tows resulted in higher fibre damage, due to the larger exposed tow area.

Greene and Holty [4] experimented both weaving and braiding of molten powder towpregs. Again, frictional fibre damage was reported as a major issue. They suggested to either size the towpreg with a matrix compatible sizing, or wrapping it with a matrix compatible filament. They thus produced highly flexible material whose shape and integrity was controlled by the sizing or filament overwrap.

Ramasamy et al. [6] studied the braidability of commingled and melt fused powder coated CF-polyamide 6 (PA6) towpregs. They concluded that excessive towpreg stiffness caused problems during the uncoiling of the feed bobbins and the guiding of the

yarns through the braiding tool. The lack of lateral coherence, and the excessive fibre to fibre friction caused the towpregs to split in both the carrier and the braiding zone. Wrapping the towpregs with a fine filament considerably improved lateral coherence and reduced tow to tow friction, thus considerably improving the braidability of the towpregs. Wrapped commingled tows exhibited the best braidability, due to their higher flexibility compared to molten powder towpregs.

Sheath coated powder towpregs of the FIT type are highly flexible, and the sheath offers a solution to fibre wear due to friction. Porcher Textile proposes a choice of FIT woven fabrics. A sample of their products is listed in Table 7.1

**Table 7.1: FIT woven fabrics proposed by Porcher Textile**

<b>Towpreg</b>	<b><math>v_f</math> [%]</b>	<b>Weave</b>
6K CF-PA12	60	satin 8
6K CF-PEEK	60	satin 8
6K CF-PEEK	60	satin 8
3K CF-PEEK	60	satin 8
3K CF-PEEK	60	satin 5
3K CF-PEEK	60	satin 4
3K CF-PEEK	60	4 / 4 twill
GF-PA12 530tex	60	2 / 2 twill
GF-PA6 320 tex	50	2 / 2 twill

## 7.2 CONSOLIDATION OF WOVEN FLAT LAMINATES

The consolidation behaviour of unidirectional (UD) flat laminates was studied in Chapter 4. It has been shown that the proposed model, based on a description of the consolidation mechanism at a microscopic level, describes well the consolidation of a UD flat laminate for the two geometries considered in §4.2. Consolidation of satin 8 woven FIT laminates is investigated in this chapter for two systems, CF-PEEK, and CF-PA12. Flat laminates have been compression moulded using FIT satin 8 fabric preforms; the experimental consolidation curves have been recorded and are compared to the model proposed in Chapter 4 (Equation 4.13).

### 7.2.1 Materials characterisation

The two systems used, 3K CF-PEEK and 6K CF-PA12 satin 8 weaves, have both been provided by Porcher Textile. The components have been characterised using the same procedure as described in §4.2.1. Table 7.2 lists the materials properties needed for the computation of the consolidation curves.



**Table 7.2: Parameters used in the consolidation modelling of FIT**

Parameter	PEEK (ICI)	PA12 (Atochem)	Unit
Fibre radius, $R_f$	3.5	3.5	$\mu\text{m}$
Matrix powder radius, $R_m$	23	10	$\mu\text{m}$
Final fibre vol. fraction, $v_{f1}$	0.67	0.67	-
Applied pressure, $P_a$	5	5	MPa
Processing Temperature	390	200	$^{\circ}\text{C}$
Melt viscosity, $\eta$	526	500 <sup>a</sup>	Pa·s
Spring pressure (Equ. 4.12):			
$A_s$	1500	1500	Pa
$\phi_0$	0.79	0.79	-
$\phi_a$	0.45	0.45	-

<sup>a</sup> measured at a shear rate of  $10 \text{ s}^{-1}$ .

## 7.2.2 Consolidation of flat laminates

The same experimental set-up used for the characterisation of the consolidation behaviour of UD flat laminates described in §4.3.3 has been used in this work. Preforms were manufactured by cutting and stacking a number of  $50 \times 50 \text{ mm}^2$  woven tapes with the warp side facing upwards (3K CF-PEEK: 10 plies, and 6K CF-PA12: 8 plies). The plies were kept in place by spot welding them to each other. The preforms were then placed into the heated square cavity mould and held 15 min at the processing temperature ( $390^{\circ}\text{C}$  for PEEK and  $200^{\circ}\text{C}$  for PA12) to allow them to equilibrate thermally. A pressure of 5 MPa was then applied and the consolidation curve recorded with an LVDT (cf. §4.3.3). After 7 min the mould was cooled at approximately  $60^{\circ}\text{C}\cdot\text{min}^{-1}$  under constant pressure. The mould was then opened and the laminate extracted.

## 7.2.3 Consolidation model

The consolidation model derived for UD powder coated laminates in Chapter 4 was based on the description of the impregnation mechanism at a microscopic level (cf. §4.1.1). During the impregnation process, each resin bridge will spread along a “channel” formed by parallel adjacent fibres (cf. Figure 4.1). In woven fabrics, however, the presence of crimps may alter the resin flow; this is particularly true in plain weaves which show high crimp densities (cf. Figure 7.1a). In satin 8 weaves, however, each end and pick passes over seven threads and under one crossing thread. It results that  $7/8$  (87.5%) of each *end* and *pick* is unidirectional in the *warp* and *weft* face, respectively (cf. Figure 7.2). The resin flow behaviour in a satin 8 fabric should thus not differ too much from flow in a unidirectional system, allowing the model derived in Chapter 4 for UD laminates to be used to describe the consolidation of satin 8 fabrics. The elastic response of the fibres in compression, termed spring pressure,  $P_s$  (cf. §4.1.5) should, however, be higher in woven than in UD arrangements. This can be verified by comparing consolidation curves of UD and woven laminates. The parameters used for the computation of  $P_s$  using Equation 4.12 are listed in Table 7.2. Note that for UD

laminates, the spring pressure could be neglected when mechanical pressures higher than approximately 1 MPa were applied (cf. §4.3.4).

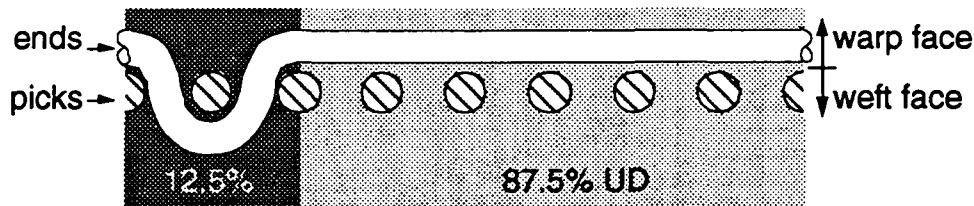


Figure 7.2: Satin 8 weave unit cell: 87.5% of each yarn is linear. The crimp volume only represents 12.5% of the total volume.

#### 7.2.4 Flat laminates consolidation curves

Experimental and predicted relationships between void volume fraction and time are shown in Figure 7.3. Figure 7.3a shows the result for CF-PEEK satin 8 laminates and Figure 7.3b shows the corresponding plots for CF-PA12. The solid line represents Equation 4.13, which includes the effects of the spring pressure, and the dotted line represents Equation 4.19, which neglects the spring pressure. It can be seen that, contrary to UD laminates, the spring pressure cannot be neglected in this case, and Equation 4.13 needs to be applied instead of Equation 4.19, using the data listed in Table 7.2. Equation 4.13 does not have an analytical solution and was therefore solved numerically. The much higher value of the spring pressure for satin 8 fabrics compared to UD arrangement can be attributed to the higher fibre waviness and to the presence of cross-over points in the former. This is quite visible in Figure 7.4 which shows a micrograph of a CF-PEEK satin 8 FIT laminate processed at 5 MPa.

Good quality parts —50 x 50 mm<sup>2</sup> flat laminates— have thus been manufactured using FIT fabrics. This process has been scaled up to larger parts with a more complex geometry —100 x 100 mm<sup>2</sup> corrugated sheets— using CF-PA12 satin 8 FIT fabrics, as described in the following section.

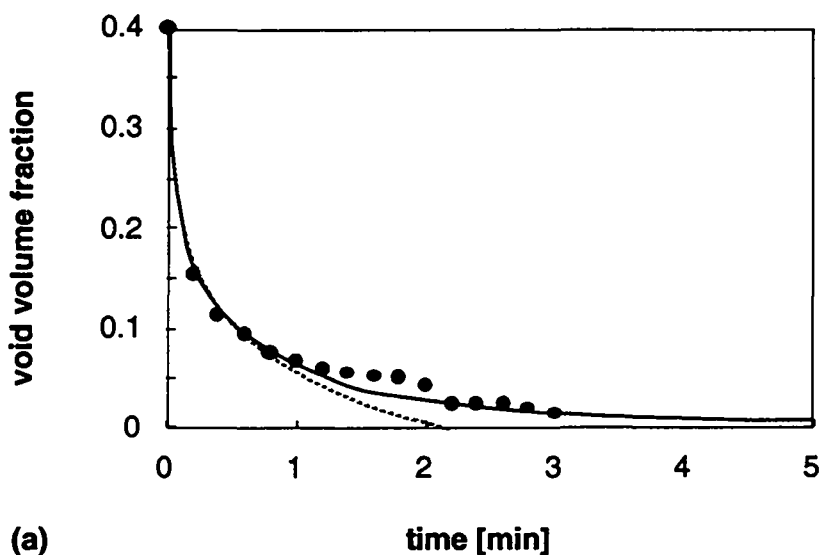


Figure 7.3: Consolidation curves of satin 8 flat laminates: (a) CF-PEEK; and (b) CF-PA12. Solid curves represent Equation 4.13, which includes  $P_s$ , and dotted lines represent Equation 19 which neglects it. Continues next page.

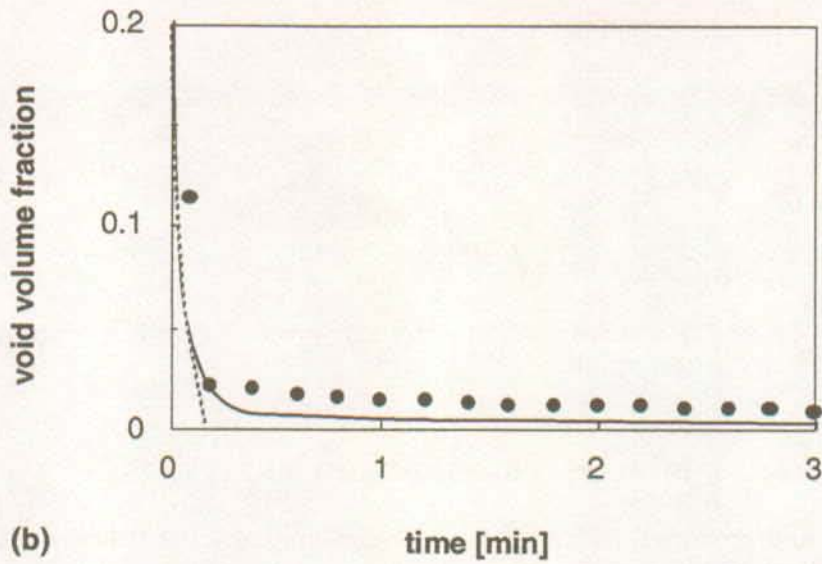


Figure 7.3 (continued): Consolidation curves of satin 8 flat laminates: (a) CF-PEEK; and (b) CF-PA12. Solid curves represent Equation 4.13, which includes  $P_s$ , and dotted lines represent Equation 19 which neglects it.



Figure 7.4: Cross section of a CF-PEEK satin 8 FIT flat laminate processed at 5 MPa (optical microscope). The waviness of the fibres and the presence of cross over points may explain the higher value of  $P_s$  when compared to UD laminates.

### 7.3 WOVEN CORRUGATED SHEETS MANUFACTURING

Carbon fibre reinforced PA12 compression moulded corrugated sheets have been manufactured to approximate a part geometry closer to industrial interests, where structural complexity is often encountered (cf. Figure 7.5). A closed match die mould, designed at Laboratoire de Technologie de Composites et Polymères (LTC) to manufacture parts with a constant thickness of 2.4 mm, was mounted on a hydraulic press.

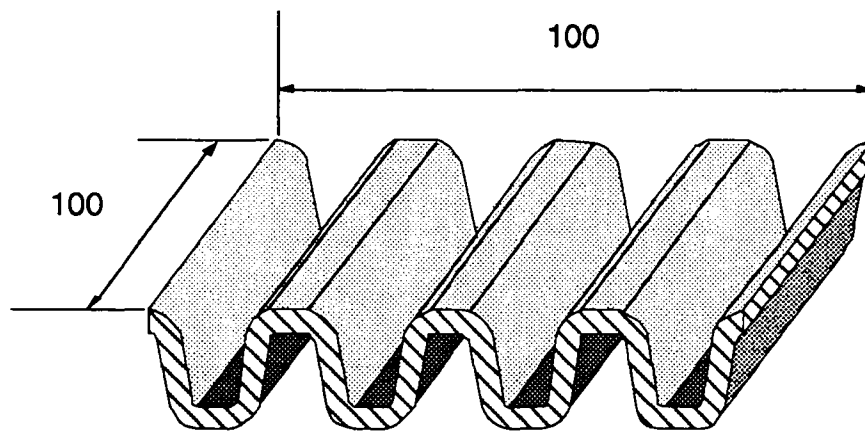


Figure 7.5: Compression moulded corrugated sheets processed using CF-PA12 satin 8 FIT fabric, and commingled CF-PA12 2D braid.

Two types of precursor have been used. Satin 8 fabrics made of FIT by Porcher Textile, and braided stretch broken commingled carbon-PA12 fibres by Schappe Techniques. The FIT satin 8 fabric consisted of 60 vol. % 6K T300 carbon fibre from Soficar reinforced PA12 AMNO TL-D from Elf Atochem; some properties of this material are listed in Table 7.2. The braided commingled fibres were made of 59 vol. % CF (HTA from Akzo) reinforced PA12 (GRILAMID L25 from EMS-Chemie). The commingled preforms used are regular (2 / 2) tubular braids with a braiding angle of  $\pm 34^\circ$  (cf. Figure 7.2b). Each yarn was wrapped with a fine PA12 filament to provide lateral coherence. Figure 7.6 compares the viscosity of the two resins (fibres and powder) measured at different shear rates. It can be seen that the PA12 fibres used in the commingled precursor have a considerably higher viscosity at 200°C than the PA12 powder used in FIT. For instance, at a shear rate of  $10 \text{ s}^{-1}$ , the former has a viscosity of about 5000 Pa·s while the viscosity of the latter is 500 Pa·s. At 250°C PA12 fibres viscosity is reduced to 2500 Pa·s. It would have been preferable, of course, to use the same fabric architecture and the same resin for the two types of precursor, but these were not available.

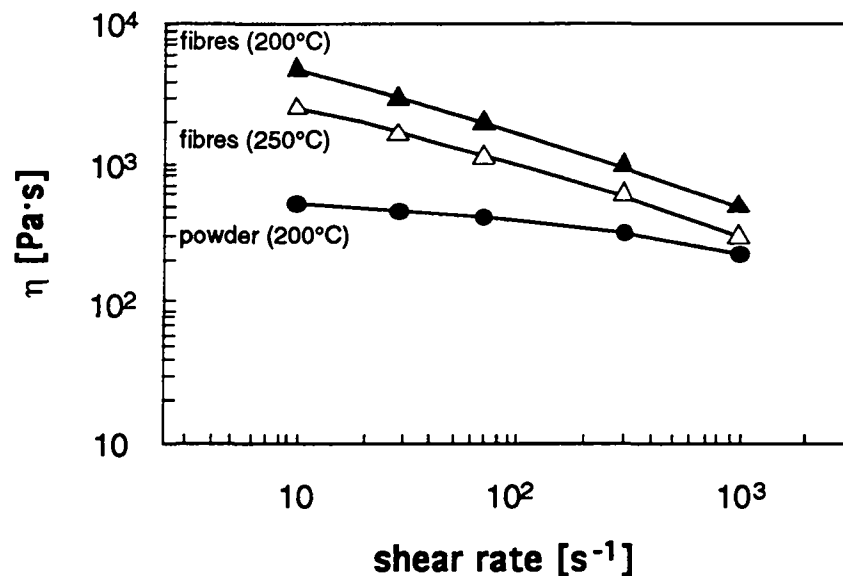


Figure 7.6: Viscosity as a function of shear rate of PA12 powder used in satin 8 FIT (at 200°C), and PA12 fibres used in the braided commingled fabrics (at 200 and 250°C).

### 7.3.1 Corrugated sheets processing

The towpreg fabrics were preshaped in order to facilitate the placement of the precursor into the mould cavity prior to the consolidation operation. A device was designed for this purpose consisting of seven cylindrical Ø10 mm pins fixed to two parallel plates, of which three of the middle pins can be removed (cf. Figure 7.7). The fabrics were laid flat on the four remaining pins (cf. Figure 7.7a). By fixing the three missing pins back into their original position, the fabrics were corrugated, thus approximating the geometry of the mould. The set-up was then covered by an aluminium hood, so that the two extremities of the fabrics were folded down (cf. Figure 7.7b). To stabilise the fabrics into this configuration, the system was placed into an oven at 200°C for 15 min, to allow a limited and controlled flow to occur. The preform was then cooled and extracted by slipping out the three removable pins (cf. Figure 7.7c). The resulting preform consisted of a semi-rigid non impregnated multi-ply corrugated sheet, which could easily be placed into the mould cavity. Six woven layers were used for the manufacturing of the FIT preforms. Six commingled tubular braids were cut open along the longitudinal axis to obtain flat braids and subsequently laid flat as described above.

The powder coated fabrics were processed at 200°C, and the commingled fibre fabrics at 200 and 250°C. Prior to consolidation, the preforms were held in the mould for 15 min at processing temperature to equilibrate thermally. The mould was attached to a servo-hydraulic press (Battenfeld BA 900 V-V-H-R-S). Next a pressure of 5 MPa was applied. The pressure was calculated as the ratio of the applied force to the projected area of the mould (i.e., 100 x 100 mm<sup>2</sup>). Three different consolidation times were used:

150 s (2.5 min), 500 s (8.3 min), and 1965 s (32.75 min). Finally, the mould was cooled at about  $11^{\circ}\text{C}\cdot\text{min}^{-1}$  under constant pressure during 800 s, opened, and then the part extracted. In order to prevent the preform from adhering to the mould, and to reduce the cleaning time between two moulding operations, Kapton film was applied to both sides of the preform. After consolidation, the release films were easily removed, and a consolidated part with good surface finish was obtained. Figure 7.8 shows the three pressure-temperature-time processing cycles used. It should be noted that the processing cycle can be shortened by pre-heating the preforms separately out of the mould.

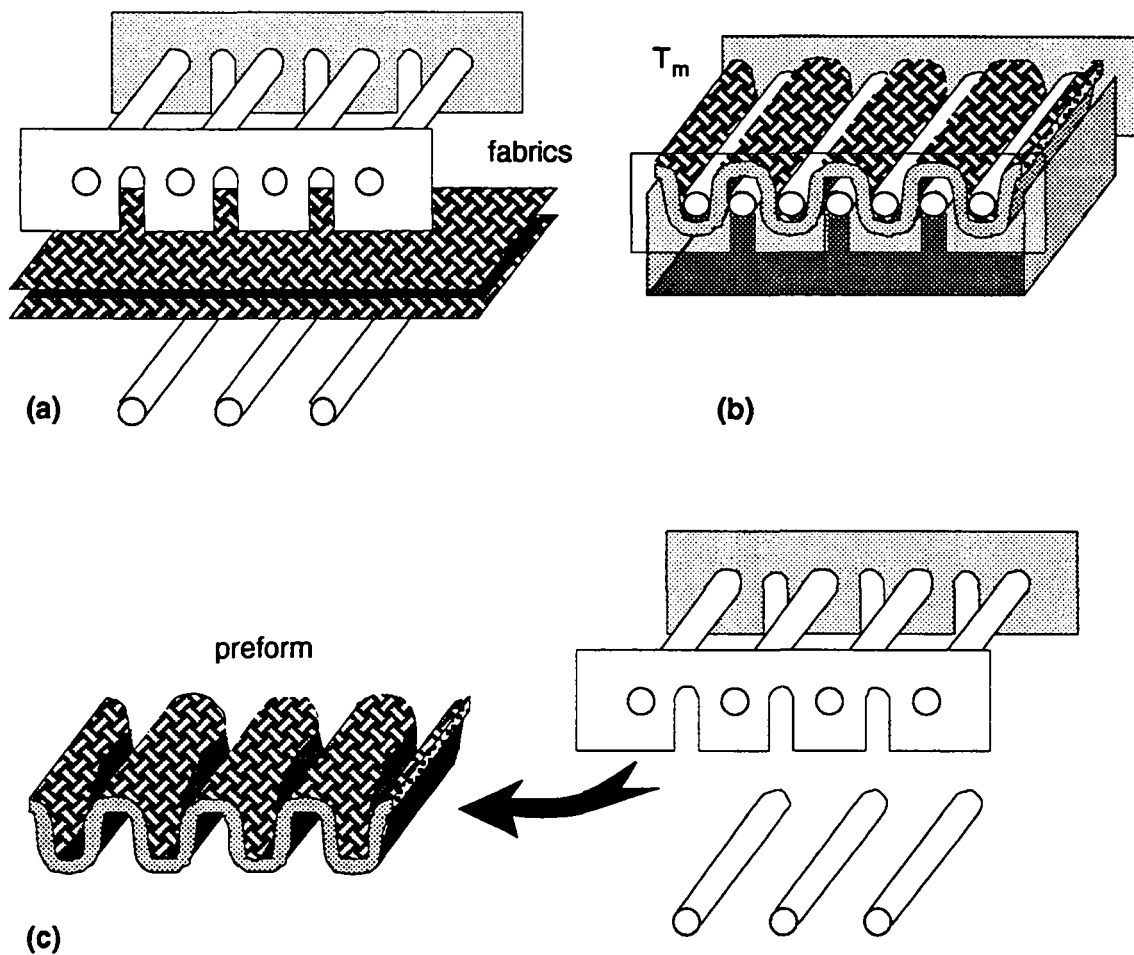


**Figure 7.7:** Preform manufacturing: (a) a number of fabrics is stacked flat on the four fixed pins; (b) the three remaining pins are fixed back into their original position, and the system is heated at processing temperature for 15 min; and (c) the preform is extracted by removing the three movable pins.

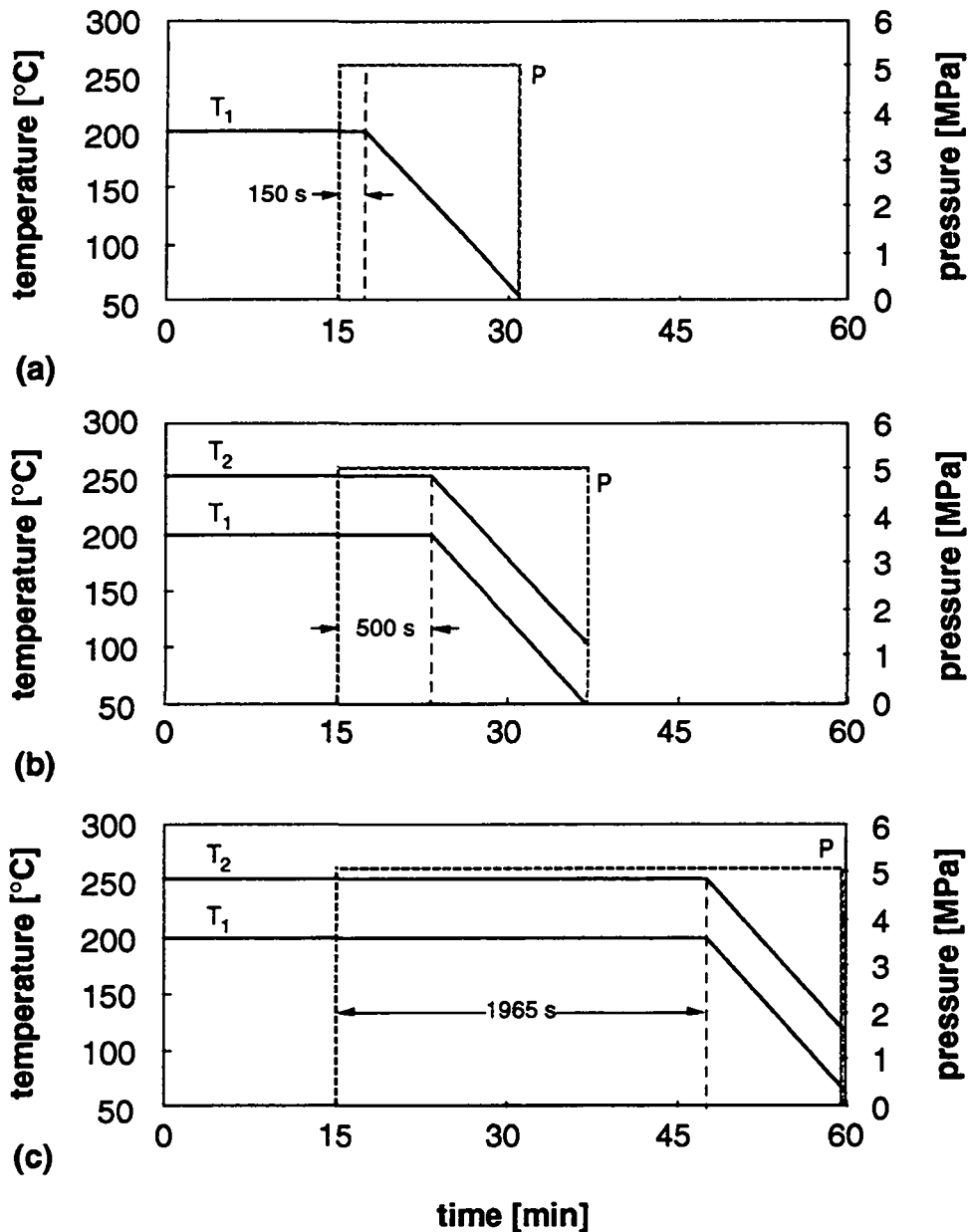


Figure 7.8: A pressure of 5 MPa was applied during three different holding times for the manufacture of CF-PA12 corrugated sheets; powder coated fabrics were processed at  $T_1 = 200^\circ\text{C}$ , and commingled braids at  $T_1 = 200$  and  $T_2 = 250^\circ\text{C}$ .

### 7.3.2 Characterisation of the corrugated parts

The microstructure of the CF-PA12 corrugated sheets has been studied by microscopy observation of polished surfaces. Mechanical tests have been performed on the composite parts and the properties of the two types of precursor —satin 8 FIT, and braided stretch broken commingled— are compared.

Three types of samples marked A, B, and C have been cut out of each part, as shown in Figure 7.9a (shaded areas). Type-A samples are 7 mm wide and 100 mm long flat plates from the *flange* (horizontal section) of the corrugated sheet. Processing

conditions in zone A should be quite similar to those observed in §7.2 for flat laminates. Type-B samples have the same geometry as sample A and come from the *web* (inclined section). Pressure conditions in zone B should be lower than in zone A, depending on the angle of projection of the pressure vector. Finally, type C samples consist of one channel section.

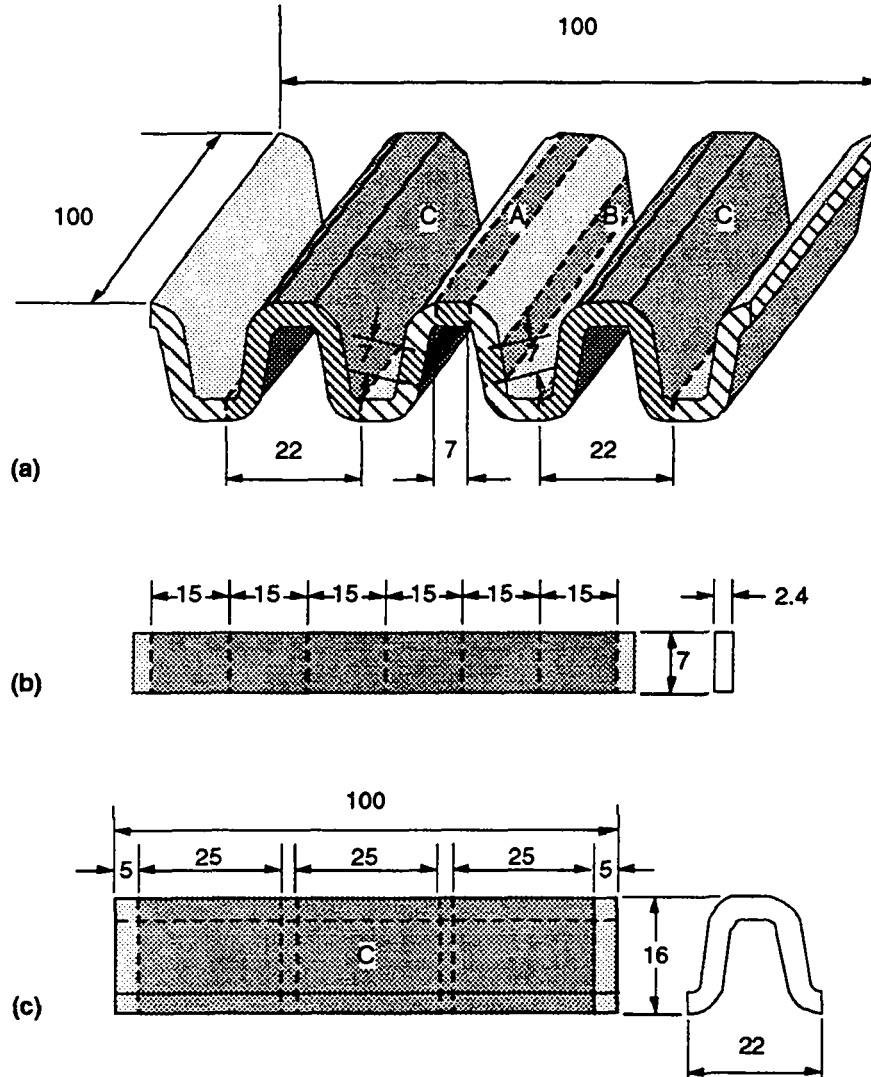


Figure 7.9: Samples cut out of each part (shadowed areas): (a) samples A, B, and C; (b) samples A and B were cut into  $7 \times 15 \text{ mm}^2$  specimens for ILSS tests; and (c) the edges of samples C were trimmed and 25 mm long parts were cut for compression testing.

### Physical characterisation

Polished cross-sections of type C samples have been prepared and are used to analyse the quality of impregnation along their corrugated profile. Void content has been measured by an immersion technique (ASTM-790M); density of CF is  $1.76 \text{ g}\cdot\text{cm}^{-3}$ , and of PA12 is  $1.03 \text{ g}\cdot\text{cm}^{-3}$ .



### Mechanical characterisation

Two types of tests have been carried out to characterise the mechanical properties of the corrugated parts: interlaminar shear strength of parallel fibre composites by short beam method, ILSS (ASTM D 234) on samples taken from zone A and B, and compression test transverse to the channel direction of C-type samples (cf. figure 7.10).

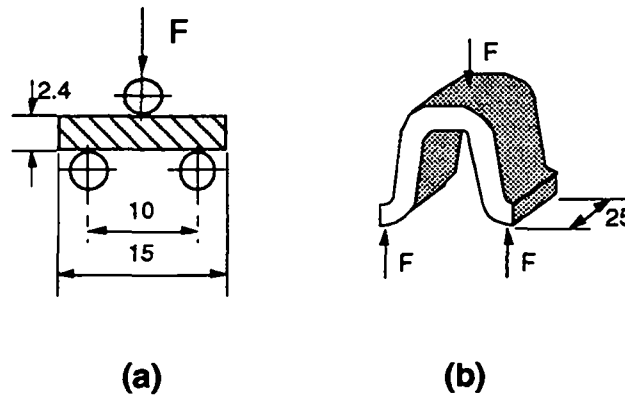


Figure 7.10: Mechanical tests made on the corrugated sheets: (a) ILSS with samples from zone A and B; (b) compression transverse to the longitudinal axis of C-type samples.

The horizontal shear test specimens are 7 x 15 mm<sup>2</sup> and approximately 2.0 mm thick, and were cut from zone A and B (cf. Figure 7.9b). The specimen rests on two supports 10 mm apart, that allow lateral motion. Load is applied on the mid-point of the specimen at a cross-head speed of 1.3 mm·min<sup>-1</sup>. Shear strength determined by the ILSS method is valid only if failure is in horizontal shear. The apparent shear strength is calculated as follows,

$$\tau_{ILSS} = 0.75 \frac{F_m}{Bd} \quad (7.1)$$

where  $F_m$  is the breaking load, and  $B$  and  $d$  are the width and thickness of the specimen, respectively. The ILSS test allows the shear strength of the flat sections (A and B) to be characterised.

Compression properties transverse to the longitudinal axis of the channel (cf. Figure 7.10b) have been tested on 25 mm long sections cut from C-type samples (cf. Figure 7.9c). The maximum stress,  $\sigma_{max}$ , is expressed as the maximum load divided by the product between sample length and smallest thickness of the channel section. Failure occurs by delamination in the radius between sections A and B.

## 7.4 RESULTS AND DISCUSSION

### 7.4.1 Void volume content

The void volume content measured in zone A and B of the corrugated sheets of woven FIT processed at 200°C and braided commingled precursors processed at 200 and 250°C

are plotted as a function of processing time in Figure 7.11. Powder impregnated parts are represented by circles, commingled parts processed at 200°C by triangles, and commingled parts processed at 250°C by squares; white symbols represent zone B and black ones, zone A.

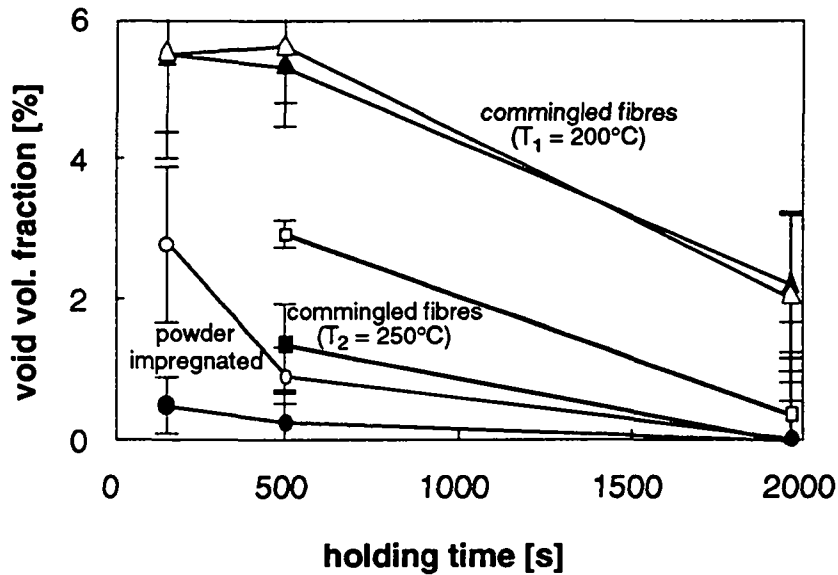


Figure 7.11: Void volume fraction as a function of processing time in zone A and B (black and white symbols, respectively) of powder impregnated (circles) and commingled corrugated laminates processed at 200°C (triangles), and 250°C (squares).

The samples made of commingled stretch broken fibres processed both at 200 and 250°C yield higher void contents than powder impregnated parts at similar holding time. This can be attributed to the large resin viscosity difference between the PA12 resins used in the two different systems (cf. Figure 7.6). For both precursor types, the degree of impregnation in zone A is better than in zone B. This is attributed to a lower local pressure in the inclined sections of the mould (zone B) compared to the horizontal ones (zone A). Furthermore, during closing of the mould, plies in zone A are primarily exposed to compression forces, while in zone B a shear contribution is added. This can be expected to have significant influence on the quality of impregnation of the laminates. Microscopy observation of the sample cross-sections confirms the results shown in Figure 7.11. Large voids can be seen in the commingled parts (higher viscosity) processed at 200°C, even after 1965 s processing, while in powder impregnated parts, voids are only visible in zone B for a holding time of 150 s. While the commingled parts processed at 250°C during 1965 s show good impregnation quality, the ones processed during 500 s show some voids principally located in zone B. Figure 7.12 compares a cross-sectional view of a zone B in a powder impregnated laminate processed during 500 s at 200°C to the same zone in a commingled laminate processed during 1965 s at 200°C. No voids are visible in the former, while large voids can be seen in the latter in spite of its processing time being nearly four times longer.



(a)



(b)

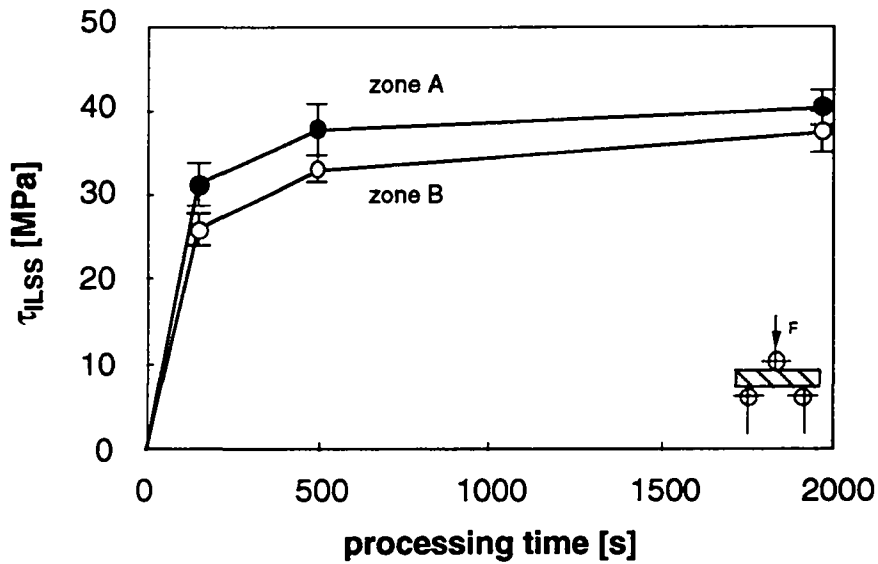
1 mm

Figure 7.12: Cross-sectional view of zone B in (a) a powder impregnated composite manufactured during 500 s; and (b) a commingled part manufactured during 1965 s at 200°C.

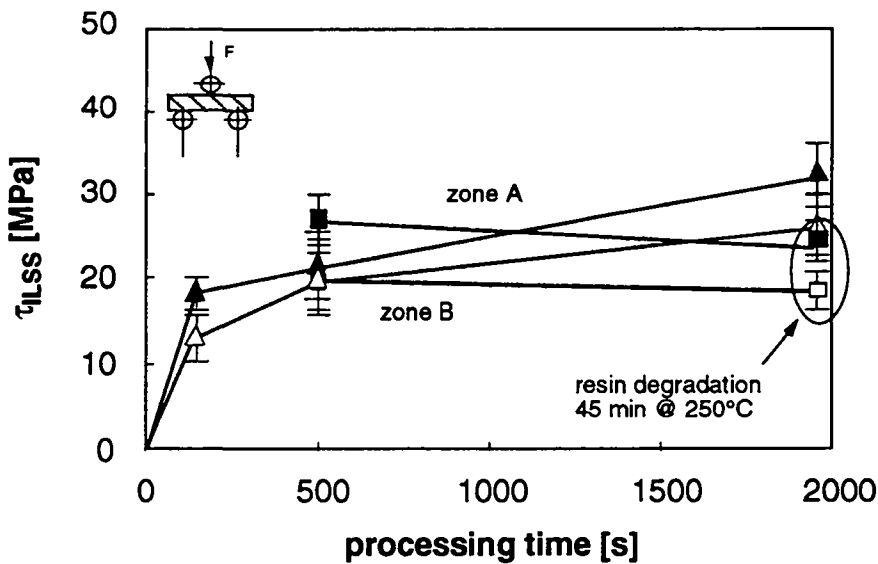
## 7.4.2 Mechanical tests

### ILSS tests

Results of the ILSS tests are plotted as a function of processing time in Figure 7.13. Black symbols represent A-type samples, while white symbols represent B-type samples.



(a)



(b)

Figure 7.13: ILSS shear strength as a function of processing time of zone A (black symbols), and zone B (white symbols): (a) FIT yarns (satin 8 weave); and (b) stretch broken commingled fibres (regular braid); the triangles were processed at 200°C, and the squares at 250°C.

It can be seen that inter-laminar shear strength in zone A is higher than in zone B for both precursor types. This could be attributed to the shear stresses and smaller effective pressure occurring in zone B during processing which affect the consolidation behaviour. The ILSS of powder impregnated parts increases between 150 and 500 s, and then stabilises for longer processing times. It results that parts with good inter-laminar properties can be obtained after 500 s consolidation time using the powder impregnation route. ILSS of commingled parts processed at 200°C increases regularly between 150 and 1965 s holding time, suggesting it could still be improved by applying a longer consolidation time. In spite of their lower void content, the parts processed at 250°C during 1965 s yield lower ILSS values than the ones processed during 500 s. This suggests that PA12 may degrade when exposed to air at 250°C during long processing times. A thermogravimetric analysis is presented in Figure 7.14. Approximately 20 mg of commingled filament was heated in air at  $T_1 = 200^\circ\text{C}$  and  $T_2 = 250^\circ\text{C}$ , at a rate of  $20^\circ\text{C}\cdot\text{min}^{-1}$ , and then held at that temperature during 60 min. This thermal cycle reproduces the thermal exposure of the composite during processing. It can be seen that, practically no weight loss is recorded at a temperature of 200°C for PA12, which can therefore be considered as thermally stable under these conditions. At 250°C, however, PA12 undergoes considerable degradation. After 45 min at 250°C—corresponding to 15 min pre-heating in the mould followed by 1965 s consolidation time—5.3% resin weight loss is recorded. After 500 s consolidation, the material is less degraded than after 1965 s, and the mechanical properties (ILSS) of the former are consequently superior to the ones of the latter in spite of their higher void content.

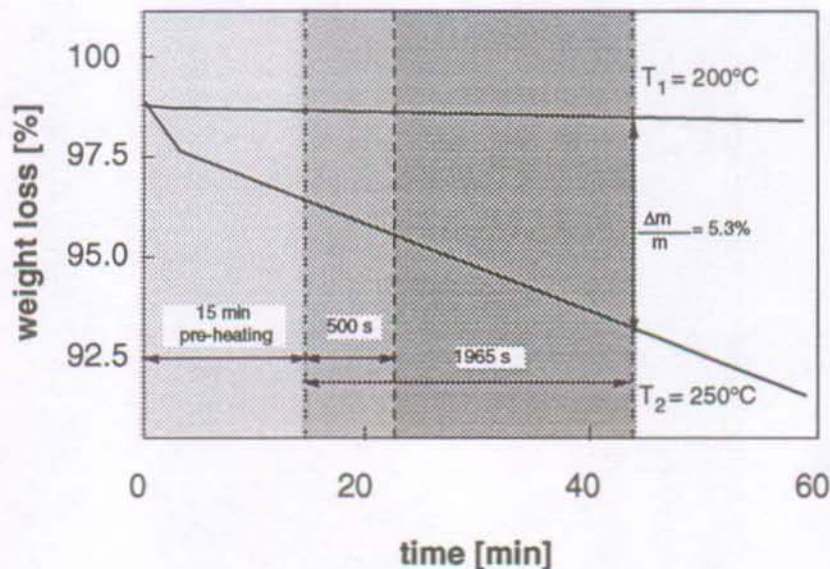


Figure 7.14: Thermogravimetric curves of PA12 used in the commingled precursor held 60 min at  $T_1 = 200^\circ\text{C}$  and  $T_2 = 250^\circ\text{C}$ .

Mechanical properties of powder impregnated satin 8 weaves and commingled regular braids cannot be compared directly, since they do not have the same reinforcement geometry. The ILSS test, however, characterises the quality of adhesion between individual plies, which mostly depends on the degree of impregnation of the fibres, and not on the reinforcement geometry (provided it is a planar configuration). Figure 7.15 shows the ILSS values measured on zone A and B for both precursor types as a function of the void volume fraction measured in §7.4.1. Apart from the degraded laminate processed at 250°C during 1965 s, there is a clear correlation between these two quantities, stressing the importance of a proper impregnation of the laminate.

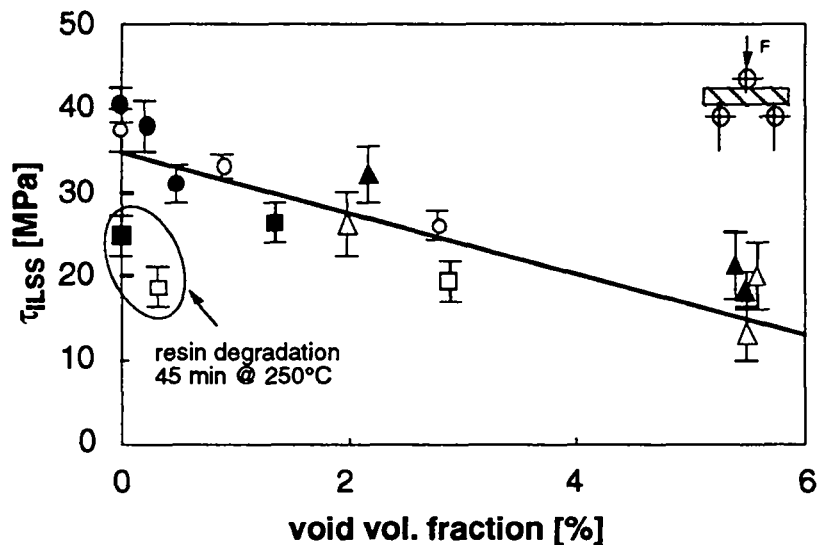
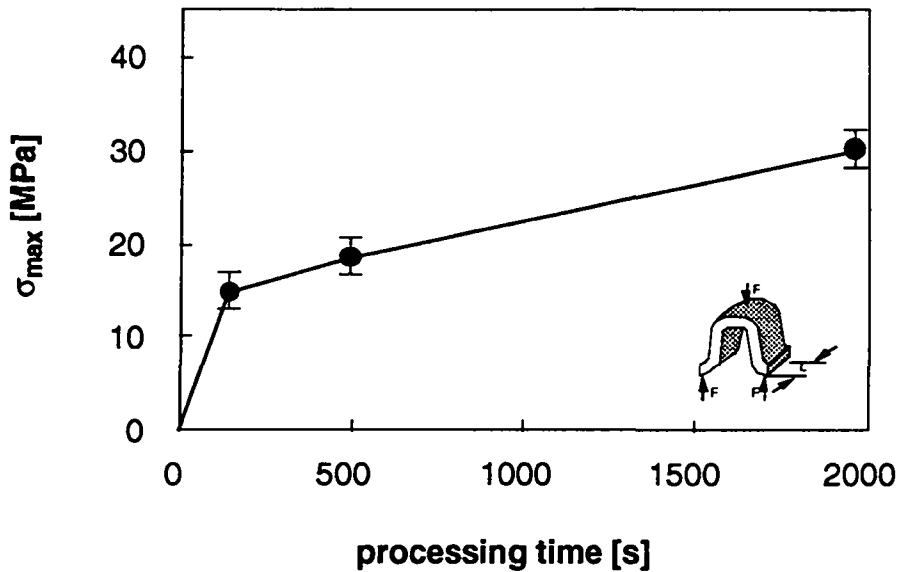


Figure 7.15: ILSS values as a function of void volume fraction: circles represent FIT laminates, and triangles and squares, commingled precursors processed at 200°C and 250°C, respectively; black symbols refer to samples in zone A, and white ones in zone B.

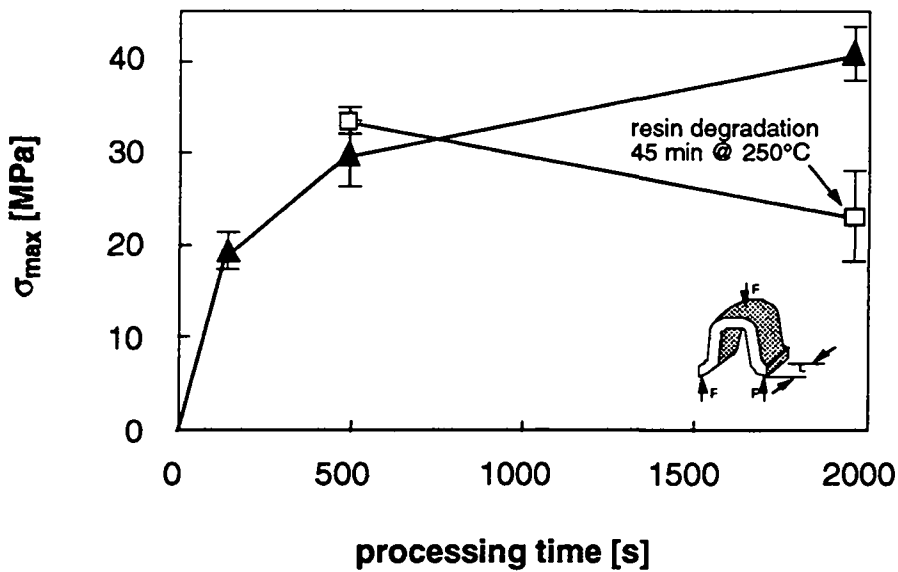
#### Transverse compression tests

Figure 7.16 shows that improved compression properties are obtained with increasing processing time for both types of precursor. This suggests that the degree of impregnation affects substantially the resistance in compression of the corrugated channels. Failure occurs by delamination followed by buckling in the outer skin of the shoulders (located between zone A and B).

Again, resin degradation at 250°C during 1965 s is detrimental to the mechanical properties in compression of the composite. Compression strength drops of approximately 10 MPa between 500 s and 1965 s consolidation time. Increasing the processing temperature from 200°C to 250°C improves the impregnation quality (cf. Figure 7.11) by decreasing the viscosity of the PA12 fibres from 5000 Pa·s to 2500 Pa·s (cf. Figure 7.6). The degradation of the resin, however, results in a substantial drop of mechanical performance. It is therefore preferable to process CF-PA12 commingled fibres at lower temperature allowing a longer time for consolidation.



(a)



(b)

Figure 7.16: Transverse compression strength of C-type samples as a function of processing time: (a) powder impregnated satin 8 weave; and (b) commingled regular braid; triangles are processed at 200°C, and squares at 250°C.

Unlike ILSS, the channel compression test depends strongly on the reinforcement architecture. The channel compression strength is plotted as a function of the void volume fraction in zone B in Figure 7.17. It can be seen that, as for the ILSS test, powder impregnated and commingled composites follow parallel straight lines (apart from the degraded parts processed at 250°C during 1965 s), but with an offset of about 20 MPa. The offset is representative of the influence of the fibre bed geometry on this test.

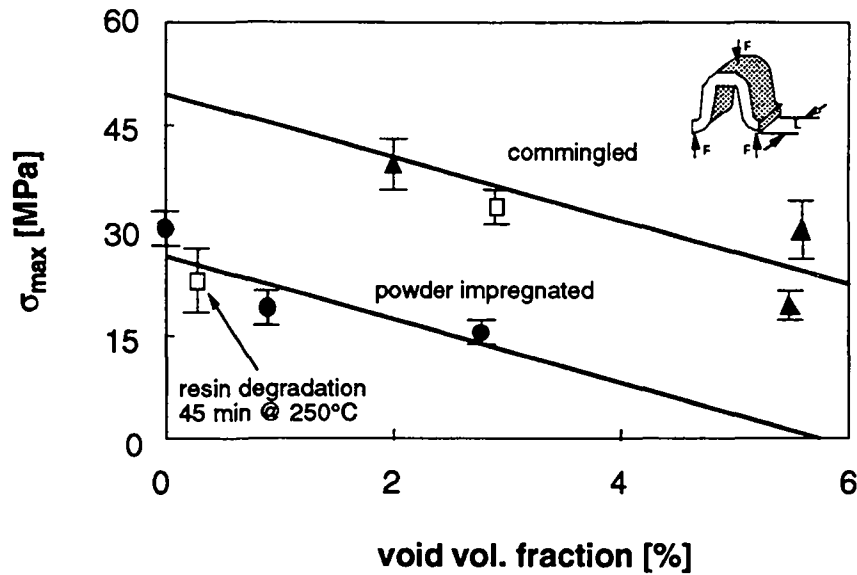


Figure 7.17: Channel compression strength as a function of void volume fraction in zone B: circles represent FIT laminates, and triangles and squares, commingled precursors processed at 200°C and 250°C, respectively.

### 7.4.3 Summary

It has been shown that 60 vol.% carbon fibre reinforced PA12 complex geometry parts could be manufactured at relatively high processing rates. Three processing cycles were used (cf. Figure 7.7) in which a pressure of 5 MPa was applied at the processing temperature of 200°C and 250°C during 150, 500, and 1965 s. Two precursor types were investigated: powder coated yarns (FIT type) and stretch broken commingled fibres. FIT fabrics yielded better degrees of impregnation than the commingled ones at similar processing conditions. This is mainly due to the viscosity of the PA12 fibres which is about 10 times higher than that of the PA12 powder at 200°C. Increasing the processing temperature from 200°C to 250°C decreased the resin fibre viscosity, yielding faster impregnation than at 200°C.

The difference in the degree of impregnation between the two types of precursors was reflected by the results of the ILSS tests. After 500 s processing time, the ILSS results of powder impregnated parts stabilised. ILSS results of the commingled parts processed at 200°C continuously increased with consolidation time, while it decreased for the parts processed at 250°C. This can be explained by the resin degradation observed at 250°C by thermogravimetric analysis (cf. Figure 7.14). A linear correlation was found between void content of the laminates and inter-laminar shear strength (the degraded parts processed at 250°C during 1965 s did not correlate). A linear correlation was also found between transverse compression strength of the channel (sample C) and void volume fraction, but the difference of fibre bed geometry did not allow a direct comparison between the two types of precursor. There was an offset of about 20 MPa between the



two systems. Again, the degradation of the resin processed at 250°C during 1965 s was reflected by poor mechanical properties in compression.

It can thus be said that, for the resin grades used in this investigation, FIT fabrics can be processed at a higher processing rate than stretch broken commingled fibre fabrics. At this stage of the investigation, this can only be attributed to the higher viscosity of the PA12 resin fibres used in the commingled precursor. It is not possible to draw any conclusion on the influence of the precursor type —powder coated or commingled fibres— on the impregnation rate and mechanical properties of the composite parts. To compare the behaviour of powder coated and commingled fibres, it would be necessary to use the same resin in both systems, or at least resins with similar viscosity characteristics. A lower viscosity resin fibre grade is undoubtedly preferable for the manufacture of high fibre content reinforced composites at high processing rate. One advantage of powder coated towpregs is that any resin can be ground into a fine powder, while low viscosity resins are more difficult to spin into fibres.

## **7.5 REFERENCES**

- 1 "Textile Terms & Definitions" 7th. Edition 1975, The Textile Institute, Manchester.
- 2a "Carbon and High Performance Fibres. Directory & Data Book" 6th. Edition, Chapman & Hall, 1995, p. 142.
- 2b Ibid., p. 183
- 3 Buckley, J. D. and Edie, D. D., "Carbon-Carbon Materials and Composites", Noyes Publications, Park Ridge, NJ, 1993, p. 80.
- 4 Greene, T. L. and Holty, W., *39th Int. SAMPE Sympos.* 1994, p. 214.
- 5 Hugh, M. K., Marchello, J. M., Baucom, R. M. and Johnston, N. J., *37th Int. SAMPE Sympos.* 1992, p. 1040.
- 6 Ramasamy, A., Wang, Y. and Muzzi, J., *39th Int. SAMPE Sympos.* 1994, p. 844.

# 8

## CONCLUSIONS

The principal aim of this work has been to assess the feasibility of the powder impregnation route in the manufacture of thermoplastic composite parts with a complex geometry. The study of an alternative thermoplastic composite processing technique is motivated by the poor performance of traditional prepregging techniques for the fabrication of complex geometry parts.

Various means of intimately incorporating polymer particles with continuous reinforcement filaments were reviewed in Chapter 2. Powder coating of continuous fibres is generally achieved in three steps:

- fibre spreading
- powder deposition
- towpreg stabilisation

The first and the last stages are particularly important for the flexibility of the final towpreg. Good spreading of the fibres allows a better powder distribution and a more flexible towpreg to be produced. The towpreg can be stabilised by melt fusing the polymer powder in place, or by enclosing the towpreg in a resin sheath (FIT system). The latter towpreg is very flexible and particularly suited for the fabrication of drapeable textile preforms. A powder coating line has been designed at the Laboratoire de Technologie des Composites et Polymères (LTC), and is now in function.

The role of surface energy and contact angle in the spreading of polymer droplets on fibre surfaces has been discussed in Chapter 3. It has been confirmed that these effects can differ significantly from one polymer/fibre system to another. When a polymer droplet bridges two or more fibres the bridge will tend to spontaneously spread if the contact angle is less than  $90^\circ$ , pulling the fibres closer together; this process can be referred to as *spontaneous impregnation*. For larger contact angles there is an equilibrium fibre spacing beyond which no further consolidation will occur unless an external pressure is applied. Spontaneous impregnation is important in the initial stage of impregnation, particularly for molten powder towpregs, when no mechanical pressure is applied.

A model for the consolidation process of UD-fibre reinforced composites has been developed in Chapter 4, relating resin viscosity, particle size and content, surface energy-driven effects, externally applied pressure, resin flow and fibre bed elasticity. In

this model a droplet of polymer is assumed to form a bridge between three fibres which spreads under the influence of applied and capillary pressure. Consolidation is resisted by the elasticity of the fibre bed. Two towpreg geometries have been considered: FIT yarns, and molten powder towpregs. The model predicts that the impregnation rate is mostly controlled by the applied pressure, the resin viscosity, the ratio between the particle and fibre size and the ratio between the matrix and fibre volume fraction.

Consolidation experiments on powder impregnated composites (FIT and molten powder towpregs) were carried out using a mould attached to a servo-hydraulic testing machine. The results show that the simple model developed in this work is capable of accurately predicting the variation in void content during consolidation of fibre reinforced laminates.

It was found that, the spring pressure is of the order of 0.1–1 MPa, and the capillary pressure ranges between  $\pm 10^{-2}$  MPa. It results that, when laminates of low void content are required, a minimum pressure level is needed to overcome the effects of fibre bed elasticity. It also means that, at the pressures needed to achieve rapid consolidation of high fibre content composites, capillary forces have a negligible effect on impregnation rate. This is not to imply that surface energy effects are unimportant, however. Adhesion at the fibre-matrix interface is largely dependent on the surface energetics of the system. A criterion for optimum adhesion has been proposed in Chapter 5, based on maximising the wetting tension, which is the solution yielding maximum work of adhesion under the condition of positive or null spreading coefficient.

It has been shown in Chapter 6 that, the transverse yield strength and strain of UD-fibre reinforced composites processed under similar conditions could be varied of 20–30% by modifying the surface energy of the fibres. The experimental results thus obtained were in agreement with the criterion of optimum adhesion proposed in Chapter 5, i.e., there is a monotonically increasing relationship between the wetting tension (calculated from measured values of the contact angle) and transverse flexural yield strength.

The full potential of powder coated towpregs for the manufacture of complex geometry parts can be achieved by the fabrication of drapeable textile preforms (e.g., weave, braid, etc.). It has been shown that, for a particular type of weave —satin 8— the consolidation model proposed in Chapter 4 for UD-composites could be applied, provided the spring pressure term was adequately modified.

Corrugated parts have been successfully produced using preforms made of satin 8 woven CF-PA12 FIT fabrics. The processing conditions have been determined from the modified consolidation model. Mechanical properties of the woven powder impregnated corrugated sheets have been tested and compared to the properties of parts of similar geometry made of braided stretch broken commingled fibres. It has been shown that, for the particular systems studied and processed in similar conditions, the powder coated parts showed better mechanical properties than commingled composites.

Finally, the influence of the following quantities on the properties and consolidation rate of compression moulded powder coated composite parts has been assessed in this work.

- *Particle size*: small particles, ideally of similar diameter as the fibres, should be used; this allows a better matrix dispersion and faster consolidation cycles to be achieved. The fluidisation of small diameter powders, however, can be difficult if the particles tend to agglomerate into clusters.
- *Tow spreading*: good spreading of the fibre tow has two beneficial effects: it improves the dispersion of the matrix in the fibre bed, and it allows more flexible towpregs to be produced.
- *Towpreg flexibility*: highly flexible towpregs can easily be converted in drapeable textile preforms. FIT towpregs are particularly easy to weave or braid. More care must be taken when weaving or braiding molten powder towpregs because of their higher rigidity than FIT yarns, and large exposed fibre area.
- *Applied pressure*: due to the high viscosity of thermoplastic resins, and to the significant elastic response of compressed high volume fraction fibre beds, pressures of the range of 1–10 MPa are required to achieve impregnation at a satisfactory rate. Higher pressures may be applied, but always at the risk of distorting the fibre arrangement.
- *Surface energy*: ideally, fibre and matrix surface energy components should be matched and maximised, to enhance spontaneous wetting of the fibres, and to improve fibre-matrix adhesion. Good wetting, but lower adhesion, is achieved if the resin has a lower surface energy than the fibres. If the matrix has higher surface energy than the reinforcement phase, however, both wetting and adhesion will be poor. These results can be applied equally well to other fields than organic matrix composites, as for instance metal matrix composites, which generally show poor wetting properties.

Once the viability of powder coated towpregs in the manufacture of thermoplastic composite parts has been assessed, future work should include the study of the influence of powder size distribution, and fabric geometry on the consolidation behaviour. Other processing techniques than compression moulding should be investigated, in particular on line production techniques (e.g., filament winding, towpreg placement) which can further increase the cost effectiveness of the powder impregnation technique for composite parts manufacturing.



## APPENDIX: LIST OF SYMBOLS

Symbol	Unit	Meaning
$a$	m	penetration depth, plate separation
$a_0^*, a_0^{**}$	-	dimensionless equilibrium distance
$A_{sl}, A_{as}, A_{la}$	$m^2$	surface area of the solid-liquid, air-solid and liquid-air interfaces
$A_{fm}, A_{fa}, A_{ma}$	$m^2$	surface area of the fibre-matrix, fibre-air and matrix-air interfaces
$A_s$	Pa	spring constant in Gutowski model
$d$	m	flow distance for full impregnation
$d_p$	m	particle diameter
$E$	J	surface energy
$F$	N, J	force, Helmholtz free energy
$f_c$	N	capillary force
$F_w$	N	air drag
$h(t)$	m	distance between platens
$h_0$	m	initial distance between platens
$h_1$	m	final distance between platens
$L$	m	final bridge length
$l(t)$	m	bridge length
$l_0$	m	initial bridge length
$P_a$	Pa	applied pressure
$P_c$	Pa	local capillary pressure
$P_c$	Pa	macroscopic capillary pressure
$P_s$	Pa	spring pressure
$P_v$	Pa	viscous pressure
$\bar{P}$	Pa	average hydrodynamic pressure within resin bridge
$R$	m	radius of the solid-liquid interfacial area
$R_1, R_2$	m	principal radii of curvature
$R_f$	m	fibre radius
$r_h$	m	hydraulic radius
$R_m$	m	matrix particle radius.
$S_s, S_l$	$m^{-1}$	solid, liquid surface area per unit volume
$t$	s	time
$T$	N	tow tension.
$t_1$	s	time to full consolidation.
$u_t$	$m \cdot s^{-1}$	tow velocity
$V$	$m^3$	volume
$V_1, V_2$	$m^3$	impregnated and unimpregnated volumes
$v_f$	-	fibre volume fraction
$v_{f1}$	-	final fibre volume fraction
$v_m$	-	matrix volume fraction
$v_{m1}$	-	final matrix volume fraction

Symbol	Unit	Meaning
$V_s, V_l$	$m^3$	solids, liquid volume
$v_v$	-	void volume fraction
$v_{v1}$	-	final void volume fraction
$V(x)$	$ms^{-1}$	flow velocity along the fibre axis.
$W_a$	$J \cdot m^{-2}$	work of adhesion
$x$	-	coordinate along the fibre axis
$x^d, x^p$	-	dispersive, polar component of surface energy
$x^{LW}, x^{AB}$	-	LW, acid-base component of surface energy
$\chi$	$J \cdot m^{-2}$	wetting parameter
$\gamma_{sl}, \gamma_{as}, \gamma_{la}$	$Jm^2$	surface energy per unit area of the solid-liquid, air-solid and liquid-air interfaces
$\gamma_{fm}, \gamma_{fa}, \gamma_{ma}$	$Jm^2$	surface energy per unit area of the fibre-matrix, fibre-air and matrix-air interfaces
$\Delta F_i$	$J \cdot m^{-2}$	wetting tension
$\eta$	$Pa \cdot s$	resin viscosity
$\lambda$	$J \cdot m^{-2}$	spreading coefficient
$\phi$	-	Good-Girifalco interaction parameter
$\phi_a$	-	maximum available fibre volume fraction, in Gutowski model
$\phi_0$	-	fibre vol. fraction at which fibres start to interfere with each other, in Gutowski model
$\phi_1, \phi_2$	-	fibre vol. fraction in $V_1$ and $V_2$
$\theta$	deg	solid-liquid contact angle
$\rho_g, \rho_p$	$g \cdot cm^{-3}$	gas and particle density
$\psi$	deg	wrapping angle

# CURRICULUM VITAE

Marco Tom Connor

born on May 6, 1966

Irish nationality

Married

## *Education*

- 1985 French Baccalauréat in Mathematics
- 1991 Dipl. Ing. (M.S.) in Materials Science  
Swiss Federal Institute of Technology, Lausanne(EPFL), Switzerland.

## *Professional Experience*

- 1991-1992 Research assistant at the Laboratoire de Conservation de la Pierre (EPFL).
- 1992-present Research assistant at the Laboratoire de Technologie des Composites et Polymères (EPFL).

## *List of Publications*

- Connor, M., P. Harding, J. Berg and J.-A. E. Månson, "Fibre Surface Energy Effects on the Mechanical Properties of Unidirectional Fibre Composites," *Proceedings of the ICCM/10*, Vancouver, 1995, VI, p. 541.
- Connor, M., P. Harding, J. Berg and J.-A. E. Månson, "Influence of Fibre Surface Properties on the Mechanical Properties of a Fibre reinforced composite," *J. Adhes. Sci. Technol.* 1995, in press (issue September).
- Connor, M., S. Toll, J.-A. E. Månson and A. G. Gibson, "A Model for the Consolidation of Aligned Thermoplastic Powder Impregnated Composites," *J. Thermoplastic Composite Materials* 1995, 8, 138.
- Connor, M., S. Toll and J.-A. E. Månson, "On Surface Energy Effects in Composite Impregnation and Consolidation," *Proceedings of the 3rd Int. Conf. in Flow Processes in Composite Materials*, Galway, 1994 p. 521. Also in *Composites Manufacturing* 1995, in press.
- Connor, M., A. G. Gibson, S. Toll and J.-A. E. Månson, "A Consolidation Model for Powder Impregnated Composites," *Proceedings of the ICCM/9*, Madrid, 1993, III, p. 575.
- Connor, M., A. G. Gibson, S. Toll and J.-A. E. Månson, "A Model for the Consolidation Process in Thermoplastic Matrix Composites Manufactured by Powder Impregnation," *Proceedings of the 9th Polymer Processing Society Annual Meeting, PPS-9*, Manchester, 1993, p. 181.



Gibson, A. G. and M. Connor, "Impregnation Technology for Thermoplastic Composites: I. A Model for the Impregnation," *Proceedings of the 7th Lausanne Polymer Meeting*, Lausanne, 1992, p. A1.

Girardet, F. and M. Connor, "Investigations sur la Dégradation des Monuments par la Pollution," *Analisis* 1992, 20, M26.

Connor, M. and F. Girardet, "Etude du Mode de Fixation du Soufre sur un Grès Calcareux". *Proceedings of the 7th Int. Congr. on Deterioration and Conservation of Stone*, Lisbon, 1991, I, p. 407.